FACULTY OF ENGINEERING AND ARCHITECTURE

Computational Modeling of Optogenetic Neuromodulation and Neural Recording for Treatment of Temporal Lobe Epilepsy

Ruben Schoeters

Doctoral dissertation submitted to obtain the academic degree of
Doctor of Biomedical Engineering

Supervisors

Prof. Emmeric Tanghe, PhD* - Prof. Robrecht Raedt, PhD** - Thomas Tarnaud, PhD*

* Department of Information Technology
Faculty of Engineering and Architecture, Ghent University

** Department of Head and Skin
Faculty of Medicine and Health Sciences, Ghent University

January 2024

GHENT UNIVERSITY

ISBN 978-94-6355-802-0
NUR 954
Wettelijk depot: D/2024/10.500/7

Members of the Examination Board

Chair

Prof. Filip De Turck, PhD, Ghent University

Other members entitled to vote

Annelies Coene, PhD, Ghent University
Denys Nikolayev, PhD, Université de Rennes, France
Prof. Georgios Spyropoulos, PhD, Ghent University
Prof. Kristl Vonck, Ghent University

Supervisors

Prof. Emmeric Tanghe, PhD, Ghent University
Prof. Robrecht Raedt, PhD, Ghent University
Thomas Tarnaud, PhD, Ghent University

Acknowledgements

Being overjoyed at the completion of this doctoral thesis, I am filled with gratitude for the incredible journey that has spanned over five years. This milestone would not have been possible without the support, encouragement, and expertise of numerous individuals.

First and foremost, I would like to express my sincerest gratitude to my main supervisor, prof. Emmeric Tanghe, whose unwavering support, guidance, and expertise have been pivotal throughout this journey. I am truly grateful for the bond we share, the mutual respect, and the encouragement you provided. Thank you for generously sharing your knowledge at any time of the day and bringing structure and rest when I was overwhelmed.

Deepest appreciation is also extended to my co-supervisor, prof. Robrecht Raedt. Thank you for being enthusiastic about my research during meetings and for sharing your expertise and knowledge on experimental research. To Emmeric and Robrecht, thank you for giving me the opportunity to pursue a PhD and for your valuable comments on my drafts for papers, conference presentations and FWO (Fonds Wetenschappelijk Ondezoek) grant proposal. Additionally, I thank the FWO for funding my research.

I also want to express my heartfelt thanks to my third supervisor and former colleague dr. Thomas Tarnaud. I am grateful for our insightful scientific discussions and conversations on both serious and less serious topics. Thank you for explaining even the most trivial problems, your everlasting optimism, sharing your profound knowledge (being a walking encyclopedia) and contributing interesting research ideas, which were pivotal for this dissertation.

I also want to thank my former supervisor prof. Wout Joseph, for consistently supporting my work and for pushing for publications. Looking back I am glad you did. Special appreciation to prof. Luc Martens for providing me with the opportunity to contribute to the IMEC project and for the stimulating weekly discussions we had during this project, resulting in highly productive and qualitative research.

To the chair of my examination board prof. Filip De Turck and the jury members prof. Kristl Vonck, dr. Denys Nikolayev, prof. Georgios Spyropoulos and dr. Annelies Coene, thank you for reading my dissertation, offering valuable suggestions to improve it, and posing interesting questions and ideas during the internal defense.

To my WAVES colleagues, thanks for the laughter, the brain-busting conversations, and for turning those mundane coffee breaks and lunches into something extraordinary. I will miss our marathon chats that could turn into the wildest topics,

ultimately forgetting how we even got there. I appreciate the good times and the unexpected detours into the weird and wonderful. A special shout-out to Brecht, Jasper, Kenneth, Maarten, Stefaan, Thomas and Tom for being there with me for the longest part of this journey. And to Ine, thanks for throwing these awesome after-work parties and barbecues. I am also grateful to have seen my previous master thesis students, Tom P. and Laila, become valuable colleagues and great conference partners.

A special shout-out to my colleagues from 4Brain, even though our paths only crossed during the last two years due to COVID, you all welcomed me with open arms making me feel like part of the team. I will always cherish our karaoke times. A special and heartfelt thanks to Erine for the amazing Wednesdays. To each one of my colleagues, thanks for being part of this journey, making work feel less like work, and contributing to the unforgettable memories we have created together.

Now, to my incredible family and friends, you have been my unwavering support system. Especially to my parents, Frank and Chantal, my parents-in-law, Hilde and Wim, and Oma and Opa. This thesis would not have been possible without your love and unconditional support. I owe you all a debt of gratitude. A special thanks to my brother-in-law, Anton, for supporting my research by paying taxes. And to my sister, Eline, and brother-in-law, Bart, your check-ins and unwavering mental support have been invaluable. I am grateful to all of you for the moments of fun and rest after work, during the weekends or at holidays, and for always being available for personal support and advice. A special shout-out to my godchild Leon for bringing joy to our family.

My final words of thanks go to my wife, Julie. Your support and love throughout this journey have been so profound that words fail to capture the depth of my gratitude. Your unwavering encouragement, understanding, and the countless sacrifices you made for me and this endeavor are beyond any expression. You have been my rock and the driving force behind every milestone. Thanks to your love, I was literally able to survive the long nights and difficult days, especially those of the last months. Thank you for being there at every step of the way.

Ghent, January 2024
Ruben Schoeters

Table of Contents

List of Figures

List of Tables

List of Acronyms

#

22OM	Double two-state opsin model
3D	Three-dimensional
4AP	4-aminopyridine
4SB	4 Stony Brook

A

AAC	Axo-axonic cell
AAV	Adeno-associated virus
AE	Acousto-electric effect
AENI	Acousto-electrophysiological neuroimaging
AHP	After hyperpolarization
AI	Artificial intelligence
AMD	Advanced micro devices
AMPA	α-amino-3-hydroxy-5-methyl-4-isoxazolepropionic acid
ANN	Artificial neural networks
ANT-DBS	Anterior nucleus of the thalamus deep brain stimulation
AP	Action potential
Arch	Archaerhodopsin-3

B

BC	Basket cell
BIPOLES	Bidirectional pair of opsins for light-induced excitation and silencing
BSC	Bistratified cell

C

C.V.	Coefficient of variation
CA (1, 2, 3)	Cornu Ammonis (1, 2, 3)
ChEF	Opsin chimera with a crossover site at loop E-F
ChETA	ChR2-E123T accelerated
ChIEF	Opsin variant of ChEF with isoleucine 170 mutated to valine

ChR	Channelrhodopsin
ChR1	Channelrhodopsin-1
ChR2	Channelrhodopsin-2
ChR2(H134R)	Channelrhodopsin-2 H134R mutant
CnChR	Chlamydomonos noctigama ChR
CNN	Convolutional neural networks
CNS	Central nervous system
CP15	Cutsuridis and Poirazi 2015
CVODE	NEURON's multi-order variable time step integration solver

D

DA	Dark adapted
DBS	Deep brain stimulation
DC	Direct current
DG	Dentate gyrus
DOI	Dipole of interest
DREADD	Designer receptors exclusively activated by designer drug

E

EC	Ethorinal cortex
ECD	Ethical committee for animal experimentation
ECL(2, 3)	Enthorinal cortex layer (II, III)
ECoG	Electrocorticography
EEG	Electroencephalography
EET	Elementary effects test
EP	Evoked potential
EPamp	Evoked potential amplitude
EPslope	Evoked potential slope
EPSP	Excitatory postsynaptic potential
EPstart	Evoked potential start time
ESI	Electrophysiological source imaging

F

FDA	United States food and drug administration
fEPSP	Field excitatory postsynaptic potential
fMRI	Functional magnetic resonance imaging
fNIRS	Functional near-infrared spectroscopy
FUS	Focused Ultrasound
FWHM	Full width at half maximum

G

GABA	Gamma-aminobutyric acid

GC	Granule cell
gcl	Granule cell layer
GtACR	Guillardia theta anion conducting rhodopsin

H

HC	Hilar perforant path associated cell
HF	Hippocampal formation
HPC	High performance computing
HS	Hippocampal sclerosis

I

IDA	Initial dark-adapted
IEEE	Institute of electrical and electronics engineers
ILAE	International League Against Epilepsy
int	Interneuron
INTERSECT	Intron recombinase sites enabling combinatorial targeting
IQR	Interquartile range

L

LA	Light adapted
LB	Lower bound
LED	Light-emitting diode
LFP	Local field potential
LIFU	Low intensity focused ultrasound
lm	Lacunosum-moleculare
loc	Location

M

M.C.	Monte Carlo
MC	Mossy cell
mChR	Mesostigma viride ChR
MCS	Multi channel systems
MEA	Multielectrode array
MEG	Magnetoencephalography
MerMAID / MM	Meta-genomically discovered, Marine, Anion-conducting and Intensely Desensitizing ChRs
MI	Mechanical index
MIDA	Multimodal imaging-based detailed anatomical model of the human head and neck
ml	Molecular layer
mPOI	Mean position of interest
mPSO	Mean position of interest same order of magnitude
MRG	McIntyre-Richardson-Grill

MRI	Magnetic resonance imaging
mTLE	Mesial temporal lobe epilepsy

N

NA	Numerical aperture
NEURON	Simulation environment for neurons and networks of neurons
NMDA	N-methyl-D-aspartic acid
NpHR	Natronomonoas pharaonis halorhodopsin

O

OCD	Obsessive-compulsive disorder
ode	Ordinary differential equation
OLM	Oriens lacunosum-moleculare cell
O-LM	Oriens lacunosum-moleculare

P

PD	Pulse duration
PET	Positron emission tomography
pl	Polymorphic layer
PNP	Peak negative pressure
PNS	Peripheral nervous system
POI	Position of interest
PP	Double product
PRF	Pulse repitition frequency
PS	Population spike
PSamp	Population spike amplitude
PSD	Power spectrum density profile
pyr	Pyramidal
PYR	Pyramidal cell

R

RAM	Random access memory
RC	Resistor–capacitor
RMSE	Root mean square error
RMSNE	Root mean square normalized error
RMSWE	Root mean square weighted error
RMSZE	Root mean square Z-score error
RNS	Responsive neurostimulation
RS	Regular spiking neuron
$RSBH^{+}$	Retinal Schiff base
RSRS	Double reciprocal sum

S

S4L	Sim4life
SDC	Strength duration curve
SEP	Medial septum
SFO	Step-function opsin
ShChR	Stigeoclonium helveticum ChR
SNN	Spiking neural networks
SoFPAN	Surface of fiber positions for the activation of neurons
sPING	Sparse Pyramidal interneuron network gamma

T

tABI	Transcranial acoustoelectric brain imaging
TAC	Temporal average current
tACS	Transcranial alternating current stimulation
tDCS	Transcranial direct current stimulation
TK21	Tomko 2021
TLE	Temporal lobe epilepsy
TMS	Transcranial magnetic stimulation

U

UB	Upper bound
UCSDI	Ultrasound current source density imaging
UNMOD	Ultrasound neuromodulaiton
US	Ultrasound

V

VChR	Volvox carteri ChR
VNS	Vagus nerve stimulation
VSVO	Variable step variable order
VTA	Volume of tissue activation

W

WiChR	Wobblia lunata K^+-conducting ChR

Nederlandse Samenvatting –Summary in Dutch–

De neurowetenschap heeft de afgelopen jaren opmerkelijke vooruitgang geboekt. Nieuwe technieken en hulpmiddelen hebben frisse perspectieven geboden. Ondanks deze vooruitgang blijven neurologische ziektes nog steeds een aanzienlijke uitdaging vormen. Een groot deel van de bevolking wordt getroffen door deze ziektes, wat leidt tot een daling van hun levenskwaliteit. Bovendien is de economische last die gepaard gaat met deze aandoeningen aanzienlijk. Dit benadrukt de noodzaak voor voortdurende klinische vooruitgang en de nood aan innovatieve therapieën. Technieken zoals cochleaire implantaten, visuele prothesen, hersen-computer interfaces en diepe hersenstimulatie bieden hoop voor de toekomst van patiënten. Deze technieken hebben reeds aangetoond de levenskwaliteit van patiënten te kunnen verbeteren. Echter, volledige herstel of genezing van ziekten is momenteel nog niet mogelijk. Veel van deze technologieën bevinden zich nog in hun beginstadium, waardoor uitdagingen aangepakt moeten worden die leiden tot potentiële verbetering. Ook neuromodulatietechnieken die momenteel alleen in preklinische setting gebruikt worden, zoals optogenetica, zijn veelbelovend. Echter, vertaling naar klinische toepassing komt met extra moeilijkheden. Toch maken de potentiële voordelen van deze geavanceerde technieken ze het nastreven waard, ondanks de complexiteiten die ermee gepaard gaan. Daarnaast is er een opmerkelijke verschuiving van open- naar gesloten-lussystemen, waarbij overbodige stimulatie wordt beperkt door realtime aanpassingen. Om met deze systemen specifieke controle te verkrijgen, is de opmeting van elektrofysiologische activiteit met een hoge ruimtelijke en temporele resolutie van cruciaal belang.

Computationele neurowetenschap, een snel evoluerend deelgebied van neurowetenschappen, bestudeert deze uitdagingen aan de hand van wiskundige modellen. Het integreert technieken uit verschillende domeinen, waaronder elektrische ingenieurswetenschappen, informatica, geneeskunde en natuurkunde. Het voordeel ten opzichte van experimenteel onderzoek is de volledige controle over de parameterruimte. De toenemende rekenkracht van computers en de komst van supercomputers maken snel en systematisch onderzoek mogelijk. Dit is waardevol voor het ontrafelen van de complexiteit van het zenuwstelsel en het verkennen van neuromodulatieparameters om therapieën te verbeteren. Het brein bevat 86 miljard neuronen en is extreem complex samengesteld. De huidige modellen en rekenmiddelen staan nog niet toe om dit uitgebreid systeem gedetailleerd te modelleren. Daarom moeten modellen vaak een balans vinden tussen biologisch realisme en

eenvoud. Bovendien kunnen modellen niet op zichzelf staan. Een voortdurende cyclus van modelvalidatie en het testen tegen experimentele data is noodzakelijk.

Dit proefschrift bevat zes hoofdstukken. In het eerste hoofdstuk wordt het vakgebied van de neurowetenschap geïntroduceerd met een basis van hersenanatomie en neurofysiologie. In het bijzonder wordt het actiepotentiaal (AP) beschreven dat de fundamentele eenheid in neuronale communicatie is. Ook wordt een overzicht gegeven van huidige en veelbelovende neuromodulatiestrategieën, allemaal met een bijzondere focus op hun potentiële toepassing bij de behandeling van temporale kwabepilepsie (TKE). In het laatste deel van dit hoofdstuk worden de fundamenten van de computationele neurowetenschap geïntroduceerd. Twee type modellen worden in meer detail besproken: de modellen gebaseerd op het Nobelprijs-winnende werk van Hodgkin en Huxley, en de dipoolmodellen. Deze modellen worden gedurende het hele proefschrift gebruikt met als doel de kennis van de optogenetische technologie, het modelleren van de hippocampus en TKE-pathologieën, en de potentiële toepassing van ultrasone golven voor functionele neurologische beeldvorming te verbeteren.

Hoofdstuk 2 bespreekt de optogenetische technologie. Optogenetica is een veelbelovende techniek met precieze controle over neurale activiteit. Deze controle wordt bereikt door lichtgevoelige eiwitten, genaamd opsines, genetisch tot expressie te brengen in hersencellen. Vervolgens kan de neuronale activiteit met hoge temporele precisie worden gecontroleerd door middel van een optische bron. Er bestaan reeds talloze opsines met verschillende eigenschappen. Twee belangrijke klassen zijn de inhiberende en exciterende opsines. Het doel van de eerste is om neuronale activiteit te onderdrukken, terwijl de laatste de generatie van actiepotentialen bevordert. Gecombineerd in een enkele neuronpopulatie maakt dit bidirectionele controle mogelijk, een unieke eigenschap van optogenetica in tegenstelling tot alle andere neuromodulatiemodaliteiten. Optogenetica wordt momenteel alleen gebruikt in preklinische studies, behalve voor de behandeling van retinitis pigmentosa met twee lopende klinische onderzoeken. Twee belangrijke uitdagingen voor de translatie naar klinische toepassing in de menselijke hersenen zijn de langetermijnveiligheid van gentherapie en implantatie van de optische bron. Een andere uitdaging is het verschil in grootte tussen knaagdier en de menselijke hersenen ($\times 1000$) waardoor een opschaling van de techniek noodzakelijk is. Computationele modellen kunnen worden gebruikt om strategieën te bestuderen met als doel om efficiëntere technieken te bekomen. Daarom is een wiskundig model van de stroom door het opsine vereist. Een nieuw dubbel tweestaten opsinemodel is ontworpen om de computationele efficiëntie en nauwkeurigheid in het modelleren van de opsinekinetiek te verbeteren. Bijkomend is een autonome procedure ontworpen die gebruikt werd om twee verschillende opsines, ChR2(H134R) en MerMAID, binnen een acceptabel tijdsbestek en met beperkte rekencapaciteit te fitten.

In hoofdstuk 3 bestudeer ik strategieën om de exciteerbaarheid van optogenetische stimulatie te verhogen. Deze zijn belangrijk voor de overgang van muis naar menselijke hersenen. De exciteerbaarheid van geïsoleerde cornu ammonis 1-cellen (CA1) met ChR2(H134R) wordt onderzocht in geavanceerde computationele modellen. De opsinestroom wordt gemodelleerd met het ontwikkelde dubbele

tweestaten opsinemodel dat in hoofdstuk 2 is beschreven. De resultaten tonen aan dat het beperken van de expressie van het opsine tot specifieke neuronale membraancompartimenten de exciteerbaarheid aanzienlijk verbetert. Bovendien zijn de simulaties gekoppeld aan een gesimuleerd lichtveld. Hierdoor is bepaling van de optimale en slechtste optrodeposities mogelijk. De lichtvelden worden bepaald via Monte Carlo-simulaties in grijs hersenweefsel. De optimale configuratie is een lichtbron loodrecht op de meest prikkelbare celgebieden, zoals, de basale dendrieten in piramidale cellen of de soma in de interneuronen. Ook wordt de simulatiefout gekwantificeerd door het uitsluiten van het lichtprofiel op het neuronale niveau. Opmerkelijk benadrukken de resultaten het belang van neuronendegeneratie dat wordt waargenomen in de variabiliteit tussen de verschillende celmodellen. Ten slotte wordt een algemene gevoeligheidsanalyse uitgevoerd om zes onzekere parameters te testen, namelijk de optische veldeigenschappen (absorptie- en gereduceerde verstrooiingscoëfficiënten), locatie en expressieniveau van het opsine, cel en optische vezel oriëntatie en de driedimensionele structurele morfologie van de cellen. De studie identificeert locatie en expressieniveaus van het opsine als belangrijkste parameters op de resultaten. Aan de andere kant is nauwkeurige bepaling van de exciteerbaarheidsdrempels door deze onzekerheden moeilijk. Samenvattend biedt dit hoofdstuk nieuwe inzichten in de optogenetische exciteerbaarheid van CA1-cellen die nuttig kunnen zijn voor de ontwikkeling van verbeterde optogenetische stimuleringsprotocollen voor de behandeling van neurologische aandoeningen zoals TKE.

Hoofdstuk 4 bespreekt de ontwikkeling van een netwerkmodel van de epileptische hippocampus. Dit model maakt het testen van neuromodulatiestrategieën binnen een meer realistische netwerkcontext mogelijk met als doel inzichten te verkrijgen in ziektepathologieën en om stimulatieparameters te verbeteren. De natuurlijke hippocampale activiteit kan effectief worden gemodelleerd met vereenvoudigde compartimentele neuronmodellen. Echter, vanwege deze vereenvoudigingen kunnen niet alle vormen van neurale activiteit worden gereproduceerd met een enkel model. Bovendien worden twee epileptische modellen getest. Verhoogd extracellulair kalium wordt in-vitro gebruikt om epileptische activiteit te induceren. Hoewel het model niet is gemaakt met het oog op verhoogde kaliumniveaus, is het wel in staat om overeenkomsten met experimentele gegevens te reproduceren. Voorbeelden zijn het optreden van spontane activiteit pas na een 2.61-voudige verhoging en de waarneming van oscillerende activiteit in de CA1 na Schaffer collaterale stimulatie. Ten tweede worden histopathologische veranderingen, aanwezig bij mesiale temporale kwab epilepsie, getest. De resultaten tonen aan dat terugkerende verbindingen cruciaal zijn voor het opwekken van epileptische aanvalachtige activiteit afkomstig uit de hippocampus. Het verlies van de korrelcellen en CA1-cellen resulteert in verminderd burstgedrag. Echter, dit zijn eerste resultaten en verdere validatie is vereist. Niettemin zijn de huidige bevindingen veelbelovend en suggereren de potentiële bruikbaarheid van dit epileptische netwerkmodel als een hulpmiddel voor het onderzoeken van technieken voor het onderdrukken van epileptische aanvallen zoals optogenetica.

Hoofdstuk 5 introduceert het concept van akoesto-elektrofysiologische neurolo-

gische beeldvorming (AENB), een potentieel transformerende techniek met slechts millimeters ruimtelijke en minder dan milliseconde temporele resolutie. Deze techniek kan van cruciaal belang zijn voor de ontwikkeling van gesloten-lussystemen. AENB maakt gebruik van gerichte ultrasone golven om hersengebieden te markeren. Vervolgens wordt hun elektrische activiteit gemoduleerd naar de ultrasone frequentie. Het onderliggend mechanisme dat wordt onderzocht, is signaalmodulatie ten gevolge van mechanische vibratie ten opzichte van de meetelektroden. De haalbaarheid van deze techniek wordt geëvalueerd aan de hand van simulaties met dipoolmodellen in een sferische benadering van muizen- en menselijke hoofden. Er worden drie verschillende radiale elektrodeposities getest, het equivalent voor natte en droge transcraniale, en corticaal geplaatste elektroden. Het intensiteitsprofiel voor de stroom lopende in het dipool is afgeleid van een opgelegde machtsfunctie voor het spectraal vermogensprofiel, dit vanwege de onzekerheid op de natuurlijke activiteit van de hersenen bij ultrasone frequenties. In het hoofdstuk werd aangetoond dat mechanische trillingen effectief endogene hersenactiviteit op de ultrasone frequentie moduleren. De signaalsterktes zijn echter niet-lineair afhankelijk van de uitlijning tussen de dipooloriëntatie, trillingsrichting en elektrodeposities. De signaalsterktes zijn laag, met sterktes slechts in de picovolt grootteorde voor een dipoolmoment van 5 nAm en ultrasone drukken binnen FDA-limieten. Bijgevolg is de haalbaarheid van de techniek afhankelijk van de natuurlijke hersenactiviteit op ultrasone frequenties, een momenteel onbekende factor, en de vooruitgang in elektrodetechnologie om pV-orde signalen te kunnen opmeten. Het scannen van hyperactieve zones zou een meer veelbelovende toepassing kunnen zijn, aangezien de signaalsterkte lineair schaalt met de activiteit in de gemarkeerde zone.

Samenvattend, demonstreert dit doctoraat de rol van computationele neurowetenschap in het uitbreiden van de kennis over neuromodulatietechnieken, neurale circuits en functionele neurologische beeldvorming. De bevindingen bieden inzichten die de ontwikkeling van effectievere behandelingen voor neurologische aandoeningen kunnen bevorderen, met als uiteindelijk doel om de levenskwaliteit van de patiënten te verbeteren.

English Summary

Neuroscience has made remarkable progress over recent years. Novel techniques and tools have offered fresh perspectives on neural circuitry. However, despite these advancements, neurological disorders continue to pose a significant challenge. A substantial part of the population is affected, causing a decline in their quality of life. Moreover, the economic burden associated with these disorders is substantial, underscoring the need for continued clinical progress and innovative therapies. Techniques like cochlear implants, visual prostheses, brain-computer interfaces, and deep brain stimulation hold promise for the future of patients. At their current state, they are able to improve patients' quality of life but do not offer complete restoration of natural functions or cure diseases. Many of these technologies are still in their early stages, with multiple improvements yet to be explored and challenges to be tackled. Also, neuromodulation techniques that are currently only being used in preclinical setting, like optogenetics, have shown promising results. However, clinical translation awaits its own set of difficult challenges. Still, the potential benefits of these advanced techniques make them worth pursuing, despite the complexities involved. Additionally, there is a notable shift from open- to closed-loop systems, mitigating redundant stimulation by providing real-time adjustments. In order for these systems to achieve on-demand control, the recording of electrophysiological activity with high spatial and temporal resolution will be pivotal.

Computational neuroscience, a rapidly evolving subfield of neuroscience, offers a unique approach to tackle these challenges by utilizing mathematical tools. It integrates techniques from various domains, including electrical engineering, computer science, medicine, and physics. Its advantage over experimental research is the full control over the parameter space. Together with the increasing computation power and arrival of supercomputers, computational models enable rapid and systematic investigations, valuable for unraveling the complexities of the nervous system and exploring neuromodulation settings to improve therapies. However, with its 86 billion neurons, the brain is extremely complex. Models and computational resources do not allow detailed modeling of such a vast system yet. Therefore, models have to strike a balance between biological realism and model simplicity. Additionally, models cannot stand on their own. A continuous cycle must exist of model validation and testing against experimental data.

This dissertation contains six chapters. In the first chapter, the field of neuroscience is introduced, including the basics of brain anatomy and neurophysiology. In particular, the action potential (AP) is described, being the fundamental unit of

neuronal signaling. Moreover, an overview of current and promising neuromodulation strategies is provided, all with a particular focus on their potential application in treating temporal lobe epilepsy (TLE). In the final part of this chapter, the field of computational neuroscience is introduced. Conductance-based models, which are based on Hodgkin and Huxley's Nobel Prize-winning work, and dipole models are described in more detail. The concepts of these models are used throughout the whole dissertation with the goal of improving our understanding of optogenetic technology, modeling of the hippocampus and TLE pathologies, and the potential application of ultrasound in functional neuroimaging.

Chapter 2 delves into a promising technique offering precise control over neural activity called optogenetics. This precise control is achieved due to genetically expressing light-sensitive proteins, called opsins, in brain cells. Subsequently, neuronal activity can be controlled with high temporal precision by an optical source. To date, numerous opsins with a variety of properties exist. Two major classes are the inhibitory and excitatory opsins. The purpose of the former is to inhibit neuronal firing, while the latter promotes AP generation. Combined in a single neuron population, this enables bidirectional control, a unique property of optogenetics compared to all other neuromodulation modalities. Except for the treatment of retinitis pigmentosa with two ongoing clinical trials, optogenetics is currently only being used in a preclinical setting. Long-term safety concerns of gene therapy and implantation of the optical source form two major challenges for clinical translation towards treatment of disorders in the human brain. Another challenge is upscaling from rodent to human brain due to the difference in size ($\times 1000$). Computational models can be used to investigate strategies in improving the technique's efficiency. Therefore, a computational model of the opsin's photocurrent is required. Chapter 2 introduces my novel double two-state opsin model designed to enhance computational efficiency and accuracy in modeling of opsin kinetics. Furthermore, an autonomous fitting procedure is presented that is used to efficiently fit two distinct opsins, ChR2(H134R) and MerMAID, within an acceptable time frame and with limited computational resources.

Chapter 3 attempts to identify strategies to increase excitability that could aid the transition from mouse to human brain. The excitability of isolated CA1 cells expressing ChR2(H134R) is investigated in state-of-the-art computational models. The photocurrent is modeled with the double two-state opsin model described in chapter 2. The results reveal that restricting opsin expression to specific neuronal membrane compartments significantly enhances excitability. Moreover, the neuron simulations are coupled with light propagation, enabling identification of optimal and suboptimal optrode positions. The light intensity fields are determined via Monte Carlo simulations for gray matter tissue. Optimal results are achieved by aligning the light beam perpendicular to the most excitable cell regions, such as the basal dendrites and soma in pyramidal cells and interneurons, respectively. Also the simulation error by excluding the irradiance profile at the neuronal level is quantified. Notably, the results underscore the importance of considering neuron degeneracy observed in the inter-cell variability. Finally, a global sensitivity study is performed to test six uncertain parameters, i.e., optical field properties (absorption

and reduced scattering coefficients), opsin expression level and location, cell-to-fiber orientation, and cellular 3D structural morphology. The study identifies opsin location and expression levels as key determinants of simulation outcomes. On the other hand, uncertainties in these parameters limit precise determination of the irradiance thresholds. This chapter provides valuable insights on optogenetic excitability of CA1 cells useful for the development of improved optogenetic stimulation protocols for neurological disorders like TLE.

Chapter 4 expands the scope to include network modeling, specifically creating a network model of an epileptic hippocampus. This model serves as a valuable tool for testing neuromodulation strategies within a network context, fine-tuning stimulation parameters, and gaining insights into disease pathologies. The native hippocampal activity can be effectively modeled with simplified compartmental neuron models. However, due to the simplifications made, not all forms of neural activity can be replicated with the single model. Two epileptic models are tested. Elevated extracellular potassium is used in-vitro to induce epileptiform activity. Although the model was not initially fit to data with elevated potassium levels, it is able to reproduce similarities with experimental data under these conditions. Examples include the occurrence of spontaneous activity only after a 2.61-fold increase and the observation of oscillatory activity in the CA1 after Schaffer collateral stimulation. Second, histopathological changes present in mesial temporal lobe epilepsy are tested. The results show that recurrent connections are crucial for inducing epileptic seizure-like activity originating in the hippocampus. The loss of granule cells and CA1 cells results in reduced burst behavior. However, these are preliminary results and further validation is required. Nevertheless, the current findings are promising and suggest the potential utility of this epileptic network model as a tool for investigating epileptic seizure suppression techniques such as optogenetics.

Chapter 5 introduces the concept of acousto-electrophysiological neuroimaging (AENI), a potentially transformative technique with millimeter spatial and sub-millisecond temporal resolution. This technique holds the potential to be pivotal for the development of closed-loop systems. AENI leverages focused ultrasound (FUS) to tag brain regions, modulating their electrical activity onto the ultrasonic frequency. The underlying mechanism investigated is signal modulation due to mechanical vibration relative to the measuring electrodes. The feasibility of this technique is evaluated through comprehensive simulations with dipole models in a spherical approximation of mouse and human heads. The simulations are solved for three different radial electrode positions, replicating wet and dry transcranial, and cortically placed electrodes. The current intensity profile of the dipoles is drawn from an artificial power-law power spectral density profile, due to the uncertainty in the brain's inherent activity at ultrasonic frequencies. In the chapter it is revealed that mechanical vibration effectively modulates endogenous brain activity onto the ultrasonic frequency. Signal strength, however, depends non-linearly on the alignment between dipole orientation, vibration direction, and recording positions. Still, the signal strengths are low, being only in the pV-range for a dipole moment of 5 nAm and ultrasonic pressures within FDA-limits. Consequently, the technique's feasibility relies on the inherent activity of the brain at ultrasonic frequencies, a

currently unknown factor, and the advance in electrode technology to measure pV-order signals. Scanning for hyperactive zones could be a more promising application, as signal strength scales linearly with the probed zone's activity.

In summary, this dissertation demonstrates the role of computational neuroscience in advancing our understanding of neuromodulation techniques, neural circuitry, and functional neuroimaging. The findings offer insights that can inform the development of more effective treatments for neurological disorders, ultimately improving the quality of life of those who are affected.

1 Introduction

Neuroscience has witnessed remarkable advancements in recent years. Various new techniques, with different underlying physics, have joined the classical biochemical and electrophysiological toolbox. These innovations have led to new insights into neural circuitry. However, approximately one in three individuals is still anticipated to experience a neurological disorder at some point in their life. Having such a disorder results in a substantial decline of their quality of life due to increased adverse psychosocial, behavioral and cognitive consequences, excess injury risk, and mortality [1]. Moreover, they impose an enormous economic burden, with an estimated cost of $1.7 trillion in the USA and Europe combined [2]. Encouragingly, clinical progress continues, leading to an improved understanding of disease pathologies and the development of innovative therapies. For instance, deaf patients are able to hear again with cochlear implants, blind people regain sight with visual prostheses, paralyzed people are able to walk again with brain-computer interfaces, and deep brain stimulation (DBS) relieves the symptoms of patients with neurological disorders like Parkinson's disease and epilepsy. It is important to note that currently these techniques do not fully restore lost functions to a natural state or cure diseases. However, they do enhance patients' quality of life by partially reinstating certain functionalities.

This dissertation falls within the field of computational neuroscience, a subfield of neuroscience that aims to unravel the complexities of the nervous system with mathematical tools. This initial chapter serves as an introduction to the field of neuroscience, focusing on aspects such as brain anatomy, neuron electrophysiology, and temporal lobe epilepsy (TLE). Following this, a comprehensive overview of current and promising neuromodulation techniques for TLE treatment is provided. The subsequent section elucidates the fundamental principles in computational neuroscience. The chapter concludes by outlining the research objectives, presenting a structured overview of the dissertation, and including a list of relevant publications.

1.1 Neuroscience

Neuroscience is a multidisciplinary field dedicated to the study of the nervous system. It is a complex system with a crucial role in controlling and coordinating physiological processes and behaviors in organisms. In order to understand the concepts discussed in this dissertation, I provide below a concise introduction to brain anatomy and neuron electrophysiology. Furthermore, I will discuss the hippocampus and its significance in temporal lobe epilepsy.

1.1.1 The Brain Anatomy

The nervous system can be divided into two main components: the central nervous system (CNS) and the peripheral nervous system (PNS). The PNS comprises the nerves that transmit signals between the CNS and the rest of the body. The CNS consists of the brain and the spinal cord. The brain is the central organ with anatomically distinct regions, each specialized for specific functions. These regions include the cerebrum, diencephalon, midbrain, pons, medulla and cerebellum. The latter, also known as little brains, is essential for motor coordination. The midbrain, pons and medulla form the brainstem. It links the spinal cord with the forebrain and is responsible for regulating vital functions, e.g., heart rate, breathing and sleep. The forebrain encompasses the cerebrum and the diencephalon. The diencephalon consists of the thalamic structures, with the thalamus being a critical relay for sensory information and the hypothalamus regulating homeostatic functions (e.g., hunger, thirst and temperature). The cerebrum can be subdivided as well. The outermost layer of the brain is called the cerebral cortex. It is responsible for higher cognitive functions, including thought, sensation and voluntary muscle movement. It exhibits a folded structure with gyri (crests) and sulci (grooves). Beneath the cortex lies white matter composed of myelinated axons, while the gray matter (cerebral cortex) houses the cell bodies. The cerebrum can further be subdivided into four lobes: frontal, temporal, parietal and occipital. A particularly important structure located in the temporal lobe is the hippocampus, known for its role in memory storage. The interested reader can find a detailed overview of all structures in Purves and Dale [3].

At the cellular level, the brain primarily comprises two types of cells: neurons and glia. The human brain is estimated to contain approximately 86 billion neurons and as many glial cells [4]. Moreover, each neuron can have thousands of connections. Neurons serve as the primary signaling units, transmitting electrical impulses throughout the nervous system. Despite variations in neuron morphology, they share common structures: the cell body (soma), dendrites, axons, and synapses, each with a specific functionality. In contrast, glia play essential support roles: astrocytes maintain chemical balance and provide structural support, oligodendrocytes myelinate axons, and microglia participate in immune responses [5, 6].

1.1.2 Neuron Electrophysiology

A phospholipid bilayer of approximately 5 nm thickness forms the cell membrane of a neuron, separating the intra- and extracellular space. It is permeable to lipophilic substances, limited permeable to water and impermeable to ions or other charged molecules. Consequently, there exist electrochemical gradients across the membrane due to differences in ion concentrations between the intra- and extracellular space. The extracellular space is seawater like, meaning high sodium and chloride concentrations are present. Intracellularly, potassium is more prevalent. There is also a Ca^{2+} gradient, with a higher concentration extracellularly. This ion concentration imbalance results in the establishment of a negative potential across the membrane, typically around -70 mV (with the outside, by conventional, defined as zero, see box 1.1).

Scattered across the membrane are numerous transmembrane proteins (see figure 1.1). These proteins enable movement of ions through the membrane. Ion channels and transporters (pumps) are two examples. Transporters use energy to transport ions against their electrochemical gradients, while ion channels form aqueous pores that permit the high fluxes of ions down their electrochemical gradients. Ion channels typically contain a charge filter, determining a cation or anion selectivity, with an additional size filter, making the channels highly selective for one specific ion.

Neurons are commonly seen as integrators [7], processing information in a unidirectional flow. They receive inputs from other neurons at their dendrites, evoking post synaptic potentials. These propagate along the dendritic tree towards the soma. At the axon hillock, these inputs are integrated over space and time. If the result surpasses a certain threshold, an action potential is initiated. This action potential subsequently travels down the axon towards the synapses. The membrane depolarization associated with the action potentials triggers calcium ion influx at the presynaptic bouton. This initiates neurotransmitter release into the synaptic cleft. These neurotransmitters then diffuse and bind to receptors located on the postsynaptic membrane, opening ligand-gated ion channels. A schematic depicting synaptic connectivity is presented in figure 1.1.

The action potential (AP) is the fundamental unit of neuronal signaling (see figure 1.5). It is this all-or-nothing event driven by opening and closing of voltage gated channels. Alan Hodgkin and Andrew Huxley were the first to record the membrane potential changes during an action potential in a giant axon of a squid using the voltage clamp technique. They quantitatively described the AP in terms of voltage-gated sodium and potassium channels [8]. A scientific breakthrough that was awarded with a Nobel Prize in Physiology and Medicine in 1963. Membrane depolarization increases the open probability of voltage-sensitive channels. Sodium channel opening causes an influx of sodium ions, further depolarizing the cell initiating a positive feedback loop. Conversely, potassium channel opening leads to potassium efflux, resulting in repolarization (a negative feedback loop). An action potential is initiated when the positive feedback loop dominates the negative feedback. Sodium channels have faster kinetics. At a strong initial depolarization,

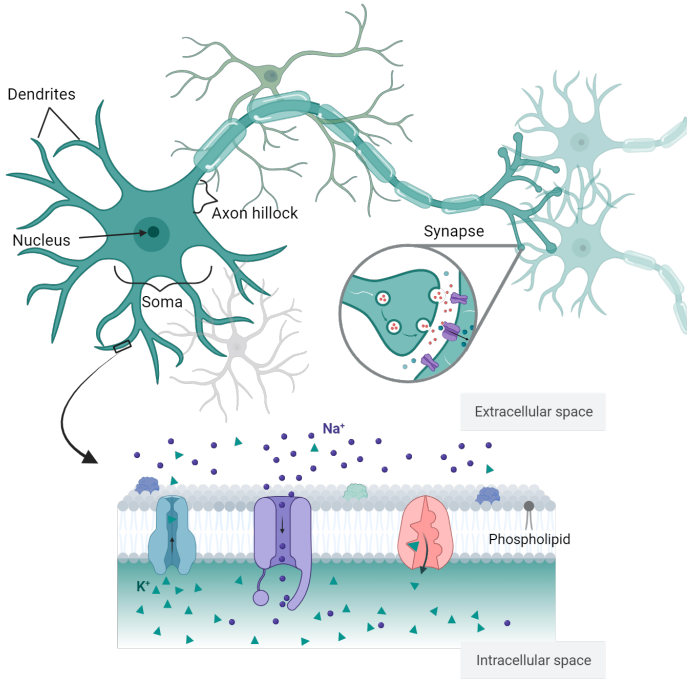

Figure 1.1: Schematic representation of a motorneuron with myelinated axon and the phospholipid bilayer. The synaptic cleft is shown in the inset. Depicted on the cell membrane are voltage gated sodium and potassium channels, and a sodium-potassium transporter. Figure created with Biorender

sodium channels open first, further depolarizing the cell towards the sodium reversal potential. Simultaneously, potassium channels open, slowing depolarization and eventually initiating repolarization. Sodium channels inactivate, driving the membrane potential back to rest. Finally, delayed closing of the potassium channels results in hyperpolarization before the neuron returns to its resting state (see definitions in box 1.1) [3, 5, 9].

1.1.3 Hippocampus and Temporal Lobe Epilepsy

The hippocampus, named for its seahorse-like shape, is situated within the medial temporal lobe (see figure 1.2). As aforementioned, it has a pivotal role in memory consolidation. The hippocampus can be subdivided into separate regions: the dentate gyrus, CA3 (Cornu Ammonis 3), CA2, CA1, and the subiculum. Unlike in other brain regions with extensive reciprocal connections, the hippocampus is predominantly unidirectional. Information from the entorhinal cortex arrives via the perforant path in the dentate gyrus. Then travels over the mossy fibers (i.e.,

the axons of the granule cells) towards the CA3 region. Subsequently, the CA3 pyramidal cells project onto the CA1 region via the Schaffer collaterals. This pathway is commonly referred to as the trisynaptic circuit (see figure 1.2 (bottom)). The CA1 then projects onto the subiculum. Finally, the CA1 and subiculum convey processed information back to the enthorinal cortex. While the actual connectivity is more complex, with the perforant path projecting to CA3 and CA1, and CA3 forming associational connections with itself, the trisynaptic circuit serves as the fundamental pathway for information processing in the hippocampus.

Both the Cornu Ammonis and the dentate gyrus exhibit a laminar structure characterized by distinct cell layers. In the CA subfields, the *stratum pyramidale* contains the pyramidal cell bodies along with a subset of basket and bistratified interneurons. The basal dendrites and the axon of the pyramidal cells reside in the *stratum oriens*. It also houses the O-LM interneuron whose axons extend toward the most distal end of the pyramidal apical dendrites in order to mediate inputs from the enthorinal cortex. This layer is called the *stratum lacunosum-moleculare*. The *stratum radiatum*, positioned between the stratum pyramidale and lacunosum-moleculare, is where the Schaffer collateral or mossy fiber connections (in CA1 or CA3, respectively) are found. The dentate gyrus comprises three layers: *stratum granulosum*, the *hilus* (polymorphic layer), and the *stratum moleculare*. Granule cell bodies are located in the stratum granulosum, with their unipolar dendrites extending towards the stratum moleculare. Their axons reside in the *hilus* together with the majority of the interneurons. The general structure of the hippocampus is conserved across species. However, substantial differences exist, particularly in size ($\times 100$, see figure 1.2) and thickness of pyramidal cell layer ($\times 6$) [10].

Temporal Lobe Epilepsy

Epilepsy is with a prevalence of 0.5-1%, one of the most common neurodegenerative diseases worldwide [11, 12]. Patients with uncontrolled epilepsy experience recurrent, unprovoked seizures. Seizures are defined by the International League Against Epilepsy (ILAE) as “transient occurrences of signs and/or symptoms due to abnormal excessive or synchronous neural activity in the brain” [13]. Temporal lobe epilepsy (TLE) is the most common type of focal epilepsy in adults and most difficult to treat with antiepileptic drugs. In TLE, seizures primarily originate in the mesial temporal lobe structure (mTLE) indicating involvement of the cortico-hippocampal circuit [14].

Two main histopathologies are observed with mTLE: hippocampal sclerosis (HS) and mossy fiber sprouting. HS is the most prevalent, characterized by the (severe) loss of hippocampal neuronal cells and pronounced astrogliosis. The CA1 region often exhibits the most significant cell loss, with over 80% reduction. The primary targeted cells are the pyramidal neurons situated within the CA1 and CA3 regions. Additionally, extensive granule cell loss is observed, up to 50%, accompanied by granule cell dispersion [15]. The second histopathology is mossy fiber sprouting, i.e., the formation of recurrent connections between granule cells [16].

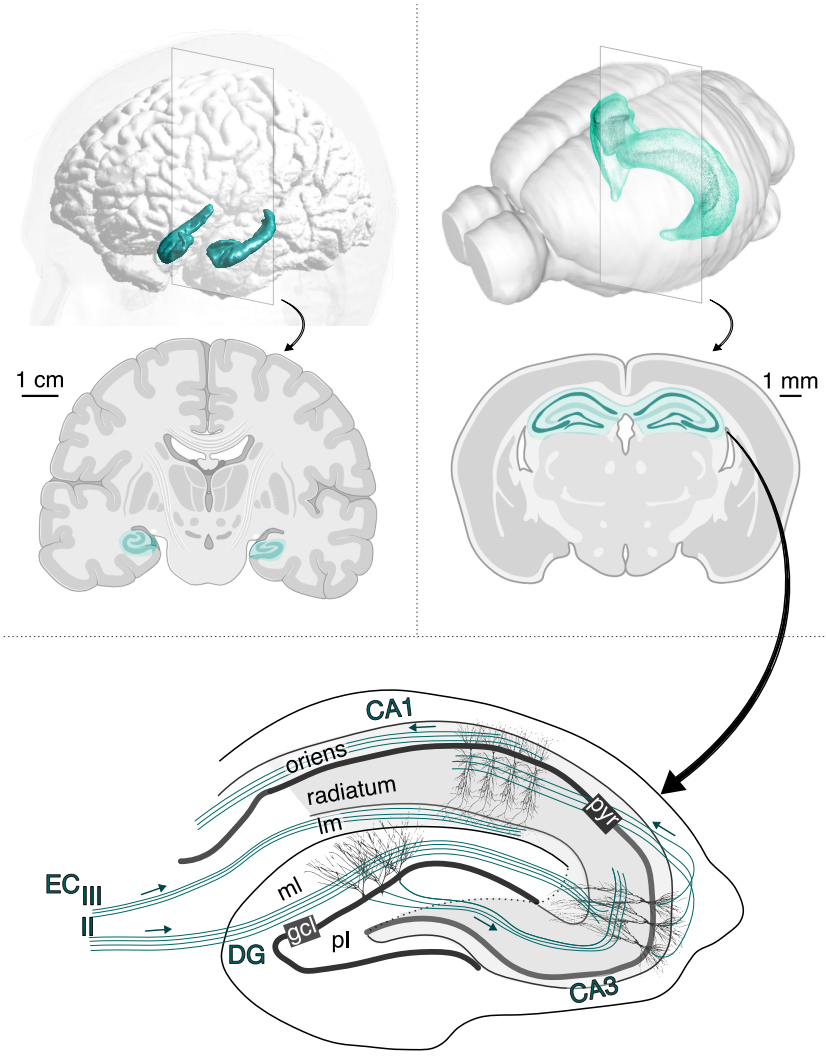

Figure 1.2: The hippocampal anatomy. 3D and coronal section views of the human and mouse hippocampus, left and right, respectively. (Bottom) The detailed laminar structure of the hippocampus, including the dentate gyrus (DG) with the molecular (ml), granule cell (gcl) and polymorphic (pl) layers; the Cornu Ammonis 3 and 1 (CA3, CA1) with the oriens, pyramidal (pyr), radiatum and lacunosum-moleculare (lm) layers. Additionally, the figure illustrates the trisynaptic circuit originating from the entorhinal cortex (EC) in teal, with arrows indicating the flow of information. Scale bars are provided for reference. The coronal sections are generated with Biorender. The 3D mouse view is adopted from the Blue Brain Cell Atlas. The 3D head view is generated with the MIDA head in S4L

1.2 Neuromodulation

Millions of people suffer from neurological disorders such as stroke, migraine, Parkinson's disease, and epilepsy. Several techniques exist to treat these disorders, attempting to restore the healthy brain state. One option is surgical removal of affected brain regions. For instance, in the case of TLE, removing the hippocampus can lead to long-term seizure freedom. However, this approach is not viable for numerous patients due to multifocality or the risk of cognitive impairments [17]. Alternatively, neuromodulation techniques aim to reversibly alter the neuronal activity (see figure 1.3). They can be categorized by their corresponding physics. These techniques fall into four main categories: chemical or pharmacological, electrical, ultrasonic, and optogenetic neuromodulation. Each of these neuromodulation modalities offers unique advantages and challenges, paving the way for innovative approaches to treat neurological disorders. Here, I provide an overview of each category's primary techniques, with a focus on their application in treating epilepsy.

1.2.1 Chemical or Pharmacological Neuromodulation

The initial line of treatment for many neurological disorders involves drug administration. Drugs have various mechanisms of action, primarily involving channel blocking or opening. For the treatment of epilepsy, more than 20 antiseizure drugs have been approved [18]. Approximately 70% of epilepsy patients treated with these drugs achieve seizure freedom, while the remaining 30% are categorized as having refractory or drug-resistant epilepsy. Moreover, the drugs affect the whole brain (figure 1.3 (A)), often resulting in side effects such as fatigue, nausea, dizziness, and cognitive or behavioral problems [17].

Chemogenetics is an innovative approach that allows for targeted neuromodulation by utilizing designer receptors exclusively activated by designer drugs (DREADD, figure 1.3 (B)). These are modified endogenous receptors responsive to exogenous ligands. Gene therapy is used to express DREADDs, offering specificity. The gene expression techniques are similar for optogenetic neuromodulation with some options discussed in section 2.1.2. While currently a research tool, chemogenetics has shown promise in preclinical seizure suppression. The main challenge for clinical translation is the long-term safety of both the gene therapy and the exogenous ligands [19–21].

Alternatively, improved spatial as well as temporal resolution can be obtained with photopharmacology (figure 1.3 (C)). It involves light sensitive drugs that can be activated with visible light. There are two mechanisms: photocages and photoswitches. Photocages are compounds that include a photocleavable protecting group. Upon illumination the drug is activated as a result of the photocleavage reaction. The second group are photoswitches. Unlike with photocages, the process is reversible with activation upon illumination and deactivation after a long enough dark period. It is an emerging technique with only preclinical results to date. Challenges for clinical translation will be the long-term safety of light sensitive compounds and the need for optical stimulator implantation due to limited light

penetration depth [22, 23].

1.2.2 Electrical Neuromodulation

Electrical neuromodulation techniques modify brain activity using electrical currents. These are either directly induced by a voltage difference over stimulation electrodes or indirectly generated by alternating magnetic fields. The existing techniques can be classified based on invasiveness. Transcranial direct current (tDCS) and alternating current stimulation (tACS) are non-invasive approaches with electrodes placed on the scalp. They provide subthreshold modulation with tDCS affecting neuronal excitability and tACS cortical oscillations. Their limitations are having a low spatial resolution, difficulty to reach deep structures and causing skin irritation. According to Boon et al. (2018), there is only low-to-moderate quality evidence that tDCS is effective in treating epilepsy [24]. Another non-invasive technique is transcranial magnetic stimulation (TMS). Here, a coil is placed near the head that creates strong alternating magnetic fields up to 1T over 100 µs, inducing counter currents in the cortex (figure 1.3 (D)). Some studies have demonstrated significant seizure reductions but insufficient data is available to support efficacy [24]. TMS is, however, FDA approved for the treatment of migraine, major depressive and obsessive-compulsive disorder (OCD) [25]. Temporal interference stimulation is a non-invasive technology currently under investigation. By applying two slightly shifted high frequency electric fields to the brain, it is postulated that deep brain stimulation could be achieved at the beat frequency (i.e., the difference of the two frequencies) where the two fields interfere, without stimulating the overlying cortex [26, 27].

With invasive modalities, the stimulation devices are implanted inside the body. Vagus nerve stimulation (VNS) targets the afferent vagus nerve fibers (figure 1.3 (E)) that are thought to modulate among others the brainstem, thalamic and limbic regions. Moreover, it has been shown to increase norepinephrine concentrations, believed to be responsible for the antiseizure effect [28]. VNS is FDA approved for treatment of epilepsy and depression [25] and could potentially be used to treat many other disorders (for example Alzheimer's disease and stroke). Extensions are transcutaneous (figure 1.3 (F)) and percutaneous vagus nerve stimulation, where the auricular branch of the vagus nerve is stimulated non-invasively and minimally-invasively, respectively [29, 30]. Although less invasive alternatives are promising, according to Boon et al. (2018), there is currently insufficient data to support their efficacy in treatment of drug resistant epilepsy [24].

A second invasive modality is deep brain stimulation (DBS). It involves implantation of an electrode lead in the brain to specifically target deep brain areas (figure 1.3 (G)). Initially FDA approved in 1997 for Parkinson's disease and essential tremor, DBS has garnered approval for various other disorders, including dystonia, OCD, and epilepsy. In case of epilepsy, DBS of the anterior nucleus of the thalamus (ANT-DBS) and responsive neurostimulation (RNS) in the seizure focus are approved techniques. ANT-DBS is an open loop modality, meaning its stimulation paradigm is preset, fixed and continuous. Its antiseizure effect is believed to

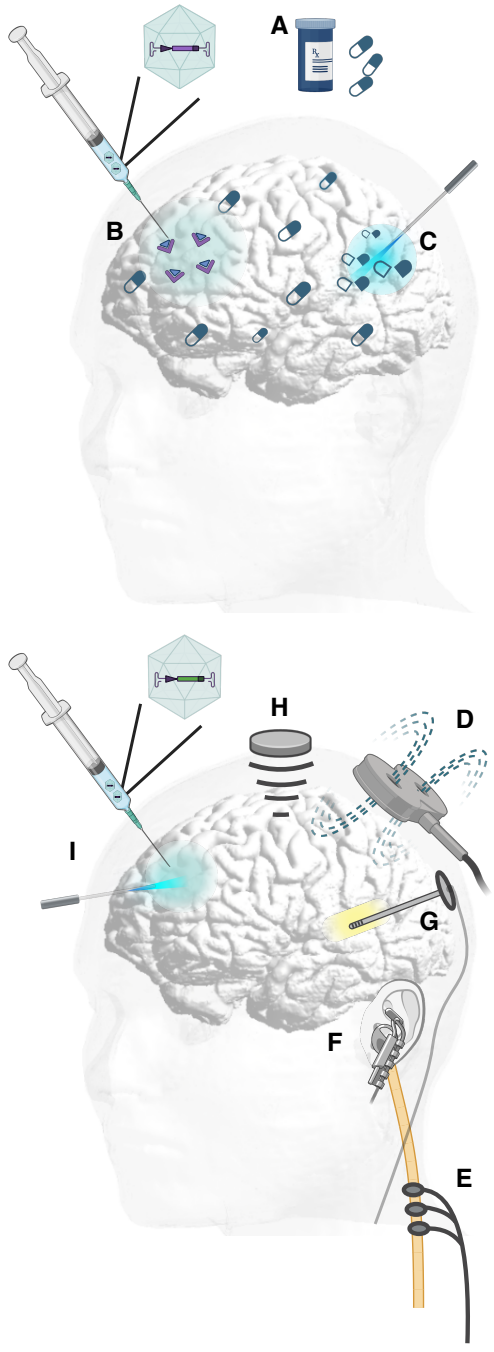

Figure 1.3: (Caption next page.)

Figure 1.3: Illustration of the different neuromodulation techniques. **A** Classical drug administration. **B** Chemogenetics with AAV injection containing the DREADD genetic material. **C** Photopharmacology with implanted optical fiber. **D** Transcranial magnetic stimulation with transcranial stimulator coils. **E** Vagus nerve stimulation with implanted cuff electrodes. **F** Transcutaneous vagus nerve stimulation. **G** Deep brain stimulation with implanted electrode. **H** Ultrasonic neuromodulation with a transcranial single element focused transducer. **I** Optogenetic neurostimulation with AAV injection containing the opsin genetic material and implanted optic fiber

result from reinforced GABAergic neurotransmission in the epileptic hippocampus [28]. In contrast, RNS is a closed loop system developed by Neuropace, where stimulation is triggered upon detection of ictal activity via intracranial EEG electrodes. Both techniques have demonstrated seizure reduction and responder rates of more than 50%, with also more than 10% becoming seizure free for several months [28, 31]. Furthermore, DBS of the hippocampus of drug-resistant TLE patients has shown promising results, as well [24].

1.2.3 Ultrasonic Neuromodulation

Ultrasonic neuromodulation (UNMOD) has emerged as a notable and promising technique over the past decade. It uses mechanical waves (sound waves) with frequencies above 20 kHz (20 kHz being the upper limit of the human hearing window). Ultrasonic waves are generated by either a single element focused transducer (figure 1.3 (H)) or a transducer array positioned on the scalp. Low intensity focused ultrasound (LIFU) is postulated to have the unique ability to non-invasively, selectively, and reversibly modulate brain activity. Moreover, it can achieve transversal and axial resolutions in the order of millimeters and centimeters, respectively, because of the millimeter wavelength of the ultrasonic wave in the brain tissue. Notably, this is all achieved without requiring genetic modifications of the target neurons. However, despite its promise, the precise underlying mechanisms remain incompletely understood. Proposed mechanisms encompass intramembrane and extracellular cavitation, acoustic radiation force, mechanosensitivity of ion channels, flexoelectricity and localized heating [32]. Encouragingly, certain studies exploring the use of LIFU for epilepsy treatment have shown promising results [33]. Nevertheless, it is imperative to acknowledge the limited scope of current research, while also carefully considering potential confounding factors arising from the auditory pathway in the evaluation of UNMOD's efficacy [32].

1.2.4 Optogenetic Neuromodulation

Optogenetics allows precise control of neuronal firing using light. This is achieved by genetically expressing opsins, typically light sensitive ion channels or pumps, in cells or cell subtypes. The merger of this genetic expression and optical stimulation

results in superior spatiotemporal resolution with respect to the other neuromodulation modalities described above. Moreover, the mechanism of action is clear with the selected opsin either being excitatory or inhibitory. However, due to the limited penetration depth of visible light, implantation of the optical devices will be necessary (figure 1.3 (I)). Moreover there are long-term safety concerns associated with gene therapy [19, 21]. The optogenetic toolbox with its challenges and possible solutions is discussed in more detail in chapter 2.

1.3 Computational Neuroscience

Computational neuroscience, a subfield of neuroscience, uses mathematical tools and theories to study the nervous system. It integrates various disciplines, including electrical engineering, computer science, medicine and physics, with the aim to understand how information is processed by the nervous system. Computational models are constructed to test hypotheses or to postulate new ones. It enables researchers to explore experimentally inaccessible aspects systematically. However, due to the complexity of the nervous system, limited computational resources, and in order to have sufficient interpretability of the model outcome, a trade-off needs to be made between biological realism and simplicity. Computational neuroscience should serve as a complementary tool to experimental research. It is essential that a continuous cycle exists of model validation and prediction testing against experimental data [34, 35].

Models can span a wide range of levels of complexity. They encompass spatial scales ranging from the single molecular scale towards the entire brain. Computational neuroscience often adopts a bottom-up approach. For example, network predictions are based on an ensemble of neuron models whose behavior is dictated by a set of individual channel models. This structure is applied in this disseration. The smallest scale addressed is modeling of a single ion-channel (see chapter 2), followed by the effect at the neuronal level (chapter 3) and hippocampal network level (chapter 4). The models used in these chapters are conductance-based models. In chapter 5, neurons are represented as dipoles, a simplification, to predict whole-brain activity. I will discuss these two types below.

1.3.1 Conductance-Based Neuronal Modeling

With conductance-based modeling, the structures of the neuronal membrane are represented by their electrical equivalent components. An example of the electrical network of a neural fiber is given in figure 1.4. It can be modeled by three components: a capacitor, a conductance/resistor and voltage sources, being the cell membrane, the ion channels or axial resistance, and equilibrium potential, respectively [7, 36]. The equilibrium potential is the transmembrane potential at which the net flux of ions is zero. For a single ion this is given by the Nernst equation. The Goldman-Hodgkin-Katz voltage equation is an extension for a set of monovalent ions, with more generalized forms available for multivalent ions [37].

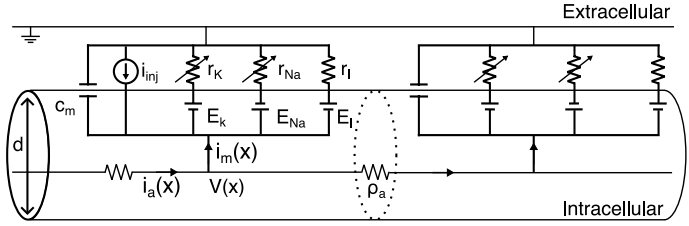

Figure 1.4: Electric equivalent network of a neuronal fiber separated into two compartments. Variable resistances are indicated with arrows

Given this electrical circuit (figure 1.4), the total transmembrane current at a specific location (x) can be calculated as follows (sign conventions are given in box 1.1):

$$i_{\mathrm{m}} = c_{\mathrm{m}}\frac{\mathrm{d}V}{\mathrm{d}t} + g_{\mathrm{K}}(V - E_{\mathrm{K}}) + g_{\mathrm{Na}}(V - E_{\mathrm{Na}}) + g_{\mathrm{l}}(V - E_{\mathrm{l}}) - i_{\mathrm{inj}} \qquad (1.1)$$

where E_{x} and $g_{\mathrm{x}} = 1/r_{\mathrm{x}}$, for x ϵ {Na, K, l}, are the reversal potential and specific ion conductance, respectively, with *l* denoting the leak current. c_m is the specific membrane capacitance (F/m^2), i_{m} the total membrane current and i_{inj} an injection current per unit area (A/m^2). The intracellular space is a lossy medium, with its axial resistivity (ρ_a [Ωm]) assumed to be homogeneous in a single compartment. The spatial variation of the membrane potential is modeled via the cable equation (equation (1.2)). A detailed derivation is given in Dayan and Abbot (2008) [36].

$$\lambda^2\frac{\partial V^2(x,t)}{\partial x^2} - \tau\frac{\partial V(x,t)}{\partial t} - (V(x,t) - V_{\mathrm{r}}) = 0 \qquad (1.2)$$

with the space constant $\lambda = \sqrt{d/4\, r_{\mathrm{m}}/\rho_{\mathrm{a}}}$ and time constant $\tau = r_{\mathrm{m}}c_{\mathrm{m}}$. V_{r} is the equilibrium rest membrane potential and r_{m} the transmembrane specific resistance. These constants set the scale of spatial and temporal variations in the membrane potential. In other words, after a local perturbation of the membrane potential, it converges back to equilibrium over a time of the order τ, and space of the order λ.

The conductance of many ion channels is variable. They depend on factors like membrane potential, ion concentration, ligands, or light intensity. An example of the latter is given in chapter 2. The voltage-gated channels are responsible for the active response of the neuron. Most well known examples are the transient sodium channel and the delayed rectifier potassium channel, enabling the generation of the action potential as discussed below. Examples of ligand-gated channels are the primary post-synaptic receptors: AMPA, $\mathrm{GABA_a}$ and NMDA. These receptors are typically modeled with an event-triggering scheme. After a presynaptic action potential, their open probability is increased, following a double exponential with a decay and rise time constant (τ_{decay} and τ_{rise}) [35]. The post synaptic current is then:

$$i_{\mathrm{s}} = g_{\mathrm{s}}(\exp(-t/\tau_{\mathrm{decay}}) - \exp(-t/\tau_{\mathrm{rise}}))(V - E_{\mathrm{s}}) \qquad (1.3)$$

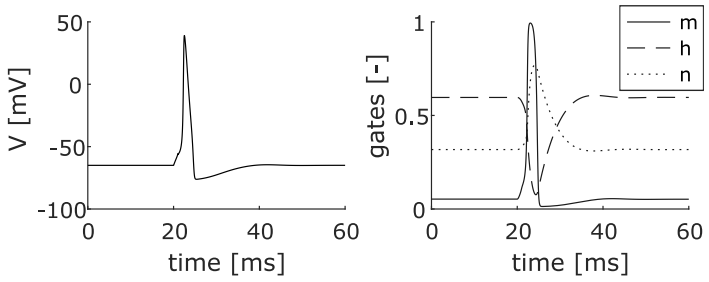

Figure 1.5: An action potential generated with the Hodgkin-Huxley equations as reported in Hodgkin and Huxley (1952) [8]. (left) The generated action potential under current conventions. (right) Evolution of the gating units during the action potential.

Hodgkin-and-Huxley model

For the field of computational neuroscience, the descriptive model of the action potential formulated by Hodgkin and Huxley was groundbreaking. They derived that an action potential could be explained with an equivalent electric circuit containing a fast transient, a delayed long-lasting, and a passive leakage current. Furthermore, they identified this fast transient and delayed long-lasting currents to be sodium and potassium carried, respectively. The Hodgkin-Huxley model [8] for an electrotonically compact single compartment model of the unmyelinated giant axon of the squid is given by:

$$c_m \frac{\mathrm{d}V}{\mathrm{d}t} = -\left(\bar{g}_{\mathrm{Na}} m^3 h (V - E_{\mathrm{Na}}) + \bar{g}_{\mathrm{K}} n^4 (V - E_{\mathrm{K}}) + \bar{g}_{\mathrm{l}} (V - E_{\mathrm{l}})\right) \tag{1.4}$$

with $\bar{g}_{\mathrm{x}}$ the maximum channel conductance. The open probability of the sodium and potassium channels is voltage-dependent. This is modeled by the activation gating units m and n, and inactivation unit h. A generic unit's transition is described by a simple first-order kinetic scheme between open (a) and closed form ($1 - a$; with $a \in \{m, n, h\}$):

$$1 - a \underset{\beta_a}{\overset{\alpha_a}{\rightleftharpoons}} a$$

Subsequently, the transition rate is given by:

$$\frac{\mathrm{d}a}{\mathrm{d}t} = \alpha_a(V)(1 - a) - \beta_a(V)a \tag{1.5}$$

with $\alpha_a(V)$ and $\beta_a(V)$ the voltage-dependent opening and closing rates. Often the rate equation is expressed in another form containing a voltage-dependent steady-state (a_∞) and time constant (τ_a):

$$\frac{\mathrm{d}a}{\mathrm{d}t} = \frac{a_\infty(V) - a}{\tau_{\mathrm{a}}(V)} \tag{1.6}$$

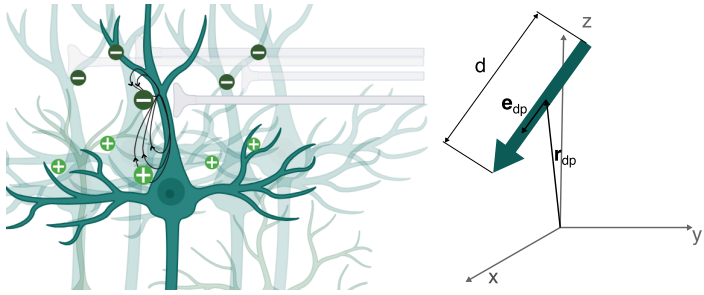

Figure 1.6: The current dipole model. (left) Illustration of the current sink (-) and sources (+) induced by synaptic transmembrane currents. (right) Schematic of the equivalent dipole and its parameters. Left figure created with BioRender

with

$$a_\infty(V) = \frac{\alpha_a(V)}{\alpha_a(V) + \beta_a(V)} \qquad \tau_a(V) = \frac{1}{\alpha_a(V) + \beta_a(V)} \tag{1.7}$$

An action potential generated with the Hodgkin-Huxley equations, given in Hodgkin and Huxley (1952) [8], is displayed in figure 1.5. The equations of the original paper were modified to match the current transmembrane potential conventions (see box 1.1).

1.3.2 Dipole Model

The conductance-based models discussed in the previous section reflect the activity that can be recorded intracellularly. In contrast, recording techniques such as electroencephalography (EEG), electrocorticography (ECoG), and extracellular field (often called local field potential (LFP)) recording with implanted electrode arrays, measure the activity of the extracellular space. These recordings detect electrical potential changes resulting from all active cellular processes, which can be expressed by a multipole expansion. The signal strength is inversely proportional to the distance from the measuring electrode. Moreover, at the electrode, there is spatial averaging of the activity of all the sources. Although there are many contributors to the extracellular fields (for an overview see Buzsaki et al. (2012) [38]), only highly synchronous activity in both space and time will give rise to measurable deflections at distant electrodes. Consequently, the major contributors are the post-synaptic potentials produced by synaptic transmembrane currents. In case of AMPA and NMDA synapses, this will give rise to a local influx of ions resulting in an extracellular sink, which is balanced by extracellular current sources along the neuron.

Especially in modeling of EEG activity, these currents are modeled with a current dipole. Here, the dipole represents the electrical activity of a small volume of parallel neurons. The model is characterized by: its position ($\mathbf{r}_{\mathrm{dp}} = [x, y, z]$, which is halfway between the current source and sink), its orientation (defined by

unit vector $\mathbf{e}_{\mathrm{dp}}$), the current intensity (I) and the distance between the monopoles (d), see figure 1.6. The dipole moment density is then

$$\begin{aligned} \mathbf{d}(\mathbf{r}_{\mathrm{dp}}) &= I\,\mathbf{d}_{\mathrm{dp}}(\mathbf{r}_{\mathrm{dp}}) \\ \text{with } \mathbf{d}_{\mathrm{dp}} &= d\,\delta^3(\mathbf{r}_{\mathrm{dp}})\,\mathbf{e}_{\mathrm{dp}} \end{aligned} \tag{1.8}$$

with δ the Dirac delta [39, 40]. Subsequently, the field propagation of the current dipole to the scalp is modeled. This is obtained by solving Poisson's equation. A numerical solver is needed to obtain the result for accurate head geometries. In contrast, an analytical solution can be obtained in simplified head models. An example is given in chapter 5.

Box 1.1. Conventions and Definitions

transmembrane potential The transmembrane potential is the electrical potential difference of the intracellular with respect to the extracellular potential ($V = V_{\mathrm{i}} - V_{\mathrm{e}}$).

equilibrium potential The equilibrium potential (V_{r}) is the transmembrane potential for which there is no net conductive current across the membrane ($\mathrm{d}V/\mathrm{d}t = 0$).

depolarization The change in transmembrane potential is positive ($\frac{\mathrm{d}V}{\mathrm{d}t} > 0$).

repolarization The current transmembrane potential is above the equilibrium potential and the change is negative ($V > V_{\mathrm{r}}$, $\frac{\mathrm{d}V}{\mathrm{d}t} < 0$).

hyperpolarization The current transmembrane potential is below the equilibrium potential and the change is negative ($V < V_{\mathrm{r}}$, $\frac{\mathrm{d}V}{\mathrm{d}t} < 0$).

current sign conventions The current is positive in case of: an outward transmembrane current, an inward electrical or injection current, and an arriving axial current.

seizures Transient occurrences of signs and/or symptoms due to abnormal excessive or synchronous neural activity in the brain $\sim$ ILAE

seizure states

- **ictal** period during a seizure
- **interictal** period between seizures

1.4 Research Aims

Neuromodulation techniques still face numerous challenges. Their efficacy is often limited due to incomplete understanding of their underlying mechanisms. Computational models emerge as ideal tools for addressing these unresolved questions. The neuromodulation technique studied in this dissertation is optogenetics. A significant hurdle in its clinical translation is the transition from rodent to human brains, marked by a substantial size difference ($\times 1000$). Another challenge involves the open-loop operation of neuromodulation systems, leading to redundant modulation. The future of neuromodulation technologies leans towards closed-loop systems. These hold the promise of real-time adjusting stimulation, based on clinically relevant physiological signals. A technique able to record (deep) electrophysiological activity minimally- to non-invasively with high spatial and temporal resolution is therefore imperative.

The aim of this dissertation is to leverage computational modeling to gain insights in the optogenetic excitation of CA1 cells, hippocampal modeling, and functional neuroimaging, all with the overarching goal of advancing the treatment of temporal lobe epilepsy. The following research questions are posed:

- What are the dominant uncertainty variables in and strategies to increase the optogenetic excitation of CA1 cells? (chapter 3)
- Can a conductance-based network model of the hippocampus, though not full-scale, produce seizure-like activity under high potassium or mesial temporal lobe epilepsy histopathological conditions? (chapter 4)
- Can electrophysiological activity of deep regions be recorded non-invasively and with high spatial resolution by probing brain tissue with ultrasound under the mechanical vibration hypothesis? (chapter 5)

To address the first research question effectively, an accurate yet computationally efficient model of the opsin under investigation is essential. Consequently, an additional research question is posed initially:

- Is it possible to model the opsin's photocurrent more efficiently, and can the model be autonomously fitted to the data? (chapter 2)

1.5 Outline

In chapter 2, I delve into the optogenetic toolbox, addressing trends, modulation strategies, challenges, and potential solutions. This chapter also provides a summary of the computational models utilized for modeling an opsin's photocurrent. Furthermore, I elaborate on our contribution to the state-of-the-art, specifically the development of a computationally efficient double two-state opsin model accompanied by an autonomous parameter inference procedure. The results presented

stem from our paper titled *Double Two-State Opsin Model with Autonomous Parameter Inference* [RS1]. I draw comparisons with conventional models and fit two distinctive opsins (ChR2(H134R) and MerMAID), followed by an evaluation of the proposed model's computational efficiency.

Chapter 3 employs the model introduced in chapter 2 to explore the optogenetic excitability of CA1 neurons. I present the findings of our study titled *Quantitative Analysis of the Optogenetic Excitability of CA1 Neurons* [RS2]. Our investigation combines simulations of light propagation and neuronal modeling to identify optimal and suboptimal stimulation positions, quantify simulation errors when changes in the light field at the neuronal level are omitted, and determine the most excitable neuronal membrane compartments. Additionally, an uncertainty analysis is conducted to pinpoint the most impactful uncertain parameters, including optical field properties, cell-to-optical fiber orientation, and 3D structural cell morphology. These insights hold significance for the development of improved stimulation protocols.

Chapter 4 outlines the development of a network model of an epileptic hippocampus, encompassing the dentate gyrus, CA3, and CA1 regions. This model evolves from a healthy baseline to incorporate in-vitro model pathologies and mesial temporal lobe epilepsy (mTLE) pathology. The emphasis is placed on the evoked potentials generated by stimulating the Schaffer collaterals, a commonly utilized marker for ongoing brain excitability. Preliminary results from this research were presented at the 44th Annual International Conference of the IEEE Engineering in Medicine and Biology Society [RS14] and at the Joint 3R Symposium, September 2023.

In the final research chapter, chapter 5, I shift the focus to neural activity recording. Here, I leverage dipole models to assess the feasibility of using ultrasound to probe the electrophysiological activity of deep brain areas with high spatial and temporal specificity. The hypothesis of neural tissue vibration being responsible for heterodyning neural activity with the ultrasonic frequency (i.e., upconverting the low frequency electrophysiological activity to higher ultrasonic frequencies) is investigated. The results presented originate from our work titled, *Simulation Study on High Spatio-Temporal Resolution Acousto-Electrophysiological Neuroimaging* [RS3].

The dissertation concludes with a summary of the conclusions drawn from my research and outlines prospective directions for future investigations in chapter 6.

1.6 Publications

1.6.1 International Journals (A1)

(peer-reviewed publications in journals listed in the ISI Web of Science)

1.6.1.1 As first author

[RS1] **R. Schoeters**, T. Tarnaud, L. Martens, W. Joseph, R. Raedt, E. Tanghe, "Double Two-State Opsin Model With Autonomous Parameter Inference", in *Frontiers in Computational Neuroscience*, 2021. doi: 10.3389/fncom.2021.688331

[RS2] **R. Schoeters**, T. Tarnaud, L. Weyn, W. Joseph, R. Raedt, E. Tanghe, "Quantitative Analysis of the Optogenetic Excitability of CA1 Neurons", in *Frontiers in Computational Neuroscience*, 2023. doi: 10.3389/fncom.2023.1229715

[RS3] **R. Schoeters**, T. Tarnaud, L. Martens, E. Tanghe, "Simulation Study on High Spatio-Temporal Resolution Acousto-Electrophysiological Neuroimaging", in *Journal of Neural Engineering*, 2023. 10.1088/1741-2552/ad169c

1.6.1.2 As co-author

[RS4] T. Tarnaud, W. Joseph, **R. Schoeters**, L. Martens, E. Tanghe, "SECONIC: Towards multi-compartmental models for ultrasonic brain stimulation by intramembrane cavitatio", in *Journal of Neural Engineering*, 2020. doi: 10.1088/1741-2552/abb73d

[RS5] T. Tarnaud, W. Joseph, **R. Schoeters**, L. Martens, E. Tanghe, "Membrane Charge Oscillations During Ultrasonic Neuromodulation by Intramembrane Cavitation", in *IEEE Transactions on Biomedical Engineering*, 2021. doi: 10.1109/TBME.2021.3086594.

[RS6] T. Tarnaud, W. Joseph, **R. Schoeters**, L. Martens, E. Tanghe, "Improved alpha-beta power reduction via combined electrical and ultrasonic stimulation in a parkinsonian cortex-basal ganglia-thalamus computational model", in *Journal of Neural Engineering*, 2021. doi: 10.1088/1741-2552/ac3f6d

[RS7] T. Plovie, **R. Schoeters**, T. Tarnaud, L. Martens, W. Joseph, E. Tanghe, "Nonlinearities and Timescales in Temporal Interference Stimulation", BioRXiv 2022. doi: 10.1101/2022.02.04.479138

1.6.2 International Conferences (P1)

(peer-reviewed publications presented at international conferences)

1.6.2.1 As first author

[RS8] **R. Schoeters**, T. Tarnaud, W. Joseph, L. Martens, R. Raedt, E. Tanghe, "Comparison between direct electrical and optogenetic subthalamic nucleus stimulation", in *1st World Conference on Biomedical Applications of Electromagnetic Fields (EMF-Med)*, Split, Croatia, 2018. doi: 10.23919/EMF-MED.2018.8526018

1.6.3 International Conferences (C1)

1.6.3.1 As co-author

[RS9] T. Tarnaud, F. Soyka, **R. Schoeters**, T. Plovie, W. Joseph, L. Martens, E. Tanghe, "EONS: evaluation of non-sinusoidal magnetic fields for electromagnetic safety to intermediate frequencies", in *the 1st Joint Meeting of The Bioelectromagnetics Society and the European BioElectromagnetics Association (BioEM2022)*, Nagoya, Japan, 2022.

[RS10] T. Plovie, **R. Schoeters**, T. Tarnaud, L. Martens, W. Joseph, E. Tanghe, "Influence of Temporal Interference Stimulation Parameters on Point Neuron Excitability", *44th Annual International Conference of the IEEE Engineering in Medicine and Biology Society (EMBC' 22)*, Glasgow, Scotland, United Kingdom, 2022. doi: 10.1109/EMBC48229.2022.9871641

[RS11] F. Soyka, C. Alteköster, T. Tarnaud, **R. Schoeters**, T. Plovie, W. Joseph, E. Tanghe, "Comparing the SENN and the MRG Electrostimulation Models in the Context of Occupational Exposure Limit Values", in *Joint Meeting of The Bioelectromagnetics Society and the European BioElectromagnetics Association BioEM2023*, Oxford, UK, 2023.

1.6.4 International Conferences (C3)

(publications presented at national and international conferences)

1.6.4.1 As first author

[RS12] **R. Schoeters**, T. Tarnaud, W. Joseph, R. Raedt, L. Martens, E. Tanghe, "Channelrhodopsin-2 model with improved computational efficiency", in *28th Annual Computational Neuroscience Meeting: CNS*2019. BMC Neurosci 20*, 2019. doi: 10.1186/s12868-019-0538-0

[RS13] **R. Schoeters**, T. Tarnaud, W. Joseph, L. Martens, R. Raedt, E. Tanghe, "Computational modelling of the Locus Coeruleus", in *29th Annual Computational Neuroscience Meeting: CNS*2020. BMC Neurosci 21*, Virtual, 2020. doi: 10.1186/s12868-020-00593-1

[RS14] **R. Schoeters**, T. Tarnaud, W. Joseph, R. Raedt, E. Tanghe, "Towards a Hippocampal Formation Model of Temporal Lobe Epilepsy", in *44th Annual International Conference of the IEEE Engineering in Medicine and Biology Society (EMBC'22)*, Glasgow, Scotland, UK, 2022.

[RS15] **R. Schoeters**, T. Tarnaud, W. Joseph, R. Raedt, E. Tanghe, "Quantitative analysis of three dimensional and subcellular optogenetics in CA1 cells". *32th Annual Computational Neuroscience Meeting: CNS*2023*, Leipzig, Germany, 2023.

1.6.4.2 As co-author

[RS16] T. Tarnaud, W. Joseph, **R. Schoeters**, L. Martens, T. Van Renterghem, E. Tanghe, "Robustness of ultrasonic modulation of the subthalamic nucleus to GABAergic perturbation", in *29th Annual Computational Neuroscience Meeting: CNS*2020. BMC Neurosci 21*, Virtual, 2020. doi: 10.1186/s12868-020-00593-1

[RS17] T. Tarnaud, T. Plovie, E. Vicari, **R. Schoeters**, E. Neufeld, N. Kuster, W. Joseph, L. Martens, S. Micera, E. Tanghe, "Towards a comprehensive model of the underlying mechanisms of ultrasound neuromodulation", in *Focused ultrasound neuromodulation conference*, Stanford, California, 2023.

[RS18] L. Weyn, **R. Schoeters**, T. Tarnaud, W. Joseph, E. Tanghe, "Towards realistic modelling of cortical spreading depolarization in migraine", in *32th Annual Computational Neuroscience Meeting: CNS*2023*, Leipzig, Germany, 2023.

[RS19] E. Neufeld, T. Tarnaud, T. Newton, T. Plovie, E. Vicari, P. B. Garcia, **R. Schoeters**, N. Kuster, W. Joseph, L. Martens, S. Micera, E. Tanghe, "Computational Pipeline for Modeling Ultrasound Propagation and Electrophysiological Impacts for Non-invasive Peripheral Nervous System Stimulation", in *2024 North American Neuromodulation Society Annual Meeting*, Las Vegas, United States, 2024

References

[1] Valery L. Feigin, Theo Vos, Emma Nichols, Mayowa O. Owolabi, William M. Carroll, Martin Dichgans, Günther Deuschl, Priya Parmar, Michael Brainin, and Christopher Murray. *The global burden of neurological disorders: translating evidence into policy*. The Lancet Neurology, 19:255–265, 3 2020.

[2] Valery L. Feigin. *The Evolution of Neuroepidemiology: Marking the 40-Year Anniversary of Publishing Studies on Epidemiology of Neurological Disorders*. Neuroepidemiology, 56:2–3, 2 2022.

[3] Dale Purves, George J Augustine, David Fitzpatrick, Willian C Hall, Anthony-Samuel Lamantia, James O Mcnamara, and S. Mark Willians. *Neuroscience*, volume 3. 2004.

[4] Frederico A.C. Azevedo, Ludmila R.B. Carvalho, Lea T. Grinberg, José Marcelo Farfel, Renata E.L. Ferretti, Renata E.P. Leite, Wilson Jacob Filho, Roberto Lent, and Suzana Herculano-Houzel. *Equal numbers of neuronal and nonneuronal cells make the human brain an isometrically scaled-up primate brain*. The Journal of Comparative Neurology, 513:532–541, 4 2009.

[5] Larry R Squire, Floyd E Bloom, Anirvan Ghosh, Darwin Berg, Sascha du Lac, and Nicholas C Spitzer. *Fundamental Neuroscience*. Elsevier Inc., 4 edition, 2014.

[6] Constance Hammond. *Cellular and Molecular Neurophysiology*. Elsevier, 2015.

[7] Eugene Izhikevitch. *Dynamical Systems in Neuroscience*. 2007.

[8] A. L. Hodgkin and A. F. Huxley. *A quantitative description of membrane current and its application to conduction and excitation in nerve*. J. Physiol, 117:500–544, 1952.

[9] Carl Petersen and Georgios Foustoukos. *Cellular mechanisms of brain function*. EPFL press, 2017, 2016.

[10] Per Andersen, Richard Morris, David Amaral, Tim Bliss, and John O'Keefe. *The Hippocampus Book*. Oxford University Press, 2007.

[11] Kirsten M. Fiest, Khara M. Sauro, Samuel Wiebe, Scott B. Patten, Churl-Su Kwon, Jonathan Dykeman, Tamara Pringsheim, Diane L. Lorenzetti, and Nathalie Jetté. *Prevalence and incidence of epilepsy*. Neurology, 88:296–303, 1 2017.

[12] Valery L. Feigin, Ibtihel Aichour, Miloud Taki Eddine Aichour, et al. *Global, regional, and national burden of neurological disorders, 1990–2016: a systematic analysis for the Global Burden of Disease Study 2016*. The Lancet Neurology, 18:459–480, 5 2019.

[13] Robert S Fisher and Helen E Scharfman. *How can we identify ictal and interictal abnormal activity?* Advances in Experimental Medicine and Biology, 813:3–23, 2014.

[14] William O. Tatum. *Mesial Temporal Lobe Epilepsy*. Journal of Clinical Neurophysiology, 29:356–365, 10 2012.

[15] Ingmar Blümcke, Maria Thom, Eleonora Aronica, et al. *International consensus classification of hippocampal sclerosis in temporal lobe epilepsy: A Task Force report from the ILAE Commission on Diagnostic Methods*. Epilepsia, 54:1315–1329, 7 2013.

[16] Alok K. Sharma, Rachel Y. Reams, William H. Jordan, Margaret A. Miller, H. Leon Thacker, and Paul W. Snyder. *Mesial Temporal Lobe Epilepsy: Pathogenesis, Induced Rodent Models and Lesions*. Toxicologic Pathology, 35:984–999, 12 2007.

[17] Mathieu Sprengers. *Deep Brain Stimulation for drug-resistant epilepsy: efficacy and mechansim of action*. PhD thesis, Ghent University, 2020.

[18] Orrin Devinsky, Annamaria Vezzani, Terence J. O'Brien, Nathalie Jette, Ingrid E. Scheffer, Marco de Curtis, and Piero Perucca. *Epilepsy*. Nature Reviews Disease Primers, 4:18024, 5 2018.

[19] Matthew C. Walker and Dimitri M. Kullmann. *Optogenetic and chemogenetic therapies for epilepsy*. Neuropharmacology, 168:107751, 5 2020.

[20] Jana Desloovere, Paul Boon, Lars Emil Larsen, Marie-Gabrielle Goossens, Jean Delbeke, Evelien Carrette, Wytse Wadman, Kristl Vonck, and Robrecht Raedt. *Chemogenetic Seizure Control with Clozapine and the Novel Ligand JHU37160 Outperforms the Effects of Levetiracetam in the Intrahippocampal Kainic Acid Mouse Model*. Neurotherapeutics, 19:342–351, 1 2022.

[21] Michael White, Michael Mackay, and Roger G Whittaker. *Taking Optogenetics into the Human Brain: Opportunities and Challenges in Clinical Trial Design*. Open Access Journal of Clinical Trials, Volume 12:33–41, 8 2020.

[22] Erine Craey, Fabian Hulpia, Jeroen Spanoghe, Simona Manzella, Lars E. Larsen, Mathieu Sprengers, Dimitri De Bundel, Ilse Smolders, Evelien Carrette, Jean Delbeke, Kristl Vonck, Paul Boon, Serge Van Calenbergh, Wytse J. Wadman, and Robrecht Raedt. *Ex Vivo Feedback Control of Neurotransmission Using a Photocaged Adenosine A1 Receptor Agonist*. International Journal of Molecular Sciences, 23:8887, 8 2022.

[23] Matthew J. Fuchter. *On the Promise of Photopharmacology Using Photoswitches: A Medicinal Chemist's Perspective*. Journal of Medicinal Chemistry, 63:11436–11447, 10 2020.

[24] Paul Boon, Elien De Cock, Ann Mertens, and Eugen Trinka. *Neurostimulation for drug-resistant epilepsy: A systematic review of clinical evidence for efficacy, safety, contraindications and predictors for response*. Current Opinion in Neurology, 31:198–210, 4 2018.

[25] Tim Denison and Martha J. Morrell. *Neuromodulation in 2035 The Neurology Future Forecasting Series*. Neurology, 98:65–72, 1 2022.

[26] Nir Grossman, David Bono, Nina Dedic, Suhasa B. Kodandaramaiah, Andrii Rudenko, Ho-Jun Suk, Antonino M. Cassara, Esra Neufeld, Niels Kuster, Li-Huei Tsai, Alvaro Pascual-Leone, and Edward S. Boyden. *Noninvasive Deep Brain Stimulation via Temporally Interfering Electric Fields*. Cell, 169:1029–1041.e16, 6 2017.

[27] Plovie Tom, Schoeters Ruben, Tarnaud Thomas, Martens Luc, Joseph Wout, and Tanghe Emmeric. *Nonlinearities and Timescales in Temporal Interference Stimulation*. bioRxiv, 2023.

[28] Philippe Ryvlin, Sylvain Rheims, Lawrence J. Hirsch, Arseny Sokolov, and Lara Jehi. *Neuromodulation in epilepsy: state-of-the-art approved therapies*. The Lancet Neurology, 20:1038–1047, 12 2021.

[29] Eugenijus Kaniusas, Stefan Kampusch, Marc Tittgemeyer, et al. *Current Directions in the Auricular Vagus Nerve Stimulation I – A Physiological Perspective*. Frontiers in Neuroscience, 13, 8 2019.

[30] Tom Van de Steene, Emmeric Tanghe, Thomas Tarnaud, Stefan Kampusch, Eugenijus Kaniusas, Luc Martens, Roel Van Holen, and Wout Joseph. *Sensitivity Study of Neuronal Excitation and Cathodal Blocking Thresholds of Myelinated Axons for Percutaneous Auricular Vagus Nerve Stimulation*. IEEE Transactions on Biomedical Engineering, 67:3276–3287, 12 2020.

[31] Mathieu Sprengers, Kristl Vonck, Evelien Carrette, Anthony G. Marson, and Paul Boon. *Deep brain and cortical stimulation for epilepsy*. Cochrane Database of Systematic Reviews, 2017, 7 2017.

[32] Thomas Tarnaud. *Computational Modeling of Ultrasonic and Electrical Brain Stimulation*. PhD thesis, Ghent University, 2021.

[33] Emma Lescrauwaet, Kristl Vonck, Mathieu Sprengers, Robrecht Raedt, Debby Klooster, Evelien Carrette, and Paul Boon. *Recent Advances in the Use of Focused Ultrasound as a Treatment for Epilepsy*. Frontiers in Neuroscience, 16, 6 2022.

[34] Thomas Trappenberg. *Fundamentals of Computational Neuroscience*, volume 2. OXFORD University press, 2010.

[35] Nicholas T. Carnevale and Michael L. Hines. *The NEURON book*. Cambridge University Press, 2006.

[36] Peter Dayan and Laurence F Abbott. *Theoretical neuroscience: computational and mathematical modeling of neural systems*. MIT press, 2005.

[37] William F. Pickard. *Generalizations of the Goldman-Hodgkin-Katz equation*. Mathematical Biosciences, 30:99–111, 1 1976.

[38] György Buzsáki, Costas A. Anastassiou, and Christof Koch. *The origin of extracellular fields and currents — EEG, ECoG, LFP and spikes*. Nature Reviews Neuroscience, 13:407–420, 6 2012.

[39] Hans Hallez, Bart Vanrumste, Roberta Grech, Joseph Muscat, Wim De Clercq, Anneleen Vergult, Yves D'Asseler, Kenneth P Camilleri, Simon G Fabri, Sabine Van Huffel, and Ignace Lemahieu. *Review on solving the forward problem in EEG source analysis*. Journal of NeuroEngineering and Rehabilitation, 4:46, 12 2007.

[40] S. Baillet, J.C. Mosher, and R.M. Leahy. *Electromagnetic brain mapping*. IEEE Signal Processing Magazine, 18:14–30, 2001.

2
Optogenetics

In this chapter, I will elaborate on the optogenetic technology and computational models of the opsin's current kinetics. First, I summarize the popular options for the three crucial components of the optogenetic toolbox, i.e., gene expression, opsins and illumination. Next, potential applications and the remaining challenges for clinical translation are discussed.

In the previous chapter, it was denoted that computational models are a valuable tool to tackle these challenges. To this end, an accurate yet computationally efficient model of the to-be-investigated opsin is required. I proposed a double two-state opsin model as an alternative to the conventional three and four-state Markov models used for opsin modeling. This double two-state opsin model comprises only two differential equations, rendering it computationally more efficient. Additionally, I developed an autonomous model fitting procedure commencing from a vast parameter space. The structure of the proposed model and the fitting procedure are discussed in this chapter, as well. The outcomes of our paper titled *Double Two-State Opsin Model With Autonomous Parameter Inference* [1] are discussed in section 2.6.

2.1 The Optogenetic Toolbox

Optogenetics is a technique that can be used to manipulate cellular activity with light [2–4]. Specific cell types are sensitized to light via the introduction of gene constructs that encode for optogenetic actuators. There are many different types of optogenetic actuators. An overview of these is given by Rost et al. (2017) [5]. In this book, I will focus on membrane-spanning actuators [5]. These *opsins* are light-gated ion channels, pumps or receptors that when illuminated allow hyper- or depolarizing currents through the cell membrane [3].

The idea of using light as a neuromodulation tool was already postulated by Francis Crick in 1979 [6]. Also the discovery of the first opsins originates in the 70's. The first opsin, i.e., bacteriorhodopsin, was discovered by Oesterhelt et al. (1971) [7], being an excitatory proton pump. Followed by halorhodopsin, an inhibitory chloride pump by Matsuno-Yagi and Mukohata (1977) [8]. It took 25 years before channelrhodopsin (ChR), the first light-gated ion channel, was reported [9], but has since revolutionized neuroscience [10–12].

To ensure the proper functioning of the optogenetic toolbox, three components are necessary. First, the optimal optogenetic actuator must be chosen, taking into account selection criteria such as ion selectivity, kinetics, spectral band, subcellular target and conductance. Second, a delivery method is essential, with viral vectors like adeno-associated or lentivirus commonly adopted. Last, a light source, e.g., LED or a laser, is required to activate the genetically modified cells [5, 11].

2.1.1 Opsins

The most well-known opsin is channelrhodopsin-2 (ChR2), responsible for phototaxis and photophobic responses in the green algae *Chlamydomonas reinhardtii* [13, 14]. Since the discovery of ChR2, the range of available options has significantly expanded. This expansion is attributable to the discovery of new natural opsins and genetic engineering of existing ones. Consequently, this has presented a large number of possibilities with a wide spectrum of characteristics, including conductance, kinetics, spectral bands, and selectivities [15].

The available opsins can be divided into two large groups: the microbial opsins (type I) and G-protein coupled receptors or the vertebrate opsins (type II). Activation of the latter group results in a cascade of neural activity with slower responses as a consequence. They are mainly used in optogenetics for biochemical control. Consequently, most effort is put into the use of type I opsins for neural control [12, 15, 16] and will thus be further revised in this book. Below, I will discuss the most commonly used, with different interesting properties. Extensive overviews of available opsins are given by Zhang et al. (2022) [17] and Gordeliy et al. (2022) [18]. A selection of common opsins, both excitatory and inhibitory, is given in figure 2.2.

2.1.1.1 Natural opsins

As already denoted, the first light sensitive ion channel was discovered in the green alga *Chlamydomonas reinhardtii*. However, ChR2 is only one of the seven opsin-related genes of the alga. Of these genes, Chlamyopsins 3 and 4 encode light-gated ion channels, respectively ChR1 and ChR2 [19]. Both these channels comprise seven transmembrane helices combined with all-trans retinal chromophore. Upon light illumination, retinal undergoes a 13 trans-to-cis isomerization, which activates a cascade of conformational changes resulting in the opening of the channel pore [20]. Although there exists a 65% sequence homology between ChR1 and ChR2, there are significant differences concerning kinetics, action spectra and conductance. Research has shown that ChR1 is highly selective for protons (H^+), while being almost impermeable for other cations resulting in a lower conductance than its counterpart, ChR2, which is permeable for most cations. On the other hand ChR2 limits fast pacing due to its rapid inactivation, whereas this is reduced in ChR1. At last, the peak activation wavelength is more red shifted for ChR1 (500 nm) in comparison with ChR2 (460 nm). Due to the red shift and faster kinetics, ChR1 could be more interesting for certain clinical applications than ChR2, though its low conductance excludes it for neuronal depolarization [9, 14, 21].

Next to ChRs of the alga *Chlamydomonas reinhardtii*, homologues were found in other chlorophycean algea, such as *Volvox carteri* (VChR), *Mesostigma viride* (MChR), *Stigeoclonium helveticum* (ShChR), *Chlamydomonas noctigama* (CnChR1) and up to 60 more [20]. Combination of the final two, for the activation of two distinct neural populations with different colors of light, has been proven to be possible. Multiple trials have been conducted to achieve this feature. This by creating red shifted mutants of ChR2 and decreasing blue light sensitivity or increased sensitivity of the counterpart, with the intention that low intensity blue stimulation would drive spiking in neurons, with the blue light version, and sub-threshold spiking in neurons with the red shifted mutant. However, altering the blue light sensitivity of ChR2 has led to a decrease of the opsin's temporal resolution. Nevertheless, the combination of these properties is exactly what enables multi-population stimulation with Chronos and Chrimson. Irradiance with red light (625 nm) causes only spike activity in cells containing Chrimson (spectral peak at 590 nm), up to 10 Hz, whereas irradiance with blue light (470 nm) and power between $0.05\ \mathrm{mW/mm^2}$ and $0.5\ \mathrm{mW/mm^2}$ causes spike activity up to 60 Hz in Chronos (spectral peak at 500 nm) containing cells [22].

2.1.1.2 Bioengineered opsins

To optimize the properties of opsins, extensive genetic engineering efforts have been dedicated to their optimization. Even machine learning has been used to guide the engineering of channelrhodopsins [24]. Different optimization strategies that have been followed are point mutations and codon optimization. Additionally, attempts have been made to combine the complementary properties of ChR1 and ChR2 leading to chimeric structures [16]. It was the crystal structure of the C1C2

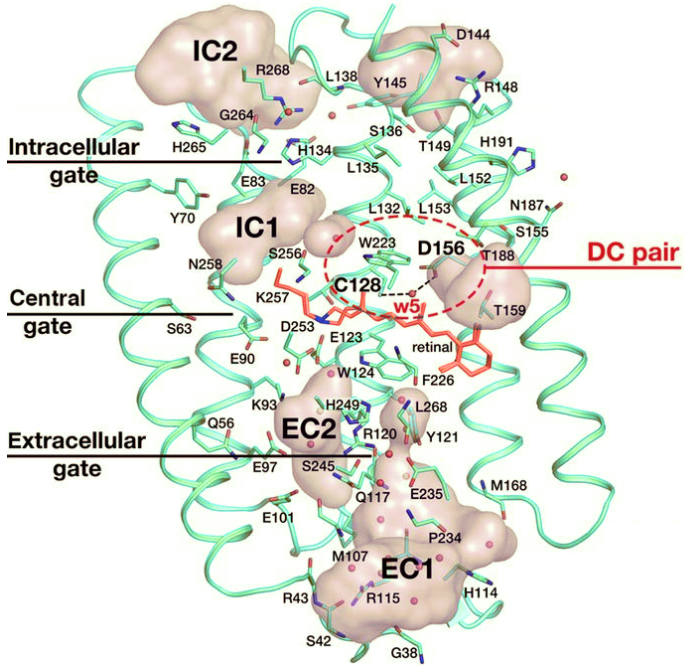

Figure 2.1: High resolution crystal structure of Channelrhodopsin 2 with four main cavities. Retinal is the structure in red. Adapted from Vokov et al. (2017) [23]

chimera that led to a breakthrough in protein engineering of ChR2 [25, 26]. Five years later, Volkov et al (2017) successfully derived the protein structure of the native ChR2 with a 2.4 Å resulotion (see figure 2.1) [26].

Red-shifted opsins The need for red-shifted opsins emerged from the need for enhanced light penetration, necessary when transitioning optogenetics from small animal models to non-human and human primates with larger brain volumes. Red light is subjected to less scattering and less absorption, hence resulting in deeper penetration and less heating. Additionally, it enables multi-population stimulation [16]. The bathochromic shift in red-shifted opsins primarily results from altered retinal conformation and the interaction of the retinal Schiff base (RSBH^{+}) with counter ions (E123 or Ci1 and E253 or Ci2). These interactions are formed due to the covalent bonding between retinal and the K257 lysine residue (see figure 2.1). For example, mutations such as E123Q and D253N in ChR2 result in a bathochromic shift, while Ci1 mutation (E162T) in C1V1 induces a hypsochromic shift [20]. Other more recently discovered or developed red-shifted opsins with improved properties are bReaChES, CsChrimson and ChRmine [27–29]

Step-function opsins Step-function opsins (SFOs) offer unique bistable, step-like control capabilities, making them suitable for modulating spontaneous firing rates. However, they are not suitable for single action potential control. The most popular SFO is the ChR2(C128S) mutant. The C128 and D156 residue form together the DC-gate (see figure 2.1). A mutation results in a remarkable decrease in kinetics, extending the lifetime of the channel's open state. Furthermore, a mutation affecting the entire DC-gate(C128S/D156A) produces a stabilized SFO with a deactivation time approaching thirty minutes [15, 20, 30].

Ultrafast opsins A complementary class to the SFOs are the ultrafast opsins. These opsins contain faster kinetics, particularly off-kinetics. This allows for single spike control, whereas multiple spikes per stimulus are typically obtained with other opsins. Their fast recovery permits the use of higher stimulation frequencies over prolonged periods without compromising action potential firing. A subset of ultrafast opsins are termed ChETAs. Here the Ci1 glutamate (E) residue is substituted for a threonine (T) or alanine (A), resulting in an acceleration of the off kinetics from $\tau_{\text{off}} = 10\,\text{ms}$ to $\tau_{\text{off}} = 4\,\text{ms}$. However, this improvement comes at the cost of reduced light sensitivity [15, 16, 20, 31–33]. There exist chimeric ultrafast opsins as well. Examples are ChEF, a chimera with a crossover site at loop E-F (this is C1C2 in figure 2.1), and ChIEF, where isoleucine 170 in ChEF is mutated into valine. Whereas ChIEF contains faster kinetics, the light sensitivity is reduced but still within the range of ($\sim 10\,\text{mW}/\text{mm}^2$). ChIEF allows for high-fidelity stimulation, achieving frequencies of up to 50 Hz, surpassing the precision of stimulation attainable with ChR2, which upper limit is typically 15 Hz [21]. Native opsins, such as Chronos from the ShChR channelrhodopsin, also fall within the category of ultrafast opsins [22].

Ion selectivity Another characteristic that has been modified is the ion selectivity. In most natural opsins, proton selectivity typically surpasses that of other ions. For instance, ChR2 exhibits a relative proton conductance estimated to be $10^5 - 10^6$ times higher than that for sodium ions, raising concerns about potential host cell acidification. The ChR2(L132C-T159C) mutant, however, displays increased sodium and magnesium conductance, and enhanced calcium selectivity [20, 30]. Furthermore, this mutation has an increased light sensitivity at the expense of reduced temporal kinetics, with an increase of 1.5 to 2 orders of magnitude [31]. Also a mutation of H134, which is part of the inner gate and sodium binding site, results in a Na^+ carried current. A well known and frequently used example is ChR2(H134R) [12, 20].

2.1.1.3 Inhibitory opsins

In addition to excitatory opsins, inhibitory opsins also play a significant role in optogenetics. They can be used for action potential inhibition, achievable via both anion and cation conducting opsins.

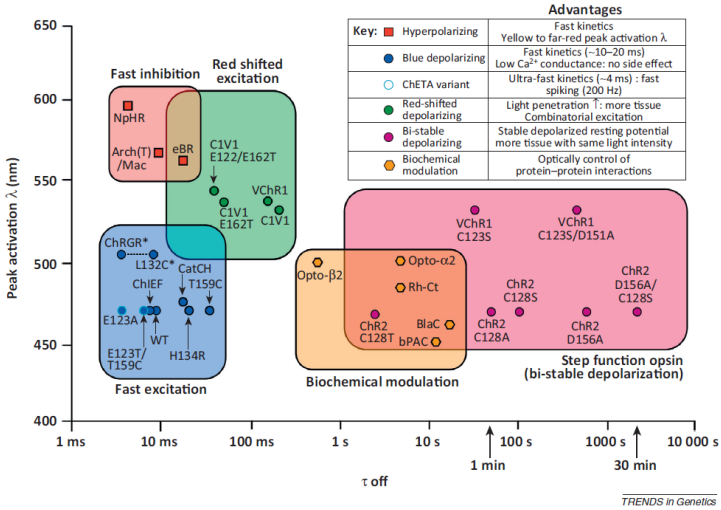

Figure 2.2: Overview of available opsins with their activation peak wavelength, decay kinetics and advantages. Adapted from Gerits and Vanduffel (2013) [16]

Anion Conducting Among the inhibitory opsins, the yellow-light-activated chloride pump halorhodopsin (NpHR) from the archaeon *Natronomonas pharaonis*, stands out as one of the most widely used. Similar to their excitatory counterparts, efforts have been made to genetically modify inhibitory opsins, altering properties like spectral sensitivity, as seen with eNpHR3.0. Furthermore, research is focused on engineering chloride channels, although some residual cation conductance may persist [34]. Recent discoveries include natural light-gated anion channels found in the genome of *Guillardia theta*, such as GtACR1 and GtACR2 [35, 36]. Additionally, a metagenomically family of phylogenetically distinct anion-conducting channelrhodopsins, termed MerMAIDS, have been identified, exhibiting intense desensitization and rapid closing kinetics [37].

Cation Conducting Disruption of the chloride homeostasis can drive anion conducting opsins to become excitatory. Although cation-conducting channels are mainly associated with excitation, cell inhibition is possible as well. The archaerhodopsin-3 (Arch) from the *Halorubrum sodomense* is a proton pump that causes hyperpolarization by pumping protons out of the cell [38]. A notable recent discovery is WiChR from the *Wobblia lunata*. It is a potassium-conducting channel with improved K^+ selectivity, elevated light sensitivity, and minimal photocurrent inactivation [39].

2.1.1.4 Bidirectional control

Furthermore, bidirectional control can be achieved through the concurrent expression of both excitatory and inhibitory opsins within the same cell population. To realize this, it is imperative that both opsins exhibit comparable expression levels while having distinct activation spectra to prevent unwanted cross-activation. Two challenges that have been shown to be difficult to overcome. In a recent study, Vierock et al. (2021) [40] combined GtACR2, an inhibitory opsin activated by blue-light, with Chrimson, an excitatory opsin responsive to red light, resulting in a novel construct referred to as *BiPOLES*. This combination yields promising results, demonstrating successful bidirectional control across various (in)vertebrate model organisms [40].

2.1.2 Gene expression

The second step involves introducing the genetic material of opsins into the target cells, commonly achieved through viral vectors. A viral vector construct typically contains four primary components (see figure 2.3). The initial component is the viral expression system itself, with lentivirus and adeno-associated virus (AAV) being the most prevalent choices. The lentivirus has a larger packaging capacity (8 kb) compared to AAV (4 kb), but incorporates into the host genome. While this causes permanent expression, it also increases the carcinogenic risk. The packaging capacity limits the promoter possibilities and thus reduces the diversity of specific targeted cells. However, AAV can be more effective due to its lower temperature sensitivity, broader distribution due to its smaller size and higher titers, and reduced immunogenicity [4, 12, 15, 16]. Cell-type specificity can be achieved

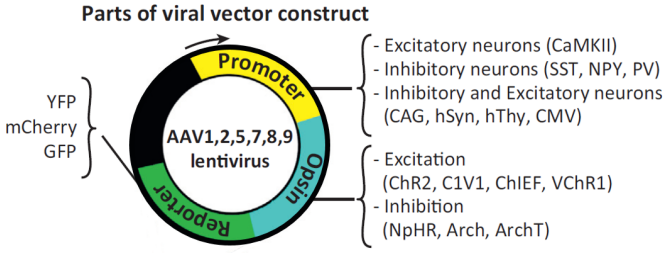

Figure 2.3: Example viral vector construct used for opsin expression. Adapted from Gerits and Vanduffel (2013) [16]

through the vector's inherent tropism, spatial targeting strategies, or the selection of a specific promoter. The latter is the second component of the vector construct. Some possibilities are denoted in figure 2.3. The third component encompasses the genetic information of the opsins themselves, as discussed in section 2.1.1. Finally, the fourth component usually comprises a reporter gene, encoding fluorescent proteins for quantifying opsin expression [16].

To overcome packaging capacity limitations, alternative techniques exist. Transgenic or knock-in animals, while offering high specificity, are restricted to research applications and cannot be extend to humans. Additionally, generating these transgenic lines demands substantial time and effort. Furthermore, the introduction of a new opsin necessitates the creation of a new animal line. Finally, spatial localization specificity is compromised. A combination of transgenic mice, such as cre recombinase-based mouse lines, with viral vector system, combines the best of both worlds enhancing specificity [15]. Stauffer et al. (2016) circumvented the need for a transgenic animal line by injecting a mix of two viral vectors. The first contains the Cre recombinase whereas the second vector delivers a Cre-recombinase-dependent opsin construct [41].

Other techniques include electroporation, gene gun [42], cell-to-myocyte electrical coupling using donor cells [43], lipofection, and optoporation [4]. Optoporation, employing an ultra-fast near-infrared laser beam in conjunction with micro-injection of opsin genes, is particularly promising in reducing tissue damage and enhancing site-specificity [4].

2.1.3 Illumination

Finally, the genetically modified cells require illumination. Several methods exist with their respective advantages and limitations. Light sources such as mercury or xenon bulbs, light-emitting diodes (LEDs), μLEDs, continuous-wave lasers, or ultrafast pulsed lasers can be employed [44, 45]. Mercury or xenon bulbs emit a broad spectrum of light, necessitating filtration. Moreover, they generate substantial heat and degrade quickly, resulting in infrequent use [45]. In optogenetics, it is advisable to use light wavelengths near the opsin's peak absorption. In this case, lower intensities are needed, reducing the chance of phototoxicity, photobleaching or spontaneous activation of the cells itself. Furthermore, it reduces the possibility for multicolored simultaneous activation. Also high temporal control is desired. These requirements make LEDs and lasers, especially ultrafast lasers which can emit light pulses of tens to hundreds of femtoseconds long, more suitable candidates. Lasers offer coherent light production, higher coupling efficiency, and superior temporal resolution but entail increased complexity and cost [4, 42, 45].

2.2 Clinical Translation

The discovery of optogenetics has revolutionized neuroscience. Due to its optimal temporal resolution, cell specificity and potential bidirectional control it is an ideal investigative tool. The latter property has simplified behavioral studies, where causality needs to be investigated in terms of necessity and specificity. Consequently, optogenetics has proven to be very useful for investigating disease mechanisms. Although there are still many challenges along its path to be an effective clinical application, several studies have already shown its benefits and high potential [5, 42, 46–49].

2.2.1 Epilepsy

As aforementioned in section 1.1.3, epilepsy is a devastating disorder with 30% of patients having refractory epilepsy [50–52]. Focal epilepsies are particularly perceptive for optogenetic neuromodulation. Studies have already shown its effectiveness in treating epileptic seizures in animal models. There are two strategies [48]. First, there is seizure control through optogenetic inhibition of the excitatory subpopulations. Proof of principle was provided by Tonnesen et al. (2009), where successfully burst attenuation in pyramidal neurons with stimulation of NpHR was obtained [53]. Several studies have followed showing decreased seizure activity via inhibition of, for instance, the hippocampus [54–56] or thalamus [57]. A second approach is excitation of the inhibitory interneurons using cation conducting opsins, such as channelrhodopsin-2 (ChR2) and variants, which has also yielded promising results [54, 58–60]. Furthermore, optogenetics can be employed in studies on the initiation and propagation of seizures, and to investigate the role different neuronal populations play in the seizure dynamics [42, 55, 61, 62]. An overview of optogenetic approaches in epilepsy research is given by Cela and Sjöström (2019) [63].

2.2.2 Beyond the brain

Optogenetics extends beyond the central nervous system. Potential applications lie in the peripheral nervous system, as well as other excitable tissues such as cardiac tissues and muscle cells. The use of optical tools in the cardiovascular field is widely embraced, ranging from optogenetic sensors to optogenetic arrhytmia management [64]. Optical defibrillation, for instance, offers the advantage of pain alleviation by avoiding stimulation of surrounding skeletal muscles [43]. Moreover, prolonged stimulation is possible due to the lack of electrochemical reactions associated with electrical stimulation. Bruegmann et al. (2010) provided already an in-vivo proof-of-concept by optogenetically altering the PQRS-complex [65].

Translating optogenetics to the spinal cord and peripheral nervous systems does not make it necessarily more accessible. They contain more complex and heterogeneous tissues, are very motile and the immune response is more prominent. However, it also opens up possibilities for diverse illumination techniques, including cuff implants and non-invasive transdermal illumination. The latter holds promise for somatosensation and pain modulation, however with current successes only demonstrated in in-vitro and ex-vivo settings [66]. Furthermore, optogenetics holds potential for therapeutic interventions in motor circuit control, offering the prospect of restoring function to damaged spinal circuits and modulating lower motor neurons [67]. Successes have been shown in rodents and recently in non-human primates [68, 69]. In case of the latter, optogenetics offers advantages over electrical stimulation, due to the physiological order of recruitment with less muscle fatigue as result [66, 70].

The currently most promising clinical application of optogenetics is the treatment of retinitis pigmentosa. The eye is easier to access and there is no need for implanted light sources [71]. Consequently, it is the first disease for which optogenetic

therapy has reached clinical trial. Two trials, NCT02556736 and NCT03326336, are ongoing. The latter, being the Gensight therapy, utilizes biomimetic goggles in order to enhance delivered light-intensities [47, 69, 72]. Although preliminary, the results of a first patient look promising [49].

2.2.3 Challenges

The previously mentioned applications represent only a fraction of the potential possibilities with optogenetics. However, the translation into clinical applications faces numerous challenges. The human brain is approximately 1000 times bigger than the brain of rodents, complicating translation from rodents to primates [48]. Diester et al. (2011) constructed an optogenetic toolbox for primates with stimulation of the motor cortex [74]. Although there was clear proof of optogenetic control of the neurons, no movements were evoked. This may be attributed to the small size of the stimulated region. Optic frequencies exhibit poor penetration in brain tissue, necessitating in-vivo implantation of the illumination source. In order to minimize structural damage due to intrusion, the light source's dimensions are constrained [44]. As a result, only a small volume is illuminated using a single optical fiber. Furthermore, light absorption by the brain tissue causes heating. Therefore the light intensity should be limited in order to prevent brain damage [81–85].

Effectively illuminating a sufficiently large volume without causing irreversible effects poses a primary challenge. One potential solution is the adoption of red-shifted opsins [12, 22]. (Infra)red light gets less absorbed resulting in greater illumination volumes and less heating [29, 82, 86, 87]. Alternatively, enhancing efficiency to generate higher photocurrents at lower irradiances could be achieved by improving single channel conductance or altering channel kinetics [12, 30, 88]. Augmenting membrane expression [5, 89, 90] or spatially confining the opsin to specific neuronal membrane compartments [5, 91–93] offer potential strategies, as well.

Another challenge is having a good understanding of the optogenetic effect itself. Prolonged activation of inhibitory opsins may disrupt the chloride balance, resulting in excitation instead of inhibition. For instance, Mahn et al. (2018) observed GtACR2-mediated axonal excitation [92]. Excessive activation of GABAergic interneurons could yield similar outcomes [48, 94, 95]. Moreover, the complex connectivity of interneuron networks can lead to disinhibition [46, 48], emphasizing the importance of precise targeting of the right interneuron subset. However, subset targeting remains challenging [42]. Inhibition via cation conducting channels such as WiChR could be a more robust solution [39]. Moreover, optogenetic modulation should not be restricted to silencing or a single strategy. Like with electrical deep brain stimulation, the excitation could be used as counter-irritation [96] with various modes of action [97] that can be tested. Ultrafast opsin are good choices to achieve high frequency stimulation. Moreover, stimulating multiple cell types could potentially restore the excitation-inhibition balance [46].

Lastly, long-term consequences must be carefully identified. On the one hand there is the possible immune response to the viral vectors and the transgene foreign

Advantages	Challenges	Possible Solutions
Cell specificity[all]	Toxicity of opsin expression[2,3,6,16]	Alter promoter vector combination[3]
High temporal resolution (ms)[all]	Heterogeneous light delivery and attenuation[2,3,6,7,14,16]	Branched fiber illumination[13], red-shifted opsins[2,5,6,13] or synthetic retinal analogues[1]
Rapid reversibility[5,6]	Heterogeneous opsin expression[2,3,6,7,14,16]	Multi site injection[10]
Co-expression and bidirectional control[3,5,6,15]	Small capacity of viral vectors limits co-expression[5,17]	viral vector mixture with Cre-recombinase[18]
No electrochemical reactions[2,15]	No subset specificity[6,7]	INTERSECT*[6], optoporation[9]
True electrical and fMRI recordings[14]	Reliable high frequency spiking[8,17]	Ultrafast opsins[5,6,8]
No extra need for cofactors (retinal) in mammals[17]	Non physiological behavior[6,7,16]	
Control studies are easy[17]	Antidromic activation[6,7]	
Silent in the dark (no effect on cell properties)[13]	Phototoxicity and bleaching[17]	High light sensitive opsins[17]
Minimally invasive beyond the brain[2,14,15]	Invasivennes of optrodes[3,16,17]	Two photon stimulation[9,10], Nanoparticle upconversion[12], sono-optogenetics[19]
	Synchronization of cells[6,7]	SFOs[6,7]
	Heating[17]	High light sensitive opsins[17], red-shifted opsins[2,5,6,13]
	Rapid evolution and discoveries delay clinical trials[14]	

1: [73] 2: [43], 3: [74], 4: [75], 5: [16], 6: [15], 7: [76], 8: [21], 9: [4] 10: [45] 11: [57] 12: [77] 13: [48], 14: [78], 15: [79], 16: [46], 17: [12], 18: [41] and 19: [80]
**intron recombinase sites enabling combinatorial targeting*

Table 2.1: Advantages and challenges with possible solutions for the translation of optogenetic neuromodulation to clinical application.

proteins. Also transgene down-regulation may occur, necessitating repetitive viral vector injection, which is a complex surgical procedure in order to target the same area [46, 49]. On the other hand, foreign body reactions to implanted optical sources can affect functionality already after weeks post-implantation. Engineering efforts are directed towards developing soft and flexible optrodes that match mechanical properties of brain tissue to limit this immune response [44]. This problem can be circumvented with non-invasive light delivery methods. A possible method uses upconversion nanoparticles which are capable of transforming near-infrared into visible light [98]. Another option are mechanoluminescent nanotransducers that are activated by ultrasound; a technique termed sono-optogenetics [80] .

2.3 Ethical Considerations

Although optogenetics is pursued with therapeutic intent, aiming to enhance patients' quality of life, it is crucial to consider ethical implications. Notably, there are no inherently new ethical considerations unique to optogenetics that do not apply to other techniques. Similar to gene therapy and electrical deep brain stimulation (DBS), it is essential to carefully assess risks and benefits. Safety concerns associated with gene therapy include immune system reactions, pleiotropic effects, insertional mutagenesis, and recombination potential. Implanting the light source also entails risks, such as local heating, tissue and acute vascular damage, localized blood-brain barrier breakdown, and potential toxicity, including the formation of reactive oxygen species [99].

Furthermore, optogenetic stimulation may result in unintended effects that could lead to personality changes, although this risk is expected to be lower compared to DBS due to the increased cell-type specificity of optogenetics. Given this risk-benefit analysis, it is imperative to ensure that patients are well-informed to provide informed consent. Moreover, considering that the neurological diseases targeted for treatment could potentially cause cognitive impairments, developing clear and understandable informed consent processes is crucial [100].

Efforts are being made towards non-invasive optogenetics, mitigating several of the aforementioned safety concerns. However, this approach introduces the risk of cells becoming susceptible to other light sources of sufficient power, posing a risk of unconsented manipulation. Additionally, there is a moral concern regarding the use of optogenetics to enhance cognitive functioning, raising subsequent concerns about fair and equal access. Finally, the feasibility of the technique requires the allocation of additional resources and (pre)clinical trials, introducing ethical concerns such as fair subject selection, the use of animals, and the allocation of computational resources [100].

2.4 The ChR2 Photocycle

In chapter 3, I explore the optogenetic excitability of CA1 neurons using a computational model of ChR2(H134R). Developing this model necessitates a thorough understanding of the opsin's photocycle. Below, I will begin by describing the ChR2 photocurrent, followed by an overview of conventional model structures and existing opsin models.

In its initial dark-adapted (IDA) state and under voltage clamp conditions, ChR2's photocurrent exhibits a peak (I_{peak}) followed by a steady-state current (I_{ss}) [101]. The peak is reached within 1-2 ms and is succeeded by fast decay onto a steady-state plateau due to light adaptation (figure 2.4). Post-illumination, a bi-exponential decay back to baseline occurs, rendering the channel in an apparent dark-adapted state (DA_{app}). This is observed when a second stimulation after a short period of time (< 10 s) is applied, resulting in a reduced transient response while maintaining the steady-state current (figure 2.4) [101, 102].

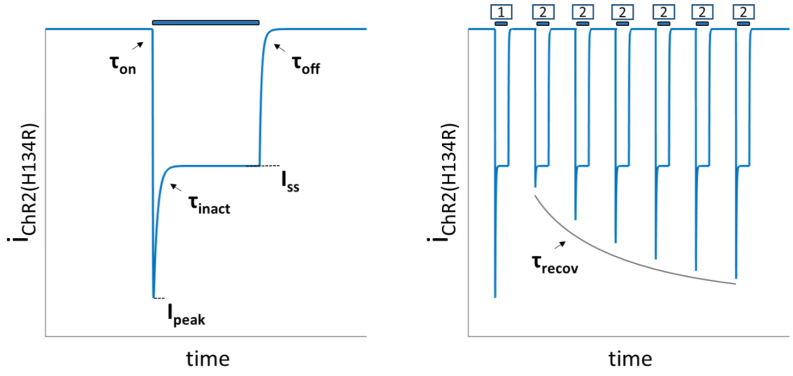

Figure 2.4: The opsin photocurrent for a single light pulse on the left. (Right) The response to a S1-S2 pulse protocol with variable inter-pulse intervals. Light pulses are indicated with blue bars and target features with black arrows.

ChR2 comprises seven transmembrane helices. These are covalently bound to a retinal chromophore forming a protonated retinal Schiff base ($RSBH^+$). In its IDA (D470), retinal is in an all-trans configuration [101]. Upon illumination, a 13-trans-cis isomerization is triggered that initiates a cascade of conformational changes, leading to pore opening (P520). Before returning back to the dark adapted state, the channel converts to a non-conducting state P470. This happens on a millisecond timescale, while complete recovery takes seconds [19, 23, 103]. There is substantial evidence supporting a second photocycle with similar intermediates: (i) existence of four kinetic intermediates identified with a short flash experiment [104], (ii) changes in selectivity between early and late photocurrents [19, 20], (iii) the presence

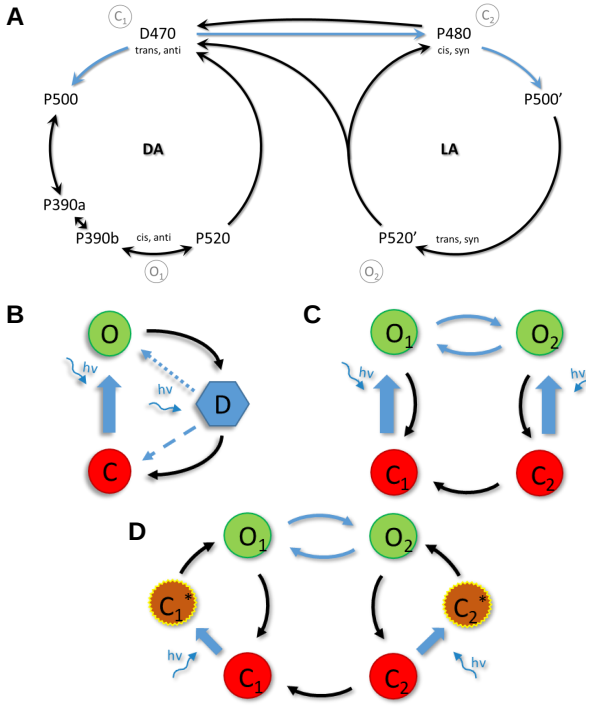

Figure 2.5: The ChR2 photocycle and previously proposed computational model structures. **A** The unifying photocycle model as proposed by Kuhne et al. (2019) [107]. **B** A three state cycle model with second light dependent step (dotted or dashed step) [108]. **C** A four state branching model [78]. **D** A six state model with two extra activation intermediates [109]. DA and LA indicate dark and light adapted molecule states, respectively. O means open, C is closed and D is the desensitized state. Blue arrows indicate light dependent rates.

of multiple retinal isoforms and (iv) a bi-exponential, post-illumination current decay [19, 101, 105, 106]. However, the transition between the two photocycles remains a topic of debate [101, 106]. Recently, Kuhne et al. (2019) [107] proposed a unifying ChR2 photocycle model consisting of two parallel photocycles with three reaction pathways as shown in figure 2.5 (A).

2.4.1 Computational Opsin Models

In computational modeling, the photocurrent is commonly represented using either a three- or four-state Markov model (figure 2.5 (B, C)). This is in accordance with the single and double photocycle hypothesis, respectively. The opening is reduced to a single state transition. This is because the D480 $\rightarrow$ P500 and P500 $\rightarrow$ P390

transitions occur on a much faster timescale. However, to account for fast closure, slow recovery, and a steady-state current, a second photon absorption step is proposed for the three-state model [14, 19, 20, 102, 110]. The photochemical transition either increases the recovery rate or acts as equilibrium modulator between the open and desensitized state. The six-state model, as depicted in figure 2.5 (D), is an extended version of the four-state model. The additional two intermediates are to correctly account for the activation time after retinal isomerizations and to avoid explicit-time dependent rates [109]. The four-state model aligns with the second photocycle hypothesis, involving modeling of two open and closed states. The transition as depicted in figure 2.5 (C) is according to the older transition hypothesis, not to the latest unifying photocycle model proposed by Kuhne et al. (2019) [107].

Several studies have been published that leverage these and other more accurate and efficient models in combination with neuron models to design in-silico experiments. Some existing three-state models are of the native ChR2 with a voltage-dependent inward rectification [10, 111] and a model of the fast Chronos opsin with an increased recovery rate as a second photon absorption step [112]. Efforts have also been made to model the native ChR2 with a four-state model [113–115]. However, in these models, only the activation rates are irradiance-dependent while the transition rates between the photocycles are fixed. Grossman et al. (2011, 2013) incorporated voltage-dependent inward rectification along with irradiance-dependent transition rates [109, 116]. Bansal et al. (2020, 2021) fitted multiple light-gated ion channels, including ChR2H134R, ChETA, Chronos, CheRiff, Vf-Chrimson, GtACR2, ChRmine, bRaeches and CsCrimson, with a four-state model incorporating irradiance-dependent transition rates but without inward rectification [27, 117]. They furthermore developed three-state models for light-gated ion pumps [117]. Williams et al. (2013) identified a positive correlation between the transmembrane potential and the opsin time constants. They, therefore, created an improved model of the ChR2(H134R) mutant that includes voltage-dependent rates and added temperature dependence, as well [78]. Schneider et al. (2013) developed models of ChR2, ChR2(L132CT159C) and C1V1 using an enzyme kinetic algorithm that takes the effective ion concentrations into account [105].

In summary, four-state models are commonly favored. The model of Williams et al. (2013) further incorporates an extra state variable to account for the non-instantaneous response of the retinal complex to light [78]. Modeling a single channel with such a model, therefore requires solving a set of four differential equations. This significantly increases the computational burden, especially in case of multi-compartment or network studies. Additionally, the selection of the correct opsin is crucial to ensure an optimal optogenetic tool. The four-state Markov models are not easily fitted, as they require prior knowledge of the parameter space and its intricate interactions. Furthermore, obtaining optimal parameters can be time-consuming, as the set of differential equations must be evaluated at each step within the chosen optimization algorithm.

2.5 Double Two-State Opsin Model

A double two-state opsin model structure (22OM) is proposed as alternative for opsin modeling (figure 2.6). Below, the model is described in full. I elaborate on the the link between parameters and certain features used in the fitting procedure. A fit is created of the ChR2(H134R) mutant and compared to the 4SB model of Williams et al. (2013) [78]. The performance of both models are tested in a regular spiking neuron [118]. The difference in computation speed is assessed as well, this in the aforementioned regular spiking neuron for different stimulation patterns and in the sparse Pyramidal-Interneuron-Network-Gamma (sPING) network model [119, 120] with increasing number of transfected neurons. Finally, the versatility of the proposed model is evaluated with a fit to a MerMAID opsin [37].

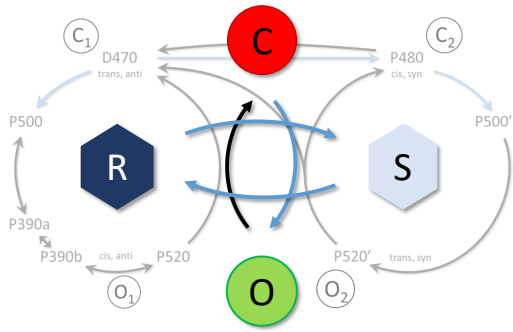

Figure 2.6: The newly proposed double two-state opsin model (22OM) with separation of open-closing mechanism and conductance change due to dark-light adaptation. The latter is captured in the mathematical R and S model state pair. The model overlays the unifying photocycle model as proposed by Kuhne et al. (2019) [107]. Blue arrows indicate light dependent rates.

2.5.1 The Model

The proposed model is based on the original voltage gated sodium model of Hodgkin and Huxley [121]. It consists of two independent two-state pairs as depicted in figure 2.6. In contrast to the sodium model, where the second two-state pair represents the inactivation gate, it represents here the change in conductance due to dark-light adaptation.

After a long enough dark period, the molecules are assumed to be all in a closed dark-adapted state. Upon stimulation, the channel opens with a transition $C \rightarrow O$. On a slightly slower time scale the equilibrium between dark and light adapted molecules is reached. Light adapted molecules have a lower conductance than those that are in the dark adapted state. This change in conductance is captured by a

transition R $\rightarrow$ S. The relationship between these mathematical model states and the physical dark and light adapted states of the opsin molecules is obtained via a linear transformation, i.e., $R = (g_{\mathrm{ChR2}} \cdot DA + g_{\mathrm{LA}} \cdot LA)/g_{\mathrm{ChR2}}$. Consequently, $R\,(S)$ is one (zero) when fully dark adapted and $g_{\mathrm{LA}}/g_{\mathrm{ChR2}}$ (respectively, $1 - g_{\mathrm{LA}}/g_{\mathrm{ChR2}}$) when fully light adapted, with g_{LA} the conductivity of a light adapted channel. DA and LA are the possibilities of the opsin molecules being in a dark or light adapted state, respectively. By using the R state in the model, g_{LA} does not need to be determined, therefore reducing the number of model parameters. The established equilibria of both state pairs depend on the level of optical excitation. After photostimulation, the channels close (O $\rightarrow$ C). Moreover, they all return to the dark adapted state after a long enough recovery period, which is on a much slower time scale than the other temporal kinetics. Because of this slower time scale, the transition S $\rightarrow$ R has to be light dependent as well. Otherwise the equilibrium would be completely on the side of S for every optical excitation level. The ChR2 photocurrent can thus be determined as follows:

$$i_{\mathrm{ChR2}} = g_{\mathrm{ChR2}} G(V)\,(O \cdot R)\,(V - E_{\mathrm{ChR2}}) \tag{2.1}$$

with

$$\frac{dO}{dt} = \frac{O_\infty(I_{\mathrm{rr}}, V) - O(t)}{\tau_O(I_{\mathrm{rr}}, V)} \tag{2.2}$$

$$\frac{dR}{dt} = \frac{R_\infty(I_{\mathrm{rr}}, V) - R(t)}{\tau_R(I_{\mathrm{rr}}, V)} \tag{2.3}$$

where g_{ChR2} is the maximal specific conductivity of the fully dark adapted channel, $G(V)$ is a rectification function, V the membrane potential, I_{rr} the light irradiance, E_{ChR2} the equilibrium potential and O the fraction of molecules in the open state, with O_∞ and τ_{O} its corresponding equilibrium and time constant. R_∞ and τ_{R} are the respective equilibrium and time constants of the R state.

Under voltage clamp conditions and a rectangular optical pulse with constant light intensity, the photocurrent can be expressed in a closed form analytical expression:

$$\begin{aligned} i_{\mathrm{ChR2}} = g_{\mathrm{ChR2}} G(V)(O^{\mathrm{on}}_{\mathrm{ChR2}}(t) + O^{\mathrm{off}}_{\mathrm{ChR2}}(t)) \\ \cdot (R^{\mathrm{on}}_{\mathrm{ChR2}}(t) + R^{\mathrm{off}}_{\mathrm{ChR2}}(t))(V - E_{\mathrm{ChR2}}) \end{aligned} \tag{2.4}$$

with

$$O^{\mathrm{on}}_{\mathrm{ChR2}}(t) = \left[O_\infty - (O_\infty - O_0)\exp\left(-\frac{t - t_{\mathrm{on}}}{\tau_{\mathrm{O}}(I_{\mathrm{rr}}, V)}\right)\right] \cdot \Theta(t - t_{\mathrm{on}})\Theta(t_{\mathrm{off}} - t) \tag{2.5}$$

$$O^{\mathrm{off}}_{\mathrm{ChR2}}(t) = O^{\mathrm{on}}_{\mathrm{ChR2}}(t_{\mathrm{off}})\exp\left(-\frac{t - t_{\mathrm{off}}}{\tau_{\mathrm{O}}(0, V)}\right)\Theta(t - t_{\mathrm{off}}) \tag{2.6}$$

$$R^{\text{on}}_{\text{ChR2}}(t) = \left[R_\infty - (R_\infty - R_0)\exp\left(-\frac{t - t_{\text{on}}}{\tau_{\text{R}}(I_{\text{rr}}, V)}\right)\right] \cdot \Theta(t - t_{\text{on}})\Theta(t_{\text{off}} - t) \tag{2.7}$$

$$R^{\text{off}}_{\text{ChR2}}(t) = \left[1 - (1 - R^{on}_{\text{ChR2}}(t_{\text{off}})) \cdot \exp\left(-\frac{t - t_{\text{off}}}{\tau_{\text{R}}(0, V)}\right)\right]\Theta(t - t_{\text{off}}) \tag{2.8}$$

with Θ the Heaviside function, O_0 and R_0 the initial values of O and R at $t = t_{\text{on}}$ (respectively, 0 and 1 when fully dark adapted) and, t_{on} and t_{off}, respectively, the onset and offset of the optical pulse.

This is of particular use during the fitting procedure as the model is fit to experimental data, recorded under the same aforementioned conditions. Moreover, strong correlations between the model time constants and experimentally determined features (figure 2.4) are observed. These can be exploited to obtain a first approximation of the model's parameters (see section 2.5.2). When $\tau_{\text{O}} \ll \tau_{\text{R}}$, the transition rate time constant τ_{O} can be easily obtained from the activation (τ_{on}) and deactivation (τ_{off}) time constants. Under the same conditions, τ_{R} strongly correlates with the inactivation time constant (τ_{inact}) when $I_{\text{rr}} \neq 0$. The recovery time constant needs to be scaled as shown in equation (2.10) to get a good approximation of the dark-light adaptation time constant under dark ($I_{\text{rr}} = 0$) conditions. This relationship is obtained by evaluating the recovery time definition with the given model equations, i.e., $\tau_{\text{recov}} = t_{\text{on},2} - t_{\text{off},1} \rightarrow I_{\text{p},2}/I_{\text{p},1} = 1 - \exp(-1)$. Here, $t_{\text{on},2}$ is the onset time of the second pulse, $t_{\text{off},1}$ the offset of the first pulse, and $I_{\text{p},2}$ and $I_{\text{p},1}$ the current peak value of second and first pulse, respectively.

$$\tau_{\text{O}}(I_{\text{rr}}, V) \approx \tau_{\text{on}}, \;\; \tau_{\text{O}}(0, V) \approx \tau_{\text{off}} \;\text{ and }\; \tau_{\text{R}}(I_{\text{rr}}, V) \approx \tau_{\text{inact}} \tag{2.9}$$

$$\tau_{\text{R}}(0, V) \approx \tau_{\text{recov}} / \left(1 - \ln\frac{1}{1 - I_{\text{ratio}}}\right) \tag{2.10}$$

Furthermore, following conditions need to be met for the relationship to hold true:

$$\begin{aligned} t_{\text{p},1} - t_{\text{on},1} &\approx t_{\text{p},2} - t_{\text{on},2} \\ t_{\text{p},1} - t_{\text{on},1} &> \tau_{\text{O}} \\ t_{\text{off},1} - t_{\text{on},1} &> \tau_{\text{R}} \end{aligned} \tag{2.11}$$

The first, $t_{\text{p,i}} - t_{\text{on,i}}$ is the time required to reach the peak value since onset of pulse i. This needs to be approximately the same in both first and second pulse, while these need to be significantly larger than the activation time constant. The last one requires that the steady-state value is reached at the end of the first pulse.

Unless specified, the time constants and time in this study are in seconds, the membrane potential in mV and the intensity in W/m^2. The units of the conductance depend on the experimental data of each opsin, i.e., mS/cm^2 and μS in case of the ChR2(H134R) and MerMAID fit, respectively.

2.5.2 The Fitting Procedure

Due to the dependency on both the potential and light intensity, more than twenty parameters need to be inferred. This vast parameter space impedes finding the optimal solution which is at a high computational cost. To alleviate this, the fitting procedure can be divided into four steps.

The first step is the extraction of the features, which is described by Williams et al. (2013) [78]. The peak current (I_{peak}) is the maximal deflection from baseline. The steady-state current (I_{ss}) is the plateau value. The current ratio (I_{ratio}) is then $I_{\mathrm{ss}}/I_{\mathrm{peak}}$. The time constants are extracted using mono-exponential curve fits. To this end, a nonlinear least-squares curve fit is performed, with a trust-region-reflective algorithm. Furthermore, a multi-start algorithm with ten starting points was used to ensure finding of the global solution. The variable and function tolerance were set to 10^{-12}. The recovery time constant, i.e., the time necessary between two pulses to have a second peak current which is 63% of the first peak (see definition in previous subsection), was determined from a set of two-pulse experiments.

Next, τ_{O} and τ_{R} are fit to the obtained target data. Both are fit to the corresponding time constants (see equation (2.9) and (2.10)) using the aforementioned nonlinear least-squares method. Again, a multi-start algorithm is used but with 2000 starting points. For the intensity dependence, sigmoidal functions on the log-scale are used while for the voltage dependence a logistic regression was selected. The two dependencies are combined by either a multiplication or a reciprocal addition. The relationships and combination schemes are given by equations (2.12)-(2.16), with $\mathrm{p_i},\ \mathrm{i} = 1 \rightarrow 6$ indicating the unknown parameters of each relationship individually.

$$\tau_{\mathrm{O}}(I_{\mathrm{rr}}) = \frac{p_3}{1 + \exp(p_1/p_2) \cdot I_{\mathrm{rr}}^{1/p_2 \cdot \ln(10)}} \tag{2.12}$$

$$\tau_{\mathrm{R}}(I_{\mathrm{rr}}) = p_1 \left(1 - \frac{p_2}{1 + \exp(p_3/p_4) \cdot I_{\mathrm{rr}}^{-1/p_4 \cdot \ln(10)}} - \frac{(1 - p_2)}{1 + \exp(p_5/p_6) \cdot I_{\mathrm{rr}}^{-1/p_6 \cdot \ln(10)}} \right) \tag{2.13}$$

$$\tau_{\mathrm{X}}(V) = \frac{p_1}{1 + \exp(-(V - p_2)/p_3)} \tag{2.14}$$

$$\tau_{\mathrm{X}}(I_{\mathrm{rr}}, V) = \tau_{\mathrm{X}}(I_{\mathrm{rr}}) \cdot \tau_{\mathrm{X}}(V) \tag{2.15}$$

or

$$\left[(\tau_{\mathrm{X}}(I_{\mathrm{rr}}))^{-1} + (\tau_{\mathrm{X}}(V))^{-1} \right]^{-1} \tag{2.16}$$

$$O_{\infty}(I_{\mathrm{rr}}) = \frac{1}{1+\exp(p_1/p_2)\cdot I_{\mathrm{rr}}^{-1/p_2\cdot\ln(10)}} \tag{2.17}$$

$$R_{\infty}(I_{\mathrm{rr}}) = 1 - \frac{p_3}{1+\exp(p_1/p_2)\cdot I_{\mathrm{rr}}^{-1/p_2\cdot\ln(10)}} \tag{2.18}$$

$$G(V) = \frac{p_1\cdot(1-p_2\exp(-(V-E_{\mathrm{ChR2}})/p_3))}{V-E_{\mathrm{ChR2}}} \tag{2.19}$$

In a third step, the parameters of the rectification function $G(V)$ and the equilibrium constants O_{∞} and R_{∞} are fit. The used relationships are given in equation (2.19), (2.17) and (2.18), respectively. The potential dependence of O_{∞} and R_{∞} are omitted because this is mostly covered by the rectification function. The parameter values are determined by minimizing the cost function described below:

$$f_{\mathrm{cost}} = \left(\frac{1}{N}\left[\sum_{i=1\rightarrow N}\Delta I_{\mathrm{peak}}(I_{\mathrm{rr},i},V_i)^2 + \Delta I_{\mathrm{ss}}(I_{\mathrm{rr},i},V_i)^2 + \Delta I_{\mathrm{ratio}}(I_{\mathrm{rr},i},V_i)^2\right]\right)^{1/2}$$
$$\Delta I_{\mathrm{x}}(I_{\mathrm{rr},i},V_i) = w_{\mathrm{x}}\left(y_{\mathrm{x}}(I_{\mathrm{rr},i},V_i) - t_{\mathrm{x,I_{rr,i},V_i}}\right), \text{with } x = \mathrm{peak,ss,ratio} \tag{2.20}$$

Here, y_{x} and $t_{\mathrm{x,I_{rr,i},V_i}}$ are respectively the model output and target value at stimulation values (I_{rr},V), with $y_{\mathrm{peak}} = \max_{\mathrm{t}}(|i_{\mathrm{ChR2}}^{\mathrm{on}}(t,I_{\mathrm{rr}},V)|)$, $y_{\mathrm{ss}} = i_{\mathrm{ChR2}}^{\mathrm{on}}(t_{\mathrm{off}})$ and $y_{\mathrm{ratio}} = y_{\mathrm{ss}}/y_{\mathrm{peak}}$. $i_{\mathrm{ChR2}}^{\mathrm{on}}(t,I_{\mathrm{rr}},V)$ is the current during the photostimulation pulse ($t\,\epsilon\,[t_{\mathrm{on}},t_{\mathrm{off}}]$) for a certain irradiance I_{rr} and voltage V. The current is calculated by evaluating equations (2.4)-(2.8) with the determined dependencies in the previous step. N is the total number of stimulation sets (I_{rr},V). The minimization of f_{cost} is performed with the MATLAB *fmincon*-function and multi-start algorithm with 3000 starting points to increase chance of finding the global optimum. The upper and lower boundaries as well as the initial conditions are summarized in table 2.2. Extra nonlinear constraints are applied to assure that O_{∞} approaches one for high intensities (see section 2.6.1 and 2.6.4) and $G(V) \geq 0$. A final constraint ensures a current decay back to baseline after the optical stimulation, i.e., $i_{\mathrm{on}}(t_{\mathrm{off}}) > i_{\mathrm{off}}(t)$ or $O^{\mathrm{on}}(t_{\mathrm{off}})\cdot R^{\mathrm{on}}(t_{\mathrm{off}}) > O^{\mathrm{off}}(t)\cdot R^{\mathrm{off}}(t)$, resulting in:

$$R_{\infty}(I_{\mathrm{rr}},V) > 1 - \frac{\tau_{\mathrm{R}}(0,V)}{\tau_{\mathrm{R}}(0,V)+\tau_{\mathrm{O}}(0,V)} \tag{2.21}$$

Finally, a global optimization is performed with the parameters of all rate functions included. First, a new parameter space is defined, which is 10% of the original parameter space but centered around the values obtained in previous steps and limited by the former. With the gathered dependencies, the ChR2 current is calculated according to equation (2.4). All model features are now extracted in the same manner as performed on the experimental data. These are used to determine a cost function which is the weighted root mean square error (equation (2.20)), with additional terms: $\Delta\tau_{\mathrm{on}}(I_{\mathrm{rr}},V)^2$, $\Delta\tau_{\mathrm{off}}(I_{\mathrm{rr}},V)^2$, $\Delta\tau_{\mathrm{inact}}(I_{\mathrm{rr}},V)^2$ and $\Delta\tau_{\mathrm{rec}}(I_{\mathrm{rr}},V)^2$. Subsequently, the problem is optimized with a bounded particle swarm optimization [122–124], containing 1000 particles and with a time limit of 24 hours. The

same solver settings and constraints are imposed as described in previous steps. The single-pulse experiments are evaluated with a time step of $1.5 \cdot 10^{-4}$ s, while for the two-pulse experiments a step of 1 ms is used.

2.5.3 Performance Tests

In our study, two opsin fits were performed. First, a fit is made to the data reported by Williams et al. (2013) of the ChR2(H134R) [78]. The model accuracy is compared to the four state Markov model created by the same group. Four metrics are used to analyze the goodness-of-fit, i.e. Root mean square error (RMSE), Root mean square normalized error (RMSNE), Root mean square weighted error (RMSWE) and root mean square Z-score error (RMSZE):

$$\mathrm{RMSWE} = \left(\frac{1}{N} \sum_{i=1 \rightarrow N} w_x^2 \cdot \left[y_x(I_{\mathrm{rr},i}, V_i) - t_{x,I_{\mathrm{rr},i},V_i} \right]^2 \right)^{1/2} \tag{2.22}$$

where w_{x} equals 1, $1/t_{\mathrm{x,I_{rr,i},V_i}}$ or $1/\sigma_{\mathrm{x,I_{rr,i},V_i}}$ in case of RMSE, RMSNE or RMSZE, respectively. $y_{\mathrm{x}}(I_{\mathrm{rr},i}, V_i)$, $t_{\mathrm{x,I_{rr,i},V_i}}$ and $\sigma_{\mathrm{x,I_{rr,i},V_i}}$ are the model output, target feature and standard deviation of target feature x under irradiance I_{rr} and voltage V of set i, and w_{x} are the weights used in f_{cost}. The metrics are also determined in the overall, time constant features ($\tau_{\mathrm{on}} + \tau_{\mathrm{off}} + \tau_{\mathrm{inact}} + \tau_{\mathrm{rec}}$) only and current features ($I_{\mathrm{p}} + I_{\mathrm{ss}} + I_{\mathrm{ratio}}$) only case. Here the squared errors of all features are summed first before taking the root and mean. The RMSWE is equivalent to the training error. However, it could not be used to compare the model fits as the used weights were not equal across fitting procedures (different weights were used in the 4SB fit, see Williams et al. (2013) [78]). Therefore, the other metrics were defined as well. Where the RMSE is biased by high values, the RMSNE is biased by values close to zero and RMSZE which includes the uncertainty of the target features via $\sigma_{\mathrm{x,I_{rr,i},V_i}}$ but could not be determined for the recovery time constant.

Both models are then implemented in a regular spiking neuron, described in Pospischil et al. (2008) [118]. The strength duration curves (SDC) are determined. When the irradiance is selected as strength for the SDC, a poor fit is obtained. This is due to the assumption of an RC equivalent circuit and a rectangular stimulation pulse in the Hill-Lapicque relationship equation (2.23) [79, 125]. Therefore, the SDC fit is performed on the average inward stimulation current or temporal averaged current ($i_{\mathrm{ChR2,avg}}$, TAC), as described by [79].

$$i_{\mathrm{ChR2,avg}} = \frac{I_{\mathrm{ChR2,rheo}}}{\left(1 - \exp(-\frac{PD}{\tau_{\mathrm{ChR2,chron}}/\ln(2)})\right)} \tag{2.23}$$

$$i_{\mathrm{ChR2,avg}} = \frac{1}{PD} \cdot \int_0^{T_{\mathrm{end}}} i_{\mathrm{ChR2}}(t)dt \tag{2.24}$$

with PD the pulse duration and T_{end} one second after the end of the pulse. The relationship between the irradiance and $i_{\mathrm{ChR2,avg}}$ is obtained through a power

series fit, which allows calculation of the irradiance rheobase (I_{rheo}) and chronaxie (τ_{chron}) as follows:

$$I_{\mathrm{rheo}} = a \cdot I_{\mathrm{ChR2,rheo}}^{b} + c \tag{2.25}$$

$$\tau_{\mathrm{chron}} = -\frac{\tau_{\mathrm{ChR2,chron}}}{\ln(2)} \ln\left(1 - \frac{I_{\mathrm{ChR2,rheo}}}{[(2\,I_{\mathrm{rheo}} - c)/a]^{1/b}}\right) \tag{2.26}$$

where a, b and c are parameters obtained in an empirically power series fit of the irradiance curve versus the inward stimulation current ($I_{\mathrm{rr}} = a \cdot (i_{\mathrm{ChR2,avg}})^{b} + c$) [79].

Moreover, the simulation speed is determined for different stimulation paradigms, i.e., simulation time (T_{end})/runtime in a regular spiking neuron [118]. Therefore, I varied the pulse repetition frequency, stimulation time and duty cycle. The intensity was fixed for each model and set to a value that elicited a firing rate of 100 Hz in the regular spiking neuron in case of a two pulse stimulation of two seconds with duty cycle 0.5 and pulse repetition frequency of 1 Hz. The models were solved by the MATLAB Variable Step Variable Order solver (VSVO) ode113-solver (order 1-13, Adams-Bashort-Moulton predictor-corrector pairs) [126], with a maximum time step of 100 μs and default tolerances, i.e., relative and absolute tolerance equal to 10^{-3} and 10^{-6}, respectively.

Finally, computational gain with the proposed model compared to the 4 state Markov model was tested in a network model with an increasing number of transfected neurons. Therefore, I used the sparse Pyramidal-Interneuron-Network-Gamma (sPING) [119], which was implemented via the DynaSim toolbox [120]. The ChR2(H134R) models were added to the pyramidal neurons. The number of inhibitory neurons was varied between 3 and 100 while the 4/1, pyramidal/interneuron-ratio was maintained. The network was fully connected and the GABAa and AMPA conductivities were scaled such that the total input per neuron stayed the same, i.e., $g_{\mathrm{GABAa}} = 2/(N_{\mathrm{intern}})[\mathrm{mS/cm^2}] = g_{\mathrm{AMPA}}$, with N_{intern} the number of interneurons in the sPING-network. In each case a single pulse stimulation of 300 ms was applied with a total simulation time of 500 ms. The irradiance was set such that the firing rates were equal for both ChR2 models. The study was performed with both a fixed step (10 μs) runge-kutta 4 solver and an ode15s-solver (stiff VSVO-solver, order 1-5, based on numerical differentiation formulas) [126] with a maximum time step of 100 μs, and a relative and absolute tolerance of 10^{-6}.

The results shown in this chapter are computed with a 3.4 GHz clock rate, quad core system and 8 GB RAM.

2.5.4 Versatility

The versatility of the proposed model structure is shown with a fit to the MerMAID1 opsin [37]. For more detail on the data set, I refer to the work of Oppermann et al. (2019) [37]. The same metrics as aforementioned are used to assess the fit accuracy.

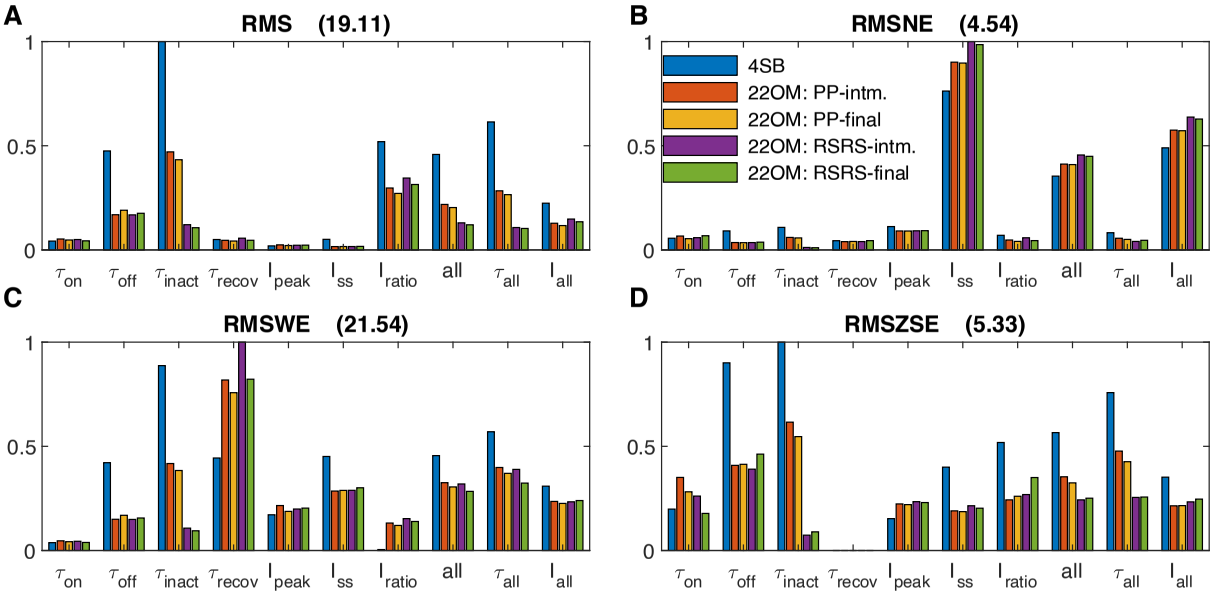

Figure 2.7: Normalized goodness-of-fit results of the model fits to the ChR2(H134R) data reported by [78]. Goodness-of-fit according to four metrics: Root-mean-square error (**A**), Root-mean-square normalized error (**B**), Root-mean-square weighted error (**C**) and Root-mean-square of z-score error (**D**). The compared models are the 4SB model reported by [78], the 22OM model with twice the product combination of time constants (intermediate fit 22OM: PP-intm and final fit 22OM: PP-final), and the 22OM model with twice the reciprocal addition combination of time constants (intermediate fit 22OM: RSRS-intm and final fit 22OM: RSRS-final). The normalization value is given in the title of each sub-figure. all, τ_{all} and I_{all}, are errors where the squared errors of all features, all time constants and all current features are, respectively, added first before taking the root and mean. The depicted legend is valid in all sub-figures

2.6 Results

The results of our study *Double Two-State Opsin Model With Autonomous Parameter Inference* [1] are given in this section, followed by the discussion in the next section (section 2.7).

To test the feasibility of the proposed double two-state opsin model structure (22OM), it was fit to two data sets. First, it was fit to the data set of a ChR2(H134R) opsin reported by Williams et al. (2013), which was collected in a ChR2(H134R)-HEK293 stable cell line [78]. By the same group already a four state Markov model was fit. This allowed detailed analyzes of the performance of my model. To this end, a comparison of the response to optical stimuli was made in a regular spiking neuron [118]. Moreover, the computational speed was determined for different stimulation paradigms in the former neuron model as well as in the sPING [119] network model with increasing number of transfected neurons. Finally the versatility of the proposed modeling scheme was assessed with a fit to a MerMAID opsin which is an anion-conducting and intensely desensitizing channelrhodopsin.

2.6.1 The ChR2(H134R) Fit

A 22OM fit of the ChR2(H134R) opsin was obtained by applying the fitting procedure, described in the materials and methods section 2.5.2, to the experimental data. As Williams et al. (2013) [78] already reported the target features, the first step could be omitted. The absence of differential equations in the fitting procedure allowed for multiple fits to be made, due to the significant reduction of the computational cost. Multiple weight sets, non-linear constraints and combinations of dependency addition of the time constants (product (equation (2.15)) and reciprocal sum (equation (2.16))) were tested. The parameters of the two best fits are shown in table 2.2, where RSRS and PP is the fit with a double reciprocal sum and product combination, respectively. Both results were obtained with $w_{\mathrm{peak}} = 10$, $w_{\mathrm{ss}} = 20$, $w_{\mathrm{ratio}} = 50$, $w_{\mathrm{on}} = 1000$, $w_{\mathrm{inact}} = 1000$, $w_{\mathrm{off}} = 1000$, $w_{\mathrm{recov}} = 20$, and a constraint where $O_{\infty}(I_{\mathrm{rr}}, V) > 0.6$ for $I_{\mathrm{rr}} \geq 5500\ \mathrm{W/m^2}$. The weights are chosen as such to level the differences between features to the same order of magnitude. As a result, all features have the same impact in the cost function with a slight preference for the current features. The time constant features are all expressed in seconds, while their values are in the order of milliseconds (except τ_{recov}), explaining the high weight values. The extra constraint is justified as the current peak already starts to saturate for the highest intensity values, thus clamping the intensity dependence of the open steady-state value above the bending point in the logistics curve.

The models' accuracy according to the four goodness-of-fit metrics equation (2.22) are shown in figure 2.7. Overall, a positive effect of the final optimization step can be observed. The largest impact is on the time constants, as expected. In the second step of the fitting procedure, the transition rate time-constants (τ_{O} and τ_{R}) are approximated with a one on one relationship of the target features (see equation (2.9) and (2.10)). These approximations are true in case of high differences in order of magnitude. However, when the differences are smaller some

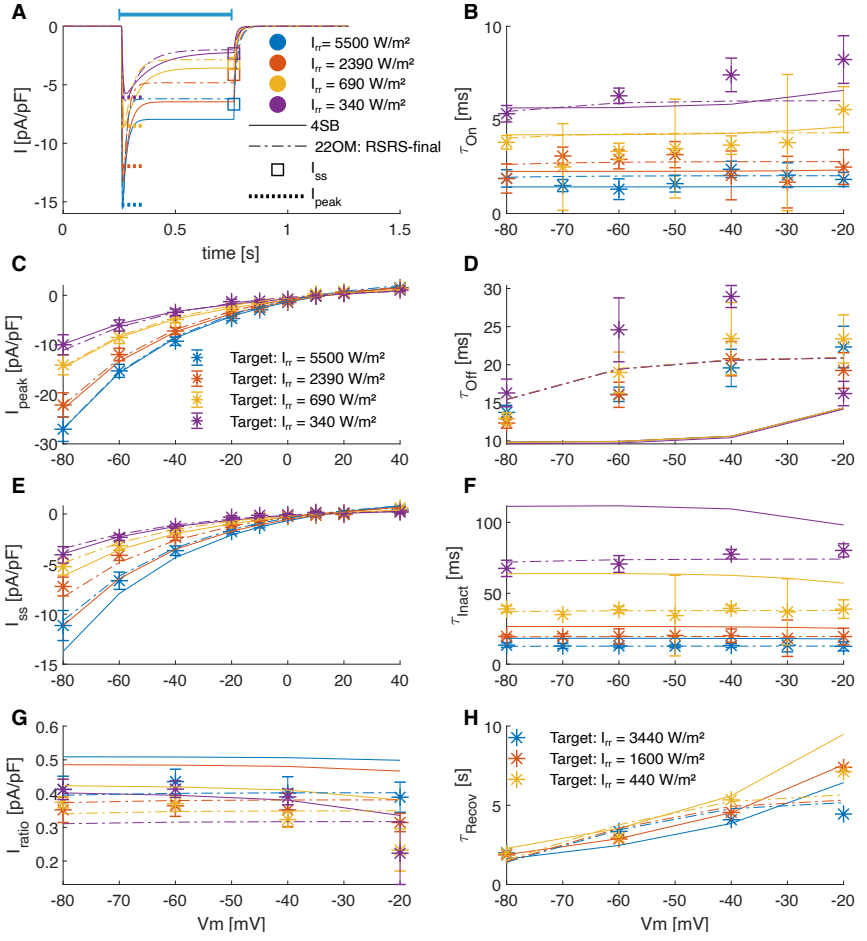

Figure 2.8: Comparison of model outcomes (4SB and 22OM: RSRS-final) with parameters obtained from experiments. **A** The ChR2(H134R) current during a pulse of 0.5 s (indicated by blue bar) at a voltage clamp of -60 mV; according to the 4SB model (full lines) and 22OM model (dashed dotted lines). The colors indicate the applied intensity and are valid in **A-G**. The dotted line and square indicate respectively the experimental current peak and steady-state current at corresponding intensity and potential. **B, D and F** Voltage dependence of respective τ_{on}, τ_{off} and τ_{inact} across four irradiance levels. **C, E and G** The current-voltage curves of the peak, steady-state and current ratio, respectively. The asterisks with errorbars indicate the experimental mean $\pm$ standard deviation. **H** The recovery time constant as function of the membrane potential for three different irradiance levels as depicted in the plot.

cross correlations exist, for instance τ_{R} strongly affects τ_{on} as well, resulting in an underestimation of τ_{O}. I denote that according to all metrics, the estimation accuracy of τ_{on} and τ_{inact} increases, however, at the cost of τ_{off}. Also, a significant improvement is observed in case of τ_{recov}. This deviation is due to the fact that the conditions equation (2.11) are not fully met. Furthermore, an increased goodness-of-fit of the inactivation time constant can be observed in case of the RSRS vs PP fit. τ_{R} predominately defines both the inactivation and recovery time constant. In case of the PP fit, a separation of variables is applied where independence is assumed. However, as can be seen in figure 2.8 (F) and (H), a more clear voltage dependency is present in τ_{recov} compared to τ_{inact}. In other words, for low intensities (with high time constants as result) the potential effect is high while the effect is low for high intensities or small time constants. This interdependence is exactly obtained with the reciprocal addition scheme. The same, however less pronounced, can be observed in case of the activation and deactivation time constants (τ_{on} and τ_{off}). Consequently, only the RSRS fit is used in further analysis.

Figure 2.8 shows a detailed comparison of the outcome of my model according to the RSRS fit and the 4SB model, versus the experimentally determined target features. Overall, it can be observed that the proposed model performs at least as well as the 4SB model. Moreover, all features are well approximated. It can be seen that with the 4SB model, the steady-state value is overestimated in case of negative potentials (figure 2.8 (A) and (E)). However, a better representation is obtained for positive potentials, which explains the lower root-mean-squared normalized error (RMSNE, figure 2.7 (B)).

2.6.2 Neural Response in Regular Spiking Neuron

To analyze the neural response, the strength duration curves (SDC) are determined of the proposed 22OM model with RSRS fit and the 4SB model in a regular spiking neuron, described in [118]. First, the Hill-Lapicque model fit is performed on temporal average current (TAC), as described in section 2.5.3. Very good fits were obtained for both models. The adjusted r^2 ($\bar{\mathrm{R}}^2$) of TAC versus PD are 0.9961 and 0.9953 for the 22OM and 4SB model, respectively. The rheobase of the 22OM model (0.49 $\mu\mathrm{A/cm}^2$) is slightly higher than when the 4SB is used (0.47 $\mu\mathrm{A/cm}^2$). Also the chronaxie is higher (47.51 ms vs. 39.45 ms). Consequently, according to the 4SB model for any pulse duration, less charge is injected optogenetically to excite a regular spiking neuron via a ChR2(H134R) opsin. The difference between the models can be attributed to the difference in deactivation time constant (τ_{off}). This is higher in the 22OM model resulting in a slower closing mechanism and thus increased current injection after the AP. A good cell-type-specific empirical mapping of TAC to irradiance was obtained as well (equation (2.25)), with $\bar{\mathrm{R}}^2$ values of 0.9449 (22OM) and 0.9638 (4SB). The parameter values are respectively, $\mathrm{a} = 8.18,\ \mathrm{b} = 1.26$ and $\mathrm{c} = 1.68$, and $\mathrm{a} = 22.30,\ \mathrm{b} = 1.51$ and $\mathrm{c} = 12.32$ in case of the 22OM and 4SB mapping. The lower $\bar{\mathrm{R}}^2$ of the 22OM mapping resulted also in a slightly lower value of 0.9298 for the irradiance to PD curve while this is 0.9509 in case of the 4SB fit.

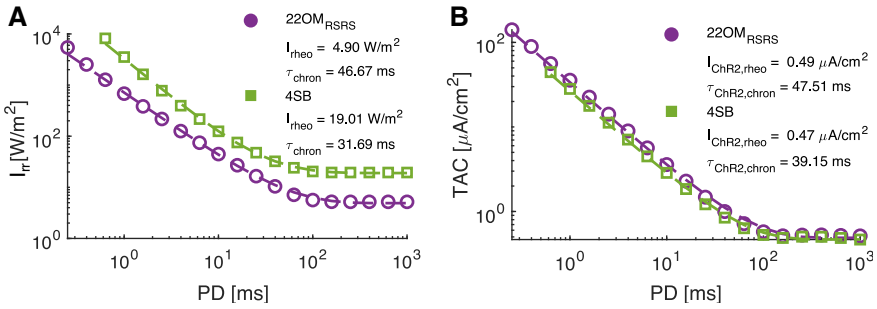

Figure 2.9: The strength duration curves (SDC) of the 22OM RSRS and 4SB model in a regular spiking neuron. **A** Irradiance versus pulse duration with a mapping (dashed line) of the SDC in **B** according to a power series. **B** Temporal average current or average injected current vs pulse duration. Dashed line represents the Hill-Lapicque model fit. The rheobase and chronaxie are depicted in the figures. The results of the 22OM and 4SB model are in purple and green, respectively.

Based on the mapping parameters and figure 2.9, it can be seen that lower intensity level results in higher injected currents when the 22OM model is used. Indeed, extrapolation of the model fit to low intensities results in higher open probabilities than for the 4SB model, hence the difference in irradiance rheobase of 4.90 $\mathrm{W/m^2}$ versus 19.01 $\mathrm{W/m^2}$. Based on the higher peak values for high intensities in case of the 4SB model, one could expect convergence of the irradiance SDCs. However, due to the slow activation kinetics, the peak value is not reached at small pulse durations. Even though the activation time constant is overall higher for the 22OM model (figure 2.8 (B)), the bi-exponential current rise due to the extra state variable $\left(\tau_{\mathrm{ChR2}} \cdot dp/dt = S0(I_{\mathrm{rr}}) - p\right.$, a time-dependent function reflecting the probabilistic, non-instantaneous response of the ChR2-retinal complex to light [78]$\left.\right)$ in the 4SB model results in a lower current value at the end of the pulse.

2.6.3 Computational Speed

The proposed model in this study contains only two differential equations, which is 50% less in comparison with the 4SB model. Consequently, a reduction of the computational time is expected. Figure 2.10 (A-F) summarizes the computational speed for different stimulation protocols in a regular spiking neuron. This for fixed irradiances (22OM: 3162 $\mathrm{W/m^2}$ and 4SB: 1259 $\mathrm{W/m^2}$) set to a value that elicit a firing rate of 100 Hz, as described in section 2.5.3. Subfigures 2.10 (A-D) show an overall increase of the computational speed in favor of the 22OM model, with a maximum of 25% for high frequency and duty cycle stimulation. On average the relative difference of the simulation speeds, i.e., simulation speed with 22OM minus simulation speed with 4SB with respect to the latter, is about 20%. Because the simulations were solved using a variable step solver, the difference in firing

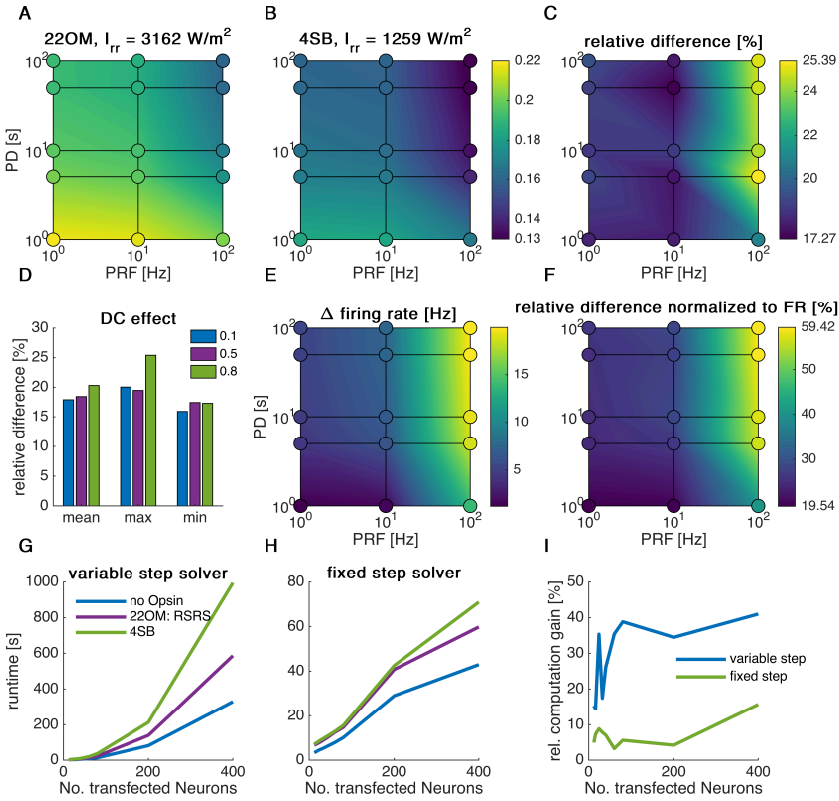

Figure 2.10: The computational speed of optogenetic neuromodulation in a regular spiking (RS) neuron and sparse Pyramidal-Interneuron-Network-Gamma (sPING). **A-F** Simulation speed, i.e. simulation time/runtime, for different stimulation protocols with varying pulse duration (PD) and pulse repetition frequency (PRF) in a regular spiking neuron, described by Pospischil et al. (2008) [118]. **A** The absolute simulation speed with the 22OM-RSRS fit. **B** The simulation speed with the 4SB model. Colorbar is valid for **A** and **B**. **C** The relative difference, i.e., (22OM-4SB)/4SB. **A-C** The results are for a fixed duty cycle of 0.8. **D** The effect of the duty cycle on the simulation speed. **E** The difference in firing rate in case of the 22OM model vs. 4SB. **F** The relative difference of simulation speed normalized to the firing rate. **G-I** Runtime of a continuous 300 ms optical pulse in the sparse Pyramidal-Interneuron-Network-Gamma (sPING), with increasing number of transfected neurons. **G** Runtime with a variable step solver. **H** Runtime with a fixed step solver. **I** Relative computation gain, i.e., -(22OM-4SB)/4SB. The used intensities are shown in the titles of **A** and **B**, which give rise to a 100 Hz firing rate (see section 2.5.3).

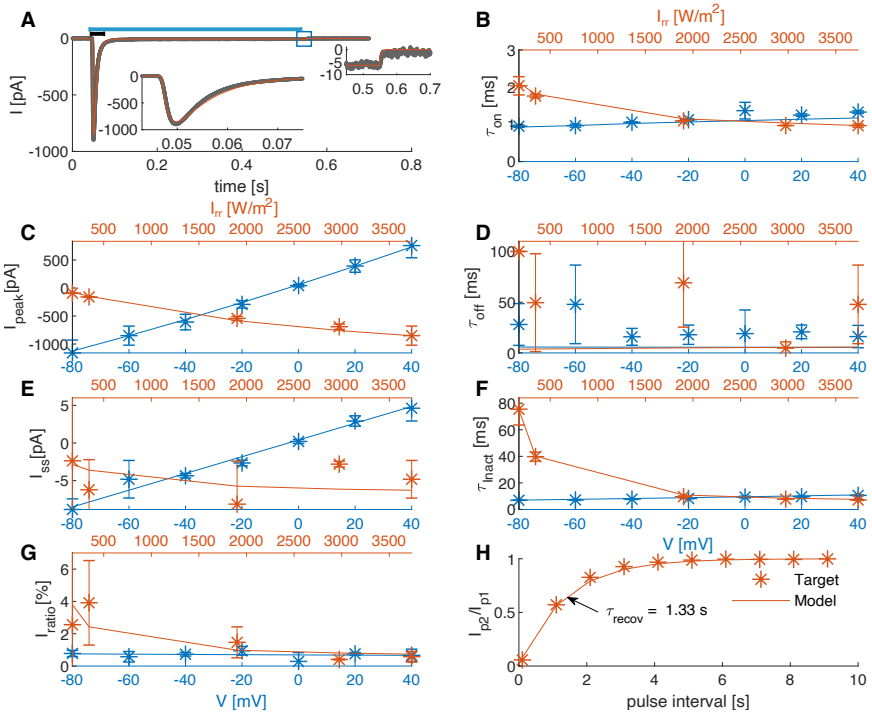

Figure 2.11: Comparison of the 22OM-Mermaid (final fit) model outcomes and experimental data. **A** In gray, the photocurrent of a voltage clamp experiment during a 0.5 s continuous illumination with an intensity of 3734 $\mathrm{W/m^2}$ (indicated with blue bar on top) [37]; In red, the corresponding model outcome. Left inset is a zoom of the current peak (0.045-0.075 s, indicated with black bar). Right inset is a zoom of the current deactivation (0.45-0.7 s, indicated with a blue square). **B-G** The voltage dependence of the target features (τ_{on}, I_{peak}, τ_{off}, I_{ss}, τ_{inact} and I_{ratio}) at an irradiance of 3734.4 $\mathrm{W/m^2}$ is shown in blue. The light dependence at a holding potential of -60 mV is depicted in red. **H** Ratio of the peak currents in response to a two-pulse stimulation protocol at -60 mV and 3734 $\mathrm{W/m^2}$ as function of the inter-pulse interval. The recovery time (the interval time necessary to have a ratio of 63%), is indicated with a black arrow.

rate could distort the effective simulation speed, as during an action potential a smaller timestep is selected. Therefore, the relative difference of the simulation speed normalized to the firing rate is depicted as well, with an increase of the gain to 60% as result. The runtime versus number of transfected neurons is depicted in figure 2.10 (G-I). The simulation outcomes were the same with the variable and fixed step solver, validating the solver settings. Moreover, the firing rate was equal for both opsin models, hence no normalization was necessary. A clear reduction

can be observed when the 22OM model is selected instead of the 4SB model, both with a fixed and variable step solver. The time gain by using the proposed model is 15% (5%) in case of 12 neurons and goes up to 40% (15%) and rising when 400 transfected neurons are included with a variable (fixed) step solver.

2.6.4 Versatility of the Proposed Model

Finally, I address the versatility of the proposed model and the fitting procedure. Due to the increasing number of possible opsins, it is favorable that their kinetics can be correctly modeled and a fit is easily obtained without preliminary knowledge. To this end, I applied the fitting procedure to experimental data of a MerMAID opsin, which has unlike classical ChR2 a very strong desensitization [37]. Starting from the photocurrent traces, the target features had to be extracted first. Next the parameter space was defined. The rectification function was omitted because this was not observed in the experimental data. Aside from this, the lower bound and initial condition of only the third parameter of R_∞ was altered (table 2.2). This straight forward adjustment was made due to the strong desensitization. The weights of the cost function were set to $w_{\mathrm{peak}} = 0.04$, $w_{\mathrm{ss}} = 1$, $w_{\mathrm{ratio}} = 250$, $w_{\mathrm{on}} = 10000$, $w_{\mathrm{inact}} = 10000$, $w_{\mathrm{off}} = 10000$, $w_{\mathrm{recov}} = 10$, again to level the errors to the same order of magnitude. Because no saturation of the current was observed at high intensity levels a constraint: $O_\infty(I_{\mathrm{rr}}, V) < 0.5$ for $I_{\mathrm{rr}} \leq 4000\mathrm{W/m^2}$, was added.

The result of the fit is shown in figure 2.11. The parameters of the final and intermediate fit are summarized in table 2.2. The model here is with a double product combination of the time constant dependencies. Because the recovery time constant was only determined under one condition, there is no evidence on the interdependence of the variables. This is also supported by the small voltage dependence of the (de)activation time constants. Overall, it can be stated that a good fit is obtained as all kinetics are expressed correctly. Only, the deactivation time constant seems to be underestimated. This is a consequence of the constraint in equation (2.21), which ensures a current decay back to baseline after optical stimulation. Due to its strong desensitization, R_∞ has to be small, thus inducing an upper limit on $\tau_{\mathrm{O}}(0, V)$, which defines the deactivation time constant. The trade off is justified due to the higher uncertainty of the deactivation time constant (see figure 2.11 (D)). Moreover, the overall effect is expected to be low as can be seen in the right inset of figure 2.11 (A).

2.7 Discussion

The proposed double two-state model structure for the modeling of opsins appears to be a good alternative to the computationally more expensive four state Markov, non-instantaneous models. All features are represented, with even some improved fit accuracy in comparison with a four state Markov variant. Furthermore, with the proposed fitting procedure, I was able to fit two opsins, ChR2(H134R) and MerMAID. Although the prominent difference of the mutants kinetics, the fitting

procedure allowed us to get these fits with only minor adjustments of the parameter space and constraints. Therefore, creating the possibility for autonomous model fitting based on photocurrent traces. Moreover, a good fit is obtained within an acceptable time frame, due to the absence of differential equations in the fitting procedure, which is not achievable in case of a four state Markov model. The intermediate fit is obtained within three hours, while the final fit always flagged the time limit of 24 hours. Increasing the limit improves the fit accuracy but only small changes were observed. Fine tuning of the optimization settings, such as number of particles or tolerances, could reduce the training error even more. However, this was out of the scope of the study.

The proposed model is an empirical model. The fit is performed on a limited dataset thus extrapolation should be treated with care. This is clear from the neural response results in section 2.6.2. Although both the 4SB and my model were fit to the same experimental data, a clear discrepancy between the fitted rheobase is observed $\left(4.90\ \mathrm{W/m^2}\right.$ (22OM) versus 19.01 $\left.\mathrm{W/m^2}\right.$ (4SB)$\big)$. Unlike the chronaxie where the difference can be attributed to the model's structure, the difference in rheobase is due to the discrepancy between opening rates after extrapolation to low intensities, attributed to the fit and intensity dependence chosen in each model. More experiments are required in order to validate this.

The dependencies chosen here are all, except the rectification, sigmoidal. Therefore, they are all bounded and monotonic. This is in accordance with a channel's behavior, i.e., increased and faster opening at higher intensities but limited to an open probability of one. I opted for a biphasic logistics function for $\tau_{\mathrm{R}}(I_{\mathrm{rr}})$ modeling. This is in agreement with the hypothesis of the necessity of two light dependent rates $\big($(R $\rightarrow$ S) and (S $\rightarrow$ R), see section 2.5.1$\big)$ and the second and third photochemical pathways described by Kuhne et al. (2019) [107] (figure 2.5 (A)). Other functions were tested, e.g., weibull or asymmetric logistics with double intensity dependence, however no improvement was observed. Initially, separation of variables was assumed to suffice due to the lack of experimental evidence of complex channel interdependence of both irradiance and potential of each feature separately. However, due to the models structure, τ_{on} and τ_{off} share the same voltage dependency, as well as τ_{inact} an τ_{recov}. The voltage dependence of τ_{recov} and τ_{off} was clearly more pronounced in the experimental data of the ChR2(H134R) mutant. Therefore, the reciprocal addition (equation (2.16)) was tested as alternative, resulting in an improved fit accuracy. However, this only scales down the voltage dependent effect on τ_{on} and τ_{inact} while the same relationship is maintained. The necessity of more complex relationships could be investigated in future work as well as the need for voltage dependence of the rate functions steady-state values (O_∞ and R_∞), which was omitted in this study.

Currently the model incorporates voltage and irradiance dependence. Studies have however shown the importance of pH on the channel kinetics in many opsins. Furthermore, ion concentrations have an impact on the reversal potentials and current rectification [19, 127]. Schneider et al. (2013) [105], postulated a model based on the kinetics of multiple ion species interacting with the channel, with an improved representation of the current rectification [78, 105]. While the

photocurrent properties are unaffected by pH-changes, the MerMAID photocurrent is strongly dependent on the Cl^- concentrations. The fit performed here was on experimental data recorded with an extracellular Cl^- concentration of 150 mM and intracellular Cl^- of 120 mM, explaining the depolarizing currents (negative sign in figure 2.11) as an anion conducting channel. By changing the extracellular concentration to 10 mM, the channel's reversal potential is shifted to the reversal potential of Cl^-. (The concentrations are exchanged with respect to a conventional neuron, where the typical intracellular and extracellular concentrations are 10 mM and 120 mM, respectively. This explains the experimentally measured depolarizing currents (negative sign), while one would expect hyperpolarizing currents (positive sign) from a Cl^- conducting channel.) Evidence of the Cl^- effect on channel kinetics is still absent but further experiments are needed [37]. Consequently, the model fit shown here can be used in computational studies but the reversal potential should be adjusted accordingly.

With the current model structure, the model responds instantaneously to light (see left inset figure 2.11 (A)). With the 4SB model this is circumvented by adding a extra state variable with a time constant of 1.5 ms. It is clear that for long (PD $>> \tau_{\mathrm{on}}$) continuous pulses its effect is negligible, as activation is dominated by the activation time constant. However, with short bursts or pulses, this non-instantaneous activation becomes prominent as observed in section 2.6.2. In future work, it could therefore be interesting to incorporate this non-instantaneous response. This could probably be obtained by adding an extra state variable, as performed with the 4SB model, however at the cost of the computational speed. Another possibility is to raise the open state, O(t), to a higher power, smoothing the transition but without irradiance control. Modification of the model's structure could be circumvented by gradually increasing the intensity, instead of applying a rectangular pulse.

2.8 Conclusion

In this chapter, I have extensively discussed the optogenetic toolbox. Optogenetics exhibits remarkable properties that make it a promising neuromodulation tool, offering selective control of excitation or inhibition with high spatial and temporal precision. However, it is evident that clinical translation faces numerous challenges, with long-term safety concerns regarding gene therapy and optrode implantation being particularly challenging. Additionally, the transition from rodent models to human brains presents its own set of challenges. Nevertheless, optogenetic research continues to progress, with ongoing investigations into potential solutions.

Computational modeling can provide valuable insights into the capabilities of these techniques. I have proposed a novel double two-state opsin model structure as an alternative to the conventional three- and four-state Markov models, aimed at facilitating the modeling of opsin current kinetics. In this proposed model, the second state-pair represents conductance regulation resulting from dark-light adaptation. This model offers a reduction in complexity, involving only two dif-

ferential equations compared to four in the preferred, non-instantaneous four-state Markov models commonly used for opsin modeling. Utilizing the provided fitting procedure, I have successfully fitted two distinctive opsins, ChR2(H134R) and MerMAID, within an acceptable timeframe. The absence of differential equations and parameter space reduction associated with the multi-step approach contributed to the efficiency of these model fits. Moreover, both models are able to represent the experimental data with great accuracy. However, it is important to note that this model structure yields an instantaneous response to light, which may result in an overestimation of the injected current during very short pulses ($< \tau_{on}$). Additionally, the model does not account for pH and ion concentration dependence. In its current form, with only two differential equations, the computational speed is increased up to 25% in a regular spiking neuron and up to 40% in a network of 400 transfected neurons.

In the next chapter, the double two-state opsin model will be used to test the optogenetic excitability in CA1 cells. As discussed in section 2.2.1, optogenetic excitation holds promise as a potential neuromodulation strategy for the treatment of epilepsy.

Table 2.2: Summary of all fitted parameters. The boundary conditions, lower bounds (LB) and upper bounds (UB), of first 2 steps of the fitting procedure and initial values (X0). The intermediate (-intm) and final (-final) model parameters of the selected mutant and model, with RSRS the H134R mutant with a double reciprocal addition combination of time constant dependencies ($\tau_X(I_{\mathrm{rr}})$ and $\tau_X(V)$, equation (2.16)), PP the H134R mutant with a double product combination of time constants dependencies equation (2.15) and the MerMAID fit (MM). Parameters that varied between ChR2(H134R) and MM fit are separated with vertical line. Between brackets is another parameter solution, resulting in the same model.

	$\tau_{\mathbf{O}}(\mathbf{I_{rr}})$			$\tau_{\mathbf{O}}(\mathbf{V})$			$\tau_{\mathbf{R}}(\mathbf{I_{rr}})$						$\tau_{\mathbf{R}}(\mathbf{V})$		
	p1	p2	p3	p1	p2	p3	p1	p2	p3	p4	p5	p6	p1	p2	p3
LB	-10	0	0	0	-100	-1000	0	0	-10	0	-10	0	0	-100	-1000
UB	10	20	1	100	100	1000	10	1	10	20	10	20	100	100	1000
X0	1	1	0.5	1	-50	10	1	0.5	0	0.125	3	0.5	1	-50	10
RSRS-intm.	1.93	0.68	0.022	23.26	0.14	12.40	10	0.56	-1.59	0.88	1.96	0.11	100	-38.94	14.70
RSRS-final	1.81	1.17	0.021	23.14	-0.39	13.19	10	0.56	-1.58	0.87	1.96	0.11	99.74	-38.69	12.02
PP-intm.	1.99	0.67	0.034	0.64	-89.16	14.31	6.74	0.50	2.00	0.11	-1.3	0.88	1.50	-70.01	19.13
PP-final	1.93	0.88	0.030	0.63	-88.67	8.37	6.73	0.50	1.98	0.11	-1.28	0.88	1.66	-64.54	28.55
MM-intm.	1.70	1.49	0.035	0.29	48.56	738.24	0.17	0.0081	-2.80	14.69	1.05	0.42	24.77	80.92	164.75
MM-final	3.70	3.35	0.037	0.20	49.99	718.60	0.18	0.0082	-3.00	15.57	0.998	0.429	24.42	80.87	172.82

	$\mathbf{O}_{\infty}(\mathbf{I_{rr}})$		$\mathbf{R}_{\infty}(\mathbf{I_{rr}})$			$\mathbf{G}(\mathbf{V})$			$\mathbf{g_{ChR2}}$	$\mathbf{E_{ChR2}}$
	p1	p2	p1	p2	p3	p1	p2	p3		
LB	-10	0	-10	0	0 | 0.8	0 | -	1.1 | -	0 | -	- | 0	- | -100
UB	10	20	10	20	1	100 | -	100 | -	500 | -	- | 100	- | 100
X0	1	1	1	1	0.1 | 0.9	1 | -	10 | -	50 | -	- | 30	- | 0
RSRS-intm.	3.45	0.71	2.03	0.13	0.71	9.91 (1)	1.24	46.17	1 (9.91)	0
RSRS-final	3.38	0.62	1.96	0.12	0.77	10.77 (1)	1.25	44.52	1 (10.77)	0
PP-intm.	3.45	0.71	1.99	0.15	0.73	8.93 (1)	1.27	42.37	1 (8.93)	0
PP-final	3.44	0.68	2.25	0.065	0.75	9.10 (1)	1.27	41.47	1 (9.10)	0
MM-intm	3.76	0.40	0.74	0.52	1.00	-	-	-	62.00	-3.64
MM-final	3.67	0.39	0.40	0.54	0.9987	-	-	-	62.22	-3.62

References

[1] Ruben Schoeters, Thomas Tarnaud, Luc Martens, Wout Joseph, Robrecht Raedt, and Emmeric Tanghe. *Double Two-State Opsin Model With Autonomous Parameter Inference*. Frontiers in Computational Neuroscience, 15, 6 2021.

[2] Edward S. Boyden, Feng Zhang, Ernst Bamberg, Georg Nagel, and Karl Deisseroth. *Millisecond-timescale, genetically targeted optical control of neural activity*. Nature Neuroscience, 8:1263–1268, 2005.

[3] Karl Deisseroth. *Optogenetics*. Nature Methods, 8:26–29, 1 2011.

[4] Samarendra K Mohanty, Physiology Group, Vasudevan Lakshminarayananan, Vision Science, and Ann Arbor. *Optical Techniques in Optogenetics*. 62:949–970, 2015.

[5] Benjamin R. Rost, Franziska Schneider-Warme, Dietmar Schmitz, and Peter Hegemann. *Optogenetic Tools for Subcellular Applications in Neuroscience*. Neuron, 96:572–603, 11 2017.

[6] Francis HC. Crick. *Thinking about the brain*. Scientific American, 241, 1979.

[7] D Oesterhelt and W Stoeckenius. *Rhodopsin-like protein from the purple membrane of Halobacterium halobium.* Nature: New biology, 233:149–52, 9 1971.

[8] A Matsuno-Yagi and Y Mukohata. *Two possible roles of bacteriorhodopsin; a comparative study of strains of Halobacterium halobium differing in pigmentation.* Biochemical and biophysical research communications, 78:237–43, 9 1977.

[9] Georg Nagel, Doris Ollig, Markus Fuhrmann, Suneel Kateriya, Anna Maria Musti, Ernst Bamberg, and Peter Hegemann. *Channelrhodopsin-1: A Light-Gated Proton Channel in Green Algae*. Science, 296:2395–2398, 6 2002.

[10] Jonathan Wong, Oscar J. Abilez, and Ellen Kuhl. *Computational optogenetics: A novel continuum framework for the photoelectrochemistry of living systems*. Journal of the Mechanics and Physics of Solids, 60:1158–1178, 2012.

[11] E. A. Claudia Pama, Lorenza S. Colzato, and Bernhard Hommel. *Optogenetics as a neuromodulation tool in cognitive neuroscience*. Frontiers in Psychology, 4:1–4, 2013.

[12] Ofer Yizhar, Lief E. Fenno, Thomas J. Davidson, Murtaza Mogri, and Karl Deisseroth. *Optogenetics in Neural Systems*. Neuron, 71:9–34, 7 2011.

[13] P. Hegemann, W. Gärtner, and R. Uhl. *All-trans retinal constitutes the functional chromophore in Chlamydomonas rhodopsin*. Biophysical Journal, 60:1477–1489, 12 1991.

[14] G. Nagel, T. Szellas, W. Huhn, S. Kateriya, N. Adeishvili, P. Berthold, D. Ollig, P. Hegemann, and E. Bamberg. *Channelrhodopsin-2, a directly light-gated cation-selective membrane channel*. Proceedings of the National Academy of Sciences, 100:13940–13945, 2003.

[15] Akash Guru, Ryan J. Post, Yi Yun Ho, and Melissa R. Warden. *Making sense of optogenetics*. International Journal of Neuropsychopharmacology, 18:1–8, 2015.

[16] Annelies Gerits and Wim Vanduffel. *Optogenetics in primates: a shining future?* Trends in Genetics, 29:403–411, 7 2013.

[17] Hanci Zhang, Hui Fang, Deqiang Liu, Yiming Zhang, Joseph Adu-Amankwaah, Jinxiang Yuan, Rubin Tan, and Jianping Zhu. *Applications and challenges of rhodopsin-based optogenetics in biomedicine*. Frontiers in Neuroscience, 16, 9 2022.

[18] Valentin Gordeliy, Kirill Kovalev, Ernst Bamberg, Francisco Rodriguez-Valera, Egor Zinovev, Dmitrii Zabelskii, Alexey Alekseev, Riccardo Rosselli, Ivan Gushchin, and Ivan Okhrimenko. *Microbial Rhodopsins*, pages 1–52. 2022.

[19] Katja Stehfest and Peter Hegemann. *Evolution of the Channelrhodopsin Photocycle Model*. ChemPhysChem, 11:1120–1126, 4 2010.

[20] Franziska Schneider, Christiane Grimm, and Peter Hegemann. *Biophysics of Channelrhodopsin*. Annual Review of Biophysics, 44:167–186, 6 2015.

[21] John Y. Lin, Michael Z. Lin, Paul Steinbach, and Roger Y. Tsien. *Characterization of engineered channelrhodopsin variants with improved properties and kinetics*. Biophysical Journal, 96:1803–1814, 2009.

[22] Nathan C. Klapoetke, Yasunobu Murata, Sung Soo Kim, et al. *Independent optical excitation of distinct neural populations*. Nature Methods, 11:338–346, 2014.

[23] Oleksandr Volkov, Kirill Kovalev, Vitaly Polovinkin, Valentin Borshchevskiy, Christian Bamann, Roman Astashkin, Egor Marin, Alexander Popov, Taras Balandin, Dieter Willbold, Georg Büldt, Ernst Bamberg, and Valentin Gordeliy. *Structural insights into ion conduction by channelrhodopsin 2*. Science (New York, N.Y.), 358:eaan8862, 11 2017.

[24] Claire N. Bedbrook, Kevin K. Yang, J. Elliott Robinson, Elisha D. Mackey, Viviana Gradinaru, and Frances H. Arnold. *Machine learning-guided channelrhodopsin engineering enables minimally invasive optogenetics*. Nature Methods, 16:1176–1184, 11 2019.

[25] Hideaki E. Kato, Feng Zhang, Ofer Yizhar, Charu Ramakrishnan, Tomohiro Nishizawa, Kunio Hirata, Jumpei Ito, Yusuke Aita, Tomoya Tsukazaki, Shigehiko Hayashi, Peter Hegemann, Andrés D. Maturana, Ryuichiro Ishitani, Karl Deisseroth, and Osamu Nureki. *Crystal structure of the channelrhodopsin light-gated cation channel*. Nature, 482:369–374, 2 2012.

[26] Albert Ardevol and Gerhard Hummer. *Retinal isomerization and water-pore formation in channelrhodopsin-2*. Proceedings of the National Academy of Sciences, 115:201700091, 2018.

[27] Himanshu Bansal, Neha Gupta, and Sukhdev Roy. *Theoretical analysis of optogenetic spiking with ChRmine, bReaChES and CsChrimson-expressing neurons for retinal prostheses*. Journal of Neural Engineering, 18:0460b8, 8 2021.

[28] James H. Marshel, Yoon Seok Kim, Timothy A. Machado, Sean Quirin, Brandon Benson, Jonathan Kadmon, Cephra Raja, Adelaida Chibukhchyan, Charu Ramakrishnan, Masatoshi Inoue, Janelle C. Shane, Douglas J. McKnight, Susumu Yoshizawa, Hideaki E. Kato, Surya Ganguli, and Karl Deisseroth. *Cortical layer–specific critical dynamics triggering perception*. Science, 365, 8 2019.

[29] Kimmo Lehtinen, Miriam S. Nokia, and Heikki Takala. *Red Light Optogenetics in Neuroscience*. Frontiers in Cellular Neuroscience, 15:532, 1 2022.

[30] André Berndt, Philipp Schoenenberger, Joanna Mattis, Kay M. Tye, Karl Deisseroth, Peter Hegemann, and Thomas G. Oertner. *High-efficiency channelrhodopsins for fast neuronal stimulation at low light levels*. Proceedings of the National Academy of Sciences, 108:7595–7600, 5 2011.

[31] Zhuo Hua Pan, Tushar H. Ganjawala, Qi Lu, Elena Ivanova, and Zhifei Zhang. *ChR2 mutants at L132 and T159 with improved operational light sensitivity for vision restoration*. PLoS ONE, 9, 2014.

[32] Matthias Prigge, Franziska Schneider, Satoshi P. Tsunoda, Carrie Shilyansky, Jonas Wietek, Karl Deisseroth, and Peter Hegemann. *Color-tuned channelrhodopsins for multiwavelength optogenetics*. Journal of Biological Chemistry, 287:31804–31812, 2012.

[33] Lisa A Gunaydin, Ofer Yizhar, André Berndt, Vikaas S Sohal, Karl Deisseroth, and Peter Hegemann. *Ultrafast optogenetic control*. Nature Neuroscience, 13:387–392, 3 2010.

[34] Andre Berndt, Soo Yeun Lee, Jonas Wietek, Charu Ramakrishnan, Elizabeth E. Steinberg, Asim J. Rashid, Hoseok Kim, Sungmo Park, Adam Santoro, Paul W. Frankland, Shrivats M. Iyer, Sally Pak, Sofie Ährlund Richter, Scott L. Delp, Robert C. Malenka, Sheena A. Josselyn, Marie

Carlén, Peter Hegemann, and Karl Deisseroth. *Structural foundations of optogenetics: Determinants of channelrhodopsin ion selectivity*. Proceedings of the National Academy of Sciences, 113:822–829, 1 2016.

[35] Elena G. Govorunova, Oleg A. Sineshchekov, Roger Janz, Xiaoqin Liu, and John L. Spudich. *Natural light-gated anion channels: A family of microbial rhodopsins for advanced optogenetics*. Science, 349:647–650, 8 2015.

[36] Jonas Wietek and Matthias Prigge. *Enhancing Channelrhodopsins: An Overview*, pages 141–165. 2016.

[37] Johannes Oppermann, Paul Fischer, Arita Silapetere, Bernhard Liepe, Silvia Rodriguez-Rozada, José Flores-Uribe, Enrico Peter, Anke Keidel, Johannes Vierock, Joel Kaufmann, Matthias Broser, Meike Luck, Franz Bartl, Peter Hildebrandt, J. Simon Wiegert, Oded Béjà, Peter Hegemann, and Jonas Wietek. *MerMAIDs: a family of metagenomically discovered marine anion-conducting and intensely desensitizing channelrhodopsins*. Nature Communications, 10:3315, 7 2019.

[38] Brian Y. Chow, Xue Han, Allison S. Dobry, Xiaofeng Qian, Amy S. Chuong, Mingjie Li, Michael A. Henninger, Gabriel M. Belfort, Yingxi Lin, Patrick E. Monahan, and Edward S. Boyden. *High-performance genetically targetable optical neural silencing by light-driven proton pumps*. Nature, 463:98–102, 1 2010.

[39] Johannes Vierock, Enrico Peter, Christiane Grimm, Andrey Rozenberg, I-Wen Chen, Linda Tillert, Alejandro G Castro Scalise, Marilù Casini, Sandra Augustin, Dimitrii Tanese, Benoît C Forget, Rémi Peyronnet, Franziska Schneider-Warme, Valentina Emiliani, Oded Béjà, and Peter Hegemann. *WiChR, a highly potassium-selective channelrhodopsin for low-light one-and two-photon inhibition of excitable cells*. 2022.

[40] Johannes Vierock, Silvia Rodriguez-Rozada, Alexander Dieter, Florian Pieper, Ruth Sims, Federico Tenedini, Amelie C. F. Bergs, Imane Bendifallah, Fangmin Zhou, Nadja Zeitzschel, Joachim Ahlbeck, Sandra Augustin, Kathrin Sauter, Eirini Papagiakoumou, Alexander Gottschalk, Peter Soba, Valentina Emiliani, Andreas K. Engel, Peter Hegemann, and J. Simon Wiegert. *BiPOLES is an optogenetic tool developed for bidirectional dual-color control of neurons*. Nature Communications, 12:4527, 7 2021.

[41] William R. Stauffer, Armin Lak, Aimei Yang, Melodie Borel, Ole Paulsen, Edward S. Boyden, and Wolfram Schultz. *Dopamine Neuron-Specific Optogenetic Stimulation in Rhesus Macaques*. Cell, 166:1564–1571.e6, 9 2016.

[42] Mingrui Zhao, Rose Alleva, Hongtao Ma, Andy G.S. Daniel, and Theodore H. Schwartz. *Optogenetic tools for modulating and probing the epileptic network*. Epilepsy Research, 116:15–26, 2015.

[43] Patrick M. Boyle, Thomas V. Karathanos, and Natalia A. Trayanova. *Beauty is a light in the heart: The transformative potential of optogenetics for clinical applications in cardiovascular medicine*. Trends in Cardiovascular Medicine, 25:73–81, 2015.

[44] Bram Vandekerckhove, Jeroen Missinne, Kristl Vonck, Pieter Bauwens, Rik Verplancke, Paul Boon, Robrecht Raedt, and Jan Vanfleteren. *Technological Challenges in the Development of Optogenetic Closed-Loop Therapy Approaches in Epilepsy and Related Network Disorders of the Brain*. Micromachines, 12:38, 12 2020.

[45] Adam M. Packer, Botond Roska, and Michael Häuser. *Targeting neurons and photons for optogenetics*. Nature Neuroscience, 16:805–815, 2013.

[46] Robert C. Wykes, Dimitri M. Kullmann, Ivan Pavlov, and Vincent Magloire. *Optogenetic approaches to treat epilepsy*. Journal of Neuroscience Methods, 260:215–220, 2 2016.

[47] Michael White, Michael Mackay, and Roger G Whittaker. *Taking Optogenetics into the Human Brain: Opportunities and Challenges in Clinical Trial Design*. Open Access Journal of Clinical Trials, Volume 12:33–41, 8 2020.

[48] Jan Tønnesen and Merab Kokaia. *Epilepsy and optogenetics: can seizures be controlled by light?* Clinical Science, 131:1605–1616, 7 2017.

[49] Akshaya Bansal, Swati Shikha, and Yong Zhang. *Towards translational optogenetics*. Nature Biomedical Engineering, 7:349–369, 1 2022.

[50] Tine Wyckhuys, Robrecht Raedt, Kristl Vonck, Wytse Wadman, and Paul Boon. *Comparison of hippocampal Deep Brain Stimulation with high (130 Hz) and low frequency (5 Hz) on afterdischarges in kindled rats*. Epilepsy Research, 88:239–246, 2010.

[51] Chris G. Dulla, Douglas A. Coulter, and Jokubas Ziburkus. *From Molecular Circuit Dysfunction to Disease: Case Studies in Epilepsy, Traumatic Brain Injury, and Alzheimers Disease*. Neuroscientist, 22:295–312, 6 2016.

[52] Paul Boon, Elien De Cock, Ann Mertens, and Eugen Trinka. *Neurostimulation for drug-resistant epilepsy: A systematic review of clinical evidence for efficacy, safety, contraindications and predictors for response*. Current Opinion in Neurology, 31:198–210, 4 2018.

[53] Jan Tønnesen, Andreas T. Sørensen, Karl Deisseroth, Cecilia Lundberg, and Merab Kokaia. *Optogenetic control of epileptiform activity*. Proceedings of the National Academy of Sciences, 106:12162–12167, 7 2009.

[54] Esther Krook-Magnuson, Caren Armstrong, Mikko Oijala, and Ivan Soltesz. *On-demand optogenetic control of spontaneous seizures in temporal lobe epilepsy*. Nature Communications, 4:1376, 1 2013.

[55] Esther Krook-Magnuson, Caren Armstrong, Anh Bui, Sean Lew, Mikko Oijala, and Ivan Soltesz. *In vivo evaluation of the dentate gate theory in epilepsy*. The Journal of Physiology, 593:2379, 5 2015.

[56] Fredrik Berglind, Marco Ledri, Andreas Toft Sørensen, Litsa Nikitidou, Miriam Melis, Pascal Bielefeld, Deniz Kirik, Karl Deisseroth, My Andersson, and Merab Kokaia. *Optogenetic inhibition of chemically induced hypersynchronized bursting in mice*. Neurobiology of Disease, 65:133–141, 5 2014.

[57] Jeanne T. Paz, Thomas J. Davidson, Eric S. Frechette, Bruno Delord, Isabel Parada, Kathy Peng, Karl Deisseroth, and John R Huguenard. *Closed-loop optogenetic control of thalamus as a new tool to interrupt seizures after cortical injury Jeanne*. Nature neuroscience, 16:64–70, 2013.

[58] Fadi Assaf and Yitzhak Schiller. *The antiepileptic and ictogenic effects of optogenetic neurostimulation of PV-expressing interneurons*. Journal of Neurophysiology, 116:1694–1704, 10 2016.

[59] Thomas P. Ladas, Chia Chu Chiang, Luis E. Gonzalez-Reyes, Theodore Nowak, and Dominique M. Durand. *Seizure reduction through interneuron-mediated entrainment using low frequency optical stimulation*. Experimental neurology, 269:120–132, 7 2015.

[60] Yi Lu, Cheng Zhong, Lulu Wang, Pengfei Wei, Wei He, Kang Huang, Yi Zhang, Yang Zhan, Guoping Feng, and Liping Wang. *Optogenetic dissection of ictal propagation in the hippocampal-entorhinal cortex structures*. Nature communications, 7, 3 2016.

[61] Elvis Cela, Amanda R. McFarlan, Andrew J. Chung, Taiji Wang, Sabrina Chierzi, Keith K. Murai, and P. Jesper Sjöström. *An Optogenetic Kindling Model of Neocortical Epilepsy*. Scientific Reports, 9:5236, 3 2019.

[62] Merab Kokaia, My Andersson, and Marco Ledri. *An optogenetic approach in epilepsy*. Neuropharmacology, 69:89–95, 6 2013.

[63] Elvis Cela and Per Jesper Sjöström. *Novel Optogenetic Approaches in Epilepsy Research*. Frontiers in Neuroscience, 13:947, 9 2019.

[64] Emilia Entcheva and Matthew W. Kay. *Cardiac optogenetics: a decade of enlightenment*. Nature Reviews Cardiology, 18:349–367, 5 2021.

[65] Tobias Bruegmann, Daniela Malan, Michael Hesse, Thomas Beiert, Christopher J Fuegemann, Bernd K Fleischmann, and Philipp Sasse. *Optogenetic control of heart muscle in vitro and in vivo*. Nature Methods, 7:897–900, 11 2010.

[66] Kate L. Montgomery, Shrivats M. Iyer, Amelia J. Christensen, Karl Deisseroth, and Scott L. Delp. *Beyond the brain: Optogenetic control in the spinal cord and peripheral nervous system.* Science Translational Medicine, 8, 2016.

[67] Warren J Alilain, Xiang Li, Kevin P Horn, Rishi Dhingra, Thomas E Dick, Stefan Herlitze, and Jerry Silver. *Light-induced rescue of breathing after spinal cord injury.* The Journal of neuroscience : the official journal of the Society for Neuroscience, 28:11862–70, 11 2008.

[68] Jordan J. Williams, Alan M. Watson, Alberto L. Vazquez, and Andrew B. Schwartz. *Viral-Mediated Optogenetic Stimulation of Peripheral Motor Nerves in Non-human Primates*. Frontiers in Neuroscience, 13, 7 2019.

[69] Yi Shen, Robert E. Campbell, Daniel C. Côté, and Marie Eve Paquet. *Challenges for Therapeutic Applications of Opsin-Based Optogenetic Tools in Humans*. Frontiers in Neural Circuits, 14, 7 2020.

[70] Michael E Llewellyn, Kimberly R Thompson, Karl Deisseroth, and Scott L Delp. *Orderly recruitment of motor units under optical control in vivo.* Nature medicine, 16:1161–5, 10 2010.

[71] Deniz Dalkara, Olivier Goureau, Katia Marazova, and José-Alain Sahel. *Let There Be Light: Gene and Cell Therapy for Blindness*. Human Gene Therapy, 27:134–147, 2016.

[72] José-Alain Sahel, Elise Boulanger-Scemama, Chloé Pagot, Angelo Arleo, Francesco Galluppi, Joseph N. Martel, Simona Degli Esposti, Alexandre Delaux, Jean-Baptiste de Saint Aubert, Caroline de Montleau, Emmanuel Gutman, Isabelle Audo, Jens Duebel, Serge Picaud, Deniz Dalkara, Laure Blouin, Magali Taiel, and Botond Roska. *Partial recovery of visual function in a blind patient after optogenetic therapy*. Nature Medicine, 27:1223–1229, 7 2021.

[73] N. Azimihashemi, K. Erbguth, A. Vogt, T. Riemensperger, E. Rauch, D. Woodmansee, J. Nagpal, M. Brauner, M. Sheves, A. Fiala, L. Kattner, D. Trauner, P. Hegemann, A. Gottschalk, and J. F. Liewald. *Synthetic retinal analogues modify the spectral and kinetic characteristics of microbial rhodopsin optogenetic tools*. Nature Communications, 5:1–12, 2014.

[74] Ilka Diester, Matthew T Kaufmann, Murtaza Mogri, and et al. *An optogenetic toolbox designed for primates*. Nature, page 22, 2011.

[75] Emilia Entcheva and John C. Williams. *Channelrhodopsin2 Current During the Action Potential: "Optical AP Clamp" and Approximation*. Scientific Reports, 4, 2014.

[76] Michael Häusser. *Optogenetics: the age of light*. Nature Methods, 11:1012–1014, 10 2014.

[77] Yanqiu Tao, Arthur J Y Huang, Yuki Hashimotodani, Masanobu Kano, Angelo H All, Iku Tsutsui-kimura, Kenji F Tanaka, Xiaogang Liu, and Thomas J Mchugh. *Near-infrared deep brain stimulation via upconversion nanoparticle mediated optogenetics*. Science, 684:679–684, 2018.

[78] Justin C. Williams and Timothy Denison. *From optogenetic technologies to neuromodulation therapies*. Science Translational Medicine, 5:1–5, 2013.

[79] John C. Williams and Emilia Entcheva. *Optogenetic versus electrical stimulation of human cardiomyocytes: Modeling insights*. Biophysical Journal, 108:1934–1945, 2015.

[80] Fan Yang, Seong-Jong Kim, Xiang Wu, Han Cui, Sei Kwang Hahn, and Guosong Hong. *Principles and applications of sono-optogenetics*. Advanced Drug Delivery Reviews, 194:114711, 3 2023.

[81] Anirudh R Acharya, Bram Vandekerckhove, Lars Emil Larsen, Jean Delbeke, Wytse J Wadman, Kristl Vonck, Evelien Carette, Alfred Meurs, Jan Vanfleteren, Paul Boon, Jeroen Missinne, and Robrecht Raedt. *In vivo blue light illumination for optogenetic inhibition: effect on local temperature and excitability of the rat hippocampus*. Journal of Neural Engineering, 18:066038, 12 2021.

[82] Joseph M. Stujenske, Timothy Spellman, and Joshua A. Gordon. *Modeling the Spatiotemporal Dynamics of Light and Heat Propagation for InVivo Optogenetics*. Cell Reports, 12:525–534, 7 2015.

[83] Scott F. Owen, Max H. Liu, and Anatol C. Kreitzer. *Thermal constraints on in vivo optogenetic manipulations*. Nature Neuroscience, 22:1061–1065, 7 2019.

[84] Helton M. Peixoto, Rossana M. S. Cruz, Thiago C. Moulin, and Richardson N. Leão. *Modeling the Effect of Temperature on Membrane Response of Light Stimulation in Optogenetically-Targeted Neurons*. Frontiers in Computational Neuroscience, 14:5, 2 2020.

[85] Younghoon Shin and Hyuk-Sang Kwon. *Mesh-based Monte Carlo method for fibre-optic optogenetic neural stimulation with direct photon flux recording strategy*. Physics in Medicine and Biology, 61:2265–2282, 3 2016.

[86] Johannes D. Johansson. *Spectroscopic method for determination of the absorption coefficient in brain tissue*. Journal of Biomedical Optics, 15:057005, 2010.

[87] A. N. Yaroslavsky, P. C. Schulze, I. V. Yaroslavsky, R. Schober, F. Ulrich, and H. J. Schwarzmaier. *Optical properties of selected native and coagulated human brain tissues in vitro in the visible and near infrared spectral range*. Physics in Medicine and Biology, 47:2059, 6 2002.

[88] Joanna Mattis, Kay M Tye, Emily A Ferenczi, Charu Ramakrishnan, Daniel J O'Shea, Rohit Prakash, Lisa A Gunaydin, Minsuk Hyun, Lief E Fenno, Viviana Gradinaru, Ofer Yizhar, and Karl Deisseroth. *Principles for applying optogenetic tools derived from direct comparative analysis of microbial opsins*. Nature Methods, 9:159–172, 2 2012.

[89] Viviana Gradinaru, Kimberly R. Thompson, and Karl Deisseroth. *eNpHR: a Natronomonas halorhodopsin enhanced for optogenetic applications*. Brain Cell Biology, 36:129–139, 8 2008.

[90] Viviana Gradinaru, Feng Zhang, Charu Ramakrishnan, Joanna Mattis, Rohit Prakash, Ilka Diester, Inbal Goshen, Kimberly R. Thompson, and Karl Deisseroth. *Molecular and Cellular Approaches for Diversifying and Extending Optogenetics*. Cell, 141:154–165, 4 2010.

[91] Benjamin R. Rost, Jonas Wietek, Ofer Yizhar, and Dietmar Schmitz. *Optogenetics at the presynapse*. Nature Neuroscience, 25:984–998, 8 2022.

[92] Mathias Mahn, Lihi Gibor, Pritish Patil, Katayun Cohen-Kashi Malina, Shir Oring, Yoav Printz, Rivka Levy, Ilan Lampl, and Ofer Yizhar. *High-efficiency optogenetic silencing with soma-targeted anion-conducting channelrhodopsins*. Nature Communications, 9:4125, 10 2018.

[93] Jessica E Messier, Hongmei Chen, Zhao-Lin Cai, and Mingshan Xue. *Targeting light-gated chloride channels to neuronal somatodendritic domain reduces their excitatory effect in the axon*. eLife, 7, 8 2018.

[94] Joseph V Raimondo, Louise Kay, Tommas J Ellender, and Colin J Akerman. *Optogenetic silencing strategies differ in their effects on inhibitory synaptic transmission*. Nature Neuroscience, 15:1102–1104, 8 2012.

[95] Matthew C. Walker and Dimitri M. Kullmann. *Optogenetic and chemogenetic therapies for epilepsy*. Neuropharmacology, 168:107751, 5 2020.

[96] Sofie Carrette, Paul Boon, Mathieu Sprengers, Robrecht Raedt, and Kristl Vonck. *Responsive neurostimulation in epilepsy*. Expert review of Neurotherapeutics, 2015.

[97] Mathieu Sprengers, Robrecht Raedt, Lars Emil Larsen, Jean Delbeke, Wytse Jan Wadman, Paul Boon, and Kristl Vonck. *Deep brain stimulation reduces evoked potentials with a dual time course in freely moving rats: Potential neurophysiological basis for intermittent as an alternative to continuous stimulation*. Epilepsia, 61:903–913, 5 2020.

[98] Yinyan Lin, Yuanfa Yao, Wanmei Zhang, Qiuyu Fang, Luhao Zhang, Yan Zhang, and Yingke Xu. *Applications of upconversion nanoparticles in cellular optogenetics*. Acta Biomaterialia, 135:1–12, 11 2021.

[99] Jean Delbeke, Luis Hoffman, Katrien Mols, Dries Braeken, and Dimiter Prodanov. *And Then There Was Light: Perspectives of Optogenetics for Deep Brain Stimulation and Neuromodulation*. Frontiers in Neuroscience, 11, 12 2017.

[100] Gidon Felsen and Jennifer Blumenthal-Barby. *Ethical Issues Raised by Recent Developments in Neuroscience: The Case of Optogenetics.*, pages 195–208. MIT Press, 2022.

[101] Sara Bruun, Daniel Stoeppler, Anke Keidel, Uwe Kuhlmann, Meike Luck, Anne Diehl, Michel Andreas Geiger, David Woodmansee, Dirk Trauner, Peter Hegemann, Hartmut Oschkinat, Peter Hildebrandt, and Katja Stehfest. *Light-Dark Adaptation of Channelrhodopsin Involves Photoconversion between the all-trans and 13-cis Retinal Isomers*. Biochemistry, 54:5400, 2015.

[102] Konstantin Nikolic, Nir Grossman, Matthew S. Grubb, Juan Burrone, Chris Toumazou, and Patrick Degenaar. *Photocycles of channelrhodopsin-2*. Photochemistry and Photobiology, 85:400–411, 2009.

[103] Eglof Ritter, Patrick Piwowarski, Peter Hegemann, and Franz J Bartl. *Light-dark adaptation of channelrhodopsin C128T mutant.* The Journal of biological chemistry, 288:10451–8, 4 2013.

[104] Christian Bamann, Taryn Kirsch, Georg Nagel, and Ernst Bamberg. *Spectral Characteristics of the Photocycle of Channelrhodopsin-2 and Its Implication for Channel Function*. Journal of Molecular Biology, 375:686–694, 2008.

[105] Franziska Schneider, Dietrich Gradmann, and Peter Hegemann. *Ion selectivity and competition in channelrhodopsins*. Biophysical Journal, 105:91–100, 2013.

[106] Karl Deisseroth and Peter Hegemann. *The form and function of channelrhodopsin.* Science (New York, N.Y.), 357, 2017.

[107] Jens Kuhne, Johannes Vierock, Stefan Alexander Tennigkeit, Max Aylmer Dreier, Jonas Wietek, Dennis Petersen, Konstantin Gavriljuk, Samir F. El-Mashtoly, Peter Hegemann, and Klaus Gerwert. *Unifying photocycle model for light adaptation and temporal evolution of cation conductance in channelrhodopsin-2*. Proceedings of the National Academy of Sciences of the United States of America, 116:9380–9389, 5 2019.

[108] Oliver P Ernst, Pedro A Sánchez Murcia, Peter Daldrop, Satoshi P Tsunoda, Suneel Kateriya, and Peter Hegemann. *Photoactivation of channelrhodopsin.* The Journal of biological chemistry, 283:1637–43, 1 2008.

[109] Nir Grossman, Vasiliki Simiaki, Claire Martinet, Christofer Toumazou, Simon R. Schultz, and Konstantin Nikolic. *The spatial pattern of light determines the kinetics and modulates backpropagation of optogenetic action potentials*. Journal of Computational Neuroscience, 34:477–488, 2013.

[110] Peter Hegemann, Sabine Ehlenbeck, and Dietrich Gradmann. *Multiple photocycles of channelrhodopsin*. Biophysical Journal, 89:3911–3918, 2005.

[111] Oscar J. Abilez, Jonathan Wong, Rohit Prakash, Karl Deisseroth, Christopher K. Zarins, and Ellen Kuhl. *Multiscale Computational Models for Optogenetic Control of Cardiac Function*. Biophysical Journal, 101:1326–1334, 9 2011.

[112] Sant Saran. *Theoretical analysis of low-power fast optogenetic control of firing of Chronos-expressing neurons*. Neurophotonics, 5:1, 5 2018.

[113] Sachin S. Talathi, Paul R. Carney, and Pramod P. Khargonekar. *Control of neural synchrony using channelrhodopsin-2: A computational study*. Journal of Computational Neuroscience, 31:87–103, 2011.

[114] Thomas J Foutz, Richard L Arlow, and Cameron C Mcintyre. *Theoretical principles underlying optical stimulation of a channelrhodopsin-2 positive pyramidal neuron*. J Neurophysiol, 107:3235–3245, 2012.

[115] R.L. Arlow, T.J. Foutz, and C.C. McIntyre. *Theoretical principles underlying optical stimulation of myelinated axons expressing channelrhodopsin-2*. Neuroscience, 248:541–551, 9 2013.

[116] Nir Grossman, Konstantin Nikolic, Christofer Toumazou, and Patrick Degenaar. *Modeling study of the light stimulation of a neuron cell with channelrhodopsin-2 mutants*. IEEE Transactions on Biomedical Engineering, 58:1742–1751, 6 2011.

[117] Himanshu Bansal, Neha Gupta, and Sukhdev Roy. *Theoretical Analysis of Low-power Bidirectional Optogenetic Control of High-frequency Neural Codes with Single Spike Resolution*. Neuroscience, 449:165–188, 11 2020.

[118] Martin Pospischil, Maria Toledo-Rodriguez, Cyril Monier, Zuzanna Piwkowska, Thierry Bal, Yves Frégnac, Henry Markram, and Alain Destexhe. *Minimal Hodgkin-Huxley type models for different classes of cortical and thalamic neurons*. Biological Cybernetics, 99:427–441, 11 2008.

[119] Christoph Börgers and Nancy Kopell. *Effects of noisy drive on rhythms in networks of excitatory and inhibitory neurons*. Neural Computation, 17:557–608, 3 2005.

[120] Jason S. Sherfey, Austin E. Soplata, Salva Ardid, Erik A. Roberts, David A. Stanley, Benjamin R. Pittman-Polletta, and Nancy J. Kopell. *DynaSim: A MATLAB Toolbox for Neural Modeling and Simulation*. Frontiers in Neuroinformatics, 12:10, 3 2018.

[121] A. L. HODGKIN and A. F. HUXLEY. *Propagation of electrical signals along giant nerve fibres*. Proceedings of the Royal Society of London. Series B - Biological Sciences, 140:177–183, 10 1952.

[122] S Chen. *Constrained Particle Swarm Optimization*. MATLAB File Exchange, 2018.

[123] Rania Hassan, Babak Cohanim, Olivier de Weck, and Gerhard Venter. *A Comparison of Particle Swarm Optimization and the Genetic Algorithm*. 46th AIAA/ASME/ASCE/AHS/ASC Structures, Structural Dynamics and Materials Conference, pages 1–13, 2005.

[124] Sabine Helwig and Rolf Wanka. *Particle swarm optimization in high-dimensional bounded search spaces*. pages 198–205, 2007.

[125] D. Noble and R. B. Stein. *The threshold conditions for initiation of action potentials by excitable cells*. J. Physiol, 187:129–162, 1966.

[126] Lawrence F. Shampine and Mark W. Reichelt. *The matlab ode suite*. SIAM Journal of Scientific Computing, 18:1–22, 7 1997.

[127] André Berndt, Matthias Prigge, Dietrich Gradmann, and Peter Hegemann. *Two open states with progressive proton selectivities in the branched channelrhodopsin-2 photocycle.* Biophysical journal, 98:753–61, 3 2010.

3

Quantitative Analysis of the Optogenetic Excitability of Cornu Ammonis 1 Neurons

Optogenetics has emerged as a promising technique for modulating neuronal activity. In the previous chapter (chapter 2), I discussed its potential applications in the treatment of neurological disorders, such as temporal lobe epilepsy, while also addressing the challenges it faces in terms of clinical translation.

This chapter delves into the investigation of optogenetic excitability in cornu ammonis (CA1) cells. The objective is to provide insights that could help guide future optogenetic experiments aimed at suppressing seizures. The results presented here stem from our article titled *Quantitative Analysis of the Optogenetic Excitability of CA1 Neurons* [1]. The opsin's kinetics are modeled with the double two-state opsin model, specifically the RSRS-final variant, as discussed in section 2.5.

3.1 Introduction

Optogenetics holds great promise for the targeted modulation of specific neuronal populations, offering a potential avenue for the treatment of various neurological disorders, including temporal lobe epilepsy [2, 3]. Possible strategies for TLE seizure suppression, their challenges and possible solutions were discussed in section 2.2.1. A significant challenge revolves around achieving effective illumination over a sufficiently large volume without causing irreversible effects. One solution lies in enhancing the efficiency of generating higher photocurrents at lower irradiances. This can be accomplished by improving single-channel conductance or modifying channel kinetics [4–6]. Additionally, enhancing membrane expression [7–9] and spatially confining the opsin to specific neuronal membrane compartments [7, 10–12] offer potential strategies, as well.

Computational modeling provides a valuable tool for enhancing our understanding of optogenetic responses while minimizing the need for in-vivo animal testing [13]. In-silico experiments allow for easy parameter manipulation and exploration of the stimulation parameter space. Opsin expression can be spatially constrained, expression in different cell types can be tested, and interaction with the 3D light intensity profile can be evaluated. Monte Carlo-based simulations [14] are employed to obtain this optical field, concurrently assessing the impact of tissue optical properties [15–17]. These optical field studies have shown that the light intensity spatial variation occurs on a neuronal scale.

However, studies combining optical field simulation with optogenetic neuron responses remain limited. Foutz et al. (2012) investigated this interaction using a multicompartment model of neocortical layer V pyramidal neurons [18]. Arlow et al. (2013) conducted a study on a myelinated axon MRG model, revealing a complex interplay of various simulation parameters on the activation threshold [19]. Additionally, Grossman et al. (2013) [20] showed that opsin spatial confinement influences action potential generation and propagation. This non-uniform opsin expression is also briefly addressed by Foutz et al. (2012) [18].

The novelty of our research (*Quantitative Analysis of the Optogenetic Excitability of CA1 Neurons* [1]) lies in the utilization of morphologically reconstructed and data-driven biophysical models of CA1 pyramidal neurons and interneurons [21]. These models are extended to include ChR2(H134R) dynamics and are subsequently subjected to Monte Carlo-simulated optic fields. The effect of opsin expression levels and spatial confinement on stimulation thresholds for multiple pulse durations is determined. Furthermore, the impact of various uncertain parameters, e.g., optical field properties, cell to optical fiber orientation and 3D structural cell morphology, is quantified. Based on these findings, potential subcellular improvement strategies, coupled with ideal optical fiber positioning, are identified.

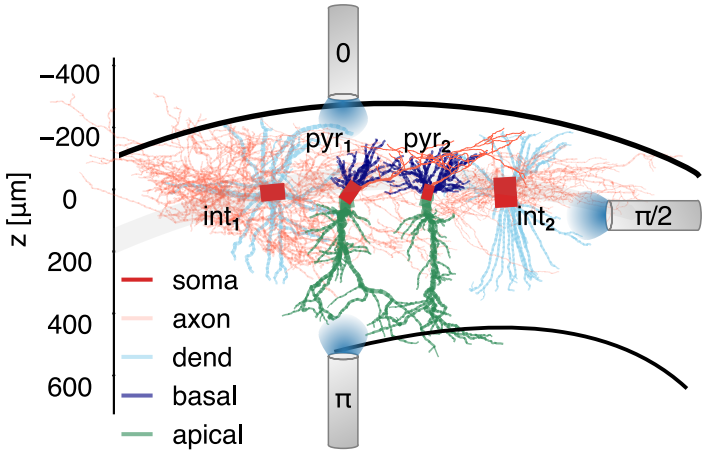

Figure 3.1: Graphical representation of the 3D reconstructed CA1 cell models used in this study: two pyramidal cells (pyr_1 and pyr_2), 1 bistratified (int_1) and 1 basket cell (int_2). The models are adopted from Migliore et al. (2018) [21]. This reference frame is applicable throughout the whole study, i.e. the soma is at z = 0 mm, and the somato-dendritic axis is parallel to the z-axis. As depicted, three optrode pitch setups are tested. The color represents the different opsin expression locations.

3.2 Methodology

The CA1 cell models used to test the optogenetic excitability are described below. Next, the light intensity fields determined via the Monte Carlo (M.C.) method and the opsin model are elaborated on. Finally, the methods and metrics used to analyze the optogenetic response are explained.

3.2.1 Neuron Models

Four models from Migliore et al. (2018) [21] are used in this chapter: two models of CA1 pyramidal cells and two CA1 interneurons located in the stratum pyramidale, i.e., a pravalbumin positive basket cell and a bistratified cell. All models have a different three-dimensional structural morphology, see figure 3.1. The cell identification number of the pyramidal cells pyr_1 and pyr_2 is *mpg141208_B_idA* and *mpg141209_A_idA*, respectively. The bistratified cell (int_1) has identification number *980513B* and the basket cell (int_2) has number *060314AM2*. Although the pyramidal cells have a different structural morphology, they are classified under the same morphological type (m-type, [22, 23]). To avoid confusion, in this chapter I will talk about difference in cell instead of morphology when comparing pyr_1 vs. pyr_2 (int_1 vs. int_2). Both pyramidal cells are continuous accommodating, while the electrical type or e-type of the interneurons is continuous non accommodating

(Petilla convention [23, 24]). The models include ten active conductances: a sodium current, three types of potassium (K_{DR}, K_M, K_A), three types of calcium (Ca_T, Ca_L, Ca_N), two Ca^{2+}-dependent potassium currents (K_{Ca}, K_{Cagk}) and a nonspecific current. Moreover, a simple calcium accumulation mechanism is included with a single exponential decay of 100 ms. The models were fitted to experimentally obtained voltage traces using a genetic algorithm. For more details of the models and the fitting procedure I refer to Migliore et al. (2018) [21]. The models themselves can be found on modelDB (`https://modeldb.science/`) under accession number 244688. The center of cell's soma is at the origin. The somato-dendritic axis of the neurons is aligned to the z-axis. This somato-dendritic axis is the first principal component determined via a principal component analysis on the 3D-positions of all compartments except the axon. In case of the pyramidal cells, the apical trunk is always directed in the positive z-direction.

3.2.2 Light Field in Gray Matter

To activate the opsins, the neurons are subjected to light. The light intensity field produced by an optical fiber (100 μm radius, 0.39 numerical aperture (NA); after the optrode in the study of Acharaya et al. (2021) [15]) is determined via the Monte Carlo method. The used method is based on the direct photon flux recording strategy of Shin and Kwon (2016) [17]. The Monte Carlo simulations are solved in cylindrical coordinates for a homogeneous medium as in Stujenske et al. (2015) [16]. Because the hippocampus is predominantly a gray matter structure, the in-vivo optical properties of gray matter are selected. The absorption coefficient (μ_a) at 470 nm is obtained by extrapolation of the data reported in Johansson (2010) [25] via a third order polynomial fit on the points between 480 and 550 nm. The scattering coefficient (μ_s) and anisotropy factor (g) are obtained via interpolation from Yaroslavsky et al. (2002) [26]. This is often combined into the reduced scattering coefficient ($\mu_s' = \mu_s(1-g)$). The refractive index (n) is 1.36. The simulations are run with 10^7 photons and a radial (dr) and axial discretization (dz) of 5 μm. The result of the Monte Carlo simulation with parameters given in table 3.1 is shown in figure 3.2, with corresponding irradiance at the neuron level given in the inset. Throughout the study three pitch orientations with respect to the CA1 cells are tested as depicted in figure 3.1.

3.2.3 ChR2(H134R) Opsin

The selected opsin is a genetically engineered Channelrhodopsin-2 (ChR2) variant: ChR2(H134R). It has an enhanced steady-state photocurrent with a slower closing mechanism than the wildtype ChR2. Its peak operation is at a wavelength of 470 nm [4, 5]. The opsin's kinetics are modeled with the double two-state opsin model, more specifically the RSRS-final reported in the previous chapter (section 2.5), because of its improved computational efficiency compared to alternative four state Markov models. It consists of two independent two-state pairs: O (opening and closing of the channel) and R (change in conductance due to dark-light adaptation).

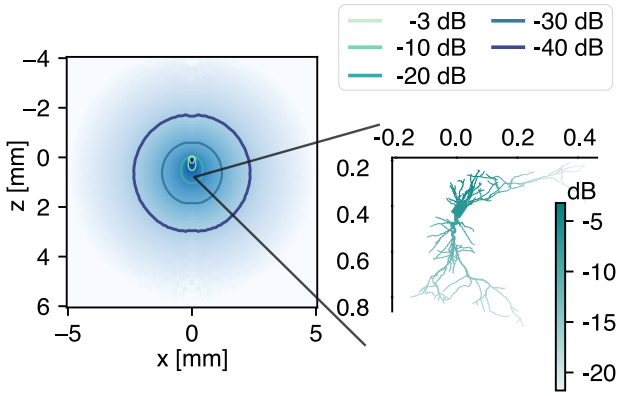

Figure 3.2: The light intensity profile in gray matter with $\mu_a = 0.42\ \mathrm{mm}^{-1}$, $\mu_s = 11.33\ \mathrm{mm}^{-1}$ and $g = 0.88$. The irradiance at the cell, with soma 400 μm bellow the fiber, is shown in the inset.

Optical	**default**	**C.V.**	**M.C. settings**	
μ_a	$0.42\ \mathrm{mm}^{-1}$	0.15	$\mathrm{n_{photons}}$	10^7
μ_s	$11.33\ \mathrm{mm}^{-1}$	0.15	dr	5 μm
g	0.88	0.03	dz	5 μm
n	1.36	-	r x z	[0, 5]x[-4, 6] mm^2

Table 3.1: Parameters used in the Monte Carlo (M.C.) simulations. Default values and coefficient of variation (C.V.).

The transmembrane current density (mA/cm^2) at a single section are repeated here for convenience:

$$i_{\mathrm{ChR2}} = g_{\mathrm{ChR2}} G(V)(O(I_{\mathrm{rr}}, V) \cdot R(I_{\mathrm{rr}}, V))(V - E_{\mathrm{ChR2}}) \tag{3.1}$$

$$G(V) = \frac{1 - 1.25 \exp\left(-\frac{V - E_{\mathrm{ChR2}}}{44.52}\right)}{V - E_{\mathrm{ChR2}}} \tag{3.2}$$

$$\frac{dX}{dt} = \frac{X_\infty(I_{\mathrm{rr}}) - X(t)}{\tau_X(I_{\mathrm{rr}}, V)} \tag{3.3}$$

$$\tau_X(I_{\mathrm{rr}}, V) = \left[\tau_X(I_{\mathrm{rr}})^{-1} + \tau_X(V)^{-1}\right]^{-1}, \text{with } X = O, R$$

$$\tau_O(I_{\mathrm{rr}}) = \frac{0.021}{1 + \exp(1.55) I_{\mathrm{rr}}^{0.37}}, \qquad \tau_O(V) = \frac{23.14}{1 + \exp\left(-(V + 0.39)/13.19\right)}$$

$$\tau_R(I_{\mathrm{rr}}) = 10\left(1 - \frac{0.56}{1 + \exp(-1.82) I_{\mathrm{rr}}^{-0.50}} - \frac{0.44}{1 + \exp(17.82) I_{\mathrm{rr}}^{-3.95}}\right)$$

$$\tau_R(V) = \frac{99.74}{1 + \exp\left(-(V + 38.69)/12.02\right)}$$

$$O_\infty(I_{\mathrm{rr}}) = \frac{1}{1 + \exp(5.45) I_{\mathrm{rr}}^{-0.70}}, \qquad R_\infty(I_{\mathrm{rr}}) = 1 - \frac{0.77}{1 + \exp(16.33) I_{\mathrm{rr}}^{-3.62}}$$

with g_{ChR2} the specific conductance (S/cm^2), $G(V)$ the rectification function given by equation (3.2), V the membrane potential (mV), I_{rr} the irradiance (mW/mm^2) and $E_{\mathrm{ChR2}} = 0$ mV the equilibrium potential. The photocurrents for an optical pulse with duration of 1 and 100 ms with increasing irradiance under voltage clamp recording of -70 mV is shown in figure 3.3.

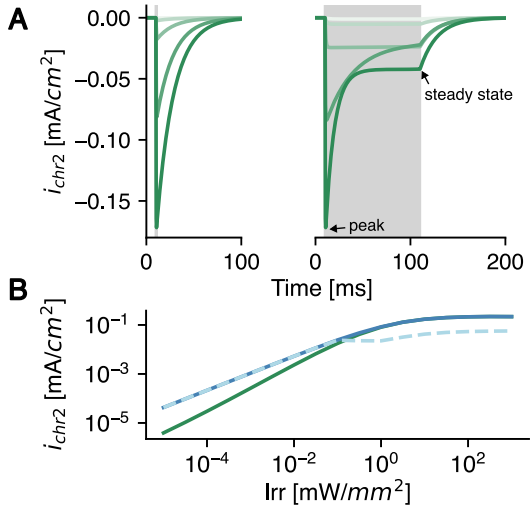

Figure 3.3: **A** The opsin current density at a voltage clamp of -70 mV for increasing irradiance (light to dark: 10^{-3}→10 mW/mm^2) of a 1 (left) and 100 ms (right) optical pulse, indicated in gray. **B** The peak (solid) and steady state (dashed) current densities as function of irradiance for a 1 and 100 ms optical pulse in green and blue, respectively.

The opsin is spatially confined to specific neuronal membrane compartments (in this chapter further denoted as subcellular region). In case of the pyramidal cells, it is located in the soma, or distributed over the axon, basal dendrites (basal),

apical dendrites (apic), all dendrites ($\mathrm{dend} = \mathrm{basal} \cup \mathrm{apic}$) or all sections ($\mathrm{allsec} = \mathrm{dend} \cup \mathrm{soma} \cup \mathrm{axon}$). In case of the interneurons, no distinction between apical and basal dendrites is made. The different regions are illustrated via the color code in figure 3.1. In each simulation, g_{ChR2} is uniformly spread over the subcellular region of interest. Its value is calculated from a preset total maximum conductance:

$$G_{\max} = g_{\mathrm{ChR2},k} \cdot A_k \tag{3.4}$$

with A_k the total membrane surface area of a subcellular region k. The surfaces are summarized in table 3.2. $G_{\max}$ are 8 points spaced evenly on a log scale between 10^{-1} and $10^{1.5}$ μS (for the uniform field 9 additional points are included between 10^{-1} and 10^{2}).

Finally, the total temporal averaged current at the excitation threshold (TAC) [27] is calculated by:

$$\mathrm{TAC} = \frac{1}{\mathrm{pd}} \sum_{j \epsilon k} A_j \int_{t_0}^{T_{\mathrm{end}}} i_{\mathrm{ChR2},j}(t)\, \mathrm{d}t \tag{3.5}$$

where pd is the pulse duration, t_0 is the pulse onset time, $T_{\mathrm{end}} = \max(500\ \mathrm{ms}, t_0 + \mathrm{pd} + 100\ \mathrm{ms})$ (to ensure to include channel closure) and j is every compartmental segment in region k. The pd varied over 5 points logarithmic evenly spaced between 0 and 100 ms (9 pds ϵ [10^{-1}, 10^{3}] are used in the simulations with uniform light field).

region	**pyr$_1$**	**pyr$_2$**	**int$_1$**	**int$_2$**
soma	699.46	417.85	778.12	1 375.16
axon	1 640.70	1 051.43	106 424.01	25 256.23
basal	5 930.95	10 670.46	-	-
apic	14 786.82	13 631.61	-	-
dend	20 717.77	24 170.88	21 827.34	21 949.07
all	23 057.93	25 640.17	129 029.47	48 580.46

Table 3.2: Total membrane surface area of subcellular regions in $\mu\mathrm{m}^2$ of the 3D reconstructed CA1 cell models

3.2.4 Analyses

The tests and metrics used to analyze the optogenetic response are described below.

3.2.4.1 Surface of Fiber Positions for the Activation of Neurons

As metric to assess the optogenetic excitability, the surface of fiber positions for the activation of neurons (SoFPAN) is determined. This metric is similar to the

more well-known volume of tissue activation (VTA) [28, 29]. In VTA, the frame of reference is the position of the stimulation device, while here, the frame of reference is the stratum pyramidale with the center of cell's soma at origin. In other words, SoFPAN encompasses the positions at which the optical fiber can be located in order to activate the neuron of interest. This is chosen because of the layered structure of the hippocampus, constraining the cell bodies of the considered neurons to the stratum pyramidale. Because the optical fiber is limited to the plane shown in figure 3.1 to reduce the number of simulations, only a 2D plane is explored resulting in a surface instead of a volume being determined.

The intensity threshold (I_{th}) to elicit an action potential (V>-10 mV) recorded in the soma for a given pulse duration and fiber position is determined first. This threshold value is the intensity at the fiber surface (I_{fiber}). It is obtained with a titration process using the bisection method for 7 iterations (i.e., $c_i = (a_i + b_i)/2$, with $b_0/a_0 = 10$). 121 fiber positions are evaluated with z taking on eleven linearly spaced values in [-400, 700] μm. For a pitch of $\pi/2$, x ϵ [-1000, 4000] μm with Δx = 500 μm. For the fiber pitch of 0 and π, x ϵ [0, 2500] μm with Δx = 250 μm. For a given pulse duration, the SoFPAN is then determined as the union of the spatial points for which the threshold is lower than the fiber intensity (true: $I_{\mathrm{th}} < I_{\mathrm{fiber}}$) multiplied by the discretization surface (i.e., 110×250 or 110×500 $\mu\mathrm{m}^2$ depending on the fiber pitch). A lower bound is determined by counting only the discretization surfaces enclosed by four true-points. In case of the upper bound, the true-false field is dilated first with a 3x3 mask before the enclosed-by-four-true-points regions are counted. For the pitches of 0 and π, the obtained SoFPAN is multiplied by two, such that the maximal SoFPAN for all pitches is equal to 5.5 mm^2. The SoFPAN is calculated for nine logarithmic evenly spaced fiber intensities 0.1 and 1000 $\mathrm{mW/mm}^2$.

If the cell's dimensions are assumed to be negligible with respect to the spatial variation of the intensity field, the irradiance is uniform over the whole neuron. The cell can thus be represented as a single point in space. The estimated SoFPAN under this assumption is denoted as $\mathrm{SoFPAN}_{\mathrm{uniform}}$.

3.2.4.2 Wilcoxon Signed-Rank Test

A single-sided, paired Wilcoxon signed-rank test is used to test whether the results from two populations are significantly different. For the uniform field 20 classes (cell and opsin location: 4×{all, axon, soma, dend} + 2×{basal, apic}) are mutually compared. In case of the M.C. field there are 42 classes $\big($pitch, cell and opsin location: $3\times\big[4\times\{$all, axon, soma$\}$ + $2\times\{$basal$\}\big]\big)$. A scoring system is used to identify the most excitable setup. Here, a 1, 0.1 and 0.01 is given if the SoFPAN is statistically greater with p-value below 0.001, 0.01 and 0.05, respectively. The maximum score is consequently 41.

3.2.4.3 Regression

A two step fitting procedure is performed to analyze the effect of pulse duration and expression level on the intensity threshold as suggested by Williams and Entcheva [27]. First Lapicque's formulation is fit to the TAC. This gives the strength-duration relationship like with electrical direct current stimulation [30]. Second a linear regression is performed with independent variables the $\log_{10}$ of $\widehat{\mathrm{TAC}}$ (μA) and $G_{\max}$ (μS).

$$\widehat{\mathrm{TAC}} = \frac{\mathrm{TAC}_0}{1 - \exp(-\mathrm{pd}/\tau_{\mathrm{TAC}})} \tag{3.6}$$

$$\log_{10} \widehat{I_{\mathrm{th}}} = a_G \log_{10} G_{\max} + a_{\mathrm{pd}} \log_{10} \widehat{\mathrm{TAC}} + c \tag{3.7}$$

Here, TAC_0, τ_{TAC}, a_G, a_{pd}, and c are the regression parameters. $\widehat{I}_{\mathrm{th}}$ and $\widehat{\mathrm{TAC}}$ are the estimators of the threshold intensity and total averaged current, respectively.

3.2.4.4 Optimal and Worst Fiber Position

The optimal and worst fiber positions for a given pulse duration are defined as the z-position where the depth of activation (amount of positions along the x-axis with $I_{\mathrm{th}} < I_{\mathrm{fiber}}$) is the highest or the lowest, respectively. As a tie-breaker, the z-position is selected where the average of TAC along x is, respectively, the lowest or the highest.

3.2.4.5 Elementary Effects

The inputs to the simulations can be divided into two categories (figure 3.4). On the one hand, there are the parameters that are known (e.g, optrode radius, NA and pitch) or controlled by the user (e.g., pd and I_{fiber}) in an optogenetic experiment. On the other hand, there are variables that cannot be controlled and contain some uncertainty, e.g., the tissue's optical properties (μ_a, μ_s'), the neuron's structural morphology (cell: pyr/int$_1$ vs. pyr/int$_2$) and orientation (roll, yaw), and the opsin expression (level ($G_{\max}$) and location). Because of the expected non-linear interactions and high computational time ($\pm$12 hours for a 121 position sweep with 5 pulse durations), the elementary effects method is adopted for global sensitivity analysis [31].

Six influential factors are investigated, i.e., μ_a, μ_s', $G_{\max}$, cell, opsin location and roll. The measure used (μ^*) is the mean of the absolute value of $r = 16$ elementary effects. Also, the standard deviation of the elementary effects (σ) is calculated to track interactions and non-linear effects. The r repetitions are sampled with the radial-based design using Sobol's numbers [32]. μ_a, μ_s' and $G_{\max}$ are normally distributed with mean and coefficient of variation (C.V.) given in table 3.1.

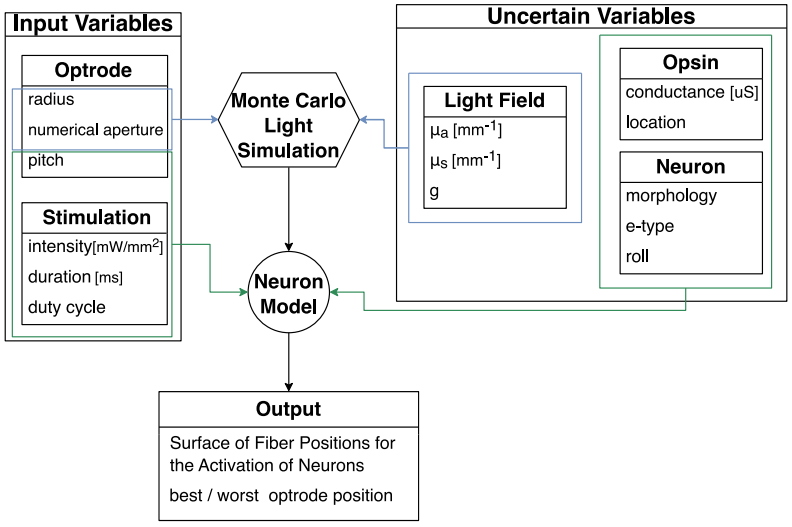

Figure 3.4: The simulation flowchart with input and uncertain parameters.

The mean and C.V. of $G_{\max}$ are 1 μS and 0.15. The roll is uniformly distributed between [-π, π[radians. Cell and location are discretely uniformly distributed, with $\{\text{pyr}_1, \text{pyr}_2\}$ ($\{\text{int}_1, \text{int}_2\}$) and {all, axon, soma, basal} ({all, axon, soma}) classes, respectively, for pyramidal (inter-) neurons.

3.2.5 Software

Simulations were done with NEURON 8.0.0 [33] and Python 3.9.12. on the HPC system with AMD Epyc 7552 processing units, provided by the Flemish Supercomputer Center.

3.3 Results

The results of this study can be subdivided into three sections. First, there is the optogenetic response under a uniform field. This means that all cell sections receive the same irradiance. This facilitates the analysis of the importance of subcellular regions, pulse durations and expression levels. Next, the Monte Carlo simulated light field is included. This allows us to indicate the effect of light propagation on optogenetic excitability and provides information on optimal or worst fiber positioning. Finally, an elementary effects study is performed to identify the most sensitive parameters.

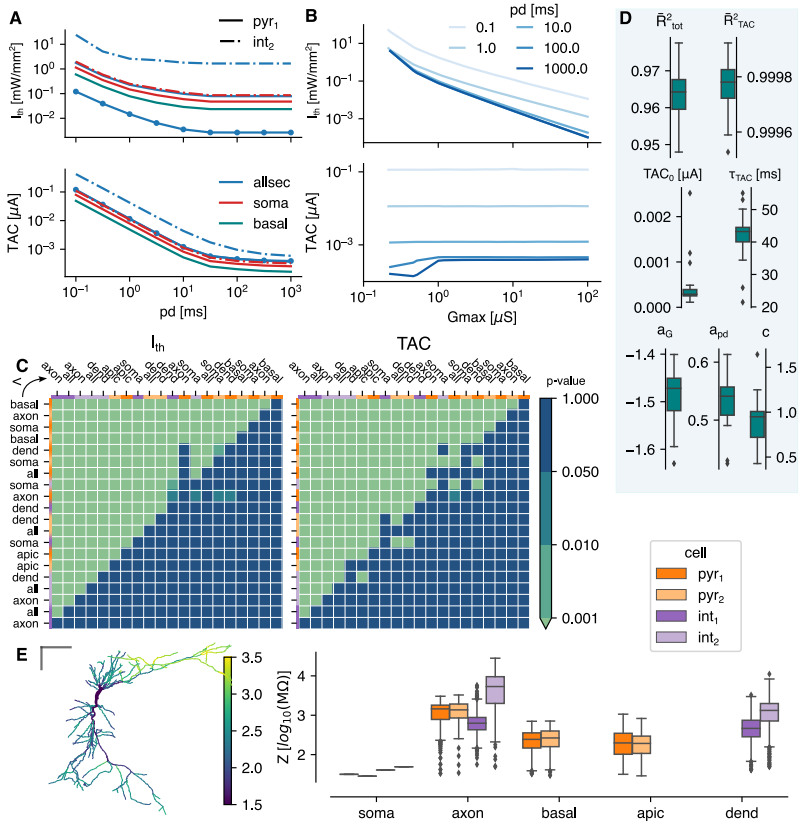

Figure 3.5: The optogenetic response under a uniform light field. **A** The intensity threshold (I_{th}) and corresponding total temporal averaged current (TAC, top and bottom, resp.) as function of pulse duration. All lines shown are for a $G_{\max} = 1\ \mu$S except the circle markers ($G_{\max} = 10\ \mu$S). **B** The intensity threshold and corresponding total temporal averaged current (top and bottom, resp.) as function of $G_{\max}$ for allsec-pyr$_1$. **C** The p-value of the mutually, paired Wilcoxon signed-rank tests. Single-sided test if class at the row is lower than class in the column for the I_{th} (left) and TAC (right). The color code at the top and left indicate the cell model. The cell opsin location combinations are sorted on their excitability score (see section 3.2.4.2). **D** The results of the two step regression. The goodness of fit is indicated with the adjusted R-squared measure: $\bar{R}^2_{\mathrm{TAC}}$ for the Lapicque fit to the TAC and $\bar{R}^2_{\mathrm{tot}}$ for the linear regression fit to the threshold. Box plots are shown for $\bar{R}^2$-values and regression parameters, calculated for the different cell-types and opsin locations. **E** Summary of the input impedance at 0 Hz, (left) the local impedance of each section in pyr$_1$, (right) the summarized impedances of the four tested cells. The gray bars are 100 μm.

3.3.1 The Optogenetic Excitability in a Uniform Light Field

Figure 3.5 (A) depicts the intensity threshold (I_{th}) and temporal averaged current (TAC) curves as function of pulse duration (pd) of several subcellular and cell combinations. Both decrease with increasing pd until a saturation value is reached. For the same subcellular region (i.e., allsec), the threshold curve is shifted down in case of pyr_1 versus int_2 (blue solid vs. blue dashed-dotted line). Staying within the same cell, it can be seen that changing the subcellular region (all $\rightarrow$ basal or soma) can result in a downward shift, as well. The same effects can be seen on the TAC, but less pronounced. Increasing the expression level ($G_{\max}$) from 1 to 10 μS (blue solid line with circle markers) results in an expected decrease of the threshold. On the other hand, the TAC remains the same. This is highlighted in figure 3.5 (B) where the TAC is constant for all pds for a $G_{\max} > 1$ μS in the allsec-pyr_1 setup. A linear relationship for I_{th} can be observed for $G_{\max} \geq 0.518$ μS. No threshold could be found for $G_{\max} < 0.215$ μS. This is because the photocurrent saturates at high intensities (see figure 3.3) and therefore cannot compensate for the low $G_{\max}$. At high pulse durations, a decrease in TAC is already observed at higher $G_{\max}$ (< 1 μS). For the corresponding I_{th}, the photocurrent is biphasic with a peak and steady-state value. At these pulse durations (100 and 1000 ms) the action potential (AP) occurs during the inactivation from peak to steady state. The occurrence of the peak is much more efficient in eliciting an AP. A large part of the total photocurrent occurs before the AP while this diminishes at higher $G_{\max}$ with monophasic photocurrents. Additionally, during the AP, the current drops to zero due to channel shunting. Consequently, the net effect of this drop on the TAC is larger here than in case of no biphasic photocurrents (at low irradiances) or lower pulse durations, where the AP is elicited during the deactivation phase of the photocurrent.

The I_{th} is determined for all pyramidal and continuous non-accomodating interneuron models of Migliore et al. (2018) [21], along with virtual clones optimized using HippoUnit [34]. The result of these additional 38 pyramidal and 39 interneuron cell models is shown in figure 3.6. Overall, for a given subcellular opsin location, the variation is within one order of magnitude, except when the opsin is expressed in the axon. This observation holds for both pulse durations of 1 and 100 ms and maximum total conductances of 1 and 10 μS. The selected cells do not appear as outliers except for the axon of the bistratified cell. Therefore, it can be concluded that the selected cells are representative for the population.

Mutually paired Wilcoxon singed-rank tests are performed to identify the most excitable subcellular region. The p-values of a single-sided test are shown in figure 3.5 (C) of the threshold intensity and TAC on the left and right, respectively. Each compared population consists of 153 points (9 pds and 17 $G_{\max}$ values). The basal-pyr_1 is the most excitable with a I_{th} significantly ($p<0.001$) lower than any other location-cell combination. The same is true for the TAC. The pyramidal cells are more excitable than the interneurons with pyr_1 the most excitable ($p<0.001$). Aside from the axon in pyr_2, the order of the excitability scores is the same in both cells (see section 3.2.4.2). The apical dendrites is the least excitable subcellular

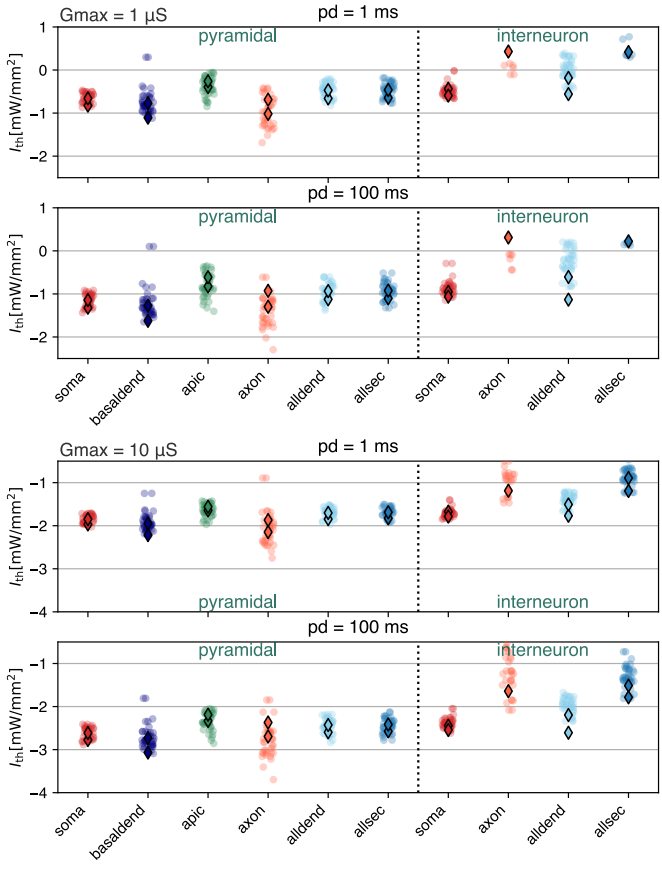

Figure 3.6: The threshold intensity (I_{th}) required for optogenetic excitation under uniform light stimulation of all pyramidal and continuous non-accommodating interneuron models of Migliore et al. (2018) [21], along with virtual clones optimized using HippoUnit [34]. The diamonds with a black outline represent the thresholds of the models analyzed in through the whole chapter. The titles of each subplot indicate the pulse duration (pd) and the total opsin conductance (G_{max}). The opsin is uniformly distributed over the subcellular regions, indicated on the x-axis. The model files are available at *https://wiki.ebrains.eu/bin/view/Collabs/live-paper-2021-saray-et-al/Live%20Paper*.

region of the pyramidal cells (p<0.001). On average a lower I_{th} is required for the basket cell than the bistratified cell (p<0.001). Overall a significantly lower threshold is accompanied with a significantly lower TAC. Some exceptions exist where the TAC is significantly greater (e.g., all-pyr$_1$ versus soma-int$_2$). The median of the relative change in I_{th} of the location-cell combinations as ranked in figure 3.5 (C) is shown in supplementary figure 3.9 (A). The average of the medians is -22.76%. Therefore, the I_{th} drops every time on average with 22.76% percent when moving from the least (axon int$_1$) to the most (basal pyr$_1$) excitable location-cell combination. Optimal subcellular expression in a cell can result in I_{th} drops of >75%. Compared to no subcellular specificity (opsin over the whole cell), I_{th} reductions of >60% can be achieved in the pyramidal cells, increasing towards 83% and 92% for the basket and bistratified cell, respectively (cf. table 3.3). The full analysis of the median relative differences of all different subcellular-cell combinations is shown in figure 3.10 (A).

The two step regression is performed on each location-cell combination separately. The combined results are shown in figure 3.5 (D). The variability on TAC is captured by Lapicque's formulation resulting in a median adjusted coefficient of determination ($\bar{R}^2_{\mathrm{TAC}}$) value of 0.99978. The median rheobase (TAC$_0$) is 3.17 nA and the median time constant (τ_{TAC}) is 42.95 ms. The variability of I_{th} is well explained by the two step regression model (median $\bar{R}^2_{\mathrm{tot}} = 0.96388$). The median parameter values of $G_{\max}$ and pd (a_G and a_{pd}) are -1.47 and 0.53, respectively. Even though the latter is positive, I_{th} decreases with pd due to the Lapicque's formulation. Based on these values, $G_{\max}$ has thus a stronger impact on I_{th} than the pd.

The input impedance of the cell's sections, measured after 100 ms after initialization at -70 mV, are shown in figure 3.5 (E). The impedance is a proportionality factor on the input current resulting in a given voltage change. Therefore, the voltage change is higher for a higher input impedance given a constant input current. The axons have on average the highest impedance but also the highest spread with many outliers. At the left, it can be seen that the impedance increases from axon hillock to the synapses. The soma has a low impedance compared to the median of the other subcellular regions.

3.3.2 The Optogenetic Response in the Monte Carlo Light Field

In this section, the cells are subjected to an intensity field produced by a 100 μm fiber. The 3D-profile is obtained via the Monte Carlo method in homogeneous gray matter tissue with the default optical parameters as summarized in table 3.1. Unlike in the previous section, the irradiance at the different neuron sections will depend now on their relative position with respect to the fiber and its orientation. Consequently, I_{th} now depends on the position in the reference frame as indicated in figure 3.1. An example is shown in figure 3.7 (A), with the I_{th} map on the left and corresponding TAC on the right, for an allsec-pyr$_1$ with $G_{\max} = 1.18$ μS, pd $= 10$ ms and a fiber pitch of $\pi/2$. A hotspot is observed around [$x = 0.43$ mm, $z = -0.036$ mm], where the threshold is the lowest. Even when the neuron lies

	I_{th}			SoFPAN		
cell	**best**	**worst**	**%**	**best**	**worst**	**%**
pyr1	basal	apic	-81.23	basal π/2	axon 0	223.08
	basal	all	-67.63	basal π/2	all π/2	33.33
pyr2	axon	apic	-76.03	axon π	all 0	152.78
	axon	all	-64.36	axon π	all π	67.42
int1	alldend	axon	-99.89	soma π/2	axon 0	947.62
	alldend	all	-91.58	soma π/2	all π/2	100.00
int2	soma	axon	-87.28	soma π/2	axon 0	233.33
	soma	all	-82.84	soma π/2	all π/2	87.47

Table 3.3: Influence of subcellular opsin expression on the optogenetic excitability. Median relative change between best and worst subcellular location, and best and no subcellular specificity (all) of all pd and $G_{\max}$ combinations. Excitability under a uniform light field (I_{th}) and with light propagation (SoFPAN).

behind the fiber, i.e., $x < 0\ \mathrm{mm}$, it is still possible to excite the cell but at higher I_{th}. Two islands can be observed for the TAC with a factor two difference between minimum and maximum. The farther away from the cell the lower the variation in TAC.

Based on these threshold maps, the surface of fiber positions for the activation of neurons (SoFPAN) can be estimated. This is shown in figure 3.7 (B) for the three investigated fiber pitches. The SoFPAN is a measure of the excitability of the subcellular optogenetic configuration in the light field. The uncertainty caused by the discretization on the SoFPAN is indicated by the shaded area (see section 3.2.4.1). There is a larger uncertainty at lower intensities due to the rough simulation grid. The soma appears to be more excitable than the opsin in all sections (red vs. blue) with already a non-zero SoFPAN for a I_{fiber} of 0.1 mW/mm^2. This is true for all fiber pitches. The SoFPAN saturates due to the finite simulation domain.

An optimal and worst z-position for each fiber pitch can be determined, as well. The result for the two cases as above are shown in figure 3.7 (C) and (D). It can be seen that the positions vary with increasing I_{fiber}. At low intensities, the optimal position is near the subcellular region (cf. soma, red) or the most excitable region (cf. allsec, blue), which is the basal dendrites. At higher intensities, it is better to illuminate the whole simulation domain, explaining the optimal positions at -0.4 mm and 0.7 mm for the 0 and π pitches, respectively. Once the whole simulation field is excited, the optimal position is completely determined by the average TAC along the x-axis. This can be seen in the sudden changes at the highest I_{fiber} ($> 100\ \mathrm{mW/mm^2}$). In green the density distribution of all 560 combinations ($\mathrm{pd} \times G_{\max} \times \mathrm{loc} \times \mathrm{cell}$) is displayed. The optimal position is more concentrated with a 0 or $\pi/2$ pitch. On the other hand, the worst position is more concentrated

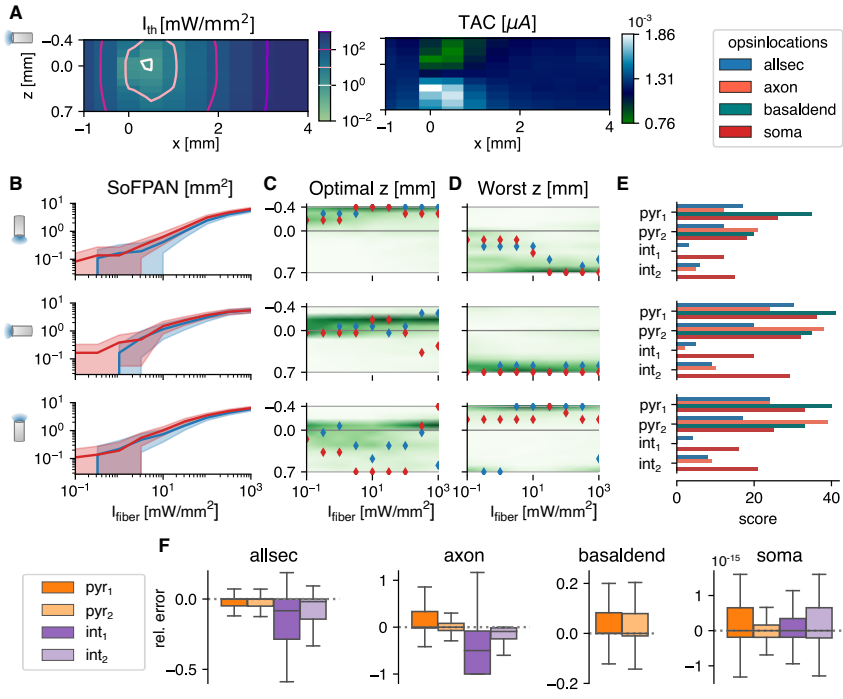

Figure 3.7: The optogenetic response in a homogeneous Monte Carlo simulated light field. **A** The threshold intensities (left) of the pyr_1 cell, with opsin distributed over all sections, and corresponding total temporal averaged current (right). In the colormaps, the position of the optical fiber is varied with respect to the soma, which is fixed at $(x, z) = (0, 0)$. **B, C and D** The Surface of Fiber Positions for the Activation of Neurons, the optimal and worst z-position for neuron activation, respectively, as function of fiber intensity. The shaded area in **B** is enclosed by the upper and lower bound. The lines are the result of the pyr_1 cell with opsin location shown in legend at the right top corner. $G_{\max} = 1.179\ \mu\mathrm{S}$ and $\mathrm{pd} = 10\ \mathrm{ms}$ in **A-D**. In **C and D** the scatter plots overlay the density, averaged over all cell, location, $G_{\max}$ and pd combinations. **E** Excitability score based on paired Wilcoxon signed-rank tests. Each population consists of 360 (5 pd $\times$ 8 $G_{\max}$ $\times$ 9 I_{fiber} values) combinations. The pitch of the fiber is illustrated by the orientation of the fiber icon on the left and valid for the whole row. **F** Relative error of SoFPAN, if the light intensity is considered uniform over the neuron: rel. error = ($\mathrm{SoFPAN}_{\mathrm{uniform}}$ - $\mathrm{SoFPAN}_{\mathrm{M.C.}}$)/$\mathrm{SoFPAN}_{\mathrm{M.C.}}$, the outliers are not shown. The errors are calculated for all the $G_{\max}$, pd, pitch and I_{fiber} combinations.

with the $\pi/2$ and π pitches. The optimal and worst fiber positions are most distant with the $\pi/2$ pitch position.

	outliers [%]	+20% [%]	median	max	min	IQR
allsec	17.42	23.96	-7.8e-16	∞	-0.59	0.12
axon	18.60	34.60	0	∞	-1	0.20
basal	20.44	18.17	1.3e-15	∞	-0.53	0.09
soma	24.57	0.17	0	∞	-1	5.4e-16

Table 3.4: Summary relative error SoFPAN Monte Carlo versus SoFPAN uniform (all cells pooled together). +20% indicates amount of simulations with a relative error above 20%

The excitability of the subcellular region is summarized in figure 3.7 (E). The scores are based on the p-values of the single-sided, paired Wilcoxon signed-rank test, as described in section 3.2.4.2. At each pitch individually, the subcellular excitability order remains, generally, the same as under the uniform field (cf. figure 3.11). Only the axons appear to be susceptible to the fiber pitch position. For instance, the axon-pyr_1 combination has an increased (decreased) excitability under the π (0) fiber pitch. Also at pitch 0, the axon of pyr_2 has a lowered excitability with a SoFPAN significantly lower ($p<0.001$) than soma-pyr_1. On the other hand, axon-int_2 has a higher SoFPAN than all-int_2 under the $\pi/2$ and π pitches. Basal-pyr_1 is under all pitches the most excitable combination, with a score of 41 at pitch $\pi/2$. Overall, pitch $\pi/2$ is significantly more excitable than π, which is in turn more excitable than 0 ($p<0.001$). The axon-pyr_2, however, has a significantly higher SoFPAN ($p<0.001$) under pitch π than $\pi/2$. The median of the relative change in SoFPAN of the location-cell-pitch combinations according to this ranking, i.e., lowest to highest score, is shown in figure 3.9 (C). The average of medians is now 10.45%. Therefore, the SoFPAN increases every time on average with 10.45% percent when moving from least (axon int_1, pitch = 0) to most (basal pyr_1, pitch = $\pi/2$) excitable location-cell-pitch combination. The same analysis is performed when restricted to a single pitch. The average of medians of the relative changes in SoFPAN increase towards 56.86, 25.89, 59.18% for a pitch = 0, $\pi/2$ and π, respectively. Matching the ideal fiber location to the subcellular expression of a single cell can result in doubling of the SoFPAN compared to the worst combination. Even a tenfold increase is observed in case of the bistratified cell. Compared to subcellular unspecificity (all), SoFPAN increases of 33-100% can be obtained by specifying subcellular expression (cf. table 3.3). The full analysis of the median relative differences of all different subcellular-pitch combinations for each cell separately is shown in figure 3.10 (B).

The SoFPAN for a light field that is considered to be uniform over the whole cell ($SoFPAN_{uniform}$, see bottom section 3.2.4.1) is calculated, as well. The relative error compared to the SoFPAN under a Monte Carlo field, i.e., ($SoFPAN_{uniform}$-$SoFPAN_{M.C.}$)/$SoFPAN_{M.C.}$, is shown in figure 3.7 (F). The errors is calculated for

all the $G_{\max}$, pd, pitch and I_{fiber} combinations. The error of the soma is negligible. The outliers are not shown. Of these, only 0.85% produce a relative error above 5%. These results validate the method as the soma should not depend on the M.C. field as its section is only one point in the 3D-space. The SoFPAN of basal dendrites gets overestimated, with 18.17% having a relative error above 20%. In case of the pyramidal cells and with the opsin distributed over the whole cell, the SoFPAN is predominantly underestimated and the interquartile range (IQR) of the relative error is 60% of the IQR for the basal dendrites. The estimation for the axon of the int_1 cell is the worst with a median relative error of -50%. At least in one test case of each subcellular region the error is either -100% or infinity (see table 3.4).

3.3.3 Parameter Uncertainties

There is uncertainty on various parameters used in this study. The optical parameters depend on multiple factors, e.g., tissue and wavelength. The absorption coefficient is extrapolated which introduces an uncertainty, as well. Moreover, the values of gray matter are used while different gradations exist. The effect of a change in optical parameters on the light field in homogeneous tissue, is illustrated in figure 3.8 (A). On the left, the field as used in the section above is depicted. The effect of an increased absorption and decreased reduced scattering coefficient is shown in the middle. The result is a more conical field with higher degradation. A more round field is obtained when the reduced scattering coefficient is higher (cf. right). Also at the cell level, there are multiple sources of uncertainty. In experimental setting, the opsin expression $G_{\max}$ will not be exactly known. Moreover, the subcellular location will probably not be discrete as used in these simulations. Finally, the morphology of the tested cells and its orientation (cf. roll) are fixed. To address the impact of these uncertainties on the output, a global sensitivity analysis is performed. The used approach is a screening method: the Elementary Effects test.

The influence of these six parameters, i.e., cell roll, μ_s', μ_a, opsin subcellular location (loc), cell model (cell) and $G_{\max}$, on the SoFPAN for the three fiber pitches and two cell types (pyr and int) is investigated. For each fiber pitch and cell type, the elementary effects test (EET) is repeated for 5 pd and 9 I_{fiber} combinations (these 45 combinations correspond with 100% in figure 3.8 (B) and (D)). The rank according to the μ^*-measure is summarized in figure 3.8 (B). For certain pd and I_{fiber} no differentiation could be made based on the μ^*-measure, explaining the bar height $>$100% at rank 0. The subcellular location has most frequently the highest impact on the excitability for all six test cases. This is followed by $G_{\max}$ in second place (rank 4). The roll and μ_a have on average the lowest impact. However, in case of the pyramidal cells and π fiber pitch, the roll has occupied the highest rank for some (pd, I_{fiber}) combinations. On the other hand, μ_s' is more important when the fiber pitch is 0 for the pyramidal cells. The μ^* and σ measures of three cases of the pyramidal cells with pd of 10 ms are shown in figure 3.8 (D). The circles indicate the setup where the roll has the highest rank, i.e., pyramidal cell with π pitch and $1\ \mathrm{mW/mm^2}$. It can be seen that even though it has the highest rank, its measures are in the same range as the other two cases. The diamonds represent the EET of a

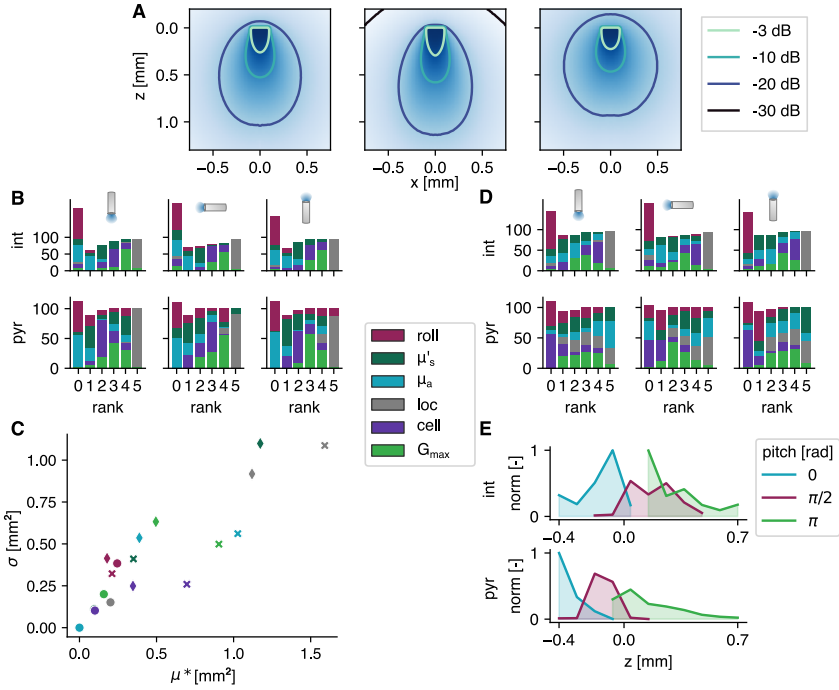

Figure 3.8: Results of the elementary effects study. **A** Intensity fields with different optical parameters; from left to right $\mu_a = 0.42, 0.52, 0.35\ \mathrm{mm}^{-1}$ and $\mu_s' = 1.36, 0.93, 2.06\ \mathrm{mm}^{-1}$. **B and D** The influential parameters on SoFPAN and optimal fiber position, respectively, ranked for 5 pds and 9 fiber intensities (in %). The fiber pitch and cell type are shown on top and left, respectively. **C** The two measures of the elementary effects of three pyramidal cell setups, i.e., pitch = π, $\pi/2$ and 0, and I_{fiber} = 1, 1000 and 1000 $\mathrm{mW/mm^2}$ indicated by circle, diamond and cross, respectively, for a $\mathrm{pd} = 10$ ms. The legend between **B** and **D** also applies on **C**. **E** Normalized optimal z-position over all results with allsec subcellular location of the elementary effects study.

$\pi/2$ pitch at $I_{\mathrm{fiber}} = 1000\ \mathrm{mW/mm^2}$. Here, the reduced scattering coefficient has the highest impact. The non-linear and interaction effects are higher in this case, reflected by the higher σ. For the 0-pitch with $I_{\mathrm{fiber}} = 1000\ \mathrm{mW/mm^2}$ (cross), the location is ranked highest with a clear difference in μ^*. The effect of cell appears to be more linear than the other parameters indicated by its shift towards lower σ values.

The same analysis is performed on the optimal position. The rank is summarized in figure 3.8 (D). For the interneurons, the subcellular location stays dominant. There is, however, a clear shift towards the optical parameters for the pyramidal cells. Here, the reduced scattering and absorption coefficient are most often ranked highest for the π and 0 pitch, respectively. Also, in case of the $\pi/2$ pitch, the

absorption coefficient is more important for the optimal position than it is for the SoFPAN. The cell and roll appear to have the lowest effect. While, on the other hand, the cell is important in case of the interneurons. The optimal position for both cell types normalized over all simulations with allsec subcellular location of the EET study, is shown in figure 3.8 (E). These exclude the preset subcellular selectivity. For the interneurons this is more smeared out and a focus towards the stratum pyramidale is observed. On the other hand, for the pyramidal cells there is a clear preference for a position such that the majority of the light reaches the stratum oriens region. At pitch π this is more smeared out due to the possibility to retract (z more positive) the fiber at higher intensities to illuminate a bigger region in the stratum oriens. This is limited for the 0 pitch explaining the high peak at $-0.4\,\mathrm{mm}$.

3.4 Discussion

The optogenetic excitability of CA1 cells is investigated in this chapter. I attempted to not only gain more insight into the effect of the various stimulation and uncertain parameters but also to identify strategies for increased optogenetic efficiency. These insights are of interest for the development of better stimulation protocols that can be used as treatment for TLE. A broad view is adopted where both the excitability of pyramidal and interneurons is investigated. Even though excitation of inhibitory neurons is one of the two main investigated strategies as treatment of TLE, insights in the excitability of pyramidal neurons can be of interest as well. Like with electrical deep brain stimulation, the latter could be used as counter-irritation [2] with various modes of action [35] that can be tested. Moreover, stimulation of both types could be beneficial for restoring the excitation-inhibition balance [36].

3.4.1 Excitability of Spatially Confined Opsin Expression

The results show that the optogenetic excitability of CA1 cells depends on various parameters. The irradiance threshold ranges over multiple order of magnitudes. As expected, an increase in expression level ($G_{\max}$) or pulse duration (pd) results in a decrease of the intensity threshold (I_{th}). There is also a clear dependence on the subcellular region of opsin expression and variance among different cells. There is no single explanation for the relative excitability of the considered subcellular opsin locations, due to the complex interplay of many non-linear relationships. By comparing the membrane areas and impedances (cf. table 3.2 and figure 3.5 (E)) of the subcellular regions some observations can be made. For a fixed $G_{\max}$, the specific channel conductance (g_{ChR2}) is locally higher for regions with a lower total surface area. Thus, for the same I_{fiber}, there will locally be a higher depolarizing current to elicit an action potential (AP). This combined with the fact that the AP is measured in the soma (therefore does not have to travel through the cell), explains why the soma-confinement is highly ranked in each cell. The observation concerning the locally raised channel conductance also holds when comparing

	all	**alldend**	**apic**	**axon**	**basal**	**soma**
pyr_3 - pyr_1	-0.32	-0.31	-0.28	0.83	0.14	-0.31
pyr_4 - pyr_2	0.29	0.23	0.47	0.92	-0.28	0.30
pyr_3 - pyr_2	-0.53	-0.53	-0.47	3.15	-0.50	-0.56
pyr_4 - pyr_1	1.06	0.97	1.07	-0.22	0.73	1.05

Table 3.5: Mean relative difference in I_{th} due to three-dimensional structural morphology (top) or by changing channel distribution (bottom; relative with respect to original).

basal dendrites with apical, all dendrites and all sections. An argument for why confinement to the basal dendrites is more excitable than the soma could be found by comparing their input impedances. For a fixed depolarizing current, a higher impedance results in a larger membrane depolarization. Because the impedance of the basal dendrites is significantly higher than that of the soma (log-scale in figure 3.5 (E)) it will facilitate AP initiation. However, this contradicts the rank of axon-pyr_1. Finally, there is the channel distribution inside the cell itself. The ratio of depolarizing (e.g., Na^+ and Ca^{2+}) and hyperpolarizing (e.g., K^+) channels defines the membrane threshold for AP initiation. This ratio is double in the axon of pyr_2 compared to pyr_1, motivating the low rank of axon-pyr_1. These observations are in agreement with the findings of Foutz et al. (2012) [18].

Confinement to the basal dendrites of pyr_1 is the most excitable, while the highest I_{th} is required for the axon of int_1 (cf. figure 3.5 (D)). Similar ranking is observed in the SoFPAN calculations (cf. figure 3.7 (E)). To identify the effect of endogenous channel distribution, the channel distributions of pyr_1 were imposed on pyr_2 (pyr_3) and vice versa (pyr_4). The mean relative difference of all pd and $G_{\max}$ combinations is shown in table 3.5. The I_{th} of pyr_3 drops with $\sim$30% and $\sim$50% versus pyr_1 and pyr_2, respectively, for all subcellular regions except for the axon (both cases) and for the basal dendrites in pyr_3 vs. pyr_1. Contrarily, the excitability of pyr_4 drops (higher I_{th}), except for the basal dendrites for pyr_4 vs pyr_2 or axon in pyr_4 vs pyr_1. Switching 3D structural morphology while maintaining endogenous channel distribution (top two) or vice versa (bottom two) impacts optogenetic excitability. It is clear that the interaction of structural morphology and channel distribution has an impact on optogenetic excitability. The axon subregion appears to be the most susceptible with tripled excitation threshold of pyr_3 vs. pyr_2. Neuron degeneracy, i.e., the ability to perform the same functioning whilst being structurally different or having different ion channel distributions [21], is thus something that should be taken into account in determining irradiance thresholds. This is also observed in the variability of I_{th} in supplementary figure S1. Still, the basal dendrites region is also the most excitable in pyr_3 and pyr_4. Combined with rank 1 and 2 for pyr_1 and pyr_2, respectively, it can be concluded that this is the most effective subcellular target region for opsin expression in CA1 pyramidal cells.

This spatial dependence was also observed in the study of Grossman et al. (2013) [20]. With the specific conductance (g_{ChR2}) as metric, they determined whole cell illumination to be most efficient, i.e., uniform opsin distribution over whole cell with a uniform light field compared to soma, axon initial segment or apical dendrite confinement. They determined that for a 20 ms pulse and irradiance of 1 mW/mm^2 the required g_{ChR2} when in all sections is only 6% of that when restricted to the soma. On the other hand, $G_{\max}$ was 60% higher. These values are in agreement with our results where the ratio of the specific conductance of all sections to soma targeted expression is 2-4% under the same conditions in the pyramidal cells. However, in this study I argue that ranking should be based on $G_{\max}$, i.e., where the number of opsin complexes is fixed. This translates towards an equal comparison of total elicited photocurrent, while, on the other hand, for a fixed g_{ChR2} the total photocurrent is scaled by the surface area. As a result, the confinement to the soma is classified here to be more excitable.

After correction for the difference in rectification function (i.e., $G(V = -68.83\ \mathrm{mV}) = 1$ in Grossman et al. (2011) [37] vs. 0.07 in our study), the absolute values of $G_{\max}$ were slightly lower but in the same order as reported in Grossman et al. (2013) [20]. For a $G_{\max}$ of 1 μS (= 0.07 μS after correction) and with a single channel conductance of 40-100 fS this translates towards expression of 0.71-1.77 10^6 opsin complexes. Spread over the whole cell this is $\pm$50 channels/μm^2 but confined only to the soma this rises towards $>$1000 channels/μm^2. This value is higher than the estimated 130 channels/μm^2 based on bacteriorhodopsin expression [18, 38] but lower than the indirectly estimated 4.4 10^4 channels/μm^2 by Arlow et al. (2013) [19]. With our tested $G_{\max}$ values up to 100 μS especially when restricted to the soma, this could pose cellular toxicity problems, if these channel numbers would be achieved [6, 7, 10]. This can be avoided if single channel conductance is increased.

The opsin is in all conditions uniformly distributed but can be restricted to a spatial region. In-vivo this highly specific and discrete separation is not possible. Still, by merging the opsin with signaling and targeting constructs, localized enhancement can be obtained. For instance, the addition of the soma-targeting motif of the soma- and proximal dendrite-localized voltage-gated potassium-channel Kv2.1 improves somato-dendritic expression [7, 11]. The real distribution in those cases is not known. A normal distribution could be imposed but this would come with two more degrees of freedom. Therefore, the spatially restricted but uniform distribution is used. Our results encourage localized enhancement and advances in this research direction. A reduction of I_{th} with more than 64% can be achieved via subcellular specificity. This is tempered towards, but still significant, increases in SoFPAN of 33-100%, when light propagation is included. Consequently, if made possible, spatial confinement of opsins to specific membrane compartments could significantly increase optogenetic efficiency. On the other hand, more than 76% reduction of I_{th} between optimal and worst subcellular regions is possible. This is also reflected in SoFPAN, where an ideal subcellular-pitch combination can result in a 1.5-10 fold increase compared to the worst combination (cf. table 3.3). A good knowledge of the optogenetic interaction at the subcellular level is therefore

required in order to achieve the optimal configuration.

3.4.2 Optimal Fiber Position

Due to the finite size and discrete nature of the test grid (121 points), the SoFPAN, and optimal and worst positions could not be unambiguously determined. An upper and lower bound of the SoFPAN is defined (cf. section 3.2.4.1), indicating a larger uncertainty at lower intensities. In case of the optimal fiber position, a tie-breaker based on the TAC is introduced. From a homeostatic point of view, it is ideal that the required result is achieved via the lowest perturbation of normal functioning. High/long transmembrane currents could lead to ion concentration imbalance. Especially when using ChR2(H134R), which has a high H^+ permeability, this can result in neuron acidification, which in turn can result in decreased neuron functioning or unexpected behavior [39–41]. Therefore, the positions that generate the lowest TAC are preferred. The results in figure 3.7 (C) show that the optimal position is at the depth of the region of subcellular expression or with a focus on the most excitable region (in case of opsin distribution over the whole or majority of the cell). Overall, the rank of excitability between uniform and M.C. field stimulation is unchanged. Subcellular excitability appears to be dominant over spatial distribution. This spatial preference was also observed in Foutz et al. (2012) [18]. In their L5 pyramidal model, they found the apical tuft and soma to be most excitable.

For the $\pi/2$ pitch, the optimal and worst position are the most stationary for increasing intensities. For the other pitches (0 and π), either the optimal or worst position is more smeared out while they are located more closely to each other for low intensities. Consequently, there is a higher risk for sub-optimal fiber positioning. Combined with the highest excitability according to the SoFPAN (cf. figure 3.7 (E)), it can be conclude that $\pi/2$ is the better fiber position.

3.4.3 Contribution of Optical Field Simulation

This study combined simulations of light propagation and neuronal modeling. Light propagation is simulated using the Monte Carlo method for a uniform medium. The hippocampus is a predominantly gray matter structure. However, there is uncertainty on the exact values of the optical parameters (amplified by inter- and extrapolation). The effect of the uncertainty of these parameters is tested using the elementary effects method. The influence of μ_s' on the excitability is ranked in the middle, while μ_a is ranked lower. On the optimal position they were ranked much higher. The median and maximum μ^* on SoFPAN are respectively 0.14 and 1.71 mm^2 (0.04 and 1.19 mm^2) for μ_s' (μ_a). These parameters have some influence, but are subordinate to the other uncertain parameters such as subcellular location, expression level and cell morphology. Moreover, the need to include the light intensity profile in the neuron simulation was addressed by calculating the SoFPAN from excitation thresholds under uniform illumination, as well. Deviations of more than 20% are observed in more than 25% of the tested setups (soma excluded). Confinement to the basal dendrites result in the lowest percentage (18.17%) while

the highest is achieved in case of the axon subcellular expression (34.60%). Overall, investigating optogenetic excitability under uniform field conditions provides a good initial approximation, but, accuracy drops for larger and asymmetrical section distributions. The latter was also observed in the strong pitch dependence of axon excitability in the pyramidal cells.

3.4.4 Limitations and Future Work

This study focused on single pulse excitation of CA1 cells. The occurrence of other spiking behavior is excluded. Likewise, when calculating the SoFPAN with high I_{fiber}, a cell near the fiber end may exhibit bursting or depolarization block due to intense irradiance [20, 37]. Unlike with electrical stimulation, the photocurrent saturates for high light intensities (see figure 3.3). Therefore, extreme behavior is not expected when short pulses are applied. Additionally, the studied ChR2(H134R) opsin exhibits light-dark adaptation, i.e., the photocurrent is higher for a full dark adapted neuron but decreases towards a steady state value under prolonged illumination. The recovery time is in the order of seconds. During pulsed stimulation, the photocurrent of the first pulse will be higher than that of the subsequent pulses. Therefore, higher irradiances will be required to reliably elicit pulse-locked spiking [18]. Future work should test the capability of eliciting reliable spiking when opsin expression is confined to a specific subcellular region. Additionally, since this study focused on isolated cells that are at rest prior to optogenetic stimulation, it is necessary to investigate if phase locking is possible in a network setting, quantify its impact on excitation thresholds, observe subcellular excitation's effects on cellular and network responses [42], and evaluate its influence on synaptic plasticity. Therefore, the interaction in neuronal networks will be of interest in future work, particularly with a focus on hyperexcitable systems such as those in temporal lobe epilepsy. Clearly, the cell's optogenetic excitability depends on multiple factors. The results in table 3.5 show both 3D structural morphology and endogenous channel distribution dependencies. Still, the individual impact and interaction effects are yet to be determined. Obtaining a better understanding will be of interest in future work.

The effective level of opsin expression in-vivo is uncertain. Furthermore, to account for potential improvements in plasma membrane expression [7, 11], $G_{\max}$ is treated as a free parameter. However, due to the presence of inward rectification, it is unclear how the model parameter g_{ChR2} relates to the actual opsin expression level in-vivo. In our formulation of $G(V)$, all proportionality factors are absorbed by g_{ChR2} (see equations (3.1) and (3.2)). While in the formulation of Grossman et al. (2011) [37] and Williams et al. (2013) [13], $G(V = -68.83\ \mathrm{mV}) = 1$ and $G(V = -76.07\ \mathrm{mV}) = 1$, respectively. These rectification functions cause a reduction of g_{ChR2} with a factor of 14.15 or 12.89 at those specific membrane potentials, compared to our formulation in equation (3.2).

As aforementioned, there is still some uncertainty on the tissue optical properties. Different studies have reported values that can differ up to an order of magnitude [25, 26, 43, 44]. Furthermore, brain tissue is binary classified as either gray or white

matter, while tissue gradation is more continuous. The impact of the uncertainty of these parameters on the optogenetic excitability is tested in this study. However, it is investigated only locally near the parameters' reported means (see table 3.1), while the reduced scattering coefficient of white matter is reported to be 7-times higher than that of gray matter [26]. Additionally, tissue alterations due to foreign body reaction occur. A fibrous capsule is formed around the implanted fiber as reaction to blood-brain-barrier injury and gliosis caused by the presence of the implanted fiber itself [45]. In future work light propagation in a heterogeneous medium and its effect on excitability could be determined. Mesh and voxel based Monte Carlo algorithms exist that can accurately compute the light field distribution in complex tissues [46]. Moreover, modern deep learning algorithms can be utilized to reduce the inherent stochastic noise of these Monte Carlo simulations [47]. Exploring the propagation of light at different wavelengths, such as for the excitation of red-shifted opsins, would also be of interest. The simulated fiber has a flat tip with fixed diameter and numerical aperture. Fiber tapering, flat tip patterning and alteration of the geometric properties can result in improved output coupling or broadened and multi-site illumination. However, this is out of the scope of this research [45, 48].

New opsins, either natural or genetically engineered, are discovered on a yearly basis [6, 39, 49–51]. While this is generally beneficial, it can hinder the development of optogenetic tools. Dividing research among multiple opsins may limit the understanding of a single opsin's interactions with neurons and its capabilities. The question arises whether the gathered insights here are transferable to other opsins as well. Previous studies have demonstrated the influence of channel kinetics on factors like irradiance thresholds, spike reliability, and behavior [4, 37, 49]. The exact values of I_{th} will thus differ for another opsin. However, these values are already uncertain due to multiple other uncertainties in other parameters like $G_{\max}$. Furthermore, these differences will affect all tested cases equally. Therefore, I expect that the observed trends and rankings regarding optogenetic excitability will be applicable across different opsins. In future work, a similar study could be performed focusing on optogenetic silencing with inhibitory opsins like GtACR2 and WiChr [51, 52].

Tissue illumination causes heating. To avoid permanent tissue damage, the local temperature increase cannot exceed 6 °C [15]. Moreover, behavioral changes are already possible at lower temperature changes ($> 1\,^{\circ}\mathrm{C}$). Several neural parameters, e.g., capacitance, ion channel conductance, and transmitter release and uptake, have been shown to be temperature dependent [15, 53–55]. The reported SoFPAN values are for fiber intensities up to 1000 $\mathrm{mW/mm^2}$. After extrapolation of the change in temperature results reported in [15] (figure 3 (A)), this intensity corresponds with an estimated temperature increase of 4.85 °C after 100 ms. Consequently, temperature-induced changes in optogenetic excitability should be included in future work.

3.5 Conclusion

In this chapter, I presented the findings from our article titled *Quantitative Analysis of the Optogenetic Excitability of CA1 Neurons* [1], which focused on the optogenetic excitability of four CA1 cells using the ChR2(H134R) model described in chapter 2. Our findings revealed that, for a fixed amount of opsin channels ($G_{\max}$), confining the opsin to specific neuronal membrane compartments significantly enhances excitability. This confinement leads to threshold reductions exceeding 64% and up to 100% gains in the surface of fiber positions for the activation of neurons. Additionally, I determined that the perpendicular orientation of the fiber relative to the somato-dendritic axis yields superior results. Furthermore, a substantial inter-cell variability was observed, with differences in thresholds above 20%. The bistratified cell exhibited the least excitability, while pyramidal cell 1 demonstrated the highest excitability, especially when the opsin is confined to the basal dendrites. These findings highlight the importance of considering neuron degeneracy while developing optogenetic tools. By screening various uncertain parameters, I identified opsin location and $G_{\max}$ having the greatest impact on simulation outcomes. Our study showed the advantages of computational modeling coupled with light propagation. An increased excitability is seen with optimal fiber positioning, i.e., perpendicular to the somatic-dendritic axis and focus on the most excitable cell region. Spatial confinement and enhancements of opsin expression levels are promoted strategies to improve optogenetic excitability. However, it should be noted that uncertainty in these parameters limits determining the exact irradiance thresholds.

The results presented in this chapter are based on isolated cell models. To investigate the potential of optogenetic excitation for seizure suppression, a conductance-based network model capable of simulating TLE activity is needed. The next chapter (chapter 4) will outline my efforts in developing a hippocampal model that replicates TLE pathology.

3.6 Supplementary Figures

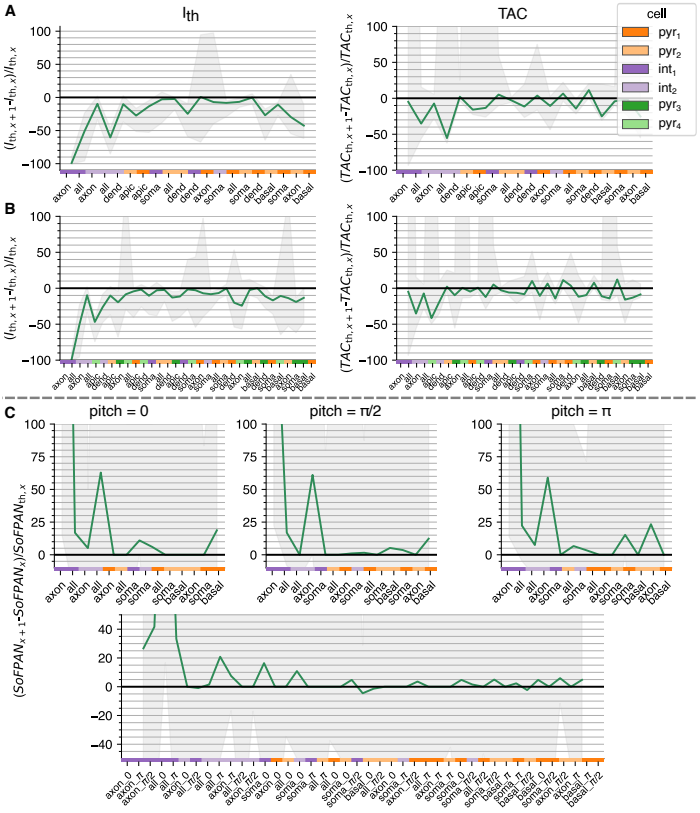

Figure 3.9: Median of relative change in optogenetic excitability of ranked metrics. **A, B** Ranked I_{th} and TAC of the original four tested CA1 cells and with additional pyramidal cells, respectively, under a uniform intensity field. **C** Ranked SoFPAN: pitch specific at the top, all combined bottom. The gray shading indicates the total variation due to the pulse duration and opsin conductancy in all subplots. Values are same as the first offset anti-diagonal of figure 3.10

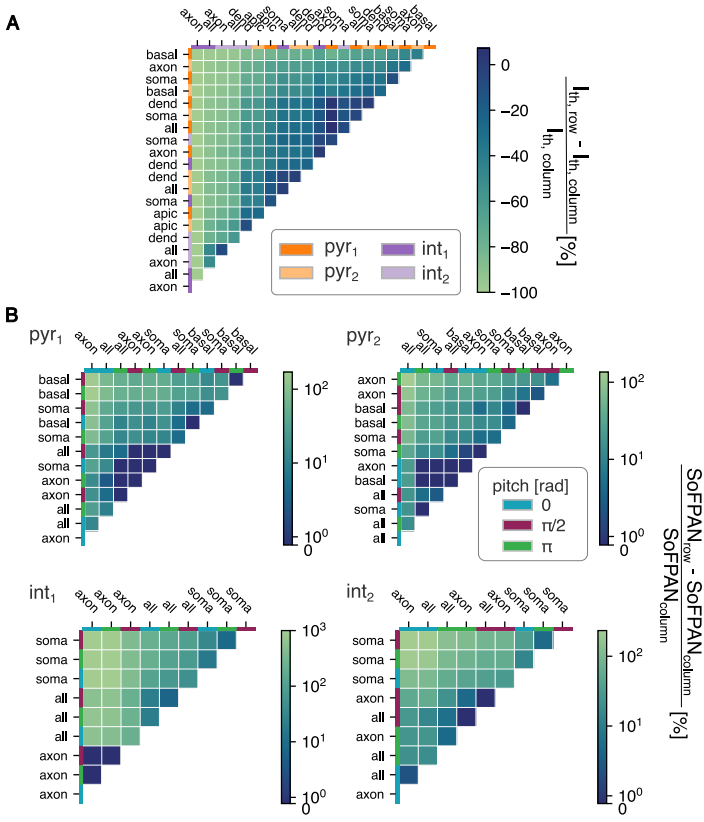

Figure 3.10: Median of relative differences in optogenetic excitability between row and column classes with respect to column class. **A** The median of relative differences in optogenetic excitation thresholds (I_{th}) under a uniform intensity field for different cell-location combinations. The values shown are the median of the relative differences calculated over all 153 combinations of pulse durations (pd) and total opsin conductance ($G_{\max}$). **B** The median of relative differences in SoFPAN under a Monte Carlo simulated light field for different combinations of opsin locations and pitches. A separate plot is given for each of the examined cells. Here, the values are the median calculated over all the 360 pd, $G_{\max}$ and intensity at the fiber surface (I_{fiber}) combinations. The classes are sorted based on their excitability score (section 3.2.4.2). The color code indicates the cell or optical fiber pitch in **A and B**, respectively.

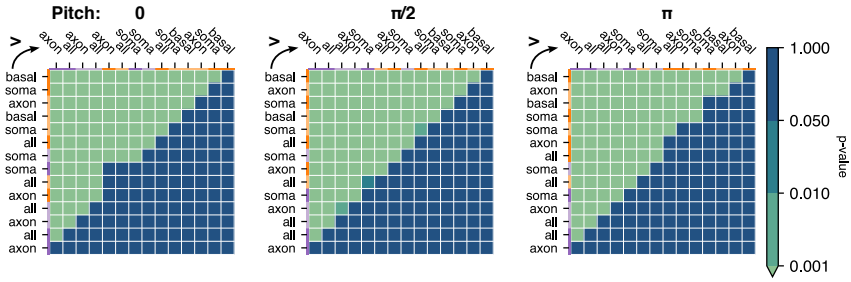

Figure 3.11: The p-values of the mutually, paired Wilcoxon signed-rank tests for SoFPAN comparison at a given fiber pitch. Single-sided test if class at row has higher SoFPAN than class in the column. The color code at the top and left indicates the cell model. Each population comprises 360 points: 5 $\mathrm{pd} \times 8\ G_{\max} \times 9\ I_{\mathrm{fiber}}$ values.

References

[1] Ruben Schoeters, Thomas Tarnaud, Laila Weyn, Wout Joseph, Robrecht Raedt, and Emmeric Tanghe. *Quantitative analysis of the optogenetic excitability of CA1 neurons*. Frontiers in Computational Neuroscience, 17, 8 2023.

[2] Sofie Carrette, Paul Boon, Mathieu Sprengers, Robrecht Raedt, and Kristl Vonck. *Responsive neurostimulation in epilepsy*. Expert Review of Neurotherapeutics, 15:1445–1454, 12 2015.

[3] Michael White, Michael Mackay, and Roger G Whittaker. *Taking Optogenetics into the Human Brain: Opportunities and Challenges in Clinical Trial Design*. Open Access Journal of Clinical Trials, Volume 12:33–41, 8 2020.

[4] Joanna Mattis, Kay M Tye, Emily A Ferenczi, Charu Ramakrishnan, Daniel J O'Shea, Rohit Prakash, Lisa A Gunaydin, Minsuk Hyun, Lief E Fenno, Viviana Gradinaru, Ofer Yizhar, and Karl Deisseroth. *Principles for applying optogenetic tools derived from direct comparative analysis of microbial opsins*. Nature Methods, 9:159–172, 2 2012.

[5] André Berndt, Philipp Schoenenberger, Joanna Mattis, Kay M. Tye, Karl Deisseroth, Peter Hegemann, and Thomas G. Oertner. *High-efficiency channelrhodopsins for fast neuronal stimulation at low light levels*. Proceedings of the National Academy of Sciences, 108:7595–7600, 5 2011.

[6] Ofer Yizhar, Lief E. Fenno, Thomas J. Davidson, Murtaza Mogri, and Karl Deisseroth. *Optogenetics in Neural Systems*. Neuron, 71:9–34, 7 2011.

[7] Benjamin R. Rost, Franziska Schneider-Warme, Dietmar Schmitz, and Peter Hegemann. *Optogenetic Tools for Subcellular Applications in Neuroscience*. Neuron, 96:572–603, 11 2017.

[8] Viviana Gradinaru, Kimberly R. Thompson, and Karl Deisseroth. *eNpHR: a Natronomonas halorhodopsin enhanced for optogenetic applications*. Brain Cell Biology, 36:129–139, 8 2008.

[9] Viviana Gradinaru, Feng Zhang, Charu Ramakrishnan, Joanna Mattis, Rohit Prakash, Ilka Diester, Inbal Goshen, Kimberly R. Thompson, and Karl Deisseroth. *Molecular and Cellular Approaches for Diversifying and Extending Optogenetics*. Cell, 141:154–165, 4 2010.

[10] Benjamin R. Rost, Jonas Wietek, Ofer Yizhar, and Dietmar Schmitz. *Optogenetics at the presynapse*. Nature Neuroscience, 25:984–998, 8 2022.

[11] Mathias Mahn, Lihi Gibor, Pritish Patil, Katayun Cohen-Kashi Malina, Shir Oring, Yoav Printz, Rivka Levy, Ilan Lampl, and Ofer Yizhar. *High-efficiency optogenetic silencing with soma-targeted anion-conducting channelrhodopsins*. Nature Communications, 9:4125, 10 2018.

[12] Jessica E Messier, Hongmei Chen, Zhao-Lin Cai, and Mingshan Xue. *Targeting light-gated chloride channels to neuronal somatodendritic domain reduces their excitatory effect in the axon*. eLife, 7, 8 2018.

[13] John C. Williams, Jianjin Xu, Zhongju Lu, Aleksandra Klimas, Xuxin Chen, Christina M. Ambrosi, Ira S. Cohen, and Emilia Entcheva. *Computational Optogenetics: Empirically-Derived Voltage- and Light-Sensitive Channelrhodopsin-2 Model*. PLoS Computational Biology, 9:e1003220, 9 2013.

[14] Lihong Wang, Steven L. Jacques, and Liqiong Zheng. *MCML—Monte Carlo modeling of light transport in multi-layered tissues*. Computer Methods and Programs in Biomedicine, 47:131–146, 7 1995.

[15] Anirudh R Acharya, Bram Vandekerckhove, Lars Emil Larsen, Jean Delbeke, Wytse J Wadman, Kristl Vonck, Evelien Carette, Alfred Meurs, Jan Vanfleteren, Paul Boon, Jeroen Missinne, and Robrecht Raedt. *In vivo blue light illumination for optogenetic inhibition: effect on local temperature and excitability of the rat hippocampus*. Journal of Neural Engineering, 18:066038, 12 2021.

[16] Joseph M. Stujenske, Timothy Spellman, and Joshua A. Gordon. *Modeling the Spatiotemporal Dynamics of Light and Heat Propagation for In Vivo Optogenetics*. Cell Reports, 12:525–534, 7 2015.

[17] Younghoon Shin and Hyuk-Sang Kwon. *Mesh-based Monte Carlo method for fibre-optic optogenetic neural stimulation with direct photon flux recording strategy*. Physics in Medicine and Biology, 61:2265–2282, 3 2016.

[18] Thomas J. Foutz, Richard L. Arlow, and Cameron C. McIntyre. *Theoretical principles underlying optical stimulation of a channelrhodopsin-2 positive pyramidal neuron*. Journal of Neurophysiology, 107:3235–3245, 6 2012.

[19] R.L. Arlow, T.J. Foutz, and C.C. McIntyre. *Theoretical principles underlying optical stimulation of myelinated axons expressing channelrhodopsin-2*. Neuroscience, 248:541–551, 9 2013.

[20] Nir Grossman, Vasiliki Simiaki, Claire Martinet, Christofer Toumazou, Simon R. Schultz, and Konstantin Nikolic. *The spatial pattern of light determines the kinetics and modulates backpropagation of optogenetic action potentials*. Journal of Computational Neuroscience, 34:477–488, 6 2013.

[21] Rosanna Migliore, Carmen A. Lupascu, Luca L. Bologna, et al. *The physiological variability of channel density in hippocampal CA1 pyramidal cells and interneurons explored using a unified data-driven modeling workflow*. PLOS Computational Biology, 14:e1006423, 9 2018.

[22] Henry Markram, Eilif Muller, Srikanth Ramaswamy, et al. *Reconstruction and Simulation of Neocortical Microcircuitry*. Cell, 163:456–492, 10 2015.

[23] Armando Romani, Felix Schürmann, Henry Markram, and Michele Migliore. *Reconstruction of the Hippocampus*, volume 1359, pages 261–283. Springer, 2022.

[24] Giorgio A. Ascoli, Lidia Alonso-Nanclares, Stewart A. Anderson, et al. *Petilla terminology: nomenclature of features of GABAergic interneurons of the cerebral cortex*. Nature Reviews Neuroscience, 9:557–568, 7 2008.

[25] Johannes D. Johansson. *Spectroscopic method for determination of the absorption coefficient in brain tissue*. Journal of Biomedical Optics, 15:057005, 2010.

[26] A N Yaroslavsky, P C Schulze, I V Yaroslavsky, R Schober, F Ulrich, and H-J Schwarzmaier. *Optical properties of selected native and coagulated human brain tissues in vitro in the visible and near infrared spectral range*. Physics in Medicine and Biology, 47:305, 6 2002.

[27] John C. Williams and Emilia Entcheva. *Optogenetic versus Electrical Stimulation of Human Cardiomyocytes: Modeling Insights*. Biophysical Journal, 108:1934–1945, 4 2015.

[28] Christopher R. Butson, Scott E. Cooper, Jaimie M. Henderson, and Cameron C. McIntyre. *Patient-specific analysis of the volume of tissue activated during deep brain stimulation*. NeuroImage, 34:661–670, 1 2007.

[29] Gordon Duffley, Daria Nesterovich Anderson, Johannes Vorwerk, Alan D Dorval, and Christopher R Butson. *Evaluation of methodologies for computing the deep brain stimulation volume of tissue activated*. Journal of Neural Engineering, 16:066024, 12 2019.

[30] J. Patrick Reilly. *Excitation Models*, pages 105–147. Springer New York, 1998.

[31] Andrea Saltelli, Ksenia Aleksankina, William Becker, Pamela Fennell, Federico Ferretti, Niels Holst, Sushan Li, and Qiongli Wu. *Why so many published sensitivity analyses are false: A systematic review of sensitivity analysis practices*. Environmental Modelling and Software, 114:29–39, 4 2019.

[32] Francesca Campolongo, Andrea Saltelli, and Jessica Cariboni. *From screening to quantitative sensitivity analysis. A unified approach*. Computer Physics Communications, 182:978–988, 4 2011.

[33] Nicholas T. Carnevale and Michael L. Hines. *The NEURON book*. Cambridge University Press, 2006.

[34] Sara Saray, Christian A. Rossert, Shailesh Appukuttan, Rosanna Migliore, Paola Vitale, Carmen A. Lupascu, Luca L. Bologna, Werner Van Geit, Armando Romani, Andrew P. Davison, Eilif Muller, Tamas F. Freund, and Szabolcs Kali. *HippoUnit: A software tool for the automated testing and systematic comparison of detailed models of hippocampal neurons based on electrophysiological data*, volume 17. 2021.

[35] Mathieu Sprengers, Robrecht Raedt, Lars Emil Larsen, Jean Delbeke, Wytse Jan Wadman, Paul Boon, and Kristl Vonck. *Deep brain stimulation reduces evoked potentials with a dual time course in freely moving rats: Potential neurophysiological basis for intermittent as an alternative to continuous stimulation*. Epilepsia, 61:903–913, 5 2020.

[36] Robert C. Wykes, Dimitri M. Kullmann, Ivan Pavlov, and Vincent Magloire. *Optogenetic approaches to treat epilepsy*. Journal of Neuroscience Methods, 260:215–220, 2 2016.

[37] N Grossman, K Nikolic, C Toumazou, and P Degenaar. *Modeling Study of the Light Stimulation of a Neuron Cell With Channelrhodopsin-2 Mutants*. IEEE Transactions on Biomedical Engineering, 58:1742–1751, 6 2011.

[38] Georg Nagel, Bettina Möckel, Georg Büldt, and Ernst Bamberg. *Functional expression of bacteriorhodopsin in oocytes allows direct measurement of voltage dependence of light induced H+ pumping*. FEBS Letters, 377:263–266, 12 1995.

[39] Johannes Vierock, Christiane Grimm, Noam Nitzan, and Peter Hegemann. *Molecular determinants of proton selectivity and gating in the red-light activated channelrhodopsin Chrimson*. Scientific Reports, 7:9928, 8 2017.

[40] Franziska Schneider, Dietrich Gradmann, and Peter Hegemann. *Ion Selectivity and Competition in Channelrhodopsins*. Biophysical Journal, 105:91–100, 7 2013.

[41] Mathias Mahn, Matthias Prigge, Shiri Ron, Rivka Levy, and Ofer Yizhar. *Biophysical constraints of optogenetic inhibition at presynaptic terminals*. Nature Neuroscience, 19:554–556, 4 2016.

[42] David Youssef, John H. Wittig, Samantha Jackson, Sara K. Inati, and Kareem A. Zaghloul. *Neuronal Spiking Responses to Direct Electrical Microstimulation in the Human Cortex*. The Journal of Neuroscience, 43:4448–4460, 6 2023.

[43] S C Gebhart, W C Lin, and A Mahadevan-Jansen. *In vitro determination of normal and neoplastic human brain tissue optical properties using inverse adding-doubling*. Physics in Medicine and Biology, 51:2011–2027, 4 2006.

[44] Elina A. Genina, Alexey N. Bashkatov, Daria K. Tuchina, Polina A. Dyachenko (Timoshina), Nikita Navolokin, Alexander Shirokov, Alexander Khorovodov, Andrey Terskov, Maria Klimova, Aysel Mamedova, Inna Blokhina, Ilana Agranovich, Ekaterina Zinchenko, Oxana V. Semyachkina-Glushkovskaya, and Valery V. Tuchin. *Optical properties of brain tissues at the different stages of glioma development in rats: pilot study*. Biomedical Optics Express, 10:5182, 10 2019.

[45] Bram Vandekerckhove, Jeroen Missinne, Kristl Vonck, Pieter Bauwens, Rik Verplancke, Paul Boon, Robrecht Raedt, and Jan Vanfleteren. *Technological Challenges in the Development of Optogenetic Closed-Loop Therapy Approaches in Epilepsy and Related Network Disorders of the Brain*. Micromachines, 12:38, 12 2020.

[46] Shijie Yan and Qianqian Fang. *Hybrid mesh and voxel based Monte Carlo algorithm for accurate and efficient photon transport modeling in complex bio-tissues*. Biomedical Optics Express, 11:6262, 11 2020.

[47] Matin Raayai Ardakani, Leiming Yu, David R. Kaeli, and Qianqian Fang. *Framework for denoising Monte Carlo photon transport simulations using deep learning*. Journal of Biomedical Optics, 27, 5 2022.

[48] Gorgi Kostovski, Paul R. Stoddart, and Arnan Mitchell. *The Optical Fiber Tip: An Inherently Light-Coupled Microscopic Platform for Micro- and Nanotechnologies*. Advanced Materials, 26:3798–3820, 6 2014.

[49] Nathan C Klapoetke, Yasunobu Murata, Sung Soo Kim, et al. *Independent optical excitation of distinct neural populations*. Nature Methods, 11:338–346, 3 2014.

[50] Johannes Oppermann, Paul Fischer, Arita Silapetere, Bernhard Liepe, Silvia Rodriguez-Rozada, José Flores-Uribe, Enrico Peter, Anke Keidel, Johannes Vierock, Joel Kaufmann, Matthias Broser, Meike Luck, Franz Bartl, Peter Hildebrandt, J. Simon Wiegert, Oded Béjà, Peter Hegemann, and Jonas Wietek. *MerMAIDs: a family of metagenomically discovered marine anion-conducting*

and intensely desensitizing channelrhodopsins. Nature Communications, 10:3315, 7 2019.

[51] Johannes Vierock, Enrico Peter, Christiane Grimm, Andrey Rozenberg, I-Wen Chen, Linda Tillert, Alejandro G. Castro Scalise, Marilù Casini, Sandra Augustin, Dimitrii Tanese, Benoît C. Forget, Rémi Peyronnet, Franziska Schneider-Warme, Valentina Emiliani, Oded Béjà, and Peter Hegemann. *WiChR, a highly potassium-selective channelrhodopsin for low-light one- and two-photon inhibition of excitable cells*. Science Advances, 8, 12 2022.

[52] Elena G. Govorunova, Oleg A. Sineshchekov, Roger Janz, Xiaoqin Liu, and John L. Spudich. *Natural light-gated anion channels: A family of microbial rhodopsins for advanced optogenetics*. Science, 349:647–650, 8 2015.

[53] Z Fekete, A C Horváth, and A Zátonyi. *Infrared neuromodulation:a neuroengineering perspective*. Journal of Neural Engineering, 17:051003, 10 2020.

[54] Eugene A. Kiyatkin. *Brain temperature and its role in physiology and pathophysiology: Lessons from 20 years of thermorecording*. Temperature, 6:271–333, 10 2019.

[55] Helton M. Peixoto, Rossana M. S. Cruz, Thiago C. Moulin, and Richardson N. Leão. *Modeling the Effect of Temperature on Membrane Response of Light Stimulation in Optogenetically-Targeted Neurons*. Frontiers in Computational Neuroscience, 14:5, 2 2020.

4

Towards a Hippocampal Formation Model

Temporal lobe epilepsy is the most common epilepsy in adults and the most difficult to treat with antiepileptic drugs. In mesial temporal lobe epilepsy (mTLE), seizures originate in the cortico-hippocampal circuit. Neurostimulation techniques are widely investigated as an alternative to hippocampal resection. The preceding chapter (chapter 3) delved into the exploration of optogenetic excitability within isolated CA1 cells. This chapter aims to encapsulate my endeavors in constructing a conductance-based network model of the hippocampal formation and offers first findings on the modeling of mTLE activity. This in-silico model could serve as a critical tool to enhance our understanding of the underlying mechanisms of various stimulation techniques, including optogenetics and deep brain stimulation. Such insights are pivotal in the quest to design more effective treatments for mTLE.

4.1 Mesial Temporal Lobe Epilepsy

Mesial temporal lobe epilepsy (mTLE), as previously introduced in section 1.1.3, is the generic term for epilepsy originating in the cortico-hippocampal circuit. This form of epilepsy represents the most prevalent type of focal epilepsy in adults and is the most difficult to treat with antiepileptic drugs [1]. Hippocampal sclerosis (HS) and mossy fiber sprouting are the two main histopathologies observed with mTLE. The former is characterized by severe cell loss up to 80% [2] while the latter denotes the formation of recurrent connections among granule cells [3]. The fundamental mechanisms underlying ictogenesis (the initiation and propagation of a seizure) and epileptogenesis (the gradual transformation of the brain into a state susceptible to spontaneous, episodic recurrent seizures) are extensively being studied in-vivo, in-vitro and in-silico. Presented below is a selection of models pertaining to seizures and epilepsy, with a more comprehensive overview available in Pitkanen et al. (2017) [4].

4.1.1 In-Vivo Models

In-vivo models of epilepsy are attainable through genetic manipulation, kindling, the use of chemical proconvulsants, or traumatic injury [5]. Kindling involves repetitive brain tissue stimulation, leading to the development of after-discharges and, eventually, seizures [6, 7]. This kindling process can be achieved chemically, electrically, and optogenetically [7]. Nonetheless, electrical kindling is the most commonly employed method, resulting in acute seizure models [8]. Prolonged kindling, known as overkindling, can lead to the emergence of spontaneous seizures in animal models. While these models exhibit some histopathological changes similar to those observed in temporal lobe epilepsy, they are limited in replicating the full spectrum of TLE pathologies [4, 5, 9].

Two frequently utilized chemoconvulsants are kainic acid and pilocarpine [5]. Systemic administration of these compounds results in models capable of generating spontaneous seizures. These models also display hippocampal sclerosis and mossy fiber sprouting. However, they come with notable drawbacks, including variability and uncertainty in the timing of the first seizure initiation, as well as the potential for off-target effects following systemic injection [10]. To address the latter concern, direct injection of pilocarpine or kainic acid into the hippocampus has been proposed as a more controlled approach [9, 11].

4.1.2 In-Vitro Models

Ex-vivo brain slice models, often categorized as in-vitro models, serve as invaluable tools for gaining insights into the fundamental physiology of neuronal circuitry, significantly enhancing our comprehension of epileptogenesis. These models offer numerous advantages, including reduced animal experimentation, clear visualization of the cytoarchitecture (especially in hippocampal slices), precise electrode placement, and control over the extracellular space useful for the administration of

test drugs due to the absence of the blood-brain barrier. However, it is important to note that ex-vivo slices represent a simplified preparation compared to in-vivo conditions. Additional limitations are cell damage due to the slicing procedure, disruption of local circuitry, perturbation of ionic homeostasis, and the absence of a blood supply [12, 13].

In the context of epilepsy, several ex-vivo slice models have been developed to induce epileptiform activity. These models employ alterations in ion composition, the use of chemical proconvulsants, or high-frequency electrical stimulation (kindling). Similar to in-vivo models, kainic acid serves as a reliable inducer of seizure-like activity. Another often used chemical compound is 4-aminopyridine (4AP), a blocker of voltage-gated potassium channels [14], which renders cells hyperexcitable and augments neurotransmitter release. Unlike in-vivo models, ex-vivo models offer precise control over ion concentrations in the extracellular space. Two notable models involve low magnesium levels, which unblock NMDA receptors, leading to interictal and seizure-like events, and elevated extracellular potassium concentrations. The latter results in a less negative equilibrium potential causing cell depolarization, increased neuronal excitability and elongated action potentials. Impaired GABAergic inhibition is also observed possibly due to chloride accumulation arising from compromised extrusion by the K^+-Cl^- cotransporter KCC2 [12, 13, 15].

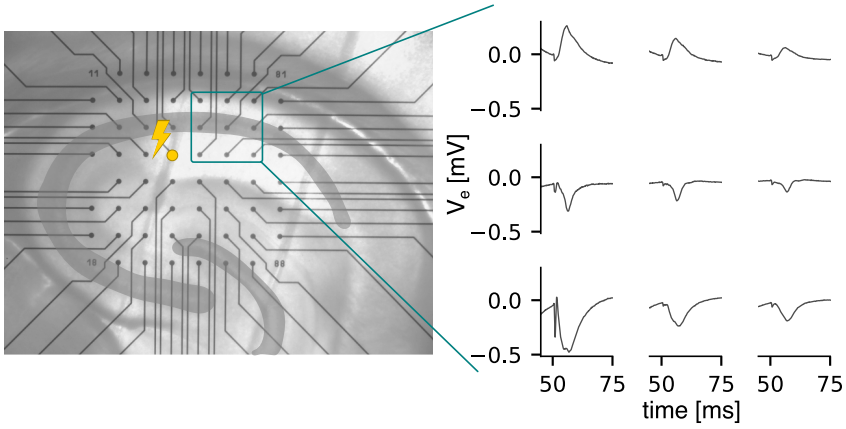

Figure 4.1: Example of hippocampal slice recording with a multi electrode array (MEA). Stimulation electrode is indicated by a yellow circle. The opacity of the stratum pyramidale in the Cornu Ammonis and dentate gyrus granule cell layer has been increased to enhance visibility.

Multielectrode arrays (MEAs, figure 4.1) are an ideal tool for recording extracellular neuronal activity in ex-vivo brain slices. These systems include multiple electrodes through which recordings from multiple sites can be received simultaneously. Consequently, they are ideal for the investigation of spatiotemporal dynamics.

Moreover, they allow fast switching between recording and stimulation modes [16].

4.1.3 Computational Models

Over the last few years, substantial effort has been dedicated to the computational modeling of the hippocampus and some of the pathologies associated with TLE [17]. Epileptic seizures manifest across various spatial and temporal scales. Researchers have employed a spectrum of models to replicate and elucidate epileptiform activity, spanning from macroscopic mean field models for investigating synchrony, to mesoscopic neural mass models representing the collective activity of interconnected subpopulations, and microscopic single cell models based on the Hodgkin-Huxley biophysical framework [18]. Of the latter, detailed network models have also been developed, albeit typically focused on specific hippocampal subregions [19–21]. Beyond neurophysiologically inspired models, mathematical models have also been created, with the Epileptor model by Jirsa et al. (2014) [22] being a notable example. This phenomenological model employs just five differential equations to abstractly describe seizure dynamics [23, 24]. For a comprehensive overview of available models, the interested reader is referred to sources such as Depannemaecker et al. (2023) [25], Wendling et al. (2016) [18], Raikov and Soltesz (2017) [26], and Case et al. (2012) [27].

As illustrated in chapter 3, computational studies are not only useful for the investigations into epileptogenesis or ictogenesis but also serve as ideal tools for exploring seizure suppression techniques. However, limited attention has been directed toward the investigation of, for instance, electrical stimulation as a treatment for TLE. Additionally, these studies have predominantly employed neural mass models in localized subregions. Consequently, only local direct effects of electrical stimulation have been investigated without the possibility for desynchronization of the subregion (an intrinsic property of neural mass models) [28–30]. Biophysically accurate models offer the advantage of incorporating detailed effects across multiple scales [27, 31], such as changes in intracellular ion concentrations impacting neuronal excitability and network activity. A great example is the recently developed, pioneering full-scale model of the healthy CA1 region by Romani et al. (2023) [32].

As aforementioned, the models are often restricted to a certain subregion, limiting the study of seizure propagation throughout the entire hippocampal formation. In the context of investigating seizure suppression, a model capable of assessing indirect effects is of considerable value. Therefore, this chapter discusses my endeavors in constructing a biophysically conductance-based computational network model of the entire hippocampal formation. Given the constraints of limited resources and time, this model is not full-scale and is constructed using reduced morphology neurons.

4.2 The Network Model

Cutsuridis and Poirazi (2015) [33] (CP15) constructed a model of the trisynaptic circuitry (see section 1.1.3) to study how theta modulated inhibition can account for long temporal windows. Their model can be found on modelDB (`https://modeldb.science/`) under accession number 181967. The code on modelDB deviates from the description in the article. However, it provides a better resemblance to their reported results. The model of the hippocampal formation used here is derived from their model available on modelDB. It is translated to NetPyNE [34], i.e., an open-source Python package to facilitate neuronal network simulations using the NEURON [35] simulator. The overall structure and modifications made on the original model are described below.

4.2.1 The Cell Models

The model includes three hippocampal subregions, i.e., the dentate gyrus (DG), Cornu Ammonis 3 and 1 (CA3 and CA1). The dentate gyrus is represented by 100 granule cells (GC), 2 mossy cells (MC), 2 basket cells (BC) and one hilar perforant path associated cell (HC). Both the CA3 and CA1 consist of 100 pyramidal cells (PYR), 2 basket cells and one axo-axonic cell (AAC). Furthermore, the CA3 includes an extra oriens lacunosum-moleculare cell (OLM) while one bistratified cell (BSC) is added to the CA1 region. The cells are modeled with multi compartment conductance based models. The simplified morphologies and number of compartments are shown in figure 4.2. The geometry of the compartments is given in Tables S1-S3 of CP15 [33]. A summary of the ionic currents present in each cell is given in table 4.1. The potassium and sodium concentrations are fixed throughout the simulation while the internal calcium concentration varies over time. All cells except for the CA3PYR follow a first order calcium accumulation given by:

$$\frac{d[\mathrm{Ca}]_i}{dt} = -\frac{i_{\mathrm{Ca}}}{z\delta F} + \frac{[\mathrm{Ca}]_\infty - [\mathrm{Ca}]_i}{\tau_{\mathrm{Ca}}} \tag{4.1}$$

with $[\mathrm{Ca}]_i$ and $[\mathrm{Ca}]_\infty$ the internal and equilibrium calcium concentration, respectively, F the Faraday constant, z the valence of calcium ions, δ the specific depth, τ_{Ca} the calcium decay time constant and i_{Ca} the total specific calcium current. The calcium reversal potential is then calculated with the Nernst equation or the Goldman-Hodgkin-Katz formalism, with an extracellular concentration ($[\mathrm{Ca}]_o$) equal to 2 mM. The passive parameters, active ionic conductances and reversal potentials of each cell are given in Tables S4-S8 of CP15 [33]. Deviations from the reported values are given in table 4.3.

4.2.2 Connectivity

The network connectivity is illustrated in figure 4.2. The arrow ends indicate the synaptic location on the postsynaptic cells. Axons are not modeled. Therefore, the pre- and postsynaptic cells are connected via an event-triggering scheme with a

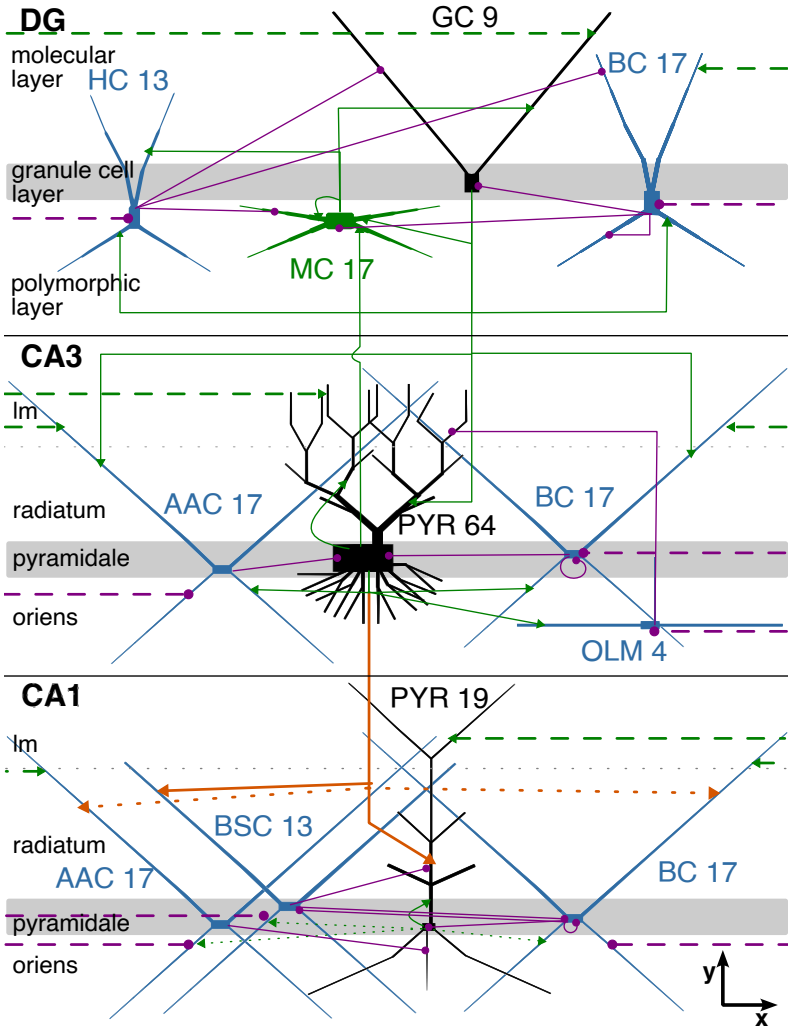

Figure 4.2: The hippocampal network model and synaptic projections. Top, the dentate gyrus with a granule cell (GC) and three interneurons: a hilar perforant path associated cell (HC), a basket cell (BC) and a mossy cell (MC). Middle, the CA3 region with the pyramidal cell, an axo-axonic cell (AAC), BC and oriens lacunosum-moleculare cell (OLM). Bottom, the CA1 with the pyramidal cell, AAC, BC and bistratified cell (BSC).

Figure 4.2: The cells' simplified morphologies are displayed with the number of compartments next to the cell name. The black cells are the principle cells each of which 100 cells are modeled. Blue cells are inhibitory interneurons while a green cell depicts an excitatory interneuron. The model contains a maximum of 2 models of each interneuron. The laminar layers are indicated on the left. The synaptic projections are shown with green and purple arrows indicating excitatory and inhibitory synapses, respectively. The Schaffer collaterals are shown in orange. The external, excitatory enthorinal cortex and inhibitory medial septum inputs are depicted by dashed arrows. Connections that are given by the dotted arrows are not included in the original model but in the alternative model (conn2).

		DG GC	**DG HC**	**DG MC**	**DG BC**	**CA3 PYR**	**CA1 PYR**	**CA3,1 BC**	**CA3,1 AAC**	**CA3 OLM**	**CA1 BSC**
transient sodium	g_{Na}	x	x	x	x	x	x	x	x	x	x
delay rectifier potassium	g_{fKdr}	f + s	f	f	f	x	x	f	f	x	f
leak	g_{l}	x	x	x	x	x	x	x	x	x	x
A-type potassium	g_{KA}	x	x	x	x	x	x	x	x	x	x
N-type calcium	g_{CaN}	x	x	x	x	x		x	x		x
L-type calcium	g_{CaL}	x	x	x	x	x	x	x	x		x
T-type calcium	g_{CaT}	x				x	x				
R-type calcium	g_{CaR}						x				
calcium dependent potassium	$g_{CagK\ (SK)}$	x	x	x	x	x	x	x	x		x
calcium and voltage dependent AHP potassium	$g_{AHP\ (BK)}$	x	x	x	x	x	x	x	x		x
non-selective AHP	g_{h}		f+s	f+s			x			x	
muscarinic potassium	g_{M}					x	x				
simple calcium accumulation		x	x	x	x		x	x	x		x
calcium buffering						x					

Table 4.1: Summary of ionic currents present in each cell model. f and s indicate a fast and slow variant, respectively. AHP denotes after hyperpolarization.

certain delay. More specifically, when the action potential threshold (-10 mV) is reached in the soma of the presynaptic cell an event with a certain delay is sent towards the postsynaptic cell eliciting a synaptic current (see equation (1.3)). The delay in the original model is fixed to 1 ms. The synaptic parameters, i.e. rise time, fall time and reversal potential, are given in tables S10-S11 of CP15 [33]. Synapses illustrated to arrive at a dendritic compartment in figure 4.2 always arrive on all dendritic branches at the same laminar level. For example, a GC-AAC connection forms two connections, one on each distal radiatum compartment of

the two dendritic branches extending towards the stratum radiatum. Similarly, 4 synapses are formed in case of the GC-CA3PYR connection. This rule differs for the HC and MCs where a connection results in 4 synapses; one on each branch. This is also the case for the GC-DGBC connections. The convergence, i.e., the number of cell connections a postsynaptic cell receives, equals the number of presynaptic cells modeled, excluding autapses. The convergence and number of synapses per connection are given in figure 4.3. The synaptic weights are given in table 4.2.

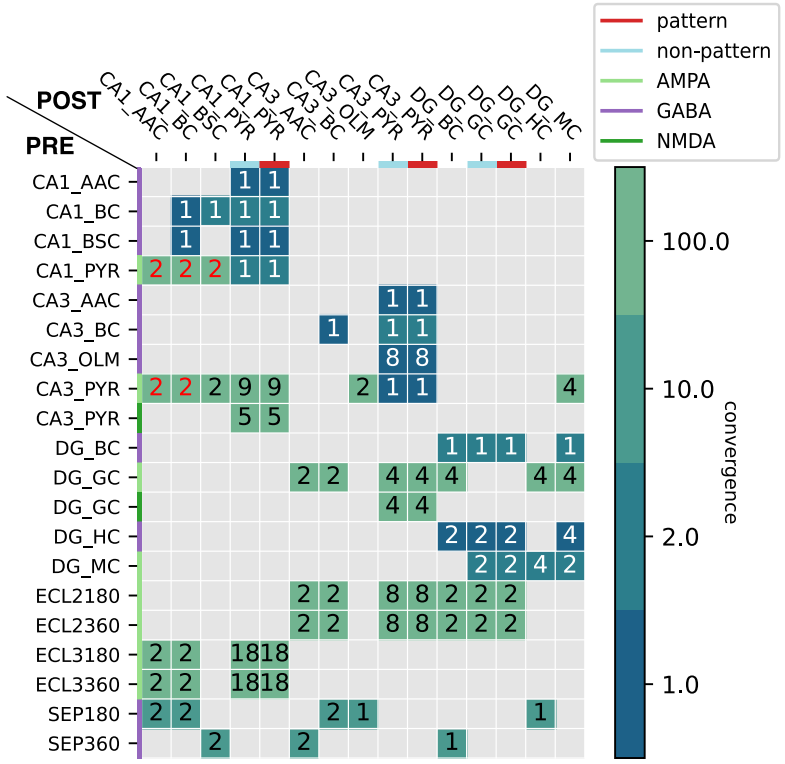

Figure 4.3: The convergence and number of synaptic connections per cell connection in the hippocampal network model. The convergence is given by the color-code while the number of synapses is given by the number. Convergence values higher or equal to 10 have a superimposed black text color. Red text color indicates connections only present in the alternative connectivity (see also table 4.2 and dotted arrows in figure 4.2)

The network receives input from the medial septum (SEP) and enthorinal cortex layers II and III (ECL2 and ECL3). These inputs are illustrated in figure 4.2 with dashed arrows. The inputs are theta modulated. Each input region is modeled as two populations firing with an average firing rate of 7.14 Hz (140 ms inter-spike-interval

(ISI)) with opposite phases (180° vs. 360°). The EC-layers and SEP-layers consist each of 100 and 10 spike generators (the cells are not explicitly modeled, only spike trains). The septal output consists of a small burst of action potentials with a max burst length of 70 ms and at mean frequency of 7.14 Hz. The individual spike times of the ECL2 and ECL3-180, and burst initiation times of the SEP are Gaussian distributed with a standard deviation of 11.2 ms (noise of 8%). The ECL3-360 population is exponentially distributed with a rate parameter of 11.2 ms.

A distinction is made for the principle cell populations between pattern and non-pattern cells. Pattern cells (*_p) receive higher input currents from the preceding region than non-pattern cells (*_n) (see table 4.2). 4% of the DG and 20% of the CA3- and CA1PYR cells are randomly selected to be pattern cells. The synaptic weight is fixed for synaptic connections between two populations except for the ECL2-GC_p and ECL3-CA1PYR_p connections. They receive a combination of elevated and non-pattern weight inputs with a ratio equal to the ratio of postsynaptic pattern and non-pattern cells.

4.2.3 Modifications

The model obtained from modelDB under accession number 181967 is translated to NetPyNE. Moreover, the channel mechanics are updated from explicitly hard-coded first order exponential Euler integration to a set of differential equations which can be solved with the more efficient *cnexp* method of NEURON. This *cnexp* method provides second order accuracy with elevated computational efficiency, appropriate for solving stiff systems [35]. This change also allows usage of the more advanced multi-order variable step (CVODE) integration. However, in all the simulations shown in this chapter a fixed step of 25 μs is imposed. Results obtained with this model are labeled *original*.

The calcium coupling is improved. Even though a calcium accumulation was provided (see equation (4.1)), the calcium currents and total $[Ca]_i$ were decoupled in the original model. Therefore the change in calcium concentration was not tracked, hence not affecting the calcium currents and calcium dependent potassium currents. Moreover, the internal and equilibrium calcium concentration is elevated from 5e-6 mM to 5e-5 mM resulting in a shift of the initial calcium Nernst potential from 170.71 mV to 140.24 mV. Finally, all cells are spatially discretized with the *d_lambda* rule [35] to reduce numerical errors. In the original model this was omitted for the CA3PYR and all DG cells. The distance between two nodes is limited by the length constant of a compartment at 100 Hz. Consequently, the number of segments is defined by:

$$n_{\text{seg}} = \text{round}\left((L/(0.1\sqrt{(D/(4\pi 100\ R_a\ c_m))}) + 0.9)/2\right) 2 + 1 \qquad (4.2)$$

with L the compartment length, D the compartment diameter, R_a the axial resistance and c_m the specific capacitance. Results shown with these modifications are labeled with the *_v2* suffix.

Table 4.2: The synaptic weights used in the hippocampal network model with pre- and postsynaptic cell population given in the rows and columns, respectively. The second column indicates the synaptic type (A: AMPA, G: GABA and N: NMDA). Cells with a gray fill are changed in the alternative network connectivity (conn2, see dotted arrows figure 4.2). The alternative values are given in the second part of the table. (p: pattern, n: non-pattern)

Pre\Post		**CA1 AAC**	**CA1 BC**	**CA1 BSC**	**CA1 PYR_n**	**CA1 PYR_p**	**CA3 AAC**	**CA3 BC**	**CA3 OLM**	**CA3 PYR_n**	**CA3 PYR_p**	**DG BC**	**DG GC_n**	**DG GC_p**	**DG HC**	**DG MC**
CA1_AAC	G				9.0e-2	9.0e-2										
CA1_BC	G		1.0e-2	8.0e-2	9.0e-2	9.0e-2										
CA1_BSC	G		6.0e-2		2.0e-1	2.0e-1										
CA1_PYR	A				3.0e-6	3.0e-6										
CA3_AAC	G									9.0e-1	9.0e-1					
CA3_BC	G							5.0e-3		5.0e-1	5.0e-1					
CA3_OLM	G									2.8	2.8					
CA3_PYR	A			6.0e-1	7.0e-5	2.5e-4			1.0e-4	1.5e-5	1.5e-5					9e-5
CA3_PYR	N				7.0e-5	2.5e-4										
DG_BC	G											5.0e-4	2.0e-2	2.0e-2		9.5e-3
DG_GC	A						2.1e-4	2.4e-3		1.5e-4	6.0e-3	3.0e-5			9.0e-2	1.5e-5
DG_GC	N									1.5e-4	6.0e-3					
DG_HC	G											5.0e-3	2.5e-1	2.5e-1		1.0e-4
DG_MC	A												1.0e-3	1.0e-3	1.0e-3	1.0e-3
ECL2_180	A						4.0e-4	8.0e-5		6.0e-5	6.0e-5	2.0e-3	1.0e-4	0.96×1e-4 + 0.04×5e-3		
ECL2_360	A						1.0e-5	2.4e-4		2.0e-5	2.0e-5	8.0e-5	8.0e-5	0.96×8e-5 + 0.04×1.5e-3		
ECL3_180	A	1.4e-4	1.4e-4		1.0e-5	0.8×1e-5 + 0.2×6.4e-2										
ECL3_360	A	5.2e-4	5.2e-4		1.0e-5	0.8×1e-5 + 0.2×8.0e-3										
SEP_180	G	8.0e-1	8.0e-1					5.0e-2	7.0e-3						6.0e-3	
SEP_360	G			3.0e-1			2.9					3.0e-1				

Modifications in connectivity 2 (Conn2)

CA1_AAC	G				1.0e-2	1.0e-2										
CA1_BC	G				1.0e-2	1.0e-2										
CA1_BSC	A				2.0e-2	2.0e-2										
CA1_PYR	A	1.5e-5	1.5e-5	1.5e-5												
CA3_PYR	A	6.0e-3	6.0e-3													
CA3_PYR	N					0.00012										

The CA1 pyramidal cell is substituted by a model created by Tomko et al. (2021) [31]. The Tomko model (CA1PYR_TK21) has a slightly altered structural morphology with three staggered obliques at the apical trunk instead of the current 2-by-2 symmetric configuration as shown in figure 4.2. Also the distal ends of the basal dendrites are subdivided giving a total of 20 compartments. The CA1PYR_-TK21 outperformed the CA1PYR_CP15 model in the standardized tests of the HippoUnit battery [36]. The CA1PYR_CP15 was shown to be weakly excitable and does not enter depolarization block. However, more important differences, for the study of the Schaffer collateral stimulation evoked potentials (EP, see below), are the weak postsynaptic potential attenuation and strong backpropagation of action potentials in the CP15-model compared to the TK21-model.

In the original model, the CA1PYR does not have any efferent connections. Therefore, I tested an alternative connectivity with projections from CA1PYR towards the CA1 interneurons. Additionally, the Schaffer collaterals branch on the CA1 interneurons. These connections are depicted with dotted arrows in figure 4.2. The alternative synaptic weights and number of connections are given in table 4.2 at the bottom and figure 4.3 in red, respectively. Simulations with this network connectivity are labeled with *conn2*.

As aforementioned, axons are not physically modeled. Therefore, synaptic connections are modeled with an event-triggering scheme with fixed delay of 1 ms between action potential detection in the soma and arrival of the event at the postsynaptic receptor. Because the original model is densely connected, i.e., the convergence equals the amount of cells in the presynaptic population (see figure 4.3), all cells of a single population receive almost the exact same input (only exceptions are the recurrent connections within a population, e.g., CA1PYR-CA1PYR). Consequently, the intra population activity is highly synchronized. In order to introduce desynchronization, the delays are made distance dependent. The cells are organized according to the laminar structure of the hippocampus (see section 1.1.3). Except for compartment's thickness, the models are 2D and placed parallel to the XY-plane. The somato-dendritic axis is aligned with the y-axis. The principle cells of each subregion are uniformly distributed over a region of 1 mm wide and 100 μm thick (x$\times$z). The interneurons of each subregion are confined to a region of 100 μm$\times$20μm around the center of the principle cells' subregion. Subsequently, the DG, CA3 and CA1 subregions are rotated around the z-axis with rotation angles 10, 0, 161°, respectively. Next, they are translated with respect to the center of the Cornu Ammonis corner (indicated by blue asterisk in figure 4.4). The translation vectors of the DG, CA3 and CA1 subregions are $[-1532.00, 263.25, 0]$ μm, $[-74.25, -850.50, 0]$ μm and $[-810.00, 1329.75, 0]$ μm, respectively. The enthorinal cortex and septum spike generators are located at $[-4443.00, 627.75, 0]$ μm. Except for the Schaffer collaterals, all distances between two connected cells are determined via the Euclidean distance. The Schaffer collateral distance is calculated following the orange path in figure 4.4. The propagation velocities are set to 300 μm/ms [37] except for the enthorinal cortex and septum inputs which are set to 1000 μm/ms because of their myelination [38–40] . Results under this network configuration are labeled *_HF*.

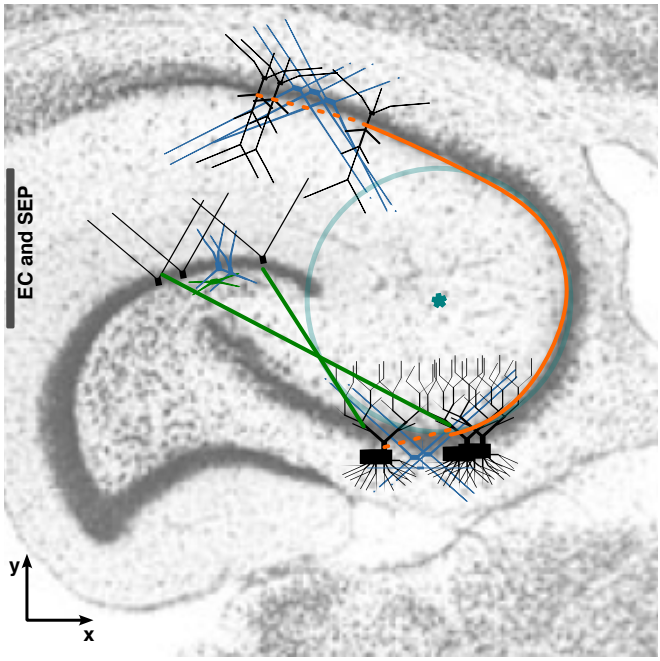

Figure 4.4: The network model according to the hippocampal formation's anatomy. The asterisk indicates the networks origin. Schaffer collateral distance follows the orange line. All other connections are calculated via the Euclidean distance as illustrated with green lines. The background figure is Nissl-stained horizontal section through the rat hippocampal formation adopted from Andersen et al. (2007) [41]

4.2.4 Derived Quantities

Extracellular Field Potentials

In order to compare the simulation results with experimental data recorded with a multi-electrode array, the extracellular field potential needs to be determined. The extracellular field potential, often called local field potential (LFP), arises from the superposition of any type of transmembrane currents [42]. This can be obtained with NetPyNE's built-in method that utilizes the line source approximation [43] in an Ohmic medium with conductivity σ = 0.3 mS/mm. For a recording electrode at a radial distance r and longitudinal distance h from the end of a line source with length l the extracellular potential (V_e) is estimated via:

$$V_{e,k} = \frac{1}{4\pi\sigma} \int_{-l}^{0} \frac{i_{\mathrm{tm}} A}{l\sqrt{r^2 + (h-s)^2}} \mathrm{ds} \tag{4.3}$$

$$V_{e,k} = \frac{i_{\mathrm{tm}} A}{4\pi\sigma l} \log \frac{\sqrt{h^2 + r^2} - h}{\sqrt{(l+h)^2 + r^2} - (l+h)} \tag{4.4}$$

where i_{tm} is the total transmembrane current of a neural segment k with length l ($l = L/n_{\mathrm{seg}}$) and membrane surface A. For a total of N individual sources the total V_e is given by:

$$V_e = \sum_{k}^{N} V_{e,k} \tag{4.5}$$

Evoked Potentials

To study the responsiveness of a neuronal circuitry, afferent axons can be stimulated to elicit evoked extracellular potentials in the postsynaptic region, in short evoked potential (EP). The experimentally recorded EPs are measured in the CA1 region after electrical stimulation of the Schaffer collaterals. Because axons are not modeled, a current is injected into the CA3PYR soma in order to elicit an action potential. A paired-pulse experiment is performed with a pulse repetition period of 20 ms and the first pulse given after 100 ms. Experimentally, the stimulation current is increased step-by-step in order to obtain the input-output curves. In the model, a single square-wave current is injected with a pulse duration of 3 ms and amplitude of 7.8 nA that initiates an AP on each pulse. Because all CA3PYR cells have the same excitation threshold, the increased recruitment experimentally obtained by elevating the stimulus current is simulated by increasing the number of CA3PYR cells that receive the current stimulus.

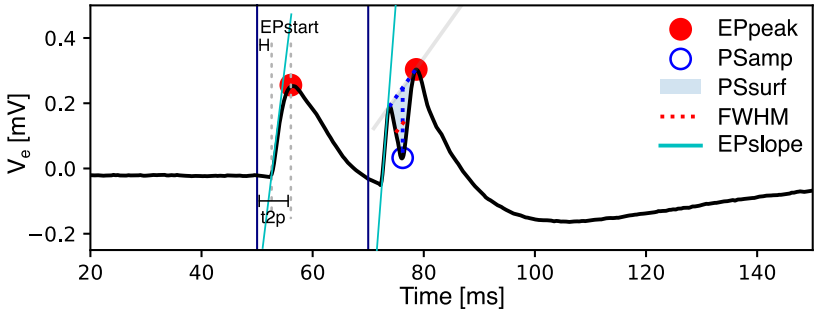

Figure 4.5: Feature extraction of the evoked potential (EP). The in CA1 stratum pyramidale recorded extracellular potential of a paired pulse stimulation of the Schaffer collaterals is shown with stimulation times indicated by the blue vertical lines at 50 and 70 ms. Extracted features are time-to-peak (t2p), EP start time (EPstart), EP peak amplitude (EPamp), population spike amplitude (PSamp), PS surface (PSsurf), the PS full width at half maximum (FWHM) and the EP slope (EPslope)

An example of the EPs in the stratum pyramidale of the CA1-region as a result

of a paired-pulse stimulation of the Schaffer collaterals is shown in figure 4.5. Interesting features are the EP peak amplitude (EPamp) and slope (EPslope), which are measures for the strength of synaptic transmission. The slope is obtained by fitting a linear function in a small window around the point of the EP's derivative's maximum. If the postsynaptic cells synchronously fire action potentials, a population spike (PS) can be observed. This is a trough on the V_e due to the sodium influx into the cells. The PS amplitude (PSamp) is determined as the maximal vertical distance between the trough and the tangent connecting the two neighboring peaks [44]. The PS surface (PSsurf) is the area in the trough, confined by the tangent. The PS surface and amplitude contain information on the excitability while the full width at half maximum (FWHM) provides information on synchrony. Additionally, the EPamp or EPslope ratios of the paired pulse experiment can give insights on short term plasticity mechanism, e.g, in this example paired-pulse facilitation can be observed.

4.2.5 Seizure-like Activity Modeling

High K^+ modeling

Elevation of the extracellular potassium concentration (high K) has been shown to introduce seizure-like epileptiform activity in-vitro. However, in the original model, the Nernst potassium potentials are fixed and changes in potassium concentration are not tracked. In order to include the elevated extracellular potassium effect, first the extracellular Na and K concentrations are set two 140 and 2.5 mM, respectively. Next, given these extracellular concentrations and the initial Nernst potentials, the intracellular concentrations of both ions are determined in each compartment by inverting the Nernst equation. Subsequently, the Nernst potassium potential is updated upon extracellular K elevation. This method affects only K-specific ion channels. The Na concentrations are determined as well in order to include the effect on non-selective ion channels like for instance i_l, i_h and i_{AMPA}. Assuming that sodium and potassium permeability are dominant for these channels, the permeability ratio can be determined via the Goldman-Hodgkin-Katz relationship.

$$E_x = \frac{RT}{F} \ln \frac{[K]_o + R_{NaK}[Na]_o}{[K]_i + R_{NaK}[Na]_i} \tag{4.6}$$

$$R_{NaK} = P_{Na}/P_K = \frac{[K]_i \exp\left(E_x F/RT\right) - [K]_o}{[Na]_o - [Na]_i \exp\left(E_x F/RT\right)} \tag{4.7}$$

with E_x the reversal potential of channel x, R, T and F the universal gas constant, the temperature and Faraday's constant, respectively. P_{Na} and P_K are the sodium and potassium permeabilities. Subsequently, given R_{NaK} the new E_x can be calculated with equation (4.6) for elevated $[K]_o$.

mTLE modeling

The two main histopathologies observed with mTLE are: hippocampal sclerosis and mossy fiber sprouting. Mossy fiber sprouting is modeled by adding recurrent connections between the DG granule cells arriving at the proximal dendrites. The used synaptic weights are equal to the weights of the ECL-GC connections. Due to the limited amount of cells in the network model, hippocampal sclerosis is included by systematically reducing synaptic weights of all CA cells.

4.3 Experimental Data

The experimental data was provided by Erine Craey of the 4Brain lab. In brief, transverse slices with a thickness of 350 μm were prepared from the ventral hippocampus of male Wistar rats of 4-6 weeks old (Janvier Labs, France). The slicing process was conducted using a VT1200S microtome (Leica Microsystems, Wetzlar, Germany). The care and handling of the animals adhered to European guidelines (directive 2010/63/EU), and were in compliance with protocols approved by the Animal Experimental Ethical Committee at Ghent University (ECD 19/29). Extracellular stimulation and recording were carried out using a planar multielectrode array (MEA) provided by MCS in Reutlingen, Germany. The MEA features 60 electrodes coated with titanium nitride, each with a diameter of 30 μm and spaced 200 μm apart. The recorded data was pre-amplified through a high-bandwidth MEA1060-BC pre-amplifier and subsequently digitized at sampling frequencies of either 10 or 25 kHz. To stimulate the Schaffer collaterals, a monophasic negative voltage pulse lasting 100 μs was applied to a nearby MEA electrode. Stimulation amplitudes were varied within the range of -500 mV to -3500 mV, adjusted in increments of -250 mV. Elevated extracellular potassium levels were induced by adding KCl, progressively increasing the concentration from 3.25 mM to 8.5 mM.

4.4 Results and Discussion

In this section, I present the results from the hippocampal formation network model and its applications. I begin by discussing modifications made to the original CP15 model. Following this, I analyze the response to Schaffer collateral stimulation and compare it to MEA recorded data in hippocampal slices. Finally, I assess the model's capability to generate seizure-like activity in response to elevated extracellular potassium levels and mesial temporal lobe epilepsy (mTLE) pathologies.

4.4.1 Network Response to Enthorinal Cortex and Medial Septum Input

To enhance the output of the evoked potential model (as discussed in next section, section 4.4.2), I made modifications to the Cutsiridis and Poirazi (2015) original model [33]. However, it is imperative that these improvements did not compromise

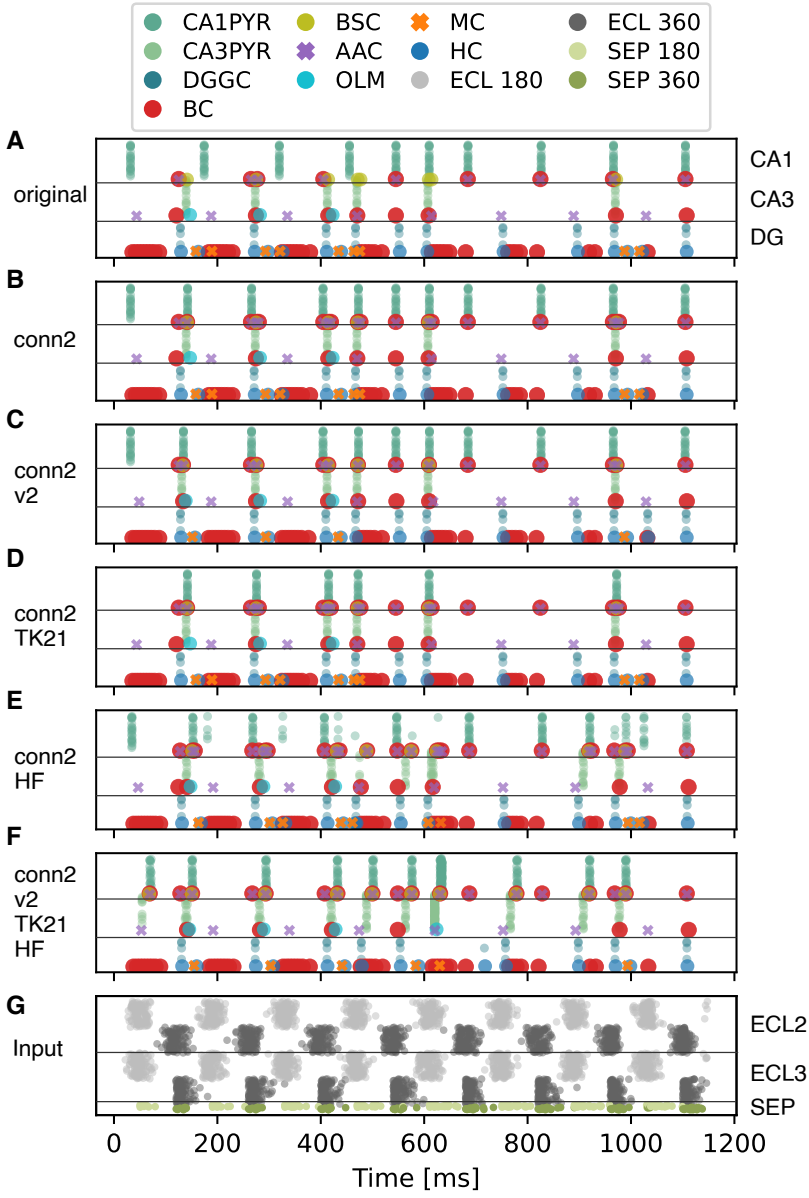

Figure 4.6: Rastergrams of different models in response to entorhinal cortex and septum input. **A** The original CP15 model. **B** Model with increased CA1 connectivity (conn2).

Figure 4.6: **C** Model with both alternative connectivity and improved calcium coupling, spatial discretization, and elevated internal calcium (conn2, v2). **D** Model with alternative connectivity and CA1PYR substitution with TK21 model. **E** Model with alternative connectivity and distance-dependent synaptic delays (HF). **F** Fully modified model. **G** Entorhinal cortex (layers 2 and 3) and medial septum theta rhythm input, each modeled by two out-of-phase spike-generating populations. **A-F** Subregion differentiation is provided on the right and applies to all subplots. Each marker indicates the crossing of the -10 mV action potential threshold.

the original model's response. The original model is able to accurately simulate firing of different hippocampal cells in response to theta rhythm input, as depicted in figure 4.6 (A). It can be observed that only the pattern cells are able to fire action potentials. Moreover, the pattern cells of a single population fire at exact the same time. Also, the CA1PYR neurons fire predominantly phase-locked to the ECL3180 input, out of sync with the Schaffer collateral stimulation. This while CA3PYR neurons do fire in response to the granule cells activity (synchronous firing).

A first alteration involves introducing additional connections within the CA1 microcircuit (referred to as conn2, see figure 4.3 and table 4.2) to establish interneuron-mediated feedback loops and reduce single synaptic strengths. The effect on the model output is given in figure 4.6 (B). Notable changes include a slight increase in the firing rate of CA1PYR cells from 9.2 Hz to 10.3 Hz and the emergence of small bursts (2-3 successive spikes) in CA1BC and CA1AAC cells. This leads to more synchronized firing of CA1PYR and CA3PYR neurons, while the response from the CA3 and DG regions remains unchanged.

Incorporating internal mechanism modifications (referred to as v2, see section 4.2.3) in combination with conn2 primarily impacts interneuron firing, resulting in fewer small bursts (see figure 4.6 (C)). The firing of principal cells remains largely unaffected. Substituting with the improved CA1PYR_TK21 model significantly reduces CA1PYR firing and synchronizes it with the Schaffer collateral input (CA3PYR action potentials, see figure 4.6 (D)).

The result of a model including both conn2 and distance dependent synaptic delays (HF) is given in figure 4.6 (E). This introduces some interesting changes in the model's behavior. Still, only the pattern cells of the CA1PYR cell reach excitation threshold. However, there is desynchronized activity with a few cells (<4) firing $\sim$40 ms out-of-phase. A single similar occurrence is observed in the CA3PYR cells. Additionally, non-pattern CA3PYR neurons are recruited. Combining all the changes above returns the synchronized activity within a single population (see figure 4.6 (F)). The individual cells fire with a small jitter (on average a 0.7 ms standard deviation, see figure 4.15). This is within the expected range from the introduced distance dependent synaptic delays. There is increased CA3PYR activity resulting in synchronized firing of the CA1PYR cells. Moreover, there is a single occurrence with recruitment of both pattern and non-pattern cells.

Overall, in the final model, the firing rate of the principle cells is increased,

shifting from 9.2 to 11.2 Hz and 8.4 to 11.1 Hz for the CA1PYR and CA3PYR pattern cells, respectively. Compared to the original model, there is a shift from predominantly ECL3180 phase-locked firing of the CA1PYR cells towards CA3PYR phase-locked activity. This shift is attributed to the substitution with the TK21 model, which is less excitable due to its lower resting membrane potential (-72 mv compared to -65 mV in the CP15 model). Notably, an increase of the ECL3180 synaptic weights did not revert to ECL3180 phase-locked activity. These modifications were aimed at enhancing biophysical realism. The combination of all changes resulted in the best outcome, maintaining a theta rhythm response. However, the mechanism behind the altered phase-locking of CA1PYR cells could be a subject of future investigation.

4.4.2 Evoked Potentials

In this section, I assess the model's ability to generate Schaffer collateral-stimulated evoked potentials (EP). The Schaffer collaterals target the stratum radiatum of the CA1 region. When an action potential arrives at the synapse, glutamate is released, activating AMPA and NMDA postsynaptic receptors. This results in depolarizing currents and the generation of excitatory postsynaptic potentials (EPSP). Therefore, at the stratum radiatum, this current sink is expected to result in a negative extracellular voltage (V_e) deflection. At the soma and basal dendrites, in the stratum pyramidale and oriens, the return current should produce a current source accompanied with a positive voltage deflection. This is observed experimentally in hippocampal slice recordings, as is shown in figure 4.1 on the right. The lower row illustrates the negative V_e in the stratum radiatum, while the upper row displays the positive V_e change in the stratum oriens. In this example the electrodes of the middle row are too close to the radiatum-pyramidale boundary, resulting in a negative V_e deflection.

The original model's prediction for an EP measured in the stratum pyramidale and radiatum during a paired-pulse stimulation is presented in figure 4.7 (A). The result is for the stimulation of 100% of the CA3PYR cells, as modeled as alternative to axon stimulation (cf. section 4.2.4). Several discrepancies from the MEA recorded EPs can be observed. In the stratum pyramidale, the positive V_e deflection is negligible compared to the population spike (PS) amplitude. Moreover, the latter consists of three troughs with only a positive V_e deflection observed prior to the PS. The first two troughs correspond to the separate spiking of pattern and non-pattern cells. The V_e recorded in the stratum radiatum initially exhibits a negative deflection followed by a high positive peak, which deviates from the experimentally measured EP. Following the second pulse, only CA1PYR pattern cells fire action potentials, resulting in a smaller peak and trough in the radiatum.

To improve the EP outcome, I integrated the model modifications discussed in the previous section. First, it was identified that the high peak in the stratum radiatum and the third trough in the pyramidale were due to GABAergic input originating from the CA1BSC. This led towards the adoption of conn2, where the GABAergic weights on the CA1PYR cells are reduced. Despite a tenfold reduction

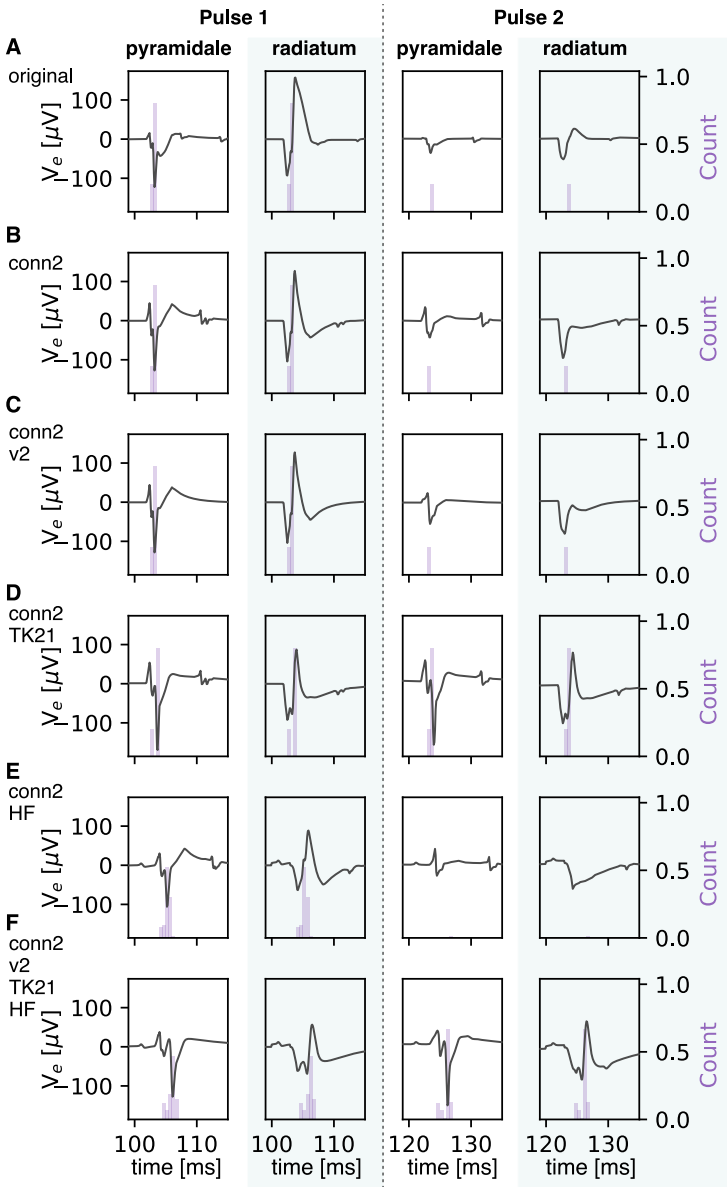

Figure 4.7: The evoked potential in the CA1 stratum pyramidale and radiatum in response to a paired-pulse Schaffer collateral stimulation for various model configurations. **A** The original CP15 model. **B** Model with increased CA1 connectivity (conn2). **C** Model with alternative connectivity, improved calcium coupling, spatial discretization, and elevated internal calcium (conn2, v2). **D** Model with alternative connectivity and CA1PYR substitution with the TK21 model.

Figure 4.7: **E** Model with alternative connectivity and distance-dependent synaptic delays (HF). **F** The fully modified model. The results are shown in response to the firing of 100% of the CA3PYR cells. The response to the first (second) pulse is presented in the two columns on the left (right). The EP measured in the stratum pyramidale and radiatum is depicted in the odd and even columns, respectively. The EP overlays a histogram of the spike count generated by CA1PYR cells relative to the total number of CA1PYR cells.

in the GABAergic weights, the peak in the stratum radiatum only slightly diminished and the positive V_e deflection in the stratum pyramidale became only slightly more prominent (see figure 4.7 (B)). This marginal effect is due to the recruitment of CA1BC, which was absent in the original model. The internal mechanism changes (v2) affect primarily interneurons. As can be seen in the transition from figure 4.7 (B) to (C), only the small ripples, generated by transmembrane currents during an action potential in CA1 interneurons at 110 ms and 135 ms, disappear.

The substitution with the TK21 model aimed to increase somatic return currents, as shown in Figure 2(D). The result is shown in figure 4.7 (D). However, the impact on the EP measured in the stratum pyramidale is minimal. The peak in the stratum radiatum decreases, primarily due to reduced action potential backpropagation in the TK21 model, which decreases shunting of the AMPA currents. The remaining peak is a result of a combination of GABA and potassium currents (see figure 4.8). Importantly, the responses to the first and second pulse are now similar.

It is clear that the EP is dominated by the active transmembrane currents during an action potential. This is illustrated in figure 4.8, with sodium currents being the main contributors to the total transmembrane current (i_{tot}). In the radiatum, the current sink created by high AMPA currents (dotted orange) is counteracted by GABA and potassium currents. Additionally, the arrival of AMPA input from the Schaffer collaterals at each cell at exactly the same time, decaying with a short time constant of 3 ms, contrasts with the observed EP width of approximately 10 ms (as seen in figure 4.5). To introduce desynchronization, I implemented distance-dependent synaptic delays (HF), which results in broader and lower troughs and peaks (see figure 4.7 (E) and (F)). However, this effect is only marginal, and the expected gradual activation of CA1PYR cells was not achieved. As seen in figure 4.10 (E), there is a discrete jump from 20% to 100% activation when stimulating 60 CA3PYR cells. In the subsequent results, I exclusively used the fully modified model (i.e., conn2_v2_TK21_HF).

The CA1 region is modeled with only 104 cells, all reaching activation threshold when 100% of the CA3PYR cells are recruited. Considering that the active currents during the AP dominate any other current, it is possible that the EP is concealed due to the limited number of simulated cells that do not fire an AP. To address this, I included 1000 dummy cells, i.e., CA1PYR cells with only passive properties (see figure 4.8). These dummy cells receive the same synaptic input as the regular CA1PYR cells. A comparison of the measured EP in the stratum oriens, pyramidale, and radiatum, with these dummy cells included, is presented

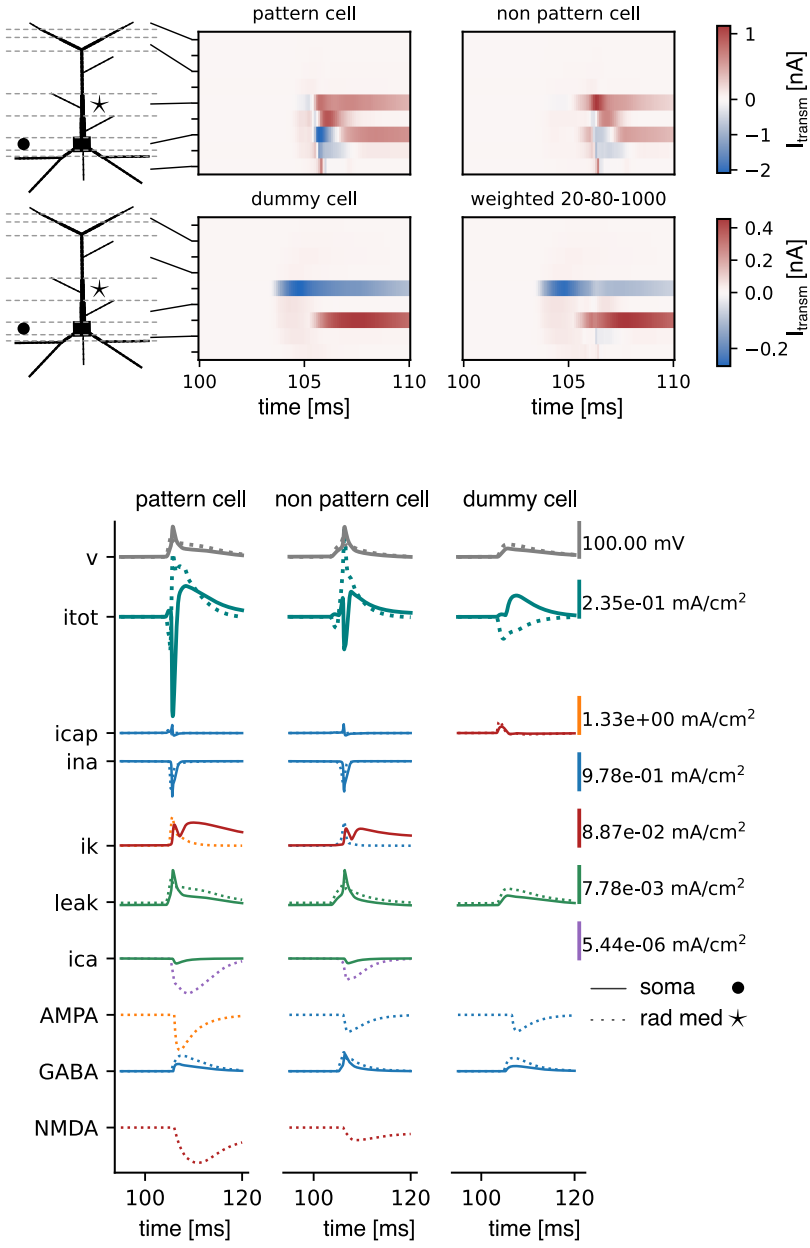

Figure 4.8: The CA1PYR transmembrane currents following the first Schaffer collateral stimulation pulse in the fully modified model. The Schaffer collaterals are stimulated at t = 100 ms.

Figure 4.8: (Top) An approximation of the current sources and sinks is derived by summing the total transmembrane (i_{tot}) currents measured at the center of each section, categorized into layers as indicated on the left. The bottom-right subplot illustrates a weighted sum of the pattern cell (top-left), non-pattern cell (top-right), and dummy cells (bottom-left), with weights of 20/1100, 80/1100, and 1000/1100, respectively. (Bottom) Depiction of individual transmembrane currents. The synaptic current of only a single synaps is displayed. The line color indicates the matching scale bar. The height of the scale bar corresponds to the given value

in figure 4.9 (A). The EP shapes now more closely resemble the experimentally measured EPs. Consequently, it could be argued that thousands of cells receive the Schaffer collateral input, with only a limited number CA1PYR cells being activated. A breakdown into the contribution of the regular CA1PYR cells and the V_e due to the other cells is given in figure 4.9 (B) and (C). Notably, while the active currents during an AP do contribute to the total EP (figure 4.9 (B)), they are not solely responsible for the troughs and peaks, as evident in figure 4.9 (C). Further examination of the transmembrane currents in the soma of the dummy cells (cf. figure 4.8) reveals that the first peak is due to the capacitive return current, while the second peak is entirely mediated by GABA. This is confirmed in figure 4.9 (D), where the GABAergic currents are omitted, resulting in the disappearance of the second peak.

In future research, it may be worth investigating whether these GABAergic currents indeed contribute to the experimentally measured evoked potentials or exploring ways to reduce their impact on the modeled EPs. Possible strategies include increasing the number of interneurons to reduce the strength of individual synapses. Together with distance-dependent synaptic delays, this would introduce some additional temporal averaging. Alternatively, spatial spreading of synaptic inputs and variance in synaptic gains could be considered. As depicted in figure 4.8 (top), the active current sources and sinks are currently highly localized, with spatially smeared-out return currents. Hence, by spreading the synaptic inputs spatially, which are currently limited to single points on the dendritic tree, it might be possible to smear-out active sources and sinks, enabling the emergence of return currents in the EP.

Finally, it is investigated whether the extracted EP features (see figure 4.5) can effectively capture the anticipated trends with respect to increased Schaffer collateral stimulation. The results are summarized in figure 4.10. In figure 4.10 (A), a logarithmically shaped trend of the EP amplitude (EPamp) within the stratum pyramidale is observed. This contrasts with the expected linear trend due to the linearly increasing recruitment of CA3PYR cells. Notably, when GABAergic connections are omitted, a reduction in the EPamp can be seen. This is indicative for the selection of the GABA-induced peak as EPamp. This is further confirmed in figure 4.10 (B), where the EPamps exceed the effective field EPSP amplitude (fEPSPamp, i.e, the peak produced by the model prior to the PS), except in the *no gaba* simulations. When all pyramidal cells are considered as pattern cells, an

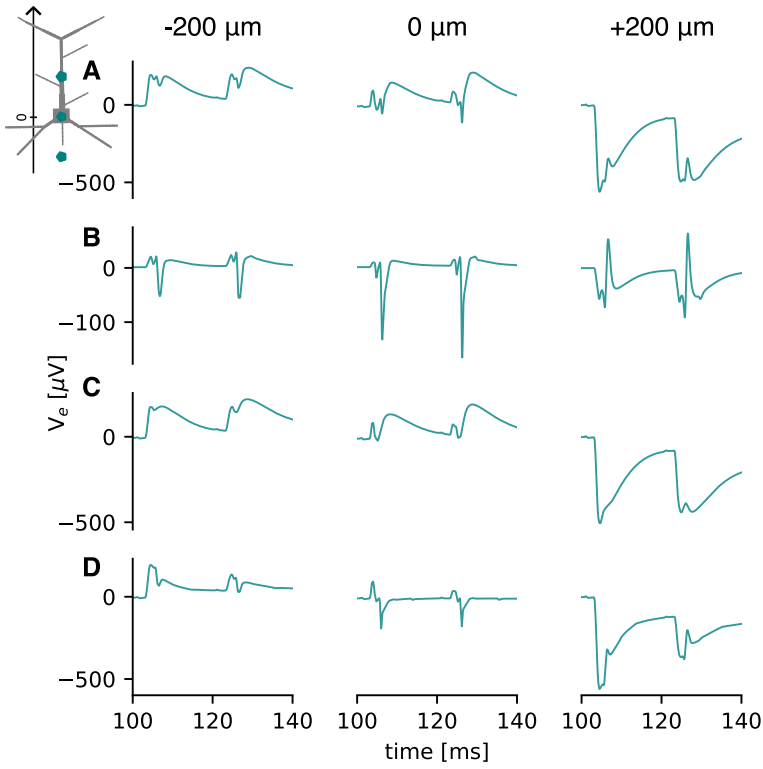

Figure 4.9: Evoked potential (EP) in the CA1 region of the fully modified model, where 100% paired-pulse stimulation is applied. Additional dummy cells are introduced to amplify the contribution of the evoked postsynaptic potentials and return currents to the recorded V_e at the electrode. The response is recorded at three electrodes positioned in the stratum oriens, pyramidale, and radiatum, with their exact locations depicted in the inset. **A** illustrates the EP response of the model, including 1000 dummy cells. **B** shows the measured EP of only CA1PYR transmembrane currents, dummy cells excluded. **C** represents the response in **A** subtracted from the one in **B**. **D** depicts the model response with dummy cells but without GABAergic connections on the CA1PYR cells.

upward shift in the EPamp is observed, suggesting contributions from both fEPSP and GABAergic peaks on the measured EPamp.

Figures 4.10 (C) and (D) illustrate the fEPSPamp and population spike amplitudes as functions of increased Schaffer collateral stimulation. The inclusion of dummy cells results in smoother trends, yet the fEPSP amplitudes after the second pulse are notably lower. Excluding the dummy cells leads to a more linear trend, although it has outliers, particularly when non-pattern cells are recruited. This

is evident in the CA1PYR spike count in figure 4.10 (E). The PSamp extracted from the EP signal generated by the normal CA1PYR cells proves to be a better metric for spike count than when the dummy cells are included, as evident in the comparison between figures 4.10 (D) and (E). Although there is not a gradual activation of CA1PYR cells, the cells fire more synchronously with increasing Schaffer collateral stimulation (as shown in figure 4.10 (E, left)), which explains the continuous increase in the measured PSamp in figure 4.10 (D). The change in EP slope is depicted in figure 4.10 (F) when dummy cells are not included. Based on these trends, the EP slope appears to be a more robust metric for the strength of synaptic transmission in the model. Given these findings, the inclusion of dummy cells, while visually more striking comparison with experimentally measured EPs, should not be included. Therefore, dummy cells are excluded in the simulations of sections 4.4.3 and 4.4.4

Although the shape differs from experimentally observed EPs, the calculation of V_e and the extraction of EP features still hold merit in identifying synaptic transmission strengths and cellular spiking. Nevertheless, it is clear that the model output does not capture the experimentally observed short-term synaptic facilitation (see figure 4.5 and figure 4.10 (G)). To address this discrepancy, the introduction of plasticity mechanisms is essential. Additionally, no population spike is observed, in-vitro, after the first pulse (cf. figure 4.10 (H)). However, these observations are contrary to in-vivo behavior, where short-lasting reductions of the fEPSP and population spike are observed [44].

4.4.3 Network Simulation with Elevated Extracellular Potassium

In this section, the model's predictions under elevated potassium conditions are assessed. The effects on both K-specific ion channels and all K-dependent channels, as outlined in section 4.2.5, are examined. Without any external input, elevation of extracellular potassium up to a factor 3, affecting only the K-specific ions, results in a transient burst of the OLM cells followed by depolarization block. Other cell types experience an elevated resting membrane potential without spontaneous firing. However, when all K-dependent channels are affected, spontaneous tonic activity in mossy cells and hilar perforant path-associated cells, and basket cells of the dentate gyrus is observed at a 1.5 and 2-fold increase, respectively. Figure 4.11 (top) displays the results for a 2.6-fold increase, affecting all K-dependent ion channels without external stimulation. Here, transient activity is observed in the CA1PYR and CA3PYR cells. Repetitive firing of the CA1PYR is evoked by the collective firing of the CA3PYR cells. The CA3PYR cells fire once, followed by an elevated plateau potential with superimposed oscillating activity. Further increases in extracellular potassium results in continuous repetitive firing of the CA1PYR cells until depolarization block occurs at a 5-fold potassium increase.

The effect on the theta-rhythmic enthorinal cortex and septum input is shown in figure 4.11 (bottom). Elevated potassium levels render the system hyperexcitable,

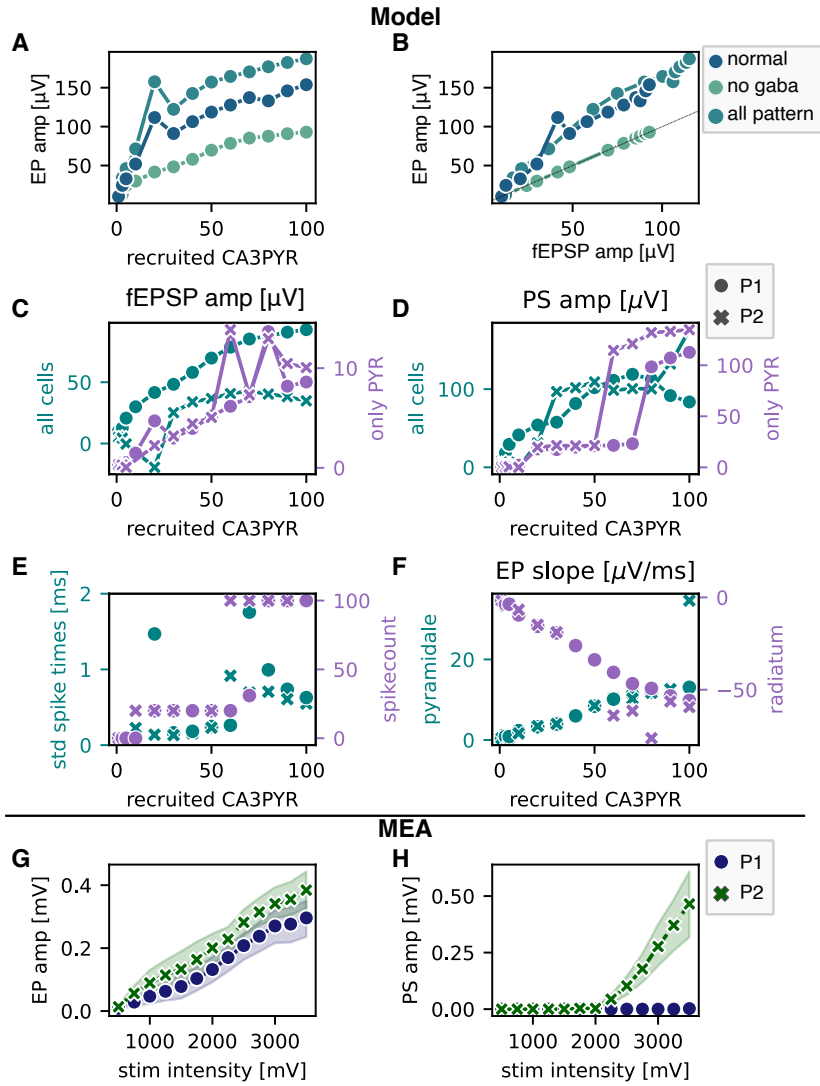

Figure 4.10: Characterization of the Schaffer collateral paired pulse stimulated evoked potential (EP). **A** EP amplitude in response to the first pulse of the model, including 1000 dummy cells, for an increasing number of recruited CA3PYR cells. **B** The EP amplitude versus the effective fEPSP amplitude. The color code in **A-B** indicates modifications to synaptic connectivity, with *no gaba* representing the absence of GABAergic input on the CA1PYR cells, and *all pattern* indicating that all CA1PYR cells receive elevated pattern cell inputs.

Figure 4.10: **C** (**D**) The EPSP (population spike (PS)) amplitude as a function of an increasing number of recruited CA3PYR cells, with dummy cells on the left (teal) and without on the right (purple). **E** The standard deviation of the spike times (left) and the effective spike count (right) of the CA1PYR cells. **F** The EP slope measured in the stratum pyramidale (left) and stratum radiatum (right) without dummy cells. **G** and **H** represent the measured EP amplitude and PS amplitude in the stratum pyramidale of hippocampal slices for increasing stimulus intensity. The shaded area indicates the 95%-confidence interval of 15 measured EPs across two slices in the stratum pyramidale. Dotted lines represent results in response to the first pulse, while crosses indicate the response to the second pulse of the paired-pulse stimulation, which applies across the entire figure.

leading to the recruitment of non-pattern cells and bursting behavior in the CA1 region. At a 1.5-fold increase (not shown here), only doublets (two-spike bursts) occur, while the overall theta-rhythm activity is preserved. Affecting only the K-specific ion channels also results in bursting, albeit with shorter bursts and minimal recruitment of non-pattern cells. At a 2.6-fold increase, the CA3PYR cells do not exhibit bursting activity. They fire synchronously, followed by a short period of depolarization block.

The impact of elevated potassium levels on the EPs is presented in figure 4.12 (top). At a 2-fold increase, the model predicts consecutive spiking of CA1PYR cells, driven by a double spike in the CA3PYR cells. Furthermore, non-pattern cells are recruited at lower stimulation levels, and increased jitter is observed. With a 2.6-fold increase, the CA3PYR cells are pushed into depolarization block after the first stimulus, not able to elicit a spike after the second stimulus. Notably, oscillations are observed at 100% stimulation, similar to what is recorded experimentally, although after the second pulse at the same increased potassium level. These oscillations result from subthreshold spikes (i.e., spikes not reaching the -10 mV threshold level) superimposed on an elevated plateau potential.

While not fit to elevated potassium levels, the model provides interesting predictions and demonstrates similarities with experimental data. Of particular interest is the spontaneous activity observed at the 2.6-fold increase, consistent with experimental findings, while absent at a 2-fold increase in both the model and experimental data. This effect is only obtained by affecting both K-specific and non-selective ion channels. This underscores the importance of considering multiple factors in computational modeling, as changes in ion concentrations are usually modeled to affect only ion-specific channels. However, my approximation of including all K-dependent channels might be an overestimation. To accurately model the effect, a more precise understanding of ion-specific permeabilities for each channel is essential, though challenging. Additionally, other mechanisms such as potassium pumps, which are absent in current models, could contribute in altering spiking behavior. It is important to note that the depolarization block observed in CA3PYR cells might indicate that the model is underfit for these high potassium changes. Recovery from depolarization block could result in more spontaneous activity.

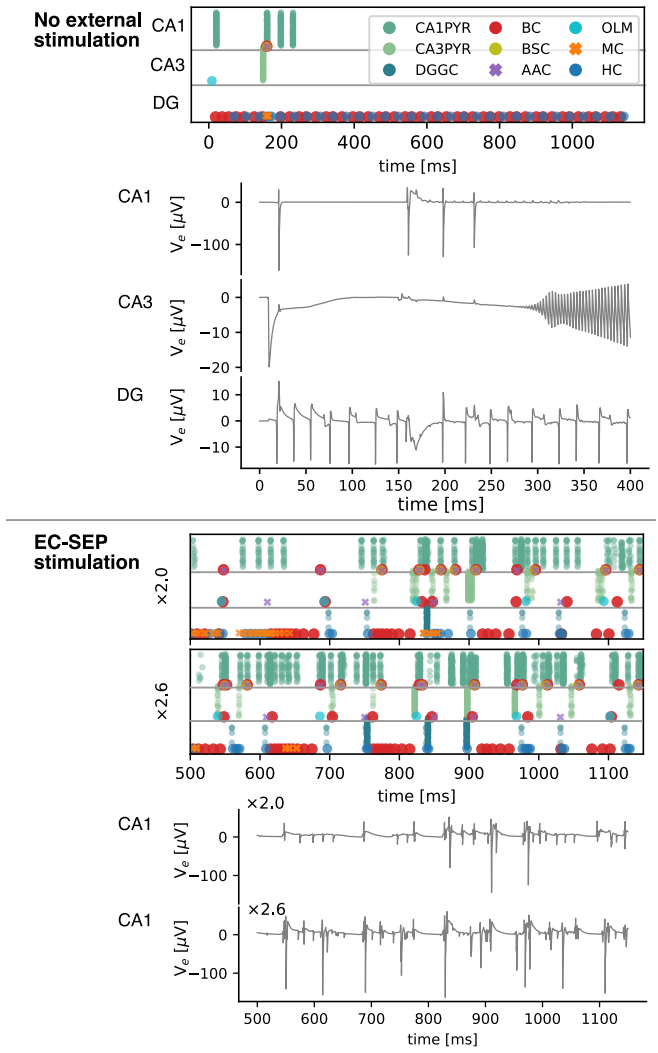

Figure 4.11: Elevated extracellular potassium simulations (top) involving a 2.6-fold increase in extracellular potassium in the absence of external input, (bottom) with the presence of entorhinal cortex and septum input for both the 2 and 2.6-fold increases. (top) Extracellular potentials recorded in the stratum pyramidale of CA1 and CA3, as well as in the granule cell layer. (bottom) Extracellular potentials recorded in the stratum pyramidale of CA1. The respective regions are indicated on the left. Each marker in the raster plots signifies the crossing of the -10 mV action potential threshold.

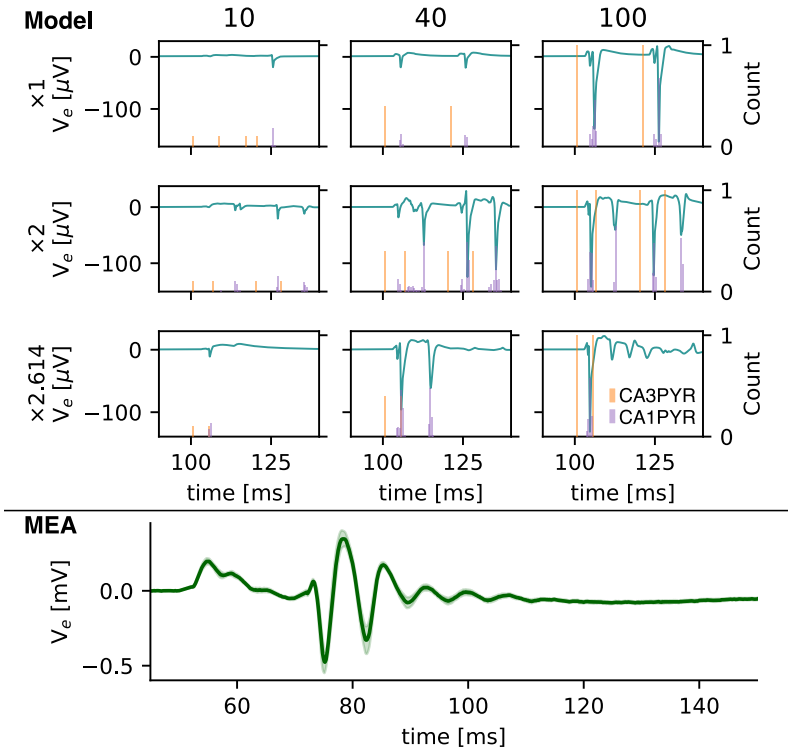

Figure 4.12: Evoked potentials in the CA1 region following Schaffer collateral stimulation with elevated extracellular potassium. (top) The model's response, with the percentage of stimulated CA3PYR cells shown above and extracellular potassium increase to the left. (bottom) The MEA-recorded EP response in the stratum pyramidale of the CA1 with a 2.6-fold increase in extracellular potassium. The shaded area represents the 95%-confidence interval of multiple responses to the same stimulus of -2350 mV, within a single hippocampal slice.

4.4.4 Network Simulation of Mesial Temporal Lobe Epilepsy

The model's response to mTLE histopathological changes is presented in figures 4.13 and 4.14. As described in section 4.2.5, the limited number of modeled cells requires modeling cellular loss by reducing synaptic weights. These reductions are based on the ILAE classified type I of hippocampal sclerosis and are applied equally to both interneurons and principal cells. When maintaining theta-rhythm input from the entorhinal cortex and septum, the model does not exhibit seizure-like activity. In fact, firing rates are even reduced.

The inclusion of mossy fiber sprouting induces bursting activity in the dentate gyrus. This subsequently propagates towards the CA3 and CA1 regions, albeit with shorter durations. Additional cellular loss in the CA3 region leads to prolonged

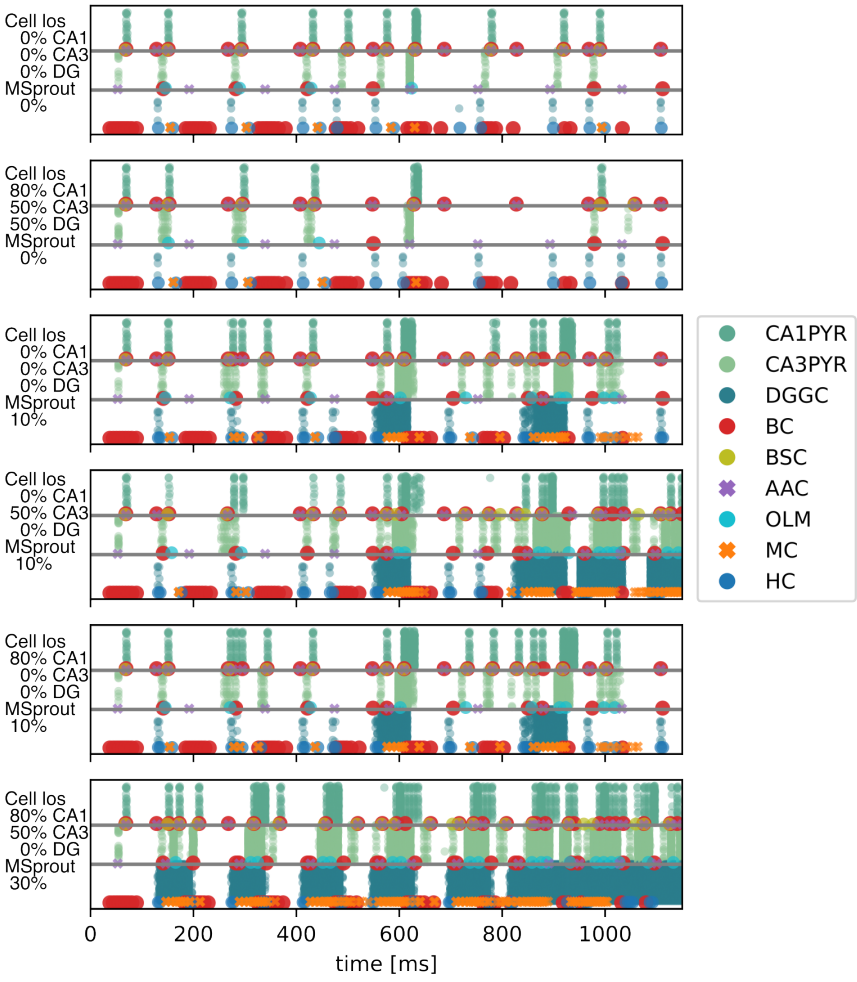

Figure 4.13: Model predictions under varying levels of temporal lobe epilepsy pathologies with entorhinal cortex and septum theta-rhythm input. Cellular loss and the percentage of mossy fiber sprouting are indicated on the left. Cellular loss is modeled through a reduction in synaptic strengths, while mossy fiber sprouting is modeled by increasing the convergence between dentate gyrus granule cells.

bursting behavior in CA3 with minimal effects on CA1. This cellular loss also causes additional bursting in the dentate gyrus due to a feedback loop via the mossy cells. However, cellular loss in CA1 has only marginal effects on the model's output. Although not shown here, granule cell loss results in a reduction of bursting

behavior. A simulation featuring a combination of all pathological changes is presented in figure 4.13 (bottom). When mossy fiber sprouting is included, the system becomes hyperexcitable, and bursts spread from the dentate gyrus towards CA1. The corresponding V_e measured in the stratum pyramidale of CA1 and CA3, as well as the granule cell layer, are depicted in figure 4.14, revealing seizure-like activity.

In summary, these results suggest that mossy fiber sprouting is a critical factor triggering seizure-like activity originating in the hippocampus. Notably, granule cell and CA1 cell loss lead to a reduction in bursting activity, while CA3 cell loss renders the system more excitable. These observations suggest that hippocampal sclerosis in CA1 and the dentate gyrus may represent the system's efforts to counteract epileptic activity. In future work, it may be beneficial to explore the decoupling of cellular loss in principle cells and interneurons.

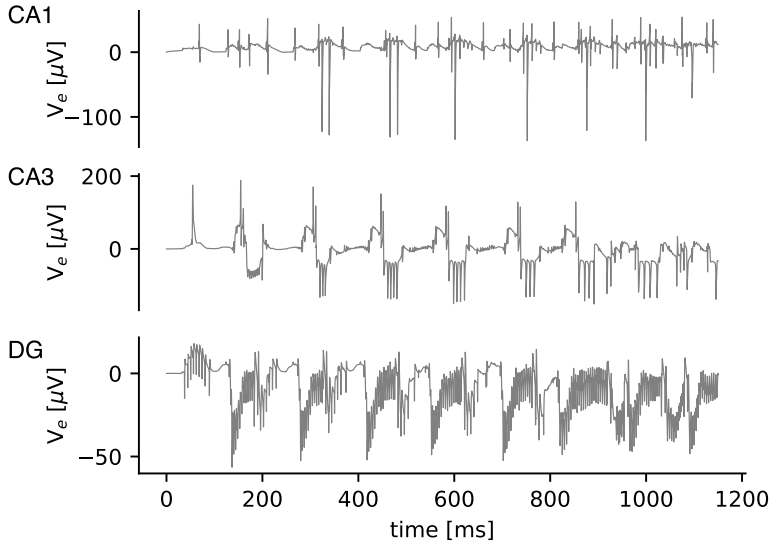

Figure 4.14: Extracellular potentials recorded in the stratum pyramidale of the CA1 and CA3, as well as the granule cell layer, in response to entorhinal cortex and septum theta-rhythm input under conditions simulating mesial temporal lobe epilepsy (mTLE). These conditions include 80% CA1, 50% CA3, and 0% DG cell loss, along with 30% mossy fiber sprouting.

4.5 Conclusion

In this chapter, I have presented the development and testing of a conductance-based network model for the epileptic hippocampus, building upon the work of Cutsuridis and Poirazi (2015) [33]. Several modifications are proposed and examined to enhance the response of the Schaffer collateral stimulation evoked potential. These changes effectively preserve the theta-rhythm response, albeit with CA1 activity phase-locked to CA3PYR instead of ECL3180. Furthermore, these adjustments improve the evoked potential response, particularly by reducing GABAergic peaks and increasing jitter. However, it is important to note that an exact match with experimental data is not achieved. Notable discrepancies include the absence of a positive evoked potential with a population spike preceding the EP peak and the presence of GABAergic peaks in the stratum radiatum. Potential avenues for further improvement include spatially spreading of synaptic inputs, variance in synaptic gains, increasing the number of interneurons, and decreasing convergence levels, which could introduce more asynchronous firing and gradual cell recruitment. Additionally, the inclusion of synaptic plasticity mechanisms may help to model the experimentally observed paired-pulse facilitation, even though it is important to note the presence of paired-pulse depression in in-vivo settings.

Furthermore, two epileptic models were tested. First, elevated extracellular potassium is used in-vitro to induce seizure-like activity. Although the model is not fit to elevated potassium levels, it is able to reproduce similarities with experimental data, such as the occurrence of spontaneous activity only after a 2.61-fold increase and the observation of oscillating activity in the CA1 following Schaffer collateral stimulation. Second, mesial temporal lobe epilepsy histopathological changes are tested. The results demonstrate that mossy fiber sprouting is crucial for triggering of seizure-like activity originating in the hippocampus. However, the loss of granule cells and CA1 cells results in reduced bursting activity. It has to be noted that these are first results, and further validation is required. Nonetheless, the current findings are promising and suggest the potential utility of this epileptic network model as a tool for investigating seizure suppression techniques like optogenetics.

4.6 Appendix

Mech	Value	Cell	loc	note
g_{Na}	0.09	MC	soma, proximal dendrites	
g_h	$2 \times$ 5e-6	MC, HC	all	both fast and slow
E_h	-40	MC, HC, CA1-PYR	all	
g_l	5e-5		all	1/Rm
g_{KAp}	0.0025	CA1-PYR	oriens	proximal KA
g_{KAd}	[0.0 12, 0.01, 0.015, 0.01625]	CA1-PYR	radiatum prox, med, dist and lm	distal KA
g_m	[6e-6, 3e-6]	CA1-PYR	$\sim$ axon, axon	
g_h	1e-4	CA1-PYR	all	
$V_{half,h}$	-73	CA1-PYR	all	time constant inflection point
g_{AHPK}	5e-5	CA1-PYR	radiatum dist	
g_{CagK}	0.01	CA1-PYR -BSC, CA1,3 -AAC -BC	all	
g_{Na}	0.2	CA1-BSC	all	
g_l	5e-5	OLM	all	
g_{Na}	0.0127	OLM	dendrite	
g_{KA}	0.004	OLM	dendrite	
g_{Kdr}	0.033	OLM	dendrite	
g_h	0.0005	OLM	soma	
E_K	50	OLM	all	
E_{Na}	-77	OLM	all	
E_h	0	OLM	soma	

Table 4.3: Mechanism values that deviate from the values reported in Tables S4-S9 in Cutsuridis and Poirazi (2015) [33]

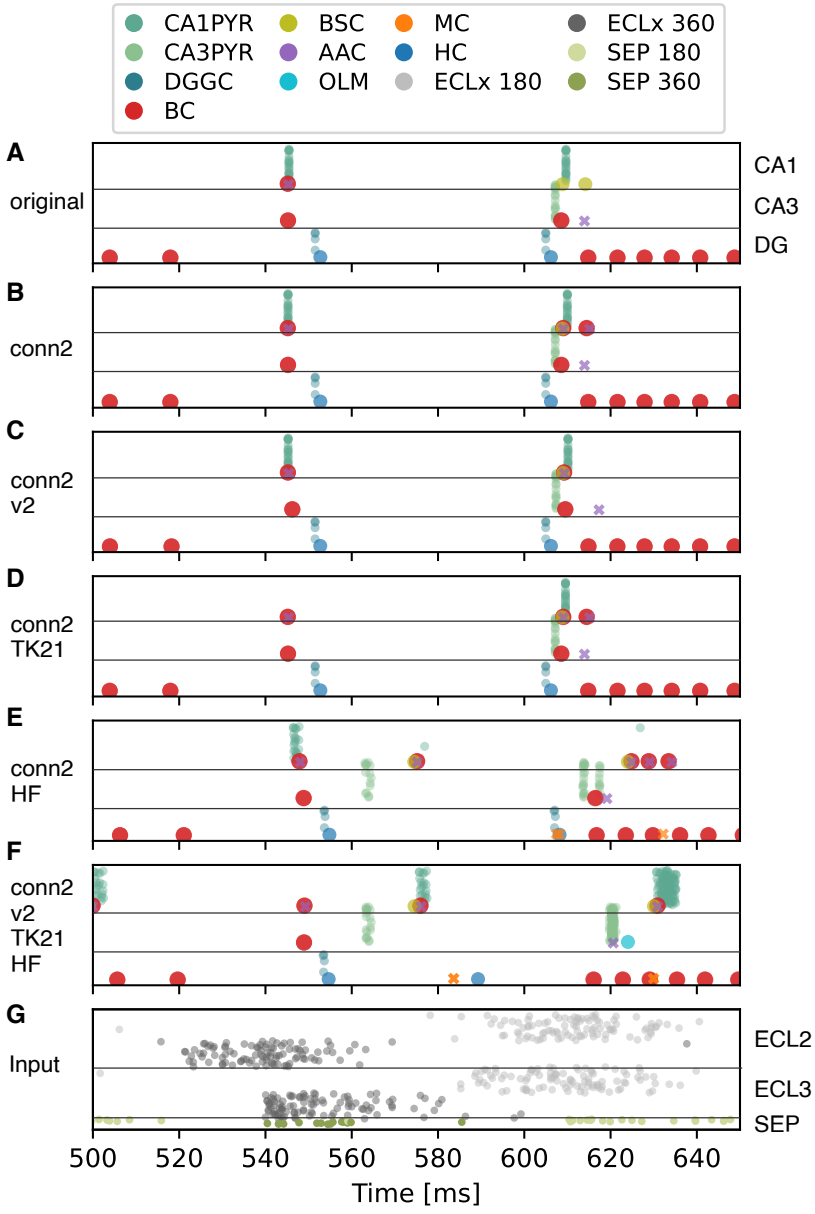

Figure 4.15: Zoom of the rastergrams given in figures 4.6.

References

[1] William O. Tatum. *Mesial Temporal Lobe Epilepsy*. Journal of Clinical Neurophysiology, 29:356–365, 10 2012.

[2] Ingmar Blümcke, Maria Thom, Eleonora Aronica, et al. *International consensus classification of hippocampal sclerosis in temporal lobe epilepsy: A Task Force report from the ILAE Commission on Diagnostic Methods*. Epilepsia, 54:1315–1329, 7 2013.

[3] Alok K. Sharma, Rachel Y. Reams, William H. Jordan, Margaret A. Miller, H. Leon Thacker, and Paul W. Snyder. *Mesial Temporal Lobe Epilepsy: Pathogenesis, Induced Rodent Models and Lesions*. Toxicologic Pathology, 35:984–999, 12 2007.

[4] Asla Pitkanen, Paul S. Buckmaster, Aristea S. Galanopoulou, and Solomon L. Moshé. *Models of Seizures and Epilepsy*. Elsevier, 2017.

[5] Wolfgang Löscher. *Animal Models of Seizures and Epilepsy: Past, Present, and Future Role for the Discovery of Antiseizure Drugs*. Neurochemical Research, 42:1873–1888, 7 2017.

[6] GRAHAM V. GODDARD. *Development of Epileptic Seizures through Brain Stimulation at Low Intensity*. Nature, 214:1020–1021, 6 1967.

[7] Elvis Cela, Amanda R. McFarlan, Andrew J. Chung, Taiji Wang, Sabrina Chierzi, Keith K. Murai, and P. Jesper Sjöström. *An Optogenetic Kindling Model of Neocortical Epilepsy*. Scientific Reports, 9:5236, 3 2019.

[8] Dan C. McIntyre and Krista L. Gilby. *Mapping seizure pathways in the temporal lobe*. Epilepsia, 49:23–30, 3 2008.

[9] A. J. Becker. *Review: Animal models of acquired epilepsy: insights into mechanisms of human epileptogenesis*. Neuropathology and Applied Neurobiology, 44:112–129, 2 2018.

[10] Elvis Cela and Per Jesper Sjöström. *Novel Optogenetic Approaches in Epilepsy Research*. Frontiers in Neuroscience, 13:947, 9 2019.

[11] Marta Rattka, Claudia Brandt, and Wolfgang Löscher. *The intrahippocampal kainate model of temporal lobe epilepsy revisited: Epileptogenesis, behavioral and cognitive alterations, pharmacological response, and hippoccampal damage in epileptic rats*. Epilepsy Research, 103:135–152, 2 2013.

[12] Anton I Ivanov and Christophe Bernard. *Chapter 18 - Hippocampus In Vitro*, pages 261–272. Academic Press, 2017.

[13] Doodipala Samba Reddy and Ramkumar Kuruba. *Experimental models of status epilepticus and neuronal injury for evaluation of therapeutic interventions*. International Journal of Molecular Sciences, 14:18284–18318, 9 2013.

[14] Makhala M Khammy, Sukhan Kim, Bo H Bentzen, Soojung Lee, Inyeong Choi, Christian Aalkjær, and Thomas A Jepps. *4-Aminopyridine: a pan voltage-gated potassium channel inhibitor that enhances K ¡sub¿v¡/sub¿ 7.4 currents and inhibits noradrenaline-mediated contraction of rat mesenteric small arteries*. British Journal of Pharmacology, 175:501–516, 2 2018.

[15] Flavio Fröhlich, Maxim Bazhenov, Vicente Iragui-Madoz, and Terrence J. Sejnowski. *Potassium Dynamics in the Epileptic Cortex: New Insights on an Old Topic*. The Neuroscientist, 14:422–433, 10 2008.

[16] Dhurgham Khudhair, Saeid Nahavandi, Hamid Garmestani, and Asim Bhatti. *Microelectrode Arrays: Architecture, Challenges and Engineering Solutions*, pages 41–59. 2017.

[17] Julian Tejada and Antonio C. Roque. *Conductance-based models and the fragmentation problem: A case study based on hippocampal CA1 pyramidal cell models and epilepsy*. Epilepsy and Behavior, 121:106841, 8 2021.

[18] Fabrice Wendling, Pascal Benquet, Fabrice Bartolomei, and Viktor Jirsa. *Computational models of epileptiform activity*. Journal of Neuroscience Methods, 260:233–251, 2 2016.

[19] Sophie Demont-Guignard, Pascal Benquet, Urs Gerber, and Fabrice Wendling. *Analysis of intracerebral EEG recordings of epileptic spikes: insights from a neural network model.* IEEE transactions on biomedical engineeringmedical engineering, 56:2782–2795, 2009.

[20] Sophie Demont-Guignard, Pascal Benquet, Urs Gerber, Arnaud Biraben, Benoit Martin, and Fabrice Wendling. *Distinct hyperexcitability mechanisms underlie fast ripples and epileptic spikes*. Annals of Neurology, 71:342–352, 3 2012.

[21] Jiannis Taxidis, Stephen Coombes, Robert Mason, and Markus R. Owen. *Modeling sharp wave-ripple complexes through a CA3-CA1 network model with chemical synapses*. Hippocampus, 22:995–1017, 2012.

[22] Viktor K. Jirsa, William C. Stacey, Pascale P. Quilichini, Anton I. Ivanov, and Christophe Bernard. *On the nature of seizure dynamics*. Brain, 137:2210–2230, 8 2014.

[23] Sebastien Naze, Christophe Bernard, and Viktor Jirsa. *Computational Modeling of Seizure Dynamics Using Coupled Neuronal Networks: Factors Shaping Epileptiform Activity*. PLOS Computational Biology, 11:e1004209, 5 2015.

[24] Kenza El Houssaini, Anton I. Ivanov, Christophe Bernard, and Viktor K. Jirsa. *Seizures, refractory status epilepticus, and depolarization block as endogenous brain activities*. Physical Review E, 91:010701, 1 2015.

[25] Damien Depannemaecker, Aitakin Ezzati, Huifang E. Wang, Viktor Jirsa, and Christophe Bernard. *From phenomenological to biophysical models of seizures*. Neurobiology of Disease, 182:106131, 6 2023.

[26] Ivan Raikov and Ivan Soltesz. *Hippocampal In Silico Models of Seizures and Epilepsy*, pages 219–232. Elsevier, 2017.

[27] Marianne J Case, Robert J Morgan, Calvin J Schneider, and Ivan Soltesz. *Computer Modeling of Epilepsy*, pages 1–18. Bethesda (MD): National Center for Biotechnology Information (US), 4 edition, 2012.

[28] Faten Mina, Arnaud Biraben, Anca Pasnicu, Pascal Benquet, and Fabrice Wendling. *Modulation of epileptic activity by deep brain stimulation: a model-based study of frequency-dependent effects*. Frontiers in Computational Neuroscience, 7:1–16, 2013.

[29] Faten Mina, Julien Modolo, Fanny Recher, Gabriel Dieuset, Arnaud Biraben, Pascal Benquet, and Fabrice Wendling. *Model-guided control of hippocampal discharges by local direct current stimulation*. Scientific Reports, 7:1–13, 2017. Printed¡br/¿Mesoscopic model (neural mass)¡br/¿investigation DC stimulation.

[30] Junsong Wang, Ernst Niebur, Jinyu Hu, and Xiaoli Li. *Suppressing epileptic activity in a neural mass model using a closed-loop proportional-integral controller*. Scientific Reports, 6:1–12, 2016.

[31] Matus Tomko, Lubica Benuskova, and Peter Jedlicka. *A new reduced-morphology model for CA1 pyramidal cells and its validation and comparison with other models using HippoUnit*. Scientific Reports, 11:7615, 4 2021.

[32] Armando Romani, Alberto Antonietti, Davide Bella, et al. *Community-based Reconstruction and Simulation of a Full-scale Model of Region CA1 of Rat Hippocampus*. bioRxiv, page 2023.05.17.541167, 1 2023.

[33] Vassilis Cutsuridis and Panayiota Poirazi. *A computational study on how theta modulated inhibition can account for the long temporal windows in the entorhinal-hippocampal loop*. Neurobiology of Learning and Memory, 120:69–83, 2015.

[34] Salvador Dura-Bernal, Benjamin A. Suter, Padraig Gleeson, Matteo Cantarelli, Adrian Quintana, Facundo Rodriguez, David J. Kedziora, George L. Chadderdon, Cliff C. Kerr, Samuel A. Neymotin, Robert A. McDougal, Michael Hines, Gordon M.G. Shepherd, and William W. Lytton. *NetpyNE, a tool for data-driven multiscale modeling of brain circuits*. eLife, 8:1–26, 2019.

[35] Nicholas T. Carnevale and Michael L. Hines. *The NEURON book*. Cambridge University Press, 2006.

[36] Sára Sáray, Christian A. Rössert, Shailesh Appukuttan, Rosanna Migliore, Paola Vitale, Carmen A. Lupascu, Luca L. Bologna, Werner Van Geit, Armando Romani, Andrew P. Davison, Eilif Muller, Tamás F. Freund, and Szabolcs Káli. *HippoUnit: A software tool for the automated testing and systematic comparison of detailed models of hippocampal neurons based on electrophysiological data*. PLOS Computational Biology, 17:e1008114, 1 2021.

[37] András Ecker, Armando Romani, Sára Sáray, Szabolcs Káli, Michele Migliore, Joanne Falck, Sigrun Lange, Audrey Mercer, Alex M. Thomson, Eilif Muller, Michael W. Reimann, and Srikanth Ramaswamy. *Data-driven integration of hippocampal CA1synaptic physiology in silico*. Hippocampus, 30:1129–1145, 11 2020.

[38] Ulrich Gärtner, Wolfgang Härtig, Kurt Brauer, Gert Brückner, and Thomas Arendt. *Immunofluorescence and immunoelectron microscopic evidence for differences in myelination of GABAergic and cholinergic septohippocampal fibres*. International Journal of Developmental Neuroscience, 19:347–352, 6 2001.

[39] Dominique Debanne, Emilie Campanac, Andrzej Bialowas, Edmond Carlier, and Gisèle Alcaraz. *Axon Physiology*. Physiological Reviews, 91:555–602, 4 2011.

[40] Mansi B. Parekh, Brian K. Rutt, Ryan Purcell, Yuanxin Chen, and Michael M. Zeineh. *Ultra-high resolution in-vivo 7.0 T structural imaging of the human hippocampus reveals the endfolial pathway*. NeuroImage, 112:1–6, 5 2015.

[41] Per Andersen, Richard Morris, David Amaral, Tim Bliss, and John O'Keefe. *The Hippocampus Book*. Oxford University Press, 2007.

[42] György Buzsáki, Costas A. Anastassiou, and Christof Koch. *The origin of extracellular fields and currents — EEG, ECoG, LFP and spikes*. Nature Reviews Neuroscience, 13:407–420, 6 2012.

[43] Harilal Parasuram, Bipin Nair, Egidio D'Angelo, Michael Hines, Giovanni Naldi, and Shyam Diwakar. *Computational modeling of single neuron extracellular electric potentials and network local field potentials using LFPsim*. Frontiers in Computational Neuroscience, 10:1–13, 2016.

[44] Mathieu Sprengers, Robrecht Raedt, Lars Emil Larsen, Jean Delbeke, Wytse Jan Wadman, Paul Boon, and Kristl Vonck. *Deep brain stimulation reduces evoked potentials with a dual time course in freely moving rats: Potential neurophysiological basis for intermittent as an alternative to continuous stimulation*. Epilepsia, 61:903–913, 5 2020.

5

Acousto-Electrophysiological Neuroimaging

In the pursuit of advancing neuromodulation modalities, the ultimate goal is the development of closed-loop systems. These systems are designed to deliver neuromodulation interventions only when necessary and in an adaptive manner. Achieving this objective depends on the acquisition of precise neural activity recordings. In the preceding chapters (chapters 2 and 3), I focused on utilizing conductance-based models to investigate the stimulation component, specifically exploring the potential applications of optogenetics.

In this chapter, I shift the focus towards the recording aspect, employing dipole models to conduct research in this domain. Specifically, I will present our work on acousto-electrophysiological neuroimaging (*A Simulation Study on High Spatio-Temporal Resolution Acousto-Electrophysiological Neuroimaging* [1]), a functional neuroimaging technique that leverages ultrasound to probe local electrophysiological activity. Within this chapter, I delve into the hypothesis suggesting that the modulation of endogenous activity onto the ultrasonic frequency (also called acousto-electric heterodyning, i.e., upconverting the low frequency electrophysiological activity to higher ultrasonic frequencies) is facilitated by mechanical vibrations relative to the recording source. The investigation in this chapter aims to shed light on the validity of this hypothesis and assess the feasibility of the technique based on this underlying mechanism.

5.1 Functional Neuroimaging

Functional neuroimaging techniques are well established in the medical world. They are used in disease diagnosis, monitoring and for signal acquisition in brain computer interfaces [2–4]. The different methods can be categorized into two groups based on the measured activity: direct electrophysiological and indirect hemodynamic [5].

Functional magnetic resonance imaging (fMRI), functional near-infrared spectroscopy (fNIRS) and positron emission tomography (PET) are modalities among the latter group. They are based on the neurovascular coupling, where changes in neuronal activity result in, for instance, altered blood flow or metabolic changes [4]. Compared to the electrophysiological measuring modalities, they have typically a better spatial resolution but a worse temporal resolution. fMRI performs best on spatial resolution. This is in the mm-range for reasonable acquisition time (1-2 s) and full brain coverage. It can even go sub-mm, however, at the cost of temporal resolution, tissue coverage or the need for complex infrastructure [6, 7]. PET has a slightly lower spatial resolution and a temporal resolution up to minutes. An important advantage of both techniques is their ability to map activity of deep regions. fNIRS is more restricted to the cortex with a maximal depth of 1-3 cm below the skull. The spatial resolution is also lower with respect to PET and fMRI, being in the upper mm-range (5-10 mm). On the other hand, the sampling rates are around 10 Hz [2, 5, 8, 9].

Electroencephalography (EEG) and Magnetoencephalography (MEG) directly and non-invasively measure the electrophysiological activity. Their spatial resolution is in general lower than that of the hemodynamic modalities. Due to the differences in electrical properties between biological tissues, such as scalp and skull, the EEG-signal strongly smears out onto a larger scalp area (>10 cm^2 [10], 3 cm^2 [11]) [12]. The differences in magnetic permeability of the tissues are negligible resulting in less dispersion. Consequently, it is argued that MEG performs better in source localization with 1 cm and 2.5 cm error for MEG and EEG, respectively [13]. On the other hand, the study of Klamer et al. (2015) [14] showed a significantly lower localization error for high-density EEG (256 channels) compared to MEG (275 channels) when individual head models were used. Thus, by using realistic models to overcome the dispersion, better localization can be obtained with EEG than with MEG for the same number of sensors [14, 15]. The electropyhsiological activity can also be measured with implanted electrode arrays. This can provide local information of a small volume of cells. Of course, they are invasive, causing tissue damage. Furthermore, electrochemical reactions can affect signal stability [5]. Finally, a less invasive approach is electrocorticography (ECoG) where electrodes are subdurally implanted. By surpassing the skull, the spatial resolution is improved with respect to EEG (5 mm) [10]. However, the coverage is restricted to the region below the electrodes [16, 17]. All these electrophysiological modalities have a superior sub-millisecond temporal resolution [13]. Furthermore, they directly measure neuronal acitivity, while there is a latency of ~ 5 s between neuronal activity and hemodynamic changes [2, 8]. Moreover, a medio-lateral shift

between hemodynamic and electrophysiological localization has been observed, as well [14].

A single technique's disadvantage could be overcome by adopting a multimodal approach. For instance, fMRI and EEG have strong complementary strengths. A hurdle, however, is the concurrent electromagnetic interference inducing artifacts [4]. On this aspect fNIRS is promising because it can be coupled with EEG, MEG or fMRI seeing it does not make use of metallic probes [8]. Although often thought as competing, also EEG and MEG provide complementary information allowing for better accuracies [12, 13].

Other important properties are cost, equipment size, and patient comfort, the latter including, portability, noise and movement freedom. Here, EEG scores the best (as well as fNIRS), making it together with its high temporal resolution an attractive and therefore highly investigated technique [5, 9].

Advances in electrophysiological source imaging (ESI) have significantly improved the localization errors of EEG. The goal is to find the underlying sources responsible for the measured EEG signal, by solving the inverse problem. This problem is strongly ill-posed due to the in theory billions of sources and only limited number of electrodes. A summary of all contributing sources to the electric field is given in [10]. A solution to this inverse problem is found by minimizing the difference between measured and calculated signals, the latter obtained by solving the forward problem. A review on the different ESI-algorithms is given in He et al. (2018) [4] and Asadzadeh et al. (2020) [18]. It has to be noted that centimeter differences in localization depending on the used ESI method exist [19, 20]. The accuracy can be improved by increasing the number of electrodes. However, the additional absolute improvement decreases with increasing number of electrodes. Also, the localization error increases with depth, while the rate drops with a higher number of electrodes [21].

The chosen forward head model strongly affects the localization accuracy, as well. It translates the activity of a source in the brain to the electrode. As aforementioned, the signals are strongly dispersed by differences in electrical properties between biological tissues. Realistic head models can improve accuracy by including anisotropy and inhomogeneity of the tissues [18, 19, 22]. Klamer et al. (2015) [14] also demonstrated a significant inter-subject variability. Consequently, a patient specific head model needs to be constructed, which can be obtained via magnetic resonance image of the head. On the other hand, this increases computational complexity preventing real-time analysis. Also the need for an MRI scan impacts the ease-of-use of EEG.

Aside from the conventional techniques discussed above, the use of ultrasound for functional neuroimaging is receiving increased attention. Functional ultrasound imaging is another hemodynamic technique with high spatial and temporal resolution (millisecond and millimeter). Although limited to two-dimensional imaging planes, transition to 4D image acquisition is being investigated [23]. Alternatively, by probing the brain with focused ultrasound (see figure 5.1 (A)), it has been hypothesized that the electrophysiological activity in the ultrasound focus will be modulated onto the ultrasound frequency. The endogenous signal can be retrieved

after demodulation. In this manner a superior spatio-temporal resolution can be obtained, where the spatial resolution depends on the size of the ultrasound focal zone (mm-range) and the temporal resolution is sub-milisecond (like with EEG). Moreover, no inverse problem needs to be solved, removing the hurdles mentioned above. Bin He (2016) [24], postulated that modulation is achieved by relative motion of the source with respect to receiver due to mechanical vibration induced by the ultrasonic field. This was tentatively called acousto-electrophyiological neuroimaging (AENI). Another possible underlying mechanism is the acousto-electric effect (AE), i.e., a pressure induced change in conductivity [25, 26].

Other research groups (Witte et al. [27], Song et al. [28], Rintoul et al. [29]) already performed in-vitro experiments, proving that the electric signal gets modulated onto the ultrasound carrier [30]. It was shown that the technique could be used for 4D ultrasound current source density imaging (UCSDI) modality [31, 32]. The spatial resolution was indeed in line with the full width at half maximum of the US-focal zone. When applied to the brain this was termed transcranial acoustoelectric brain imaging (tABI) [33, 34]. Barragan et al. (2020) confirmed that a broadband EEG-like signal from deep within the brain (40 mm) could be retrieved [34].

5.2 Simulation Study on High Spatio-Temporal Resolution AENI

The framework used to test the mechanism as stated by He (2016) [24] is described below. A quasi-static approach is adopted to model the displacement of the brain regions. I opted for a simplified solution of the problem for mathematical convenience, i.e., the head is modeled as a set of concentric spheres. Next, I elaborate on the dipole moments and their time dependent signals, important for the static interference contribution. A synthetic ultrasonic field is applied to control the influence of vibrational interference. Both are biological noise sources that interfere with the signal of interest. The former originates from the static field. The latter is due to vibrating regions not being the region of interest. Finally, the signal demodulation method, metrics and FDA limits, used to test the method's feasibility are described. The full study was performed in MATLAB R2021b.

5.2.1 Spherical Four-Layer Head Model

The head is modeled as a set of concentric homogeneous spheres, figure 5.1 (B). An analytical solution can be obtained by solving the general Poisson equation in spherical coordinates. For a current dipole with moment $I_{\max} f(t) \mathbf{d}_{\mathrm{dp}}$ on the z-axis, the induced electric potential V_l in volume l for an arbitrary point on the XZ-plane

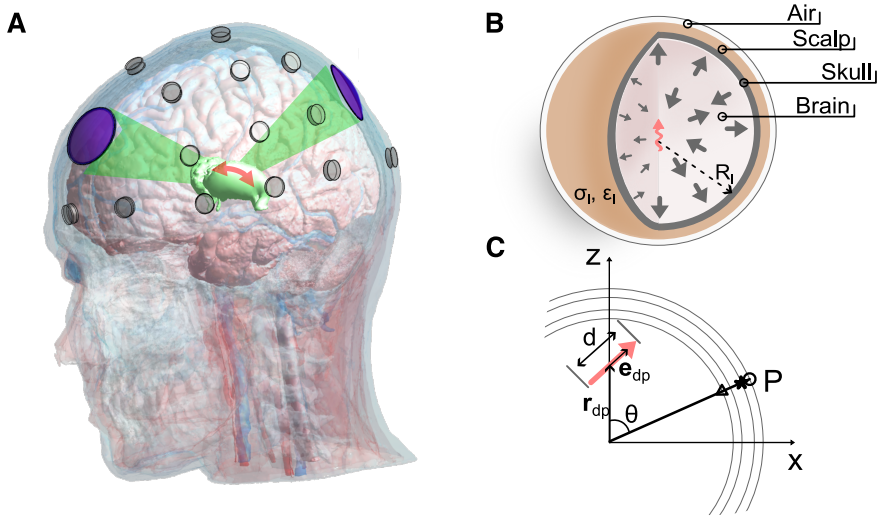

Figure 5.1: Concept of acousto-electrophysiological neuroimaging and used models **A** A highly focalized ultrasonic field is applied to the brain to mark a specific region. Mechanical vibration of the tagged region modulates the biological signal on the ultrasound's carrier frequency, spatially encoding the electrical brain activity. Demodulation of the measured EEG signal should return the marked region's activity. **B** The spherical four-layer head model, with each layer specified by its conductivity σ_l, permittivity ϵ_l and radius R_l. The electrical activity of different brain regions are represented as dipoles (arrows) with the tagged region in red. **C** Schematic of the equivalent dipole and its parameters. The potential is measured at P in the xz-plane. The circle, asterisk and triangle indicate the corresponding positions of the dry, wet and cortical electrodes.

can be determined via:

$$V_l(r,\theta,\phi=0,t) = \frac{I_{\max} f(t) \mathbf{d}_{\mathrm{dp}}}{4\pi\sigma_l} \cdot \sum_{i=1}^{\infty} \left[\left(\frac{A_{l,i}}{r^{i+1}} + B_{l,i} r^i \right) \right. \\ \left. \left(P_i^0 \left(\cos(\theta)\right) \mathbf{e}_r - P_i^1 \left(\cos(\theta)\right) \cos(\phi=0) \mathbf{e}_t \right) \right] \tag{5.1}$$

where σ_l is the conductivity of volume l. r, θ and ϕ are spherical coordinates. The terms $P_i^0 \left(\cos(\theta)\right) \mathbf{e}_r$ and $P_i^1 \left(\cos(\theta)\right) \cos(\phi) \mathbf{e}_t$ correspond to radial and tangential components of the dipole, respectively, with $\mathbf{e}_t = \mathbf{e}_\theta$ for a point in the XZ-plane, and P_i^0 and P_i^1 the associated Legendre polynomial of zeroth and first order [35, 36]. For an arbitrarily located dipole, the electric potential can be calculated using equation (5.1) after linear transformation of the dipole onto the z-axis. Equivalently, it is determined by splitting the dipole moment in a radial and tangential component

in the plane defined by the dipole location and measuring point vectors. Here, $\theta = \cos^{-1}\left(\mathbf{r}_{\mathrm{dp}} \cdot \mathbf{r}_{\mathrm{POI}} / \left(|\mathbf{r}_{\mathrm{dp}}||\mathbf{r}_{\mathrm{POI}}|\right)\right)$ and $\mathbf{e}_t = \left(\mathbf{r}_{\mathrm{dp}} \times \mathbf{r}_{\mathrm{POI}}\right) \times \mathbf{r}_{\mathrm{dp}} / \left(|\mathbf{r}_{\mathrm{dp}}|^2 |\mathbf{r}_{\mathrm{POI}}|\right)$, with $\mathbf{r}_{\mathrm{dp}}$ and $\mathbf{r}_{\mathrm{POI}}$ the location of the dipole and measuring point, respectively (see below) [36]. The Condon-Shortley phase is included in calculating the associated Legendre polynomials, explaining the minus sign between radial and tangential dipole terms (unlike in Arthur and Geselowitz (1970) [35]).

Three electrode types are of interest, i.e., cortical, and wet and dry scalp electrodes. Although, no actual electrodes are modeled, these types can be associated with different positions in the head. Therefore, the model consists of four concentric shells, each defined by an outer radius R_l. From inside to outside: the first is brain matter, followed by the skull, next the scalp and finally a layer of air. For the cortical electrode, the point of interest is at the brain skull boundary (R_{brain}). The wet scalp measurement occurs at the scalp air boundary (R_{scalp}). The dry scalp is inside the air shell (R_{air}). Under the following conditions, a solution for equation (5.1) can be found.

$$\begin{aligned} V_l &= V_{l+1} \\ \sigma_l \frac{\partial V_l}{\partial r} &= \sigma_{l+1} \frac{\partial V_{l+1}}{\partial r} \\ V_l(r) &\to 0 \ \text{ for } \ r \to \infty \end{aligned} \tag{5.2}$$

Due to the interest in multiple radial positions, the solution to equation (5.1) cannot be simplified. Therefore, it is not depicted here but the complete set of equations to be solved can be found in section 5.6.2. The radius of each shell can be found in table 5.1 [22]. The number of terms included in the numerical simulation in equation (5.1) is regulated by an absolute and relative tolerance, i.e., 10^{-13} and 10^{-10}, respectively, limited by a maximum of 5000 terms.

5.2.2 The Dipole Moment

The dipole model was already described in section 1.3.2. For the reader's convenience the description is repeated here. EEG response is caused by extracellular neuron currents in response to transmembrane currents, also known as secondary return, or volume currents. These currents can be modeled by a multipole expansion [3, 22]. However, typically only the first order expansion is used, i.e., the current dipole. Here, it represents the activity of a small volume of parallel neurons [3, 22, 35, 36]. The dipole is characterized by: its position ($\mathbf{r}_{\mathrm{dp}} = [x, y, z]$, halfway between the current source and sink), its orientation (defined by unit vector $\mathbf{e}_{\mathrm{dp}}$), the current intensity (I) and distance between the monopoles (d), see figure 5.1 (C). The dipole moment density is then:

$$\begin{aligned} \mathbf{d}(\mathbf{r}_{\mathrm{dp}}) &= I\, \mathbf{d}_{\mathrm{dp}}(\mathbf{r}_{\mathrm{dp}}) \\ \text{with } \ \mathbf{d}_{\mathrm{dp}} &= d\, \delta^3(\mathbf{r}_{\mathrm{dp}})\, \mathbf{e}_{\mathrm{dp}} \end{aligned} \tag{5.3}$$

and δ the Dirac delta. Unless otherwise specified, the dipoles are radially oriented (i.e., $\mathbf{e}_{\mathrm{dp}} = \mathbf{e}_r$). Moreover, they are uniformly distributed on n (= 3, 5 or 10)

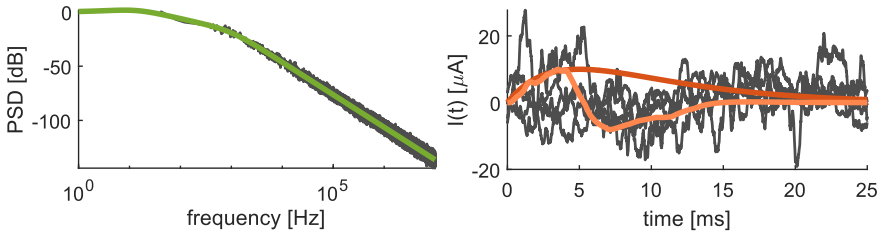

Figure 5.2: The time dependent current intensities of the different dipoles. Left, the power spectral density (PSD) profile from which the time signals are reconstructed (green line without noise). Right, the time dependent signals, with red and orange (i.e., respectively, alpha-function and alpha-train) the time signal of the tagged dipole and the gray lines the signal of the background dipoles derived from the PSD-profile on the left.

concentric spheres in the brain. The layers are equidistant, with the most outer layer at $R_{\mathrm{dp,max}}$, and have the same dipole densities.

The current intensity varies over time. An appropriate time dependent signal needs to be chosen to obtain an estimate of the noise level at the ultrasonic frequency (f_{us}). The time dependent signals of any dipole not being the dipole of interest is derived from a power spectrum density profile:

$$\mathrm{PSD}(f) = \frac{1 + f/(\zeta f_1)}{\prod_{i=1}^{N_{\mathrm{f}}} \left(1 + (f/f_i)^{\alpha_i}\right)} \tag{5.4}$$

with f_i the ith cut-off frequency, α_i the attenuation coefficient and $N_{\mathrm{f}} = 2$ or 3, for the vibrational and static interference analysis, respectively. ζ is randomly chosen between [0.3, 1]. Consequently, the PSD reaches a maximum between ζf_1 and f_1. Extra noise is added to increase the variance amongst the dipoles. This is drawn from $\log \mathcal{N}(0, 0.5)$. The time varying current intensity is then obtained via:

$$I(t) = I_{\max}\, \mathcal{F}^{-1}\left(\sqrt{\mathrm{PSD}\left(|f|\right)}\, \exp(i\Phi(f))\right) = I_{\max}\, f(t) \tag{5.5}$$

with $\Phi(f)$ an odd function of random phases, i the imaginary unit and $\mathcal{F}^{-1}$ the inverse Fourier transform. The maximum current intensities are drawn from $\mathcal{N}(I_{\mathrm{DOI}}, 3)$ uA. The parameter values are summarized in table 5.1. The time signal for the dipole of interest (DOI, see section 5.2.3) follows an alpha-function (equation (5.7)) or if explicitly specified an alpha-train (equation (5.8)).

$$g(t, \tau) = \frac{t}{\tau} \exp\left(1 - \frac{t}{\tau}\right) \Theta\left(t\right) \tag{5.6}$$

$$I_{\mathrm{DOI}}(t) = I_{\mathrm{DOI}}\, g(t, \tau = 5\,\mathrm{ms}) \tag{5.7}$$

or

$$I_{\mathrm{DOI}}(t) = I_{\mathrm{DOI}} \sum_{i=1}^{100} B_i\, g\left(t - t_{0,i}, \tau_i\right) \tag{5.8}$$

Head Model			**Dipoles**	
	H	M		
R_{brain} [mm]	70	4.6	$\mathbf{e}_{\text{dp,DOI}}$	[0,0,1]
R_{skull} [mm]	75	5.2	$\mathbf{r}_{\text{dp,DOI}}$	[0,0,0 or $R_{\text{dp,max}}$]
R_{scalp} [mm]	82	5.9	I_{DOI} [μA]	10
R_{air} [mm]	87	6.9	d [mm]	0.5
$R_{\text{dp,max}}$ [mm]	65	4.1	f_1 [Hz]	14
σ_{brain} [S/m]	0.33		f_2 [Hz]	10^3
σ_{skull} [S/m]	0.0132		f_3 [Hz]	10^4
σ_{scalp} [S/m]	0.33		$\alpha_{1,2}$	2
σ_{air} [S/m]	$5.5606\ 10^{-6}$		α_3	10
Electrode positions			**Ultrasound**	
POI_1	[1,0,0]		f_{us} [Hz]	10^6
POI_2	[0,0,1]		$\mathbf{v}_{\text{us}}$	[0,0,1]
POI_3	[0,1,0]		f_{band} [Hz]	$2 \cdot 10^3$
POI_4	$\mathbf{e}_{\text{dp,DOI}}$		T_{sim} [ms]	25
POI_5	[1,1,1]		Z_{ac} [Pa s/m]	$1.5 \cdot 10^6$

Table 5.1: Summary of all parameters values used in the AENI simulations. Unless otherwise specified, these values are used in each simulation. (H = Human, M = Mouse)

with τ_i drawn from $\mathcal{N}(2, 0.2)$ ms, $t_{0,i}$ from $|\mathcal{N}(0, 6.5)|$ ms and B_i from $\mathcal{N}(0, 1.5)$. $\Theta(t)$ is the Heaviside step function. Furthermore, B_i is normalized with respect to the largest absolute B_i value. The maximum dipole moment of the DOI is set to 5 nAm, after the synchronous activity of 10^4 neurons with a single dipole moment of 0.5 pAm. With a $d = 500\ \mu\text{m}$, this results in a $I_{\text{DOI}} = 10\ \mu\text{A}$ [37, 38]. An example of the applied current intensities is shown in figure 5.2.

5.2.3 Ultrasonic Field

Application of the ultrasonic field causes brain regions to move with respect to the EEG-electrodes. A synthetic ultrasonic field is used to provide more control of the displacement field distribution.

$$A(\mathbf{r}) = A_{\max} \exp\left(-\frac{|\mathbf{r} - \mathbf{r}_{\text{dp,DOI}}|}{\kappa}\right) \tag{5.9}$$

with κ the spatial constant in mm. Here, the displacement vector is always in the z-direction. Therefore, $\mathbf{r}_{\text{dp}}(t) = \mathbf{r}_{\text{dp},0} - A\left(\mathbf{r}_{\text{dp},0}\right) \sin\left(2\pi f_{\text{us}} t\right) \mathbf{e}_z$, with $\mathbf{r}_{\text{dp},0} = \mathbf{r}_{\text{dp}}(t = 0)$. The field and effect of κ is illustrated in figure 5.3. The dipole of interest (DOI) is the dipole at the location ($\mathbf{r}_{\text{dp,DOI}}$) where the displacement is maximal ($A_{\max}$). This is the tagged region.

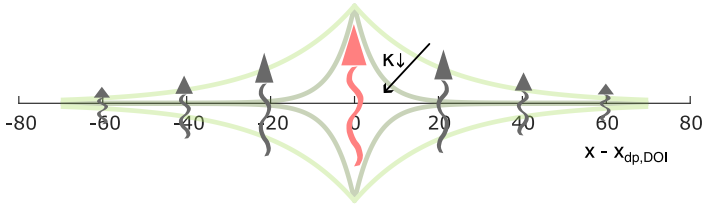

Figure 5.3: The one dimensional applied displacement field for decreasing values of the spatial constant κ.

5.2.4 Quasi-Static Electromagnetic Field

Given the displacement of current dipoles, the conventional static solution for the forward EEG problem will not suffice. A quasi-static electromagnetic field approximation is selected. The decision is based on an order of magnitude analysis using the Liénard-Wiechert fields (see section 5.6.1). The analysis showed that quasi-static electric potential contributions dominate all relativistic components (i.e., due to the Doppler effect, source acceleration and finite propagation speed of light) for an angular ultrasonic frequency:

$$\omega_{\mathrm{us}} \ll 20.58/d_{\mathrm{dp,POI}}\,\mathrm{GHz} \tag{5.10}$$

with $d_{\mathrm{dp,POI}}$ the distance between observer and oscillating source in cm. Under quasi-static assumptions, the induced electric potential (ψ) for a displacement in the z-direction is:

$$\psi(x,y,z,t) = V(x,y,z - A\sin(\omega_{\mathrm{us}}t),t) \tag{5.11}$$

with A the displacement amplitude, ω_{us} the angular ultrasonic frequency and V the induced electric potential in the reference frame of the source. A Taylor series for $\mathrm{A} \ll 1$ yields:

$$\psi = V - A\sin(\omega_{\mathrm{us}}t)\frac{\partial V}{\partial z} + \mathcal{O}(A^2) \tag{5.12}$$

Consequently, given the Fourier transformation:

$$\begin{aligned}\Psi &= I_{\max}\widehat{f}(\omega)G \\ &\quad - i\frac{AI_{\max}}{2}\left(\widehat{f}(\omega+\omega_{\mathrm{us}}) - \widehat{f}(\omega-\omega_{\mathrm{us}})\right)\frac{\partial G}{\partial z} + \mathcal{O}(A^2)\end{aligned} \tag{5.13}$$

with separation of variables: $V\,(x,y,z,t) = I_{\max}f(t)G(x,y,z)$, it is clear from the second term that the measured signal (ψ) contains the information of the source ($f(t)$) near the applied ultrasonic frequency, with $\widehat{f}(\omega) = \mathcal{F}\,(f(t))$. In other words, it is modulated onto f_{us}. ψ is obtained by evaluating equation (5.1) over a time period T_{sim} with a sampling frequency of $20f_{\mathrm{us}}$.

5.2.5 Signal Processing

The electric potential is measured at 5 locations or positions of interest (POIs). The POIs are defined as the location vector connecting the origin and the measurement point (see table 5.1). Two additional POIs are included as well: mPOI and mPSO. The former being the mean of all POIs, the latter is the mean of POIs that received DOI's signal within the same order of magnitude of the highest received signal. Depending on the electrode type of interest (see section 5.2.1), the POI is then located at $R_l \cdot \mathrm{POI}_i/|\mathrm{POI}_i|$. Subsequently, the signal at $f_{\mathrm{us}} \pm f_{\mathrm{band}}/2$ is demodulated following (figure 5.4):

1. Fourier transform: $\psi\left(POI_i, t\right) \rightarrow \Psi\left(POI_i, f\right)$
2. bandpass filter ($f_{\mathrm{us}} \pm f_{\mathrm{band}}/2$) followed by demodulation to baseband
3. zero order detrend, i.e., subtracting mean from real and imaginary parts.
4. compensate for phase shift due to sine (see equation (5.13))
5. inverse Fourier transform

Normalization of the obtained signal results in:

$$\tilde{f}(t) = f(t) + \epsilon(t) \tag{5.14}$$

where $f(t)$ is the normalized time varying current intensity (see equation (5.5)) and $\epsilon(t)$ the error due to interference of other dipoles. Finally, the root mean square error (RMSE), with respect to the input signal is determined, to asses the reconstruction accuracy.

$$\mathrm{RMSE} = \sqrt{\frac{1}{T_{\mathrm{sim}}} \int_0^{T_{\mathrm{sim}}} \epsilon^2(t)} \tag{5.15}$$

A titration process is used to determine the thresholds of the displacement amplitude $A_{\max}$ and spatial constant κ to obtain a given RMSE-value. This process adopts the bisection method where the midpoint is the logarithmic mean of the interval $[a, b]$ (i.e., $\log_{10} c = (\log_{10} a + \log_{10} b)/2$). At the start $b/a = 10$. To limit computation time only a max of 5 iterations are evaluated.

Due to the interest of the signal at $f_{\mathrm{us}} \pm f_{\mathrm{band}}/2$, the used conductivities in equation (5.1) are the modulus of the complex conductivities ($\tilde{\sigma_l}$) near f_{us}. At f_{us}, the capacitive effects are negligible for the brain, skull and scalp conductivities. Therefore, $|\tilde{\sigma}_l| \approx \sigma_l$. In the air layer, on the other hand, capacitive effects dominate, resulting in $|\tilde{\sigma}_{\mathrm{air}}| \approx 2\pi f_{\mathrm{us}} \epsilon_{\mathrm{air}}$ with ϵ_{air} the permittivity of air. The values are summarized in table 5.1, taken from the IT'IS database [39].

5.2.6 FDA Limits

The FDA limits are used to asses the methods feasibility [40].

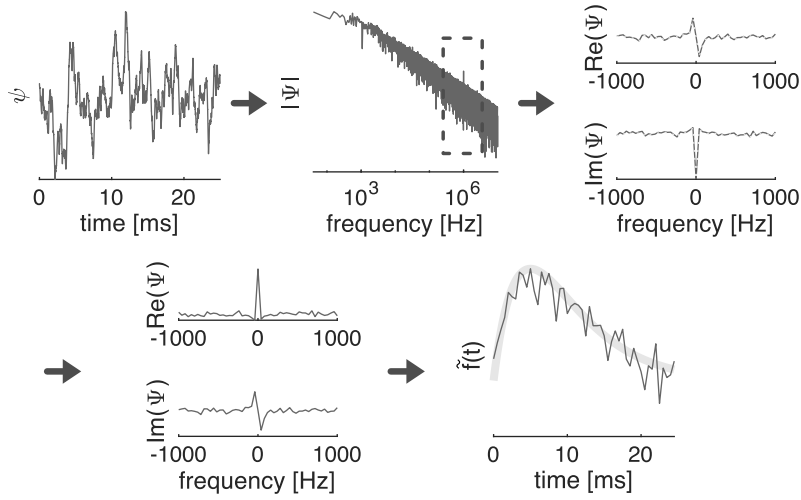

Figure 5.4: The signal demodulation protocol. From left to right: Fourier transform, band-pass filter and demodulation to baseband, zero order detrend followed by phase shift correction and finally inverse Fourier transform.

- Pulsed average intensity:

$$I_{\mathrm{pa}} = Z_{\mathrm{ac}} A^2 \omega_{\mathrm{us}}^2 / 2 < 190\,\mathrm{W/cm^2}$$

- Temporal average intensity:

$$I_{\mathrm{ta}} = \mathrm{dc}\; I_{\mathrm{pa}} < 720\,\mathrm{mW/cm^2}$$

- Mechanical index:

$$\begin{aligned}\mathrm{MI}[-] &= \mathrm{PNP}[\mathrm{MPa}]/\sqrt{f_{\mathrm{us}}[\mathrm{MHz}]} \\ &= 2\pi Z_{\mathrm{ac}} A[\mathrm{Pa\,s}]\sqrt{f_{\mathrm{us}}[\mathrm{MHz}]} < 1.9\end{aligned}$$

with Z_{ac} the specific acoustic impedance, PNP the peak negative pressure in [MPa] and dc the duty cycle. Here, a plane wave approximation is applied in the focus ($p_{\mathrm{us}}/v_{\mathrm{us}} = Z_{\mathrm{ac}}$), which is valid under the assumption of a small transducer convergence angle [41].

5.3 Results

Below the results of this simulation study are shown. First the measurable signal strength of a single dipole is investigated. This led to a preferred displacement direction and dipole orientation combination that is further maintained in following

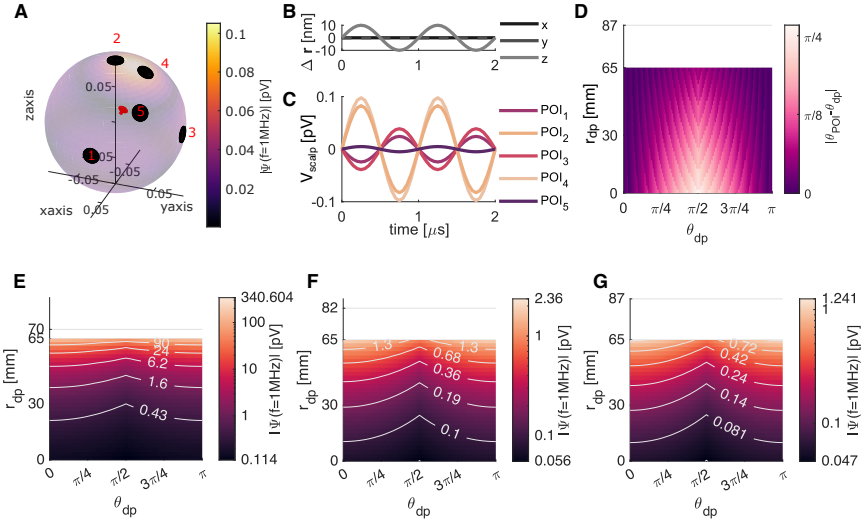

Figure 5.5: Measurable signal strength for a single dipole with constant dipole moment of 5 nAm. The dipole is located in the yz-plane, and is moved radially (r_{dp}) and with changing co-elevation (θ_{dp}). **A** Distribution of the amplitude of the f_{us} component measurable at the scalp-air interface (R_{scalp}). The tagged dipole is indicated by a red arrow. The point of interests (POIs) are displayed by black discs. **B** The displacement of the tagged dipole. x and y do overlap at 0 nm. **C** The signal measured at the different POI-locations as indicated in **A** for two periods of the ultrasonic wave. POI_4 has the highest amplitude. **D** The absolute difference between co-elevation of optimal POI location (θ_{POI}, i.e., point where highest signal amplitude is measured) and θ_{dp}. **E**, **F** and **G** The signal strength at the optimal POI for POIs at the cortex (R_{brain}), the scalp (R_{scalp}) and with extra air-layer (R_{air}), respectively. The gray horizontal line indicates the radial location of the POI.

subsections. Next, two different interference sources are addressed. The vibrational interference is investigated followed by the static interference. Finally, the importance of the imposed reconstruction accuracy and dipole current waveform is analyzed.

5.3.1 Measurable Signal Strength of Single Vibrating Dipole

The relationship between dipole position ($\mathbf{r}_{\mathrm{dp}}$), orientation ($\mathbf{e}_{\mathrm{dp}}$), measurement position (POI) and displacement direction ($\mathbf{e}_{\mathrm{z}}$) is investigated first. A single dipole is used, with a constant dipole moment of 5 nAm. The dipole is moved radially (r_{dp}) from 0 to $R_{\mathrm{dp,max}}$. Moreover, it is rotated in the yz-plane for a varying polar angle (θ_{dp}) from 0 to π radians. At each position, the dipole is oriented radially

outwards ($\mathbf{e}_{\mathrm{dp}} = \mathbf{e}_{\mathrm{r}}$). The displacement amplitude ($A_{\max}$) is 10 nm. The results are shown in figure 5.5.

For a dipole at $r_{\mathrm{dp}} = 20$ mm and $\theta_{\mathrm{dp}} = \tan^{-1}(1/2)$, the signal strength measurable at the scalp is shown in figure 5.5 (A). Here signal strength denotes the magnitude of the measured signal's frequency component at f_{us} (i.e., $|\Psi(f = 1\ \mathrm{MHz})|$). A hotspot between POI_2 and POI_4 can be observed. The signal strength does not monotonically decrease away from the hotspot. This is highlighted in figure 5.5 (C), where the signal at POI_5, although closer to the hotspot, is lower than that at POIs 1 and 3. Furthermore, a clear oscillation of the signal can be seen at each POI. The oscillation is either in phase or antiphase with the ultrasonic displacement and has a period equal to $1/f_{\mathrm{us}}$. For this setup, the maximal signal amplitude is only 0.1 pV.

For aforementioned dipole positions, the center of the hotspot is located in the yz-plane. The optimal polar angle (θ_{POI}) depends both on r_{dp} and θ_{dp}, as can be seen in figure 5.5 (D). When the dipole is close to the center, the optimal angle is between the dipole's orientation and the displacement direction. At the center itself, this is the mean vector of both directions. On the other hand for a dipole closer to the outer surface, the optimal θ_{POI} is closer or equal to θ_{dp}.

The maximal signal strengths measurable at the cortex, scalp or with an extra 5 mm thick air layer are shown in figures 5.5 (E), (F) and (G), respectively. As expected, the highest signals are measured with POIs at the cortex level (R_{cortex}), while the lowest are measured with POIs in the air layer (R_{air}, the dry electrode). The absolute maximum is 340.604 pV while the minimum is only 0.047 pV. For a cortical electrode, there is a three orders of magnitude difference between the lowest and highest measurable signal strengths. At the scalp (R_{scalp}), this reduces to a difference of a factor 40. The lowest measured signal is half the one measured at the cortex. This while the maximum is more than a 100 times lower. The extra air layer reduces the maximum further with a factor 2, while the minimum is only reduced with 16%. For $\theta_{\mathrm{dp}} = 0$, introduction of the skull and scalp (and air) layer results in a signal reduction of 68% and 30% (11% and 7%) for a fixed distance of 22 mm and 70 mm with respect to the measuring electrodes, respectively. This slightly increases to 70% and 36% (11% and 9%) when the dipole orientation is perpendicular to the vibration direction. For all electrode setups, the minimum is for a dipole at the center with an orientation perpendicular to the displacement direction. The absolute maximum is found near the surface ($r_{\mathrm{dp}} = R_{\mathrm{dp,max}}$) and for a $\theta_{\mathrm{dp}} = 0$. Consequently, maximal signal strength is obtained when the dipole orientation, displacement direction and POI position are perfectly aligned.

5.3.2 Vibrational Interference

The applied ultrasonic waves propagate through the whole brain. A spatially distributed displacement field arises. In the focus, the displacement is maximal. The dipole located at this maximum is called the tagged region or dipole of interest (DOI). Although lower in amplitude, the dipoles outside the focus will vibrate as well. This will induce some interference on the signal of interest, as also these

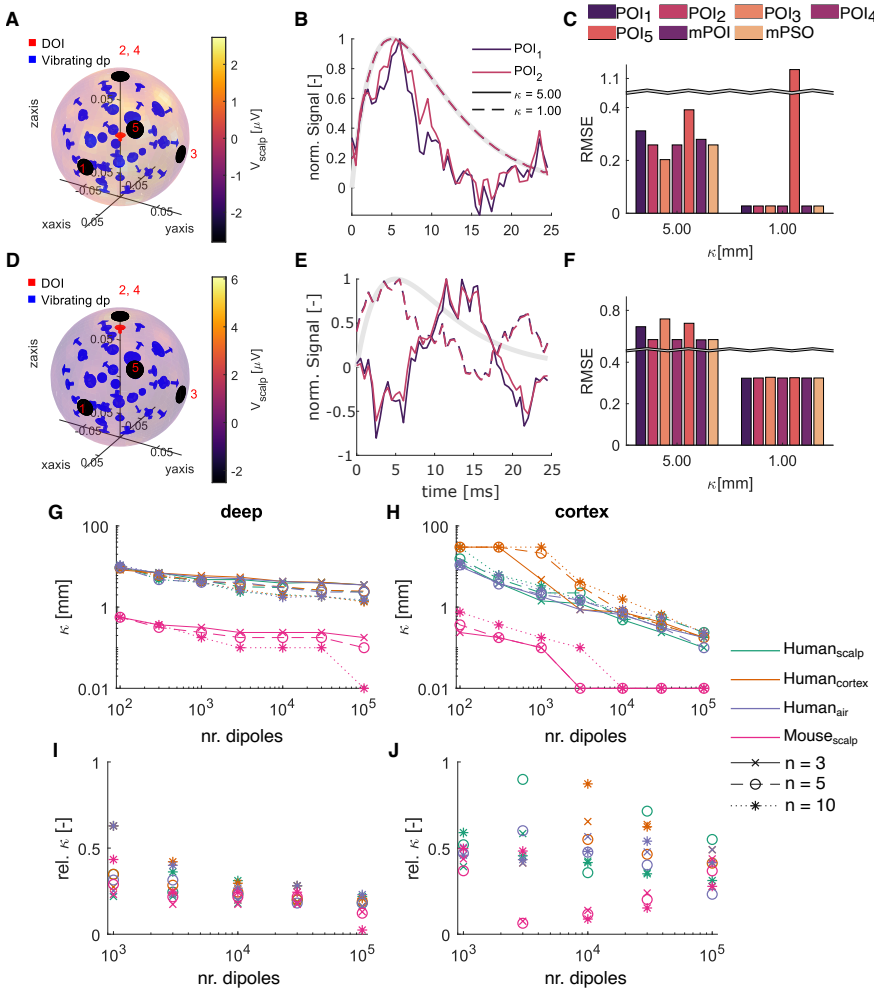

Figure 5.6: The effect of the displacement field's spatial constant (κ) on vibrational interference and reconstructed signal quality. **A** Simulation setup for dipole of interest (DOI) at the center (deep) indicated by a red arrow. Blue arrows are the surrounding dipoles responsible for the vibrational interference. The POIs are indicated by black discs. The color code indicates the actual measured potential at a single time point. **B** The demodulated signal measured at indicated POIs for different spatial constants. The applied current intensity to the DOI is shown in gray. **C** The root mean square error (RMSE) of the demodulated signals measured at indicated POIs. mPOI, demodulation after the mean of the signals at the five POIs is taken first. mPSO, the mean of POIs with same order of magnitude before demodulation.

Figure 5.6: **D** Simulation setup for DOI at r_{dp} = 65 mm (cortex). **E** and **F** Similar to **B** and **C**, respectively, but for DOI at the cortex. **G** and **H** The required spatial constant to get an RMSE of 5% on at least one POI for indicated models and number of dipole layers (n) with increasing number of surrounding dipoles, for a deep and cortex DOI, respectively. **I** and **J** The required relative spatial constant, i.e., κ divided by the distance between DOI and its nearest neighbor. In **B**, **C**, **E** and **F** The result shown is for 10^5 dipoles and n = 3 layers, measured in the human scalp setup. To remove static interference, a PSD with three cut-off frequencies is used for the surrounding dipoles current intensity.

signals will be modulated onto f_{us}. This type of interference is called vibrational interference. Moreover, the displacement field linearly scales with the transducer outputs. As such, only the displacement field profile itself is of importance for the vibrational interference generated by the surrounding dipoles. A synthetic displacement field is used, see equation (5.9). Manipulation of the spatial constant κ allows for the investigation of the displacement field decay. The used PSD, see equation (5.4), for the surrounding dipoles consists of three cut-off frequencies with attenuation factors $\alpha_{1,2} = 2$ and $\alpha_3 = 10$. This to remove static interference (see section 5.3.3).

The results of the κ analysis are shown in figure 5.6. For a DOI at the center (see figure 5.6 (A)), reducing κ to 1 mm results in almost perfect reconstruction of the input signal (see figure 5.6 (B)). Also for $\kappa = 5$ mm, resemblance to the input signal is observed. In case of the cortex DOI (DOI at $R_{\mathrm{dp,max}}$, see figure 5.6 (D)), no and rather small resemblance between input signal and reconstructed is observed for $\kappa = 5$ and 1 mm, respectively. This is reflected in the RMSE as depicted in figures 5.6 (C) and (F). The RMSE is below 3% at almost all POIs for a deep DOI and $\kappa = 1$ mm. This increases to values between 20 and 40% for a $\kappa = 5$ mm. It increases above 60% for a cortex DOI (κ = 5 mm), with only values of 30% for $\kappa = 1$ mm. Also a difference in optimal POI position can be observed, for the deep DOI the optimal is POI_3 and the worst is POI_5. While the best POI for the cortex DOI is POI_2 (equal to POI_4). This being in agreement with the conclusion from section 5.3.1. Inclusion of the artificial POIs, mPOI and mPSO, does not result in significant improvement. It is clear that even smaller κ is required for the signal of interest to be higher than the vibrational interference, in case of the cortex DOI.

The required κ to get on at least one POI an RMSE $\leq 5\%$ is shown in figures 5.6 (G) and (H), for a deep and cortex DOI, respectively. It can be noted that the measurement position, i.e. at the scalp, cortex or air, has little to no effect on the required κ for the deep DOI in the human head model. In case of the mouse model this is one order of magnitude lower. For a cortex DOI, in comparison with a deep DOI, a higher κ is acceptable for a relatively small number of dipoles. However, κ drops more quickly with increasing number of dipoles. The number of layers (n) has a clear influence in case of the deep DOI, as well. With a higher number of layers, a lower κ is required for all model setups. For the cortex dipole, this is overall opposite with a lower required κ for the lowest amount of layers.

nr. layers (n)	**3**		**5**		**10**	
POI | DOI	deep	cortex	deep	cortex	deep	cortex
$\text{human}_{\text{scalp}}$	1.76	0.050	1.176	0.119	0.711	0.089
$\text{human}_{\text{cortex}}$	1.758	0.089	1.236	0.089	0.676	0.119
$\text{human}_{\text{air}}$	1.758	0.089	1.176	0.050	0.748	0.119
$\text{mouse}_{\text{scalp}}$	0.089	0.005	0.050	0.005	0.005	0.005

Table 5.2: Used spatial constants (κ) in displacement amplitude simulations. Half of κ to get RMSE of 5% for 10^5 dipoles.

A slightly decreasing and no clear trend can be observed for the relative κ shown in figure 5.6 (I) and (J), respectively. Here, relative κ (rel. κ) equals to κ divided by the distance between DOI and its nearest neighbor. For the deep dipole, the layer, and human versus mouse models differentiation disappears. From these relative κ plots, it is clear that the most important factor defining the required spatial constant is the distance between the DOI and its nearest neighbor. The mouse model is smaller. Therefore, for a same number of dipoles, it is more densely packed than the human models. The difference, for a changing number of dipole layers, between the deep and cortex DOI plots can be explained by this, as well. The n layers are distributed equidistant from 0 to $R_{\text{dp,max}}$ (0 excluded). In case of the deep DOI and for a higher n, the closest neighbor is thus much closer than for a lower n. As a result, the required κ decreases with n for a deep dipole. In contrast, for a cortex dipole, the κ-threshold tends to increase with n, because the dipoles are uniformly distributed onto these layers. For a fixed number of dipoles, each layer will thus be occupied more in case of low layer count, reducing the distance between the DOI and the nearest neighbor on the same layer. The sudden drop between 10^3 and 10^4 dipoles indicates the shift from nearest neighbor on another layer to the same layer. The strong decreasing trend for a cortex dipole is thus explained by the decreasing distance to the nearest neighbor at the same layer. This while in case of the deep DOI (figure 5.6 (G)), the slight decrease is due to combined contribution of all vibrating dipoles because the distance to the nearest neighbor, located at the next layer, is fixed.

5.3.3 Static Interference

A second type of interference originates from the electrical activity in the brain itself. This is called the static interference. Because the EEG energy at MHz-range is not known, the applied current intensities to the dipoles are based on a power-law power spectral density, see equation (5.4). Unlike in the previous section, the PSD only consist of two cut-off frequencies. For $\alpha_2 = 2$, this results in a drop of 110 dB at $f = 1$ MHz, with respect to DC (f = 0 Hz). To minimize the vibrational interfer-

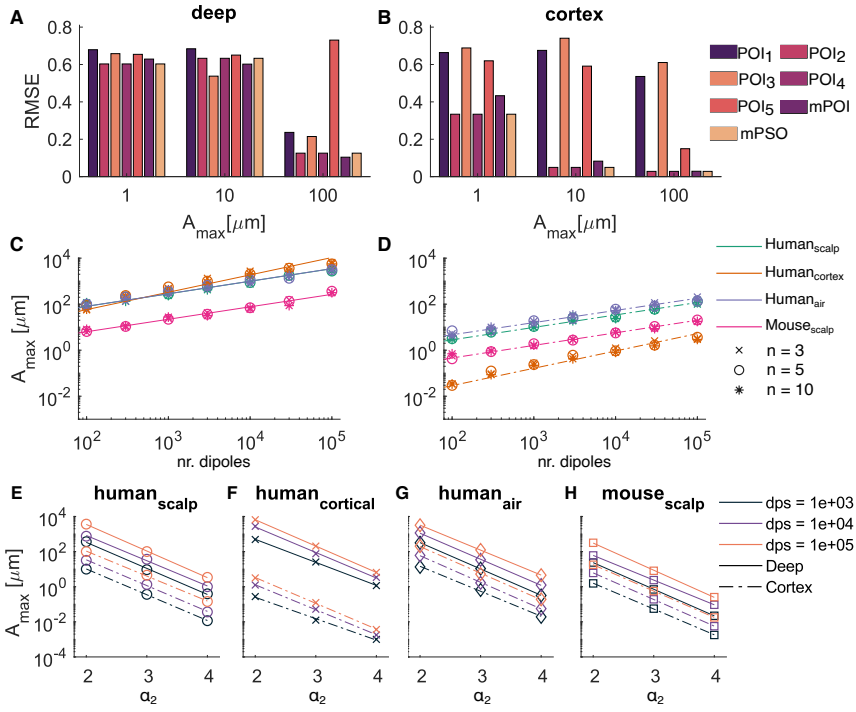

Figure 5.7: Analysis of the necessary displacement amplitude (A_{max}) to overcome the static interference. **A** and **B** The root mean square error (RMSE) between target and demodulated signal measured at indicated POIs with different A_{max}, for deep and cortex DOI, respectively (n = 3 layers and nr. of dipoles dps = 10^5, measured in human scalp setup). mPOI, demodulation after the mean of the signals at the five POIs is taken first. mPSO, the mean of POIs with same order of magnitude before demodulation. **C** The required A_{max} to obtain an RMSE of 5% on at least one POI for indicated models and number of dipole layers (n) with increasing number of surrounding dipoles. Results are for a deep DOI. **D** DOI at the cortex. The plotted lines indicate the linear regression for each model and POI position combination. **E**, **F**, **G** and **H** Effect of the second attenuation coefficient (α_2) on the required A_{max} (n = 3 dipole layers). The used model and electrode position is shown in the title.

ence, half of the required κ to achieve an RMSE of 5% with 10^5 dipoles is used. The values are summarized in table 5.2. Increasing the displacement amplitude ($A_{\max}$) increases the signal-to-noise ratio with respect to the static interference. The results of the $A_{\max}$ analysis are shown in figure 5.7.

The RMSE of the reconstructed signals obtained at the different POIs for the human scalp setup, are shown in figures 5.7 (A) and (B). As expected, with increasing $A_{\max}$, the RMSE drops at almost all POI positions. POI_2 is the best location,

nr. dipoles		**1000**		**10000**		**100000**	
DOI	POI	α_2	$-L_{\mathrm{P}}$	α_2	$-L_{\mathrm{P}}$	α_2	$-L_{\mathrm{P}}$
deep	$\mathrm{human}_{\mathrm{scalp}}$	4.58	184	4.93	194	5.20	202
	$\mathrm{human}_{\mathrm{cortex}}$	5.05	198	5.24	203	5.41	209
	$\mathrm{human}_{\mathrm{air}}$	4.54	183	4.93	194	5.38	208
	$\mathrm{mouse}_{\mathrm{scalp}}$	3.76	159	4.19	172	4.45	180
cortex	$\mathrm{human}_{\mathrm{scalp}}$	3.57	154	3.93	164	4.34	177
	$\mathrm{human}_{\mathrm{cortex}}$	2.57	123	2.99	136	3.24	144
	$\mathrm{human}_{\mathrm{air}}$	3.73	158	4.02	167	4.41	179
	$\mathrm{mouse}_{\mathrm{scalp}}$	3.02	137	3.38	148	3.70	157

Table 5.3: Summary of the second attenuation coefficient needed to have an RMSE $< 5\%$ with a displacement amplitude of 50 nm. L_{P} denotes the level of dipole moment power $L_{\mathrm{P}}[dB] = 10\log_{10}(\mathrm{PSD}(f = 1\ \mathrm{MHz})/\mathrm{PSD}(f = 0\ \mathrm{MHz}))$.

both for deep and cortex DOI. The necessary $A_{\max}$ to get an RMSE $< 10\%$ is 1 to 2 orders of magnitude lower for the cortex than the deep DOI.

The $A_{\max}$ to obtain an RMSE $= 5\%$, for a deep and cortex DOI, are shown in figure 5.7 (C) and (D), respectively. For each model setup, the required $A_{\max}$ increases linearly on the log-log scale, with increasing number of dipoles, i.e., $\log_{10} A_{\max} = a \log_{10}(\text{nr. dipoles}) + b$. The different model setups have similar slopes, around 0.54. Except the cortex measurements, these have a slope around 0.75. Interesting is the different order of model setups between the deep and cortex DOI. In case of the former, the highest displacement amplitude is required for a human cortex setup, while this requires the lowest amplitude when the DOI is at the cortex. The extra air layer has negligible effect for the deep DOI with an intercept difference of only 0.0021. On the other hand, there is a significant effect when the DOI is at $r_{\mathrm{dp}} = R_{\mathrm{dp,max}}$, leading to an intercept difference of 0.2439. Moreover, there is a 1 (2) order(s) of magnitude difference between the mouse and human model in case of the deep (cortex) DOI. Finally, It can be seen that the number of layers (n) has no effect on $A_{\max}$.

The static interference is strongly governed by α_2. As the real value is unknown, the effect of this parameter was further investigated. As shown in figure 5.7 (E-H), the required $A_{\max}$, to have an RMSE = 5%, decreases with increasing α_2 for each model setup and fixed number of dipoles. Moreover, a similar slope around -1.5 is observed in case of all model setups and DOI locations. From equation (5.4), the relationship between α_2 and the level of dipole moment power L_{P} at f_{us} compared to DC is roughly:
$L_{\mathrm{P}}\ [\mathrm{dB}] = 10\log_{10}(\mathrm{PSD}(f = 1\ \mathrm{MHz})/\mathrm{PSD}(f = 0\ \mathrm{MHz})) \approx -30\alpha_2 - 50$. Consequently, $\log_{10}(A_{\max}) \approx -1.5\alpha_2 + b \approx \frac{1}{20}L_{\mathrm{P}} + b + 2.5$, where b depends on nr. dipoles, DOI position and model setup. The signal strength increases linearly with

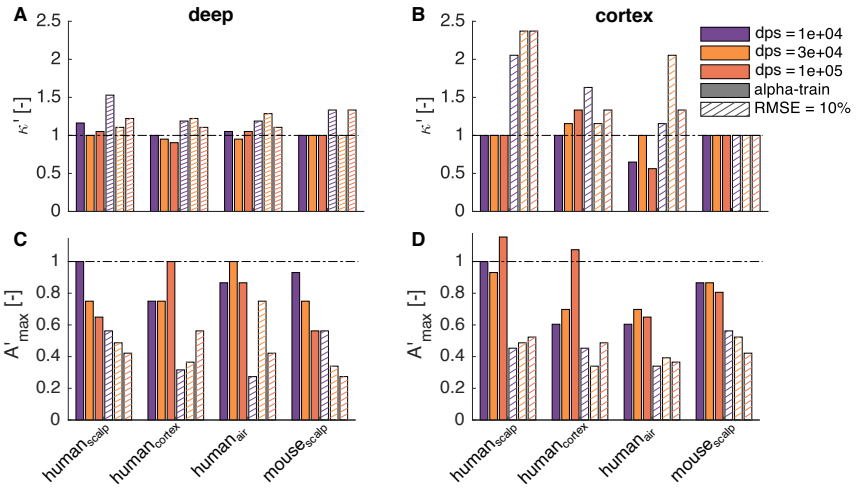

Figure 5.8: The effect of an altered intensity current (alpha-train) and changed cut-off RMSE level (10%). **A** The relative change in spatial constant κ with respect to simulation with original target settings, i.e., alpha-fun and RMSE of 5%, for the different models. The dipole of interest (DOI) is at r_{dp} = 0 mm. The results shown are for different number of surrounding dipoles. **B** a DOI at r_{dp} = 65mm (cortex). **C** and **D** The relative change in required displacement amplitude (A_{max}) with respect to simulation with original target settings, i.e., alpha-fun and RMSE of 5%.

A_{max} (see equation (5.12)) Therefore, the power increases with $20 \log_{10} A_{\mathrm{max}}$, explaining the obtained relationship.

For the technique to be safe, the FDA limits (see section 5.2.6) may not be exceeded. The minimal α_2 to have an RMSE $< 5\%$ for a displacement amplitude of 50 nm is determined via interpolation and summarized in table 5.3. For this A_{max}, the corresponding MI and I_{pa} are 0.45 and 7.4 W/cm^2, respectively. Consequently, a maximal dc of 9.74% is allowed in order to meet the I_{ta} limit for our pulse active time of 25 ms. The corresponding power L_{P} (in dB) is shown as well. It is clear that for a deeper DOI the static interference should be much lower.

5.3.4 Reconstruction Accuracy and Dipole Current Waveform

Finally, the effect of the chosen target parameters is addressed. The results above were for a target RMSE of 5%. Ideally, a perfect reconstruction of the target's current intensity profile could be obtained. Due to the aforementioned interferences, this can only be achieved with an infinitesimal small κ and infinitely high A_{max}. Capturing the general trend on the other hand can be informative as well. To investigate the effect of the imposed reconstruction accuracy, the required κ and

$A_{\max}$ for 10^5 dipoles are determined for an RMSE of 10%. Also, the current intensity profile of the DOI is switched from an alpha-function to an alpha-train (see equation (5.8) and figure 5.2). The relative change in parameters are shown in figure 5.8 (i.e., the required κ ($A_{\max}$) for the new target settings, either altered input current intensity (alpha-train) or altered RMSE target value (10%), divided by the required parameter value for the alpha-function intensity profile and RMSE = 5%).

The change of target function is expected to give values of 1 for both $A'_{\max}$ and κ'. In case of some simulation setups, there is a large deviation from this value. From figure 5.6 (B), it was already concluded that the RMSE is a very strict metric for the alpha-function input. Moreover, due to the interferences, the reconstructed signal will be noisy. This can potentially favor highly time-varying signals such as the alpha-train.

For a target RMSE of 10%, an increase in κ and a decrease in $A_{\max}$ is expected. Overall, this is observed although for some setups less pronounced. In case of the deep DOI, only small changes (< 1.5) in κ are observed. These go up to 2.5 for the cortex dipole. For almost all setups and DOI locations, $A_{\max}$ is halved or lower. It is clear that the opposed restrictions can have significant effect but do not result in differences in several orders of magnitude, which is more of interest in this simulation study.

5.4 Discussion

The results showed that it is possible to reconstruct the input intensity profile current of a mechanically vibrating dipole from the frequency content near the ultrasonic frequency. In the used model, the head is represented as a set of concentric spheres and the signal generators as dipoles. An optimal signal strength is obtained when dipole orientation, vibration direction and POI are perfectly aligned. When perpendicular, this is minimal. Inclusion of a skull and scalp layer causes a reduction in maximal signal strength of two orders of magnitude. An extra air layer causes an extra reduction of a factor 2. The smallest signals only decrease by a factor two and 16% by including a skull-scalp and air layer, respectively. It is clear that that there is a large signal reduction due to the extra distance between source and receiver. The introduction of extra layers account for large additional losses (both propagation and conductive). Conductive loss is more prominent with the introduction of the skull and scalp tissues. The signal strengths are, however, small. For a fixed dipole moment of 5 nAm and a vibration amplitude within FDA limits, the strength is in the order of pV.

Two interference types are identified and investigated. First, the vibrational interference which originates from a vibrating region excluding the dipole of interest. Second, the static interference that comes from the electrical activity of the regions itself. Concerning the vibrational interference, it was found that lower spatial constants are needed to achieve accurate reconstructed signals (i.e., RMSE$<$5%) with increasing number of dipoles. The κ in the mouse model is on average an order of magnitude lower than that in the human head model setups. Although

opposite for the deep and cortex DOI, there is also a clear effect of the number of layers (n) modeled. As aforementioned (section 5.3.2), these three aspects can be explained by taking into account the distance between DOI and nearest neighbor, as also indicated by rel. κ. It should be noted that all dipoles vibrate in phase. Consequently, the current vibrational interference reflects the upper limit. For the cortex DOI, also an effect of the electrode position is observed. This is due to the strong non-linear dependence between dipole vibration direction, orientation and POI position as is shown in figure 5.5. This is more pronounced if the dipole is closer to the POI than further away. Meaning that the contributions of neighboring dipoles are relatively lower for the cortex setup than for the scalp and air setups (see cortex versus scalp or air POI in figure 5.6 (G) and (H)).

The difference in $A_{\max}$ between the deep and cortex DOI is completely explained by the signal drop due to increasing distance between source and observer (see figure 5.5). This holds also for the deep mouse scalp setup. The reason for the mouse scalp setup to require a larger $A_{\max}$ than human cortex is attributable to the relative distance difference between the DOI and the surrounding dipoles to the POI. Finally, the increased slope of the required $A_{\max}$ with increasing number of dipoles for human cortex measurement can be explained by the increasing density of dipoles near the POI. This due to the $1/r^i$ dependence as seen in equation (5.1). When the distance is small (cortical electrode), a small change has relatively a higher impact than when initial distance is larger (scalp electrode). Consequently, a steeper slope is expected for the scalp versus air setup but this is below the simulation setup's accuracy limits.

Focusing an ultrasonic beam is complicated by the distortion imposed by crossing the skull [42]. Although, adaptive focusing techniques exist, determining the field for each setup is too tedious and therefore out of the scope of the study. Moreover, a field induced by a transducer array is not monotonically decreasing but contains sidelobes. The sidelobes' characteristics strongly depend on the transducer setup [43]. To avoid dipoles to be located at the trough of a sidelobe, a monotonically exponential decaying field was selected (see equation (5.9)). With its spatial constant, the selected field distribution allows for systematic investigation, capturing the essential spatial decay from the ultrasonic focus, which could be used as guideline for transducer development in the future. Moreover, the spatial constant is strongly correlated to the spatial resolution that be obtained by acousto-electrophysiological neuroimaging, however, limited by the ultrasonic field. As discussed above, the closer the nearest neighbor, the lower the required κ. Or in other words, for a fixed κ the distance to the nearest neighbor is defined, this being the spatial resolution. For the cortex DOI in the human (mouse) model, this is $0.36(0.023) \cdot \sqrt{10^5/\text{nr. dipoles}}$ mm. In case of the deep DOI, this is 6.5 mm (0.41 mm).

The dipole is an anatomically constraint representation of current generators, a model that is typically used in ESI. Murakami 2015 showed that, in the brain, the dipole density has a maximum value between 1-2 nAm/mm^2 across different species. The dipole moment itself can vary over 1-3 orders of magnitude depending on the volume of active tissue. A cortical column comprises around 10^5 cells/mm^2.

Consequently, with a single neuron's dipole moment between 0.1-1 pAm [44] this results in a synchronously active fraction of 1-20% [37].

For the investigated method to be safe, the FDA limits cannot be exceeded. The important parameter here is $A_{\max}$. The required $A_{\max}$ is determined by the static interference and thermal or instrumental noise. The latter is not included in the study as it is defined by the recording device (EEG-instrumentation). As the frequency content of the brain at US-frequency range is not known, the input current intensities were drawn from a power-law power spectral density profile. This has been studied in literature as this $1/f^{\alpha}$-like power spectrum is observed at many spatio-temporal scales. Power-laws with α between 0-4 have been reported depending on the measured scale for frequencies below 1 kHz [45–47]. Dipole moment calculation were performed on morphologically accurate neuron models [48, 49] to gain more insight in the energy content of realistic current dipoles for f $>$ 1 kHz [50]. Our calculations showed fitted power law coefficients of 4 to 5 for f ϵ $[1, 25]$ kHz (see section 5.6.3). This corresponds to an α_2-value of 3 to 4. Although not conclusive, it justifies the tested PSD profiles but further investigation is necessary. The results shown in table 5.3 showed that if the level of dipole moment power (L_{P}) is -210 dB at 1 MHz, good signal reconstruction (RMSE = 5%) can be obtained for all tested model setups with only a displacement amplitude of 50 nm. This amplitude is well within FDA limits, if a dc of 9.74% is used with our pulse active time of 25 ms. As expected, the L_{P} correlates with the number of dipoles. These dipoles represent a small volume of neurons. Therefore, the number of dipoles and their strength $I_{\max}$ is limited, depending on the represented volume. Although the static interference level depends on the number of dipoles in this simulation setup, the static interference will be fixed in the brain. On the other hand, the strength of the tagged region decreases with increasing spatial resolution as the represented volume decreases. Consequently, the signal-to-noise ratio still drops with increasing nr. dipoles and the same effect on the required $A_{\max}$ is thus expected. Therefore, because the number of dipoles dictates the spatial resolution, retrospectively, if the static interference is known, a decision can be made whether or not and at which resolution the technique will be safe, within FDA limits.

5.4.1 The Acousto-Electric Effect

Witte et al. experimentally validated that indeed the electrophysiological activity gets modulated on the harmonic frequency when selectively probed with ultrasound. This was shown in numerous experiments, e.g., in a rabbit heart [32, 51], lobster nerve [27], bath with 0.9% NaCl solution [31, 52] and a human head phantom [33, 34]. Broadband-EEG like signals can be retrieved and current sources localized with high spatial accuracy. The latter is defined by the US focal zone, being only a couple of millimeters, not only for superficial but also for deep regions [34]. By scanning with the ultrasonic beam, a 4D image can be made with unprecedented spatiotemporal resolution. Results of this group and others are summarized in Zhang et al. (2022) [30]. The postulated underlying mechanism, the acousto-electric effect, i.e., a pressure induced change in resistivity, differs from the one

hypothesized here. The mathematical formulation of modulation due to the AE is as follows:

$$\begin{aligned} \Delta\rho &= -K\rho_0\Delta P \\ V_i^{EEG} &= \iiint (\mathbf{J}_i^{\mathrm{L}} \cdot \mathbf{J}^{\mathrm{I}})(x,y,z)\rho_0 \mathrm{d}x\mathrm{d}y\mathrm{d}z \\ V_i^{AE} &= \iiint (\mathbf{J}_i^{\mathrm{L}} \cdot \mathbf{J}^{\mathrm{I}})(x,y,z)(-K\rho_0\Delta P)\mathrm{d}x\mathrm{d}y\mathrm{d}z \end{aligned} \tag{5.16}$$

with ρ_0 the direct current resistivity, K the acousto-electric interaction constant, ΔP the ultrasound pressure field, and $\mathbf{J}_i^{\mathrm{L}}$ and $\mathbf{J}^{\mathrm{I}}$ the lead field of lead i and current source density field, respectively. For the derivation I refer to Olafsson et al. (2008) [52]. In the literature on the acousto-electric effect, the potential term V_i^{AE} is caused by ultrasound-induced oscillations of the electrical resistivity $\Delta\rho$, while the lead field $\mathbf{J}_i^{\mathrm{L}}$ and the current source $\mathbf{J}^{\mathrm{I}}$ are implicitly assumed to be undisturbed by the pressure field. However, I argue that the AE-induced resistivity oscillations will cause direct changes to the current density fields ($\mathbf{J}_i^{\mathrm{L}}$ and $\mathbf{J}^{\mathrm{I}}$). Conversely, in this chapter, modulation of the DOI current on the ultrasonic sine occurs due to the relative motion of the dipole of interest. Consequently, both the acousto-electric effect and the vibration of dipoles (or equivalently, the oscillation of current sources $\mathbf{J}^{\mathrm{I}}$ and lead fields $\mathbf{J}_i^{\mathrm{L}}$) can be interpreted as complementary tentative underlying mechanisms of acousto-electrophysiological neuroimaging. Furthermore, the results clearly show that the latter mechanism (vibrating dipoles) also suffices to modulate the endogenous signal onto the ultrasonic frequency.

Wang et al. (2011) [31] reported a 27 nV/mA peak signal strength with 500 kPa pressure, and 5 mm distance between current source and sink, measured at 5 mm from current source. This equals to $10.8\ \mathrm{pV/(nAm \cdot MPa)}$. Performing an equivalent simulation, i.e., dipole at [0, 0, 0], orientation [0, 1, 0], vibration direction [0, 0, 1], d = 5 mm and electrode at [0, 7.50, 0] mm, results in $6.1\,10^{-6}\ \mathrm{pV/(nAm \cdot MPa)}$. However, our results showed a strong nonlinear dependence on the alignment between the dipole, displacement direction and electrode position. Subsequently, a 1% misalignment (electrode at [0, 7.50, 0.075] mm) gives $1.8\ \mathrm{pV/(nAm \cdot MPa)}$. It should be noted, that the dipole vibrates as a whole. Moreover, d only affects the dipole moment as no distinction between current source and sink is made (see equation (5.1)). Taken this into account, still, a comparable strength is expected for a vibrating current dipole. A maximum of $91.0\ \mathrm{pV/(nAm \cdot MPa)}$ is obtained with an electrode at the optimal POI location [0, 5.3, 5.3] mm.

5.4.2 Limitations and Future Work

As already mentioned in section 5.3.4, the used RMSE metric is prone to randomness in the results. It is very strict in the sense that only low values are returned when almost perfect profile match is obtained. As visible in figure 5.6 (B), already a clear peak is observed for $\kappa = 5\,\mathrm{mm}$, while only a minimum RMSE of 20%

was calculated. Consequently, more favorable spatial constants or displacement amplitudes than the ones determined for RMSE = 5% could already give feasible reconstructions, for instance when scanning for hyperactive regions, like in epilepsy. Here, the dipole moments will be 1-2 orders of magnitude higher as well, increasing the signal strength with the same amount [37]. On the other hand, as depicted in figure 5.8, sometimes no clear trends can be observed. This is due to the randomness introduced in the simulations (e.g., the current intensity profile and strength, and dipole positions). Simulations could be repeated for different random seeds. However, it was deemed not feasible due to the need for large computational resources and the expected change only being in same order of magnitude.

There was opted not to use frequency dependent electrical properties for the different tissues. This is because the frequency dependence for the sub-MHz range is not clearly established [53]. Moreover, the small changes do not outweigh the big increase in computation time. A single test was performed with the frequency-dependent values obtain from [39], which resulted in a 20% increase of the signal strength received from a single dipole. Also, the electrical properties were set to be homogeneous, confined to each sphere, and isotropic. However, experiments have shown those to be inhomogeneous and anisotropic [10]. This will clearly impact the signal strength. However, the effect was deemed to be inferior to the spherical approximation with respect to the correct morphological shape. Moreover, the in-vivo values are still under debate [22]. While this impacts ESI greatly, with possible localization errors up to several centimeters, here this will only impact the signal strength without affecting the achievable resolution.

In our study the AE-effect is not taken into account (i.e., the conductivity is assumed to be non-oscillating). In future research, the acousto-electric effect could be included and other possible mechanisms (e.g., acoustic streaming, radiation force and charge displacements in the Stern layer) should be investigated. Moreover, further research is necessary to determine the interaction effects of these various underlying mechanisms and investigate their dominance in the brain for given conditions (e.g., waveform, transducer placement, dipole location). The brain regions are modeled as rigid dipoles. As such, the current source and sink vibrate in phase. The contribution of stretching and rotation could be further investigated. Also, the dipole assumption itself compared to discrete monopoles or a multipole expansion could be of interest in future work. The ultrasonic frequency was kept constant throughout the whole study. Lowering the frequency will both lower the MI and the I_{pa} for a fixed displacement amplitude, but this will increase the static noise.

In future work, the added value of modulated focused ultrasound [54] can be investigated with the goal of reducing the MI. This would be beneficial, if the acoustic particle velocity amplitude is proportional to the beat frequency f_{b} ($v_{\mathrm{us}} \approx 2\pi A f_{\mathrm{b}}$) due to the low-pass filter property of the constitutive equation of the viscoelastic brain. In this case, the mechanical index is $\left(\mathrm{MI} = \mathrm{PNP}[\mathrm{MPa}]/\sqrt{f_{\mathrm{c}}[\mathrm{MHz}]} = (2\pi A Z_{\mathrm{ac}} f_{\mathrm{b}})/\sqrt{f_{\mathrm{c}}}\right)$. In other words, a small ratio of beat to carrier frequency $f_{\mathrm{b}}/\sqrt{f_{\mathrm{c}}}$, results in a smaller mechanical index.

Finally, a limit on possible neuromodulation should be considered, as well. Ultrasound has been demonstrated to modulate brain activity in animals and humans [55, 56]. The underlying mechanisms of ultrasound neuromodulation are not well understood with multiple mechanisms being postulated to be active simultaneously (e.g., radiation force, intramembrane cavitation, thermal effects, ion channel mechanosensitivity [56–62]). However, the goal of AENI is to record endogenous activity, i.e., the intrinsic activity and not the activity induced by ultrasonic activation. In future work, computational modeling of ultrasonic neuromodulation can be used to determine the region of the parameter space in which AENI is feasible without significant modulation of the endogenous activity [62–64]. Although a single 25 ms ultrasonic pulse was adopted in our study, signal reconstruction is still possible with pulsed ultrasonic fields with a signal period of 25 ms. In the current literature, relatively large duty cycles are adopted in order to achieve neuromodulation [65]. Moreover, an exponential increase of neuromodulation thresholds is observed with lowering the duty cycle [66], while only a linear relationship is expected concerning the signal-to-noise ratio with respect to the static interference.

With pulsed fUS, a rise in recorded activity at the pulse repetition frequency (prf) was also observed in [67]. It is expected that the measured signal at the prf is either the signal induced by neuromodulation (as stated by the authors of [67]) [66, 68] or by hearing confounds [69, 70]. It is hypothesized in [67] that also endogenous activity of the targeted area could be modulated on the recorded signal at the pulse repetition frequency. However, based on the mechanism described above, the relative signal strength at $f = \mathrm{prf}$ with respect to the strength at f_{us} should be $\mathrm{sinc}((\mathrm{prf} - f_{\mathrm{us}})/(\mathrm{prf}/\mathrm{dc}))$. Using the values reported in Darvas et al. (2016) [67] this results in $\approx 5 \cdot 10^{-5}$, implying that demodulation of endogenous activity at the repetition frequency is unlikely, at least for the vibrating dipole mechanism of AENI.

Feasibility of acousto-electrophysiological neuroimaging will depend on the currently unknown biophysiological activity at ultrasonic frequencies. Unlike with high-density EEG, accurate reconstruction of a tagged region's signal is possible, with just one electrode (and one reference electrode). Moreover, no MRI or complex ESI algorithm is necessary to solve the ill-posed inverse problem. On the other hand 4D imaging with UCSDI currently takes up several hours in experimental setups. This could probably be dramatically improved with modern scanners. Additionally, B-mode ultrasound and normal EEG could be coregistered with AENI [31]. Finally, spatially encoding the brain with different ultrasonic frequencies could be an interesting path to investigate in the future.

5.5 Conclusion

In this chapter I showed that mechanical vibration, introduced by an ultrasonic field, modulates the endogenous signals onto the ultrasonic frequency. In this spherical representation of the head where the active brain is discretized into a set of dipoles, the signal strength strongly depends on the alignment between dipole

moment, displacement direction and point of measurement. Inclusion of extra layers results in a signal reduction, attributable to the extra distance between source and receiver and conductive losses. For a displacement amplitude of 10 nm and a dipole moment of 5 nAm the signal strengths are low, with a maximal signal strength of 341.60, 2.36 and 1.24 pV that can be measured with a cortical, wet and dry scalp electrode, respectively. For a dipole at the center, the strengths are below 0.16 pV. Accurate reconstruction of a tagged region's activity can be obtained if two interference sources are overcome. The vibrational interference originates from other vibrating regions. This can be decreased by decreasing the spatial constant of the ultrasonic field. It was shown that the dominant factor is the distance to the nearest neighboring dipole. Therefore, the spatial resolution is strongly correlated to this spatial constant. The static interference comes from the endogenous activity of non-vibrating brain regions self at the ultrasonic frequency. The signal-to-noise ratio increases with increasing displacement amplitude. This is, however, limited by the mechanical index and average pulse intensity limits set by the FDA. Log-log relationships are observed between the required displacement amplitude and the power of the static interference at f_{us}, and the number of dipoles. For a deep region of interest, dry and wet electrodes deliver similar and best results. An accurate signal reconstruction (RMSE $< 5\%$) can be obtained if the level of dipole moment power $\approx -154 - 10\log_{10}(\mathrm{nr.dipoles})$ dB. This under safe conditions with only 50 nm displacement amplitude. For the cortex region, cortical electrodes give the best result, with a required level of dipole moment of $\approx -94 - 10\log_{10}(\mathrm{nr.dipoles})$ dB. With the mouse model, lower vibration amplitudes are required for detection, but a spatial constant in the order of 10 μm is required. Depending on the spatial constant, resolutions up to millimeter could theoretically be achieved in humans but will completely depend on the ultrasonic field.

5.6 Appendix

5.6.1 The Liénard-Wiechert Fields

The Liénard-Wiechert field, which is the time varying electromagnetic field for a point charge (q) at position ($\mathbf{r_s}$) in arbitrary motion, is given by:

$$\mathbf{E}(\mathbf{r},t) = \frac{q}{4\pi\epsilon_0}\left(\frac{\mathbf{n}}{\gamma^2(1-\mathbf{n}\cdot\boldsymbol{\beta})^3|\mathbf{r}-\mathbf{r_s}|^2}\right. \\ \left. - \frac{\boldsymbol{\beta}}{\gamma^2(1-\mathbf{n}\cdot\boldsymbol{\beta})^3|\mathbf{r}-\mathbf{r_s}|^2} + \frac{\mathbf{n}\times\left((\mathbf{n}-\boldsymbol{\beta})\times\dot{\boldsymbol{\beta}}\right)}{c(1-\mathbf{n}\cdot\boldsymbol{\beta})^3|\mathbf{r}-\mathbf{r_s}|}\right)_{tr} \tag{5.17}$$

with ϵ_0 the vacuum permittivity and c the speed of light. $\mathbf{n}(t) = (\mathbf{r}-\mathbf{r_s}(t))/|\mathbf{r}-\mathbf{r_s}(t)|$, $\boldsymbol{\beta}(t) = \mathbf{v}(t)/c$, where $\mathbf{v}(t)$ is the source's velocity. $\dot{\boldsymbol{\beta}}$ is the charge's acceleration with respect to c (i.e., $\mathbf{a}(t)/c$, with $\mathbf{a}(t) = \mathrm{d}\mathbf{v}(t)/\mathrm{d}t$), $\gamma(t)$ is the Lorentz factor $\left(1/\sqrt{1-|\boldsymbol{\beta}(t)|^2}\right)$ and $t_r = t - |\mathbf{r}-\mathbf{r_s}|/c$ is the time retardation.

It can be divided into five components:

$$\mathbf{E} = \mathbf{E_s} + \mathbf{E_{qs}} + \mathbf{E_v} + \mathbf{E_a} + \mathbf{E_{t_r}} \tag{5.18}$$

where

1. The static field:
   $\mathbf{E_s} = \mathbf{E}$ when $\mathbf{v} = \mathbf{0}$ and $\mathbf{a} = \mathbf{0}$
2. The quasi-static field:
   $\mathbf{E_{qs}} = \mathbf{E} - \mathbf{E_s}$ when $v << c$ and $\frac{aq}{\epsilon_0} << c|\mathbf{r} - \mathbf{r_s}|$
3. Relativistic effects due to velocity (Doppler):
   $\mathbf{E_v} = \mathbf{E} - \mathbf{E_s} - \mathbf{E_{qs}}$ when $\frac{aq}{\epsilon_0} << c|\mathbf{r} - \mathbf{r_s}|$
4. Relativistic effects due to acceleration (Electromagnetic Radiation):
   $\mathbf{E_a} = \mathbf{E} - \mathbf{E_s} - \mathbf{E_{qs}}$ when $v << c$
5. Relativistic effects due to finite propagation speed:
   $\mathbf{E_{tr}} = \mathbf{E} - \mathbf{E_s} - \mathbf{E_{qs}} - \mathbf{E_v} - \mathbf{E_a}$ when $t \neq t_r$

For a oscillating movement in the x-direction ($A\sin(\omega t)\mathbf{e}_x$) and an observer on the y-axis or x-axis, the dominant term of th Taylor expansion for A$\rightarrow$0 is given in table 5.4. The quasi static contribution dominates if $\frac{|\mathbf{E_v}|}{|\mathbf{E_{qs}}|} \ll 1$ and $\frac{|\mathbf{E_a}|}{|\mathbf{E_{qs}}|} \ll 1$. A critical frequency can be found form $\frac{y(2\omega_c^2 y + 3c\omega_c)}{3c^2} = 1 \Rightarrow \omega_c = 20.58/y[\mathrm{cm}]$ GHz. For an overestimation of y = 20 cm, $\omega_c = 1.029$ GHz. Thus, for ultrasonic frequencies in the MHz range the quasi-static contributions dominate ($\omega_{us} \ll \omega_c$).

5.6.2 Solution to General Poisson Equation Spherical 4-Layer Head Model

A semi-analytical solution can be obtained by solving the general Poisson equation in spherical coordinates. Values for $A_{l,i}$ and $B_{l,i}$ of equation (5.1) can be determined under following boundary conditions, i.e., the potential needs to be continues (i) with reference at infinity (iii) and there is conservation of charge at the interface (ii):

1. $V_l = V_{l+1}$
2. $\sigma_l \frac{\partial V_l}{\partial n} = \sigma_{l+1} \frac{\partial V_{l+1}}{\partial n}$
3. $V_l(r) \rightarrow 0$ for $r \rightarrow \infty$

Observer	**y-axis**		**x-axis**
Component	$\mathbf{e}_x$	$\mathbf{e}_y$	$\mathbf{e}_x$
$\mathbf{E_s}$	-	$\frac{1}{y^2}$	$\frac{1}{x^2}$
$\mathbf{E_{qs}}$	$\frac{A}{y^3}$	$\frac{3}{2}\frac{A^2}{y^4}$	$\frac{2A}{x^3}$
$\mathbf{E_v}$	$\frac{A\omega}{cy^2}$	$\frac{A^2(2\omega^2 y+3c\omega)}{2c^2y^3}$	$\frac{A\omega}{cx^2}$
$\mathbf{E_a}$	$\frac{A\omega^2}{c^2y}$	$\frac{A^2\omega^2}{c^2y^2}$	0
$\frac{\lvert\mathbf{E_v}\rvert}{\lvert\mathbf{E_{qs}}\rvert}$	$\frac{\omega y}{c}$	$\frac{y(2\omega^2 y+3c\omega)}{3c^2}$	$\frac{\omega x}{2c}$
$\frac{\lvert\mathbf{E_a}\rvert}{\lvert\mathbf{E_{qs}}\rvert}$	$\left(\frac{\omega y}{c}\right)^2$	$\frac{2}{3}\left(\frac{\omega y}{c}\right)^2$	0

Table 5.4: Dominant term of Taylor expansion (A→0) of each component of the electromagnetic field. Motion is in x-direction: $A\sin(\omega t)\mathbf{e}_x$. All values divided by $q/4\pi\epsilon_0$

Due to iii, B_4 has to be zero. A_1 is defined by the unbound solution. This gives $A_1 = b^{i-1}p$, where $b = |\mathbf{r}_{\mathrm{dp}}|$ and $p = |\mathbf{d}|$. Next, i provides a set of 3 equations:

$$\begin{aligned}
\frac{b^{i-1}p\,R_{\mathrm{brain}}^{-i-1} + B_1\,R_{\mathrm{brain}}^{i}}{4\pi\sigma_1} &= \frac{A_2\,R_{\mathrm{brain}}^{-i-1} + B_2\,R_{\mathrm{brain}}^{i}}{4\pi\sigma_2} \\
\frac{A_2\,R_{\mathrm{skull}}^{-i-1} + B_2\,R_{\mathrm{skull}}^{i}}{4\pi\sigma_2} &= \frac{A_3\,R_{\mathrm{skull}}^{-i-1} + B_3\,R_{\mathrm{skull}}^{i}}{4\pi\sigma_3} \\
\frac{A_3\,R_{\mathrm{scalp}}^{-i-1} + B_3\,R_{\mathrm{scalp}}^{i}}{4\pi\sigma_3} &= \frac{A_4\,R_{\mathrm{scalp}}^{-i-1}}{4\pi\sigma_4}
\end{aligned}$$

Finally, the last set of equations is given by ii:

$$\begin{aligned}
b^{i-1}p\,R_{\mathrm{brain}}^{-i-2} - \frac{iB_1\,R_{\mathrm{brain}}^{i-1}}{(i+1)} &= A_2\,R_{\mathrm{brain}}^{-i-2} - \frac{iB_2\,R_{\mathrm{brain}}^{i-1}}{(i+1)} \\
A_2\,R_{\mathrm{skull}}^{-i-2} - \frac{iB_2\,R_{\mathrm{skull}}^{i-1}}{(i+1)} &= A_3\,R_{\mathrm{skull}}^{-i-2} - \frac{iB_3\,R_{\mathrm{skull}}^{i-1}}{(i+1)} \\
A_3\,R_{\mathrm{scalp}}^{-i-2} - \frac{iB_3\,R_{\mathrm{scalp}}^{i-1}}{(i+1)} &= A_4\,R_{\mathrm{scalp}}^{-i-2}
\end{aligned}$$

Consequently, the set of equations is defined and a solution can be found. The solution was obtained in Maple 2021.

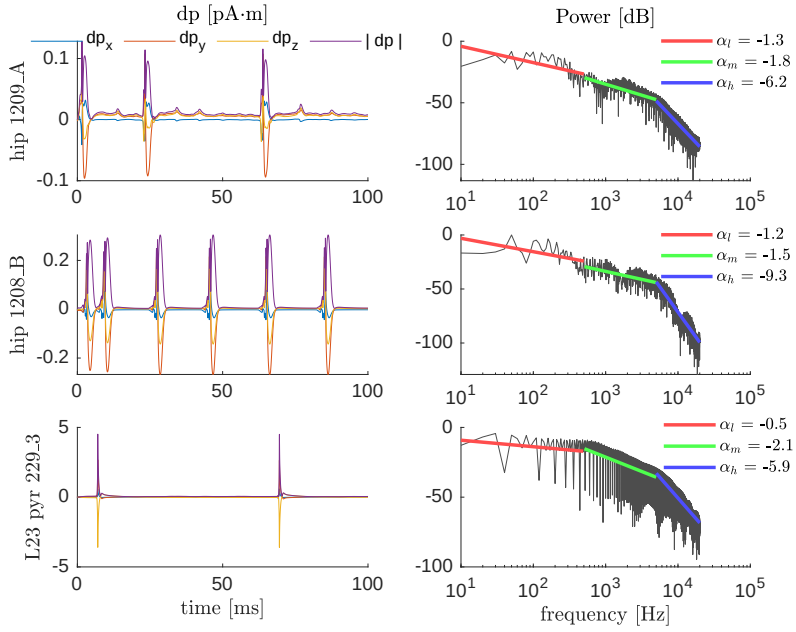

Figure 5.9: Dipole moment calculated using morphologically accurate neuron models (y-label) in response to a pulsed synaptic input. (Left) signals in time domain. (right) corresponding power spectral density profile. The fitted power law coefficients for fixed frequency range are displayed in the legend. $\alpha_l : f\epsilon[0, 500[$ Hz, $\alpha_m : f\epsilon[0.5, 5[$ kHz and $\alpha_h : f\epsilon[5, 40[$ kHz

5.6.3 Time-Dependent Dipole Moment

In the model, dipoles are used to model the endogenous activity sources. Due to the interest in measured signal content at the ultrasonic frequency (f_{us}), an appropriate dipole's current intensity profile needs to be chosen to correctly capture the static interference (see section 5.3.3). The simulations are solved with an sampling frequency $F_s = 20\ f_{\text{us}}$. To avoid distortion of the frequency content due to linear interpolation in the time domain, the time dependent signals are derived from a power spectral density profile (PSD). The formulation of the PSD (equation 5.4), is repeated here for convenience.

$$\text{PSD}(f) = \frac{1 + f/\zeta f_1}{\prod_{i=1}^{N_f} (1 + (f/f_i)^{\alpha_i})} \tag{5.19}$$

with f_i the ith cut-off frequency, α_i the attenuation coefficient and N_f = 2 or 3, for the vibrational and static interference analysis, respectively. ζ is randomly chosen

between [0.3, 1]. Consequently, the PSD reaches a maximum between ζf_1 and f_1. This formulation was chosen based on the power-law ($1/f^\alpha$) power spectrum observed at many spatio-temporal scales inside the brain [45–47, 71]. The reported power-law coefficients in literature are typically fit for frequencies below 1 kHz. To obtain insights in the behavior at the higher frequencies ($>$ 1 kHz). Dipole moments were calculated using morphologically accurate neuron models.

The used neuron models are multi-compartmental. Two hippocampal pyramidal models (morphologies: mpg141208_B_idA and mpg141209_A_idA) from Migliore et al. (2018) [49] were tested, and one L2/3 cortical pyramidal cell from Aberra et al. (2018) [48]. The models were obtained from ModelDB [72]. The accession numbers are 244688 and 241165, respectively. The transmembrane voltage V of a single compartment can be determined by:

$$C_\mathrm{m}\frac{\mathrm{d}V}{\mathrm{d}t} = -I_\mathrm{m} + I_\mathrm{ax} - I_\mathrm{syn} \tag{5.20}$$

where C_m is the membrane capacitance, I_m the transmembrane current flowing out of the considered compartment, I_ax the axial current flowing into the considered compartment and I_syn an AMPA-like synaptic current. The latter is modeled as follows:

$$I_\mathrm{syn} = G_\mathrm{syn}\, A\, (\exp(-t/\tau_2) - \exp(-t/\tau_1))(V - E_\mathrm{syn}) \tag{5.21}$$

Synapses were randomly allocated to half of the apical dendritic compartments. A synaptic event was triggered every 2 ms. The rise time (τ_1) equals 0.4 ms, the decay time (τ_2) 1 ms and the weight G_syn 3 nS. A is a normalization factor in order to have a peak conductance of G_syn. The simulations are performed with the NEURON simulation software [73] for 100 ms and with a fixed time step of 25 μs. According to Murakimi et al. (2003) [50], the time dependent current dipole ($\mathbf{d}(t)$) is calculated as follows:

$$\mathbf{d}(t) = [\mathrm{dp}_x, \mathrm{dp}_y, \mathrm{dp}_z](t) \tag{5.22}$$

$$\mathrm{dp}_j(t) = \sum_k \mathrm{dp}_j^k(t) \tag{5.23}$$

$$\mathrm{dp}_j^k(t) = I_\mathrm{ax}^k L_j^k \tag{5.24}$$

with Q_j^k the current dipole and L_j^k the length in direction $j = x, y, z$ of compartment k.

Next, the PSD of the current dipole magnitude ($|\mathbf{d}|(t)$) is determined. The frequency domain is divided into three regimes: low ($f \in [0, 500[\ Hz$), medium ($f \in [0.5, 5[\ kHz$) and high ($f \in [5, 40[\ kHz$). A power-law is fit to each regime for each model via linear regression of the PSD at the log-log scale. The results and corresponding α coefficients are shown in figure 5.9.

References

[1] Ruben Schoeters, Thomas Tarnaud, Luc Martens, and Emmeric Tanghe. *Simulation study on high spatio-temporal resolution acousto-electrophysiological neuroimaging*. Journal of Neural Engineering, 20:066039, 12 2023.

[2] Paola Pinti, Ilias Tachtsidis, Antonia Hamilton, Joy Hirsch, Clarisse Aichelburg, Sam Gilbert, and Paul W. Burgess. *The present and future use of functional near-infrared spectroscopy (fNIRS) for cognitive neuroscience*. Annals of the New York Academy of Sciences, 1464:5–29, 3 2020.

[3] S. Baillet, J.C. Mosher, and R.M. Leahy. *Electromagnetic brain mapping*. IEEE Signal Processing Magazine, 18:14–30, 2001.

[4] Bin He, Abbas Sohrabpour, Emery Brown, and Zhongming Liu. *Electrophysiological Source Imaging: A Noninvasive Window to Brain Dynamics*. Annual Review of Biomedical Engineering, 20:171–196, 6 2018.

[5] Luis Fernando Nicolas-Alonso and Jaime Gomez-Gil. *Brain Computer Interfaces, a Review*. Sensors, 12:1211–1279, 1 2012.

[6] Saskia Bollmann and Markus Barth. *New acquisition techniques and their prospects for the achievable resolution of fMRI*. Progress in Neurobiology, 207, 12 2021.

[7] N Logothetis. *MR imaging in the non-human primate: studies of function and of dynamic connectivity*. Current Opinion in Neurobiology, 13:630–642, 10 2003.

[8] Richard P. Kennan, Silvina G. Horovitz, Atsushi Maki, Yuichi Yamashita, Hideaki Koizumi, and John C. Gore. *Simultaneous Recording of Event-Related Auditory Oddball Response Using Transcranial Near Infrared Optical Topography and Surface EEG*. NeuroImage, 16:587–592, 7 2002.

[9] Valentina Quaresima and Marco Ferrari. *Functional Near-Infrared Spectroscopy (fNIRS) for Assessing Cerebral Cortex Function During Human Behavior in Natural/Social Situations: A Concise Review*. Organizational Research Methods, 22:46–68, 1 2019.

[10] György Buzsáki, Costas A. Anastassiou, and Christof Koch. *The origin of extracellular fields and currents — EEG, ECoG, LFP and spikes*. Nature Reviews Neuroscience, 13:407–420, 6 2012.

[11] Mansoureh Fahimi Hnazaee, Elvira Khachatryan, and Marc M. Van Hulle. *Semantic Features Reveal Different Networks During Word Processing: An EEG Source Localization Study*. Frontiers in Human Neuroscience, 12:503, 12 2018.

[12] Dahlia Sharon, Matti S. Hämäläinen, Roger B.H. Tootell, Eric Halgren, and John W. Belliveau. *The advantage of combining MEG and EEG: Comparison to fMRI in focally stimulated visual cortex*. NeuroImage, 36:1225–1235, 7 2007.

[13] Sylvain Baillet. *Magnetoencephalography for brain electrophysiology and imaging*. Nature Neuroscience, 20:327–339, 3 2017.

[14] Silke Klamer, Adham Elshahabi, Holger Lerche, Christoph Braun, Michael Erb, Klaus Scheffler, and Niels K. Focke. *Differences Between MEG and High-Density EEG Source Localizations Using a Distributed Source Model in Comparison to fMRI*. Brain Topography, 28:87–94, 1 2015.

[15] Arthur K. Liu, Anders M. Dale, and John W. Belliveau. *Monte Carlo simulation studies of EEG and MEG localization accuracy*. Human Brain Mapping, 16:47–62, 5 2002.

[16] Agrita Dubey and Supratim Ray. *Cortical Electrocorticogram (ECoG) Is a Local Signal*. The Journal of Neuroscience, 39:4299–4311, 5 2019.

[17] Chiara Todaro, Laura Marzetti, Pedro A. Valdés Sosa, Pedro A. Valdés-Hernandez, and Vittorio Pizzella. *Mapping Brain Activity with Electrocorticography: Resolution Properties and Robustness of Inverse Solutions*. Brain Topography, 32:583–598, 7 2019.

[18] Shiva Asadzadeh, Tohid Yousefi Rezaii, Soosan Beheshti, Azra Delpak, and Saeed Meshgini. *A systematic review of EEG source localization techniques and their applications on diagnosis of brain abnormalities*. Journal of Neuroscience Methods, 339:108740, 6 2020.

[19] Gwénael Birot, Laurent Spinelli, Serge Vulliémoz, Pierre Mégevand, Denis Brunet, Margitta Seeck, and Christoph M. Michel. *Head model and electrical source imaging: A study of 38 epileptic patients*. NeuroImage: Clinical, 5:77–83, 2014.

[20] Laurent Koessler, Christian Benar, Louis Maillard, Jean-Michel Badier, Jean Pierre Vignal, Fabrice Bartolomei, Patrick Chauvel, and Martine Gavaret. *Source localization of ictal epileptic activity investigated by high resolution EEG and validated by SEEG*. NeuroImage, 51:642–653, 6 2010.

[21] Abbas Sohrabpour, Yunfeng Lu, Pongkiat Kankirawatana, Jeffrey Blount, Hyunmi Kim, and Bin He. *Effect of EEG electrode number on epileptic source localization in pediatric patients*. Clinical Neurophysiology, 126:472–480, 3 2015.

[22] Hans Hallez, Bart Vanrumste, Roberta Grech, Joseph Muscat, Wim De Clercq, Anneleen Vergult, Yves D'Asseler, Kenneth P Camilleri, Simon G Fabri, Sabine Van Huffel, and Ignace Lemahieu. *Review on solving the forward*

problem in EEG source analysis. Journal of NeuroEngineering and Rehabilitation, 4:46, 12 2007.

[23] Claire Rabut, Mafalda Correia, Victor Finel, Sophie Pezet, Mathieu Pernot, Thomas Deffieux, and Mickael Tanter. *4D functional ultrasound imaging of whole-brain activity in rodents*. Nature Methods, 16:994–997, 10 2019.

[24] Bin He. *Focused Ultrasound Help Realize High Spatiotemporal Brain Imaging? - A Concept on Acousto-Electrophysiological Neuroimaging*. IEEE Transactions on Biomedical Engineering, 63:2654–2656, 12 2016.

[25] Francis E. Fox, Karl F. Herzfeld, and George D. Rock. *The Effect of Ultrasonic Waves on the Conductivity of Salt Solutions*. Physical Review, 70:329–339, 9 1946.

[26] J. Jossinet, B. Lavandier, and D. Cathignol. *The phenomenology of acousto-electric interaction signals in aqueous solutions of electrolytes*. Ultrasonics, 36:607–613, 2 1998.

[27] Russell Witte, Ragnar Olafsson, Sheng-Wen Huang, and Matthew O'Donnell. *Imaging current flow in lobster nerve cord using the acoustoelectric effect*. Applied Physics Letters, 90, 4 2007.

[28] Xizi Song, Xinrui Chen, Jiande Guo, Minpeng Xu, and Dong Ming. *Living Rat SSVEP Mapping With Acoustoelectric Brain Imaging*. IEEE Transactions on Biomedical Engineering, 69:75–82, 1 2022.

[29] Jean L. Rintoul, Esra Neufeld, Chris Butler, Robin O. Cleveland, and Nir Grossman. *Remote focused encoding and decoding of electric fields through acoustoelectric heterodyning*. Communications Physics, 6:79, 4 2023.

[30] Hao Zhang, Minpeng Xu, Miao Liu, Xizi Song, Feng He, Shanguang Chen, and Dong Ming. *Biological current source imaging method based on acousto-electric effect: A systematic review*. Frontiers in Neuroscience, 16, 7 2022.

[31] Z. H. Wang, R. Olafsson, P. Ingram, Q. Li, Y. Qin, and R. S. Witte. *Four-dimensional ultrasound current source density imaging of a dipole field*. Applied Physics Letters, 99, 9 2011.

[32] Ragnar Olafsson, Russell S. Witte, C. Jia, Sheng-Wen Huang, K. Kim, and Matthew O'donnell. *Cardiac activation mapping using ultrasound current source density imaging (UCSDI)*. IEEE Transactions on Ultrasonics, Ferroelectrics, and Frequency Control, 56:565–574, 3 2009.

[33] Yexian Qin, Pier Ingram, Alex Burton, and Russell S. Witte. *4D acoustoelectric imaging of current sources in a human head phantom*. volume 2016-November, pages 1–4. IEEE, 9 2016.

[34] Andres Barragan, Chet Preston, Alex Alvarez, Tushar Bera, Yexian Qin, Martin Weinand, Willard Kasoff, and Russell S Witte. *Acoustoelectric imaging of deep dipoles in a human head phantom for guiding treatment of epilepsy*. Journal of Neural Engineering, 17, 10 2020.

[35] R. Martin Arthur and David B. Geselowitz. *Effect of Inhomogeneities on the Apparent Location and Magnitude of a Cardiac Current Dipole Source*. IEEE Transactions on Biomedical Engineering, BME-17:141–146, 4 1970.

[36] Y. Salu, L.G. Cohen, D. Rose, S. Sxato, C. Kufta, and M. Hallett. *An improved method for localizing electric brain dipoles*. IEEE Transactions on Biomedical Engineering, 37:699–705, 7 1990.

[37] Shingo Murakami and Yoshio Okada. *Invariance in current dipole moment density across brain structures and species: Physiological constraint for neuroimaging*. NeuroImage, 111:49–58, 5 2015.

[38] Daniel P. Buxhoeveden and Manuel F. Casanova. *The minicolumn hypothesis in neuroscience*. Brain, 125:935–951, 5 2002.

[39] PA Hasgall, F Di Gennaro, C Baumgartner, E Neufeld, B Lloyd, MC Gosselin, D Payne, A Klingenböck, and N Kuster. *IT'IS Database for thermal and electromagnetic parameters of biological tissues*. 4.0, 5 2018.

[40] Center for Devices and Radiological Health. *Food and drug administration, U.S. Department of Health and Human Services Marketing Clearance of Diagnostic Ultrasound Systems and Transducers*. 6 2019.

[41] H. T. O'Neil. *Theory of Focusing Radiators*. The Journal of the Acoustical Society of America, 21:516–526, 9 1949.

[42] Jerel K Mueller, Leo Ai, Priya Bansal, and Wynn Legon. *Computational exploration of wave propagation and heating from transcranial focused ultrasound for neuromodulation*. Journal of Neural Engineering, 13, 10 2016.

[43] D. N. Stephens, D. E. Kruse, Shengping Qin, and K. W. Ferrara. *Design aspects of focal beams from high-intensity arrays*. IEEE Transactions on Ultrasonics, Ferroelectrics and Frequency Control, 58:1590–1602, 8 2011.

[44] Shingo Murakami and Yoshio Okada. *Contributions of principal neocortical neurons to magnetoencephalography and electroencephalography signals*. The Journal of Physiology, 575:925–936, 9 2006. Info on dipole moment strength.

[45] Biyu J. He. *Scale-free brain activity: past, present, and future*. Trends in Cognitive Sciences, 18:480–487, 9 2014.

[46] Klas H. Pettersen, Henrik Lindén, Tom Tetzlaff, and Gaute T. Einevoll. *Power Laws from Linear Neuronal Cable Theory: Power Spectral Densities of the Soma Potential, Soma Membrane Current and Single-Neuron Contribution to the EEG*. PLoS Computational Biology, 10, 11 2014.

[47] Steven X. Moffett, Sean M. O'Malley, Shushuang Man, Dawei Hong, and Joseph V. Martin. *Dynamics of high frequency brain activity*. Scientific Reports, 7, 12 2017.

[48] Aman S Aberra, Angel V Peterchev, and Warren M Grill. *Biophysically realistic neuron models for simulation of cortical stimulation*. Journal of Neural Engineering, 15, 12 2018.

[49] Rosanna Migliore, Carmen A. Lupascu, Luca L. Bologna, et al. *The physiological variability of channel density in hippocampal CA1 pyramidal cells and interneurons explored using a unified data-driven modeling workflow*. PLOS Computational Biology, 14, 9 2018.

[50] Shingo Murakami, Akira Hirose, and Yoshio C. Okada. *Contribution of Ionic Currents to Magnetoencephalography (MEG) and Electroencephalography (EEG) Signals Generated by Guinea-Pig CA3 Slices*. The Journal of Physiology, 553:975–985, 12 2003.

[51] Qian Li, Ragnar Olafsson, Pier Ingram, Zhaohui Wang, and Russell Witte. *Measuring the acoustoelectric interaction constant using ultrasound current source density imaging*. Physics in Medicine and Biology, 57:5929–5941, 10 2012.

[52] Ragnar Olafsson, Russell S. Witte, Sheng-Wen Huang, and Matthew O'Donnell. *Ultrasound Current Source Density Imaging*. IEEE Transactions on Biomedical Engineering, 55:1840–1848, 7 2008. Afleiding UCSDI reconstruction.

[53] Julius Zimmermann and Ursula van Rienen. *Ambiguity in the interpretation of the low-frequency dielectric properties of biological tissues*. Bioelectrochemistry, 140, 8 2021.

[54] Edin Mehić, Julia M. Xu, Connor J. Caler, Nathaniel K. Coulson, Chet T. Moritz, and Pierre D. Mourad. *Increased Anatomical Specificity of Neuromodulation via Modulated Focused Ultrasound*. PLoS ONE, 9, 2 2014.

[55] Wynn Legon, Tomokazu F Sato, Alexander Opitz, Jerel Mueller, Aaron Barbour, Amanda Williams, and William J Tyler. *Transcranial focused ultrasound modulates the activity of primary somatosensory cortex in humans*. Nature Neuroscience, 17:322–329, 2 2014.

[56] David P. Darrow, Parker O'Brien, Thomas J. Richner, Theoden I. Netoff, and Emad S. Ebbini. *Reversible neuroinhibition by focused ultrasound is mediated by a thermal mechanism*. Brain Stimulation, 12:1439–1447, 11 2019.

[57] Sangjin Yoo, David R. Mittelstein, Robert C. Hurt, Jerome Lacroix, and Mikhail G. Shapiro. *Focused ultrasound excites cortical neurons via mechanosensitive calcium accumulation and ion channel amplification*. Nature Communications, 13:493, 1 2022.

[58] Michael Plaksin, Einat Shapira, Eitan Kimmel, and Shy Shoham. *Thermal Transients Excite Neurons through Universal Intramembrane Mechanoelectrical Effects*. Physical Review X, 8:011043, 3 2018.

[59] Mike D. Menz, Patrick Ye, Kamyar Firouzi, Amin Nikoozadeh, Kim Butts Pauly, Pierre Khuri-Yakub, and Stephen A. Baccus. *Radiation Force as a Physical Mechanism for Ultrasonic Neurostimulation of the Ex Vivo Retina*. The Journal of Neuroscience, 39:6251–6264, 8 2019.

[60] Ben Sorum, Robert A. Rietmeijer, Karthika Gopakumar, Hillel Adesnik, and Stephen G. Brohawn. *Ultrasound activates mechanosensitive TRAAK K+ channels through the lipid membrane*. Proceedings of the National Academy of Sciences, 118, 2 2021.

[61] Martin Loynaz Prieto, Kamyar Firouzi, Butrus T. Khuri-Yakub, and Merritt Maduke. *Activation of Piezo1 but Not NaV1.2 Channels by Ultrasound at 43 MHz*. Ultrasound in Medicine and Biology, 44:1217–1232, 6 2018.

[62] Thomas Tarnaud, Wout Joseph, Ruben Schoeters, Luc Martens, and Emmeric Tanghe. *Improved alpha-beta power reduction via combined electrical and ultrasonic stimulation in a parkinsonian cortex-basal ganglia-thalamus computational model*. Journal of Neural Engineering, 18, 12 2021.

[63] Théo Lemaire, Esra Neufeld, Niels Kuster, and Silvestro Micera. *Understanding ultrasound neuromodulation using a computationally efficient and interpretable model of intramembrane cavitation*. Journal of Neural Engineering, 16:046007, 7 2019.

[64] Thomas Tarnaud, Wout Joseph, Ruben Schoeters, Luc Martens, and Emmeric Tanghe. *SECONIC: Towards multi-compartmental models for ultrasonic brain stimulation by intramembrane cavitation*. Journal of Neural Engineering, 17:056010, 10 2020.

[65] Taewon Kim, Christine Park, Pratik Y. Chhatbar, Jody Feld, Brian Mac Grory, Chang S. Nam, Pu Wang, Mengyue Chen, Xiaoning Jiang, and Wuwei Feng. *Effect of Low Intensity Transcranial Ultrasound Stimulation on Neuromodulation in Animals and Humans: An Updated Systematic Review*. Frontiers in Neuroscience, 15, 4 2021.

[66] Michael Plaksin, Eitan Kimmel, and Shy Shoham. *Cell-Type-Selective Effects of Intramembrane Cavitation as a Unifying Theoretical Framework for Ultrasonic Neuromodulation*. eneuro, 3, 5 2016.

[67] Felix Darvas, Edin Mehić, Connor J. Caler, Jeff G. Ojemann, and Pierre D. Mourad. *Toward Deep Brain Monitoring with Superficial EEG Sensors Plus Neuromodulatory Focused Ultrasound*. Ultrasound in Medicine and Biology, 42:1834–1847, 8 2016.

[68] Thomas Tarnaud, Wout Joseph, Luc Martens, and Emmeric Tanghe. *Computational Modeling of Ultrasonic Subthalamic Nucleus Stimulation*. IEEE Transactions on Biomedical Engineering, 66:1155–1164, 4 2019.

[69] Tomokazu Sato, Mikhail G. Shapiro, and Doris Y. Tsao. *Ultrasonic Neuromodulation Causes Widespread Cortical Activation via an Indirect Auditory Mechanism*. Neuron, 98:1031–1041.e5, 6 2018.

[70] Hongsun Guo, Mark Hamilton, Sarah J. Offutt, Cory D. Gloeckner, Tianqi Li, Yohan Kim, Wynn Legon, Jamu K. Alford, and Hubert H. Lim. *Ultrasound Produces Extensive Brain Activation via a Cochlear Pathway*. Neuron, 98:1020–1030.e4, 6 2018.

[71] György Buzsáki and Kenji Mizuseki. *The log-dynamic brain: how skewed distributions affect network operations*. Nature Reviews Neuroscience, 15:264–278, 4 2014.

[72] Robert A. McDougal, Thomas M. Morse, Ted Carnevale, Luis Marenco, Rixin Wang, Michele Migliore, Perry L. Miller, Gordon M. Shepherd, and Michael L. Hines. *Twenty years of ModelDB and beyond: building essential modeling tools for the future of neuroscience*. Journal of Computational Neuroscience, 42:1–10, 2 2017.

[73] Nicholas T. Carnevale and Michael L. Hines. *The NEURON Book*. Cambridge University Press, 1 2006.

6

Conclusions and Future Perspectives

6.1 Conclusions

Neuroscience has made remarkable progress in recent years. Despite these advancements, a significant part of the population remains vulnerable to neurological disorders. These disorders severely impact a patient's quality of life and impose a substantial economic burden. Encouragingly, new insights into neural circuitry emerge daily, and promising techniques for the treatment of neurological disorders are being investigated. Additionally, there is a notable shift from open- to closed-loop systems, aiming to reduce redundant stimulation by enabling real-time adjustments. For these systems to achieve on-demand control, the recording of electrophysiological activity with high spatial and temporal resolution is crucial. Nonetheless, further research and development is necessary to unlock the full potential of current systems and make clinical translation possible.

This dissertation falls within the field of computational neuroscience, aiming to contribute to unraveling the complexities of the nervous system using mathematical models. The chapters within this dissertation explored optogenetic neuromodulation, hippocampal modeling, and functional neuroimaging, all with the overarching goal of advancing the treatment of temporal lobe epilepsy.

In chapter 2, I extensively discussed the optogenetic toolbox. Optogenetics is a promising neuromodulation technique, offering precise control over neural activity with high spatial and temporal precision. While theoretically offering the ideal properties for effective neural control, practical challenges, including gene therapy safety concerns, invasiveness of optical stimulators, and the transition from rodents to humans hinder its clinical translation. I also introduced a novel double two-state

opsin model, improving computational efficiency and accuracy in opsin modeling. Furthermore, an autonomous fitting procedure was described, which was used to successfully fit two distinctive opsins, ChR2(H134R) and MerMAID, within an acceptable timeframe and with acceptable computational resources.

Chapter 3 presented the results from my study on the optogenetic excitability of CA1 neurons. I coupled opsin modeling with light propagation to study the effect of various uncertain parameters. Moreover, it allowed me to pinpoint optimal fiber positions. I showed that confinement of the opsin to a specific neuronal membrane compartment can significantly enhance excitability. Notably, the findings demonstrated threshold reductions exceeding 64%, with up to 100% gains in the surface area of fiber positions for neuronal activation. Additionally, the simulations showed that the perpendicular orientation of the optical source relative to the somato-dendritic axis yielded the highest excitability when aligned towards the neuron types most excitable regions, i.e., the basal dendrites and soma in the pyramidal cells and interneurons, respectively. My study also identified significant inter-cell variability, highlighting the importance of considering neuron degeneracy in optogenetic tool development. The results shown in this chapter contribute towards the development of more effective stimulation protocols.

Chapter 4 outlined my efforts to create a network model of an epileptic hippocampus. Such a model is a valuable tool for testing neuromodulation strategies within a network context, fine-tuning stimulation parameters, and gaining insights into disease pathologies. In the chapter, I showed that native hippocampal activity can be effectively modeled with a limited number of simplified compartmental neuron models, and seizure-like activity can be partially replicated by incorporating epileptic pathologies. Two epileptic models are tested: the in-vitro elevated extracellular potassium model and mesial temporal lobe epilepsy histopathologies. Although the model was not fit to data with elevated potassium levels, it successfully reproduces similarities with experimental data. Examples include spontaneous activity occurring only after a 2.61-fold increase and the observation of oscillatory activity in the CA1 following Schaffer collateral stimulation. Subsequently, the results of histopathological changes characteristic of mesial temporal lobe epilepsy indicate that recurrent connections play a crucial role in inducing epileptic seizure-like activity originating in the hippocampus. Moreover, the loss of granule cells and CA1 cells results in reduced burst behavior. However, these findings are preliminary, requiring further validation. Additionally, the study highlights the limitations of simplifications in reproducing all forms of neural activity. Nevertheless, it suggests the potential utility of this epileptic network model as a tool for investigating epileptic seizure suppression techniques, such as optogenetics.

In chapter 5, I explored the potential of ultrasound-based functional neuroimaging, termed acousto-electrophysiological neuroimaging, by investigating the feasibility of using mechanical vibration to probe local electrophysiological activity. It is hypothesized that such an approach allows recording of activity, minimally to non-invasively, with high spatial and temporal resolution. This would be an important advancement for the development of closed-loop neuromodulation systems. The study was performed using dipole models in a simplified head model consisting

of concentric spheres. I showed that endogenous activity gets modulated onto the ultrasonic frequency via mechanical vibration. Moreover, the signal strengths strongly and non-linearly depend on the alignment between the dipole, vibration direction, and measuring positions. For a displacement amplitude of only 10 nm (a US-field amplitude well within FDA-limits) and a 5 nAm dipole moment, only signal strengths of 1.24 pV can be measured at the scalp. For a dipole at the center of the brain, these drop even below 0.16 pV. My study showed that feasibility strongly depends on the inherent, currently unknown, activity of the brain at ultrasonic frequencies. Given these results, the technique is likely not feasible with current technology given the low signal strengths of normal activity. However, scanning for hyperactive zones could be more promising, as signal strength scales linearly with the activity of the probed zone.

In conclusion, this dissertation demonstrated the role of computational neuroscience in advancing our understanding of neuromodulation techniques, neural circuitry, and functional neuroimaging. The results of this dissertation can aid in the development of more effective treatments for neurological disorders, ultimately improving the quality of life for those who are affected.

6.2 Future Work and Perspectives

The roots of computational neuroscience trace back to 1952 with Hodgkin and Huxley's pioneering work on the descriptive model of the action potential. However, the field's exponential growth has only been realized in the past two decades, driven by the surge in computational power. Construction of a biophysically accurate conductance-based model of a cortical column, and the ongoing development of a full CA1 mouse region model, are now achievable due to the arrival of supercomputers [1, 2]. While the ambitious vision of the Human Brain Project to create a detailed model of the entire brain still faces criticism, recent developments like EBRAINS (ebrains.eu) and modelDB (modeldb.science), offering open access to models, tools, and data, have the potential to further propel the field by enhancing accessibility and lowering entry barriers.

The results in this dissertation only scratch the surface. To truly refine and expand therapies and interventions in neuroscience, continued investigation is imperative. Limitations and interesting aspects for future work were already presented at the end of each chapter. I reiterate some of the key aspects here and introduce additional perspectives in computational modeling.

Extensions in Optogenetic Neuromodulation Modeling

In chapter 3, I presented my work on the optogenetic excitability of CA1 cells. This initial step, focused on isolated cells, provided crucial insights into stimulation thresholds, inter-cell variability, optimal optrode locations, and the influence of various uncertain parameters. In a next step, it is essential to extend this study towards excitability in network simulations. Isolated neurons at rest differ from

those submerged in a network where they receive diverse synaptic inputs. The impact on the required intensity levels should be tested. Additionally, my study was limited to single-pulse excitation, while DBS uses high-frequency stimulation (>100 Hz) to suppress seizures. It should be examined whether reliable phase-locked spiking can be achieved with short optical pulses. Furthermore, potential upper limits on excitable frequencies due to opsin light adaptation and closing rates should be explored. Similarly, it could be meaningful to investigate the modulation effect under prolonged illumination. Even though long illumination paradigms are less likely to be used in a clinical setting due to tissue heating limitations.

A promising avenue of research entails enhancing biophysical realism in modeling optogenetic modulation. There are two interesting improvements. The first extension involves incorporating the opsin current's impact on local ion concentrations. Therefore, the permeability profile must be known. High transmembrane currents could disrupt ion balance, potentially altering neuron function. For example, Mahn et al. (2018) observed GtACR2-mediated axonal excitation [3] due to the disruption of the chloride balance. Second, the model could include temperature effects. Visible light gets highly absorbed by brain tissue resulting in heating. Behavioral changes can manifest even with modest temperature fluctuations ($> 1\,^{\circ}\mathrm{C}$). Several neural parameters, e.g., capacitance, ion channel conductance, and transmitter release and uptake, have been shown to exhibit temperature dependence [4–7]. The change in temperature can be determined by solving the bioheat equation.

Another interesting research avenue is the investigation of neuromodulation with inhibitory opsins, interesting opsins to be studied are GtACR2 and WiChr [8, 9]. The advantage of excitatory opsin studies is the clear and unambiguous, quantifiable metric of action potential generation. However, the difficulty of inhibitory studies lies in the typical shunting effect of the opsin's photocurrent. For a neuron at rest, this will result in an unobservable voltage deflection. The go-to metric will be action potential inhibition. However, the metric contains at least two degrees of freedom, being the input strength responsible for action potential generation, and the light intensity for the opening of the opsin. This poses an additional challenge in this type of studies.

In the context of an epileptic network model, it is crucial to ascertain whether optical excitation of interneurons results in seizure suppression or disinhibition [10]. Other interesting research hypotheses include assessing suppression via information lesion by stimulating pyramidal cells with high-frequency, phase-locked stimulation, investigating axonal conduction block under prolonged illumination, exploring synaptic depression, and studying network desynchronization. The inclusion of inhibitory opsins opens up the possibility of bidirectional control and localized synaptic input mitigation, affecting synaptic plasticity and seizure suppression [11].

As described in section 2.1.1, in the last decade numerous new opsins were discovered and genetically engineered. The vast expansion makes it difficult for computational modeling to keep up. Even though I presented an autonomous fitting procedure, a difficulty lies in gathering comprehensive datasets for model fitting. Datasets like the one reported by Williams et al. (2013) [12], encompassing a complete raster of holding potentials and irradiances for single and two-pulse

experiments, are scarce. Ideally, computational modeling should transition to a proactive approach, where the model specifies the ideal opsin properties based on predefined targets. However, achieving this goal requires defining a clear set of targets, given the model's high dimensionality and otherwise mathematical underdetermination.

In addition to neuronal modeling, light propagation in neural tissue merits further research attention. The binary classification of brain tissue into gray and white matter oversimplifies the continuum of tissue properties. The impact of the uncertainty of these parameters on the optogenetic excitability was tested in chapter 3. The results showed that the influence is only marginal for variations near the parameters' reported means. However, the tissue parameters of white matter differ from gray matter [13]. Additionally, tissue alterations due to foreign body reaction occur. A fibrous capsule is formed around the implanted fiber as a reaction to blood-brain-barrier injury and gliosis caused by the presence of the implanted fiber itself [14]. Therefore, light propagation modeling should be extended to heterogeneous tissues. Advanced mesh and voxel-based Monte Carlo algorithms can accurately model the light field distribution in complex tissues, providing insights into light propagation in realistic brain environments [15]. Furthermore, exploring the propagation of light at different wavelengths, such as for the excitation of red-shifted opsins, would also be of interest. Other interesting topics are fiber tapering, flat tip patterning and alteration of the geometric properties which can result in improved output coupling or broadened and multi-site illumination [14, 16].

Acousto-Electrophysiological Neuroimaging

In future research, several avenues for advancing acousto-electrophysiological neuroimaging (AENI) are worth exploring. Firstly, considering the acousto-electric (AE) effect by accounting for oscillating conductivity in the brain [17] could enhance the accuracy of AENI models. This may involve investigating the relative dominance of both underlying mechanisms, i.e., AE and mechanical vibrating current sources, under various conditions like waveform, transducer placement, and dipole location.

Secondly, exploring the potential benefits of modulated focused ultrasound [18], with a focus on reducing the mechanical index (MI), is another avenue. Investigating whether the acoustic particle velocity amplitude is linked to the beat frequency could help in increasing the AENI signal-to-noise ratio. In this case, the mechanical index would be $\mathrm{MI} = \mathrm{PNP}[\mathrm{MPa}]/\sqrt{f_\mathrm{c}[\mathrm{MHz}]} = (2\pi A Z_\mathrm{ac} f_\mathrm{b})/\sqrt{f_\mathrm{c}}$. A smaller ratio of beat to carrier frequency might result in a reduced MI, enhancing the safety and efficacy of AENI.

Finally, it is crucial to establish limits on neuromodulation induced by ultrasound during AENI. While the primary aim of AENI is to record endogenous brain activity, ultrasound has demonstrated the ability to modulate brain activity. Computational modeling can aid in defining the parameter space in which AENI remains feasible without significantly affecting the endogenous neural activity.

Closed Loop Optogenetics

Currently, most neuromodulation systems operate in an open-loop mode. Here, the system provides continuous stimulation based on manually selected settings set by a clinician. This approach presents notable shortcomings. First, continuous stimulation may disrupt normal brain function. Second, it imposes high energy demands, necessitating advancements in battery technology or wireless power delivery for implanted devices [19].

The future of neuromodulation technologies lies in closed-loop systems. These hold the promise of real-time adjusting stimulation based on clinically relevant physiological signals, providing a dynamic and personalized approach to therapy. Due to their on-demand control, the aforementioned drawbacks of open-loop are mitigated. The technologies are already slowly shifting towards closed-loop systems. However, most closed-loop systems are currently limited to on-demand control with fixed stimuli. Probably most challenging is the identification of reliable biomarkers, potentially a combination of mesoscopic oscillations, microscopic neural firing, and non-neural activity like heart rate. Crucial here will be the recording of electrophysiological activity with high spatial and temporal resolution, which could potentially be achieved with acousto-electrophysiological neuroimaging. Based on these biomarkers, the system should be able to assess neurological states, triggering stimulation, and ideally be able to predict state changes for proactive adjustments. Such improvements would minimize time-lag and pave the way for personalized therapy. In this context, computational modeling can play an important role in pinpointing essential biomarkers and optimizing control parameters [19, 20].

Optogenetic neuromodulation integrates perfectly with closed-loop systems, offering an alternative to traditional electrical stimulation sources. Unlike electrical stimulation, which introduces artifacts into recordings, optogenetics provides artifact-free stimulation, enabling continuous recording. Despite the current relatively limited applications, closed-loop optogenetic manipulations have proven to be useful in elucidating the functional and behavioral roles of specific neural activity patterns [21, 22]. The models developed in this dissertation can serve as the foundation for constructing a computational framework to investigate closed-loop optogenetic neuromodulation for the treatment of temporal lobe epilepsy.

Furthermore, an interesting avenue involves exploring the modulation of non-neural cells, such as astrocytes. This offers the potential to influence the ionic composition of the interstitial fluid and, consequently, neuronal excitability. Astrocyte-based interventions could provide sustained optogenetic control. This is particularly valuable in conditions like temporal lobe epilepsy, characterized by astrocyte proliferation and necessitating long-term therapeutic strategies [23].

Computational Neuroscience and Experimental Research

Computational neuroscience employs mathematical tools and theories to study the nervous system. Its main advantage is its ability to systematically explore experimentally inaccessible aspects. Consequently, it proves to be an ideal tool for

enhancing the understanding of underlying mechanisms, exemplified in this dissertation by the investigation of optogenetic interactions with CA1 cells. The insights gained from such studies can guide more targeted research, thereby improving therapies. Computational modeling has demonstrated effectiveness in electrostimulation, facilitating the design of novel electrode configurations and optimization of applied waveforms. The models developed in this dissertation can also be utilized to identify optimal fiber positions and stimulation protocols for optogenetic neuromodulation, as was demonstrated in isolated CA1 neurons (chapter 3). When integrated into a network model (chapter 4), these tools can pinpoint effective stimulation strategies for treating temporal lobe epilepsy. However, due to uncertainties inherent in the models, predictions may not yield the "ideal" stimulation set. Nevertheless, they can reveal the safety limits and provide an estimation of the optimal configuration.

However, computational models are only a complementary tool to experimental research. To make a computational model useful, an initial investment in experimental data collection is essential. Subsequently, the developed models can be employed to test and postulate new hypotheses, as seen in the exploration of increased optogenetic excitability due to subcellular opsin restriction or perpendicular fiber positioning (chapter 3). These hypotheses then require experimental validation. To align models with experimental results, they can be fine-tuned to enhance biological realism. Examples of valuable model improvements in this dissertation that necessitate additional experimental data include the impact of local ion concentrations, pH and temperature dependence on cell and channel behavior, improved opsin model responses to short pulses, and the endogenous noise at MHz-frequencies.

Accurate representation of neural activity by models has the potential to reduce the need for animal experiments. This reduction is achieved by refining research questions after systematic exploration with computational models first. Consequently, only targeted experiments are required. The long-term goal is replacement by the development of digital twins. However, due to the nervous system's complexity, limited computational resources, and the need for interpretability, a trade-off between biological realism and simplicity remains necessary to date.

Artificial Intelligence

The arrival of generative artificial intelligence (AI), like ChatGPT, is literally transforming daily life with its ability to handle laborious tasks. These applications span a wide range, including the generation of new images, text summarization, code generation based on textual prompts, and proofreading and enhancement of textual coherence (applied in this dissertation). The innovative pace of AI is currently so fast that even voices are raised expressing concerns [24]. It is also finding its way into (computational) neuroscience. Therefore, in this final section, I would like to discuss the intersection of AI and neuroscience.

The relationship between neuroscience and AI has a rich history of mutual influence. Neuroscience has served as a source of inspiration for the development of various algorithms and architectural designs. A prominent example is artificial neural networks (ANN, what's in a name), where the basic elements, known as

perceptrons, are modeled after neurons. Deep neural networks, resembling the brain's information processing, consist of multiple layers of diverse building blocks. Some AI architectures, like long short-term memory networks, also draw inspiration from neuroscience. Conversely, AI has offered valuable insights into neuronal processes. For instance, convolutional neural networks (CNNs) have contributed to the comprehension of high-level visual areas. An interesting overview of these reciprocal contributions is given by Hassabis et al. (2017) [25].

AI has already proven to be useful in neuroscience, especially in classification. Convolutional neural networks excel in tasks like tumor recognition in medical images. Machine learning algorithms have proven highly accurate in identifying disease episodes, such as seizures, tremors, and other motor symptoms. Overall, there is an evolving trend towards deep learning, where raw data serves as input and systems autonomously learn feature extraction, unlike with machine learning, which relies on predefined features. This shift not only holds the potential to enhance outcomes but also analyzing the neural network's architecture layers can improve understanding of how biological systems process information. Furthermore, ongoing efforts are directed toward training algorithms capable of predicting forthcoming episodes, a development that could significantly advance closed-loop stimulation systems [20].

ANNs are progressively finding their place in computational neuroscience. For instance, Golabek et al. (2023) developed ANN models aimed at rapidly and accurately predicting the neuronal response to DBS stimulation [26]. Their models were trained using data generated from multi-compartment cable models of axons subjected to predictions from a finite-element model of the implanted DBS system. Remarkably, their ANN models exhibited a speed enhancement of 4 to 5 orders of magnitude while maintaining low prediction errors. Another example is given by Baby et al. (2020). They introduced a hybrid model that incorporates a CNN. This model can serve as a real-time end-to-end solution for simulating human cochlear mechanics, delivering a speed boost of 3 orders of magnitude compared to conventional transmission line models [27].

An adaptation of the ANN is spiking neural networks (SNN). In ANNs, the biophysical analog of perceptron inputs is typically represented by neuron firing rates. In contrast, SNNs include individual spike times from multiple neurons, more closely resembling biological neuronal networks hence having a higher empirical content [28]. The fundamental components of SNNs are typically leaky integrate-and-fire models, a model often used in computational neuroscience as a faster alternative to Hodgkin-and-Huxley model. Compared to Hodgkin-and-Huxley networks, a SNN is more easily fit, being, for instance, not affected by ion channel degeneracy [29]. Furthermore, Brette (2015) even argued that a SNN is biologically more realistic than single compartment Hodgkin-and-Huxley networks [30].

In conclusion, the integration of AI in neuroscience is inevitable, however, providing a valuable new tool. AI can be harnessed to study the complex nervous system by training deep neural networks on electrophysiological data and drawing conclusions from the ideal architectural fits. Alternatively, AI can replace computationally intensive models to enhance prediction speed in cases where detailed

voltage traces are unnecessary. Moreover, AI holds promise for numerous clinical applications, with classification and prediction in closed-loop systems representing just the beginning of its potential impact in the field.

References

[1] Henry Markram, Eilif Muller, Srikanth Ramaswamy, et al. *Reconstruction and Simulation of Neocortical Microcircuitry*. Cell, 163:456–492, 10 2015.

[2] Armando Romani, Alberto Antonietti, Davide Bella, et al. *Community-based Reconstruction and Simulation of a Full-scale Model of Region CA1 of Rat Hippocampus*. bioRxiv, page 2023.05.17.541167, 1 2023.

[3] Mathias Mahn, Lihi Gibor, Pritish Patil, Katayun Cohen-Kashi Malina, Shir Oring, Yoav Printz, Rivka Levy, Ilan Lampl, and Ofer Yizhar. *High-efficiency optogenetic silencing with soma-targeted anion-conducting channelrhodopsins*. Nature Communications, 9:4125, 10 2018.

[4] Anirudh R Acharya, Bram Vandekerckhove, Lars Emil Larsen, Jean Delbeke, Wytse J Wadman, Kristl Vonck, Evelien Carette, Alfred Meurs, Jan Vanfleteren, Paul Boon, Jeroen Missinne, and Robrecht Raedt. *In vivo blue light illumination for optogenetic inhibition: effect on local temperature and excitability of the rat hippocampus*. Journal of Neural Engineering, 18:066038, 12 2021.

[5] Z Fekete, Á C Horváth, and A Zátonyi. *Infrared neuromodulation:a neuroengineering perspective*. Journal of Neural Engineering, 17:051003, 10 2020.

[6] Eugene A. Kiyatkin. *Brain temperature and its role in physiology and pathophysiology: Lessons from 20 years of thermorecording*. Temperature, 6:271–333, 10 2019.

[7] Helton M. Peixoto, Rossana M. S. Cruz, Thiago C. Moulin, and Richardson N. Leão. *Modeling the Effect of Temperature on Membrane Response of Light Stimulation in Optogenetically-Targeted Neurons*. Frontiers in Computational Neuroscience, 14:5, 2 2020.

[8] Elena G. Govorunova, Oleg A. Sineshchekov, Roger Janz, Xiaoqin Liu, and John L. Spudich. *Natural light-gated anion channels: A family of microbial rhodopsins for advanced optogenetics*. Science, 349:647–650, 8 2015.

[9] Johannes Vierock, Enrico Peter, Christiane Grimm, Andrey Rozenberg, I-Wen Chen, Linda Tillert, Alejandro G. Castro Scalise, Marilù Casini, Sandra Augustin, Dimitrii Tanese, Benoît C. Forget, Rémi Peyronnet, Franziska Schneider-Warme, Valentina Emiliani, Oded Béjà, and Peter Hegemann. *WiChR, a highly potassium-selective channelrhodopsin for low-light one- and two-photon inhibition of excitable cells*. Science Advances, 8, 12 2022.

[10] Robert C. Wykes, Dimitri M. Kullmann, Ivan Pavlov, and Vincent Magloire. *Optogenetic approaches to treat epilepsy*. Journal of Neuroscience Methods, 260:215–220, 2 2016.

[11] Mathieu Sprengers, Robrecht Raedt, Lars Emil Larsen, Jean Delbeke, Wytse Jan Wadman, Paul Boon, and Kristl Vonck. *Deep brain stimulation reduces evoked potentials with a dual time course in freely moving rats: Potential neurophysiological basis for intermittent as an alternative to continuous stimulation*. Epilepsia, 61:903–913, 5 2020.

[12] John C. Williams, Jianjin Xu, Zhongju Lu, Aleksandra Klimas, Xuxin Chen, Christina M. Ambrosi, Ira S. Cohen, and Emilia Entcheva. *Computational Optogenetics: Empirically-Derived Voltage- and Light-Sensitive Channelrhodopsin-2 Model*. PLoS Computational Biology, 9:e1003220, 9 2013.

[13] A. N. Yaroslavsky, P. C. Schulze, I. V. Yaroslavsky, R. Schober, F. Ulrich, and H. J. Schwarzmaier. *Optical properties of selected native and coagulated human brain tissues in vitro in the visible and near infrared spectral range*. Physics in Medicine and Biology, 47:2059, 6 2002.

[14] Bram Vandekerckhove, Jeroen Missinne, Kristl Vonck, Pieter Bauwens, Rik Verplancke, Paul Boon, Robrecht Raedt, and Jan Vanfleteren. *Technological Challenges in the Development of Optogenetic Closed-Loop Therapy Approaches in Epilepsy and Related Network Disorders of the Brain*. Micromachines, 12:38, 12 2020.

[15] Shijie Yan and Qianqian Fang. *Hybrid mesh and voxel based Monte Carlo algorithm for accurate and efficient photon transport modeling in complex bio-tissues*. Biomedical Optics Express, 11:6262, 11 2020.

[16] Gorgi Kostovski, Paul R. Stoddart, and Arnan Mitchell. *The Optical Fiber Tip: An Inherently Light-Coupled Microscopic Platform for Micro- and Nanotechnologies*. Advanced Materials, 26:3798–3820, 6 2014.

[17] Ragnar Olafsson, Russell S. Witte, Sheng-Wen Huang, and Matthew O'Donnell. *Ultrasound Current Source Density Imaging*. IEEE Transactions on Biomedical Engineering, 55:1840–1848, 7 2008. Afleiding UCSDI reconstruction.

[18] Edin Mehić, Julia M. Xu, Connor J. Caler, Nathaniel K. Coulson, Chet T. Moritz, and Pierre D. Mourad. *Increased Anatomical Specificity of Neuromodulation via Modulated Focused Ultrasound*. PLoS ONE, 9, 2 2014.

[19] Tim Denison and Martha J. Morrell. *Neuromodulation in 2035 The Neurology Future Forecasting Series*. Neurology, 98:65–72, 1 2022.

[20] Anirudha S. Chandrabhatla, I. Jonathan Pomeraniec, Taylor M. Horgan, Elizabeth K. Wat, and Alexander Ksendzovsky. *Landscape and future directions of machine learning applications in closed-loop brain stimulation*. npj Digital Medicine, 6:79, 4 2023.

[21] Antonio Fernandez-Ruiz, Azahara Oliva, and Hongyu Chang. *High-resolution optogenetics in space and time*. Trends in Neurosciences, 45:854–864, 11 2022.

[22] Mingrui Zhao, Rose Alleva, Hongtao Ma, Andy G.S. Daniel, and Theodore H. Schwartz. *Optogenetic tools for modulating and probing the epileptic network*. Epilepsy Research, 116:15–26, 2015.

[23] Jan Tønnesen and Merab Kokaia. *Epilepsy and optogenetics: can seizures be controlled by light?* Clinical Science, 131:1605–1616, 7 2017.

[24] Toby Shevlane, Sebastian Farquhar, Ben Garfinkel, et al. *Model evaluation for extreme risks*. 5 2023.

[25] Demis Hassabis, Dharshan Kumaran, Christopher Summerfield, and Matthew Botvinick. *Neuroscience-Inspired Artificial Intelligence*. Neuron, 95:245–258, 7 2017.

[26] Justin Golabek, Matthew Schiefer, Joshua K. Wong, Shreya Saxena, and Erin Patrick. *Artificial neural network-based rapid predictor of biological nerve fiber activation for DBS applications*. Journal of Neural Engineering, 20, 2 2023.

[27] Deepak Baby, Arthur Van Den Broucke, and Sarah Verhulst. *A convolutional neural-network model of human cochlear mechanics and filter tuning for real-time applications*. Nature Machine Intelligence, 3:134–143, 2 2021.

[28] Kashu Yamazaki, Viet Khoa Vo-Ho, Darshan Bulsara, and Ngan Le. *Spiking Neural Networks and Their Applications: A Review*. Brain Sciences, 12, 7 2022.

[29] Christian Pozzorini, Skander Mensi, Olivier Hagens, Richard Naud, Christof Koch, and Wulfram Gerstner. *Automated High-Throughput Characterization of Single Neurons by Means of Simplified Spiking Models*. PLOS Computational Biology, 11:e1004275, 6 2015.

[30] Romain Brette. *What Is the Most Realistic Single-Compartment Model of Spike Initiation?* PLOS Computational Biology, 11:e1004114, 4 2015.